

Polymer Nanocomposites

September 1, 2012 | <http://pubs.acs.org>
Publication Date: November 6, 2001 | doi: 10.1021/bk-2002-0804.fw001

ACS SYMPOSIUM SERIES **804**

Polymer Nanocomposites
Synthesis, Characterization, and
Modeling

Ramanan Krishnamoorti, Editor
University of Houston

Richard A. Vaia, Editor
Air Force Research Laboratory



American Chemical Society, Washington, DC

In Polymer Nanocomposites; Krishnamoorti, R., et al.;
ACS Symposium Series; American Chemical Society: Washington, DC, 2001.



**Polymer nanocomposites :
synthesis, characterization,**

Library of C

Polymer nanocomposites : synthesis, characterization, and modeling / Ramanan Krishnamoorti, editor, Richard A. Vaia,, editor.

p. cm.—(ACS symposium series ; 804)

“Developed from a symposium sponsored by the Division of Polymeric Materials: Science and Engineering at the 219th National Meeting of the American Chemical Society, San Francisco, California, March 26–30, 2000.”

Includes bibliographical references and index.

ISBN 0–8412–3768–9

1. Nanostructure materials—Congresses. 2. Polymeric composites— Congresses..

I. Krishnamoorti, Ramanan. II. Vaia, Richard A. III. American Chemical Society. Meeting (219th : 2000 : San Francisco, Calif.) IV. American Chemical Society. Division of Polymeric Materials: Science and Engineering. V. Series.

TA418.9.N35 P66 2001
620.1'92—dc21

2001046392

The paper used in this publication meets the minimum requirements of American National Standard for Information Sciences—Permanence of Paper for Printed Library Materials, ANSI Z39.48–1984.

Copyright © 2002 American Chemical Society

Distributed by Oxford University Press

All Rights Reserved. Reprographic copying beyond that permitted by Sections 107 or 108 of the U.S. Copyright Act is allowed for internal use only, provided that a per-chapter fee of \$20.50 plus \$0.75 per page is paid to the Copyright Clearance Center, Inc., 222 Rosewood Drive, Danvers, MA 01923, USA. Republication or reproduction for sale of pages in this book is permitted only under license from ACS. Direct these and other permission requests to ACS Copyright Office, Publications Division, 1155 16th St., N.W., Washington, DC 20036.

The citation of trade names and/or names of manufacturers in this publication is not to be construed as an endorsement or as approval by ACS of the commercial products or services referenced herein; nor should the mere reference herein to any drawing, specification, chemical process, or other data be regarded as a license or as a conveyance of any right or permission to the holder, reader, or any other person or corporation, to manufacture, reproduce, use, or sell any patented invention or copyrighted work that may in any way be related thereto. Registered names, trademarks, etc., used in this publication, even without specific indication thereof, are not to be considered unprotected by law.

PRINTED IN THE UNITED STATES OF AMERICA

American Chemical Society

Library

1155 16th St., N.W.

Washington, D.C. 20036

Foreword

The ACS Symposium Series was first published in 1974 to provide a mechanism for publishing symposia quickly in book form. The purpose of the series is to publish timely, comprehensive books developed from ACS sponsored symposia based on current scientific research. Occasionally, books are developed from symposia sponsored by other organizations when the topic is of keen interest to the chemistry audience.

Before agreeing to publish a book, the proposed table of contents is reviewed for appropriate and comprehensive coverage and for interest to the audience. Some papers may be excluded to better focus the book; others may be added to provide comprehensiveness. When appropriate, overview or introductory chapters are added. Drafts of chapters are peer-reviewed prior to final acceptance or rejection, and manuscripts are prepared in camera-ready format.

As a rule, only original research papers and original review papers are included in the volumes. Verbatim reproductions of previously published papers are not accepted.

ACS Books Department

Preface

The reinforcement of polymers using fillers is common in the production and processing of polymers. The use of nanoscale fillers to augment the properties of polymers has led to the development of polymer nanocomposites (PNCs) and has provided a radical alternative to conventional polymer composites. Significant interest was generated by the development of nylon-6 layered silicate PNCs where significant improvements in tensile strength and heat distortion temperature without significant loss of impact strength were obtained with as little as 2 vol% added layered silicate. However, despite some notable successes during the past 15 years, a fundamental understanding of the mechanism of property changes associated with such PNCs is quite primitive. Further, recent interest in extending these achievements to layered silicate-based polyolefins and thermoset nanocomposite systems as well as the development of a range of chemically and physically distinct nanoscale fillers has called for a fundamental understanding of PNCs. A better understanding of the properties of PNCs may be possible by utilizing new techniques to measure structure–property relationships and by utilizing techniques and expertise developed in the conventional filled polymer composites.

Thus, interest in new nanoscale fillers, synthesis approaches, processing techniques, morphological characterization, structure–property relationships, as well as rheology and physics of nanoscopically confined polymers is rapidly growing, as demonstrated by the large (300+) attendance during the Polymer Nanocomposites symposium during the Spring 2000 American Chemical Society meeting. The book, which is based on the contributions to that symposium, focuses on techniques developed to better understand and extend the application of nanocomposite materials. We have developed this volume by focusing on the three most important aspects for the development of PNCs: synthesis, characterization, and modeling. The synthesis aspects cover the methods to develop nanoparticles and polymer nanocomposites. Characterization techniques, particularly structural characterization, have proven to be extremely difficult because of the range of length-scales associated with these materials. Radiation scattering, atomic force microscopy, and viscoelastic measurements are three techniques that are currently being fine-tuned and applied for the characterization of such hierarchical materials and are described in the book. Finally, theoretical and modeling, particularly computer modeling methods, are described in the book and are crucial in the development of design strategies for the next generation of nanocomposite materials.

This book highlights recent accomplishments and trends in the field of polymer nanocomposites and filled polymers. The contributions examine the unique chemical and physical aspects associated with polymer-based nanocomposite materials and discuss the latest fundamental and applied research in this area as well as possible future directions for the development of high-performance materials. We anticipate that this book will be of significant interest to scientists working on the basic issues surrounding nanocomposites and nanoparticulate filled polymers, as well as those working in industry on applied problems, such as processing. Because of the multidisciplinary nature of this research, this book will attract a broad audience including chemists, materials scientists, physicists, chemical engineers, and processing specialists, who are involved and interested in the future frontiers of blends of polymers and inorganic nanoparticles.

The editors are especially grateful for the dedication and effort of our colleagues who participated and contributed to the symposium and the present volume. Additionally, without the tireless effort of the ACS publication staff (K. Dennis, S. VanDerWall, M. Brown, and A. Wilson), this book would have not been possible. Finally, it is our pleasure to acknowledge financial contributions by the Air Force Research Laboratory's Materials and Manufacturing Directorate to support this symposium.

Ramanan Krishnamoorti

Department of Chemical Engineering
University of Houston
Houston, TX 77204-4004

Richard A. Vaia

Materials and Manufacturing Directorate
Air Force Research Library
2941 P Street
Wright-Patterson Air Force Base, OH 45433

Chapter 1

Polymer Nanocomposites: Introduction

Richard A. Vaia¹ and Ramanan Krishnamoorti²

¹Materials and Manufacturing Directorate, Air Force Research Library,
Wright-Patterson Air Force Base, OH 45433

²Department of Chemical Engineering, University of Houston,
Houston, TX 77204-4004

INTRODUCTION

Reinforcement of polymers with a second organic or inorganic phase to produce a polymer composite is common in the production of modern plastics. Polymer nanocomposites (PNCs) represent a radical alternative to these conventional polymer composites [1-5]. The most noteworthy effort in the last 15 years has demonstrated a doubling of the tensile modulus and strength without sacrificing impact resistance for nylon-layer silicate nanocomposites containing as little as 2 vol. % inorganic layered silicate. In addition, the heat distortion temperature of the nanocomposites increases by up to 100 °C, extending the use of the composite to higher temperature environments, such as for under-the-hood parts in automobiles.

Besides their improved properties, these nanocomposites materials are also easily extruded or molded to near-final shape, simplifying their manufacturing. Since high degrees of stiffness and strength are realized with far less high-density inorganic material, they are much lighter compared to conventional polymer composites. This weight advantage could have significant impact on environmental concerns amongst many other potential benefits. For example, it has been reported that widespread use of PNCs by US vehicle manufactures could save 1.5 billion liters of gasoline over the life of one year's production of vehicles and reduce related carbon dioxide emissions by more than 10 billion pounds [6]. In addition, their outstanding combination of barrier and mechanical properties may eliminate the need for a multipolymer layer design in packaging materials, enabling greater recycling of food and beverage packaging.

Even though significant progress has been made in developing polymer nanocomposites with varying polymer matrices and inorganic nanoparticles, a general understanding has yet to emerge. For example, the combination of enhanced modulus, strength and toughness is a unique feature of only a fraction of PNCs fabricated to date. A major challenge in developing nanocomposites for systems ranging from high performance to commodity polymers is the lack of even simple structure – property models. In the absence of such models and the role of processing in affecting the structure and properties, progress in the engineering of nanocomposites has remained largely empirical. Similarly, predicting the ultimate material limits or maximum performance for different classes of nanocomposites is almost impossible at present.

This book compiles the current status of research in nanocomposite, with regards to both the established polymer-clay nanocomposite systems for mechanical enhancements and emerging polymer-organic and other novel polymer-inorganic systems for electrical, optical, thermal and magnetic applications.

The ‘Nanocomposite’ Concept

What are nanocomposites and what makes them especially interesting? Why are they different and worthy of the rapidly increasing scientific and technological excitement? The answer to these questions, in our opinions, resides in the fundamental length scales dominating the morphology and properties of these materials.

The nanoparticles have at least one characteristic length scale that is of the order of nanometers and can range from essentially isotropic to highly anisotropic needle-like to sheet-like elements. Uniform dispersion of these isotropic and anisotropic nanoscopically-sized particles (or nanoelements) can lead to ultra-large interfacial area between the constituents, for example, approaching 700 m²/cm³ in dispersions of layered silicates in polymers. In addition to the large interfacial area, the distance between the nanoelements begins to approach molecular dimensions at extremely low loadings of the nanoparticles. Thus, for a system comprising of 1 nm thick plates, the distance between plates (considered as discs with a diameter 1 μm) approaches 10 nm at only 7 vol. % of plates!

This large internal interfacial area and the nanoscopic dimensions between constituents differentiate polymer nanocomposites from traditional composites and filled plastics. The dominance of interfacial regions resulting from the nanoscopic phase dimensions implies the behavior of polymer nanocomposites cannot be understood by simple scaling arguments that begin with the behavior of traditional polymer composites.

Three major characteristics define and form the basis of PNC performance: nanoscopically confined matrix polymer, nanoscale inorganic constituents, and nanoscale arrangement of these constituents. The driver for current research is to develop the tools – synthesis, processing, characterization and theory – to optimize and enable full exploitation of the potential of the combination of these unique characteristics.

The proliferation of internal inorganic-polymer interfaces means the majority of polymer chains reside near an inorganic surface. Since an interface limits the conformations that polymer molecules can adopt, the free energy of the polymer in this interfacial region is fundamentally different from that of polymer far removed from the interface (i.e. bulk). The influence of an interface is related to a fundamental length-scale of the matrix adjacent, which for polymers is on the order of the radius of gyration of a chain, R_g (5-20 nm) [7]. Thus, in PNCs with only a few volume percent of dispersed nanoparticles, the entire matrix polymer may be considered as nanoscopically confined interfacial polymer. The restrictions in chain conformations will alter molecular mobility, relaxation behavior and the consequent thermal transitions such as the glass transition temperature. More complicated is the picture for semi-crystalline polymers and mesostructured liquid-crystalline polymers and ordered block-copolymers, where the interface will alter the degree of ordering and packing perfection and thus crystallite and domain growth, structure and organization.

The second major characteristic of PNCs is the dimensions of the added nanoelements. As with the matrix polymers, when the dimensions of the cluster or particle approach the fundamental length scale of a physical property, new mechanical, optical and electrical properties arise, which are not present in the macroscopic counterpart. Examples include superplastic forming of nano-grained ceramics, plasmon absorption in metal nanoparticles, quantum confinement in semiconductor nanoparticles, and superparamagnetic response in nanoparticle magnets. Dispersions of nanoelements exhibiting these unique properties create bulk materials dominated by solid-state physics of the nanoscale. A short list of potential nanoparticles includes layered chalcogenides, metal nanoparticles, graphitic layers, carbon nanotubes, metal oxide, nitride and carbide clusters, quantum dots and biological components.

Finally, as with any composite, the arrangement of constituents critically determines the material's behavior. Conceptually, spatial ordering of spherical, rod - like or plate – like nanoparticles (0, 1 or 2 dimensional) into positional (1, 2 or 3 dimensional) arrays with varying degrees of orientational order will manifest in an enormous variety of systems. The possibilities are further expanded by varying degrees of particle-particle association, clustering, percolation and heterogeneous distribution of particles. The final properties of the PNC system will depend as much on the individual properties of the

constituents (characteristics 1 and 2) as on the relative arrangements and subsequent synergy between the constituents.

Ultimately, polymer nanocomposites offer the possibility of developing a new class of materials with their own manifold of structure-property relationships, only indirectly related to their components and their micron and macro-scale composite counterparts. Though nanocomposites with inorganics of different dimensionality and chemistry are possible, efforts have only begun to uncover the wealth of possibilities for these new materials.

Overview

In this book we have compiled the current research in PNCs. We have tried to stress the connections between the developments in PNCs with those in more conventional filled systems such as carbon black filled polymer systems. Further, the collection of chapters provide a snapshot of the current experimental, theoretical and computer simulation tools being used to advance our understanding of polymer nanocomposites.

In Chapter 1, Collister discusses the commercial viability of polymer nanocomposites. In Chapters 2 – 4, the synthesis aspects of nanocomposites development are discussed. Balazs and coworkers examine the thermodynamic considerations in the development of PNCs in Chapter 5. Characterization of such nanofilled polymer composites by scattering, adsorption and NMR measurements are discussed in Chapters 6 through 10. Hjelm discusses the application of small angle neutron scattering (SANS) to examine the structure and aggregation of carbon black (Chapter 6), while Vaia and Lincoln apply small angle x-ray scattering to examine nylon-6 based PNCs (Chapter 8) and Ho and coworkers use SANS to examine the dispersion of organically modified layered silicates (Chapter 10). Thin film properties, viscoelastic properties and crystallization behavior of layered – silicate based PNCs are discussed in Chapters 11 through 13. In Chapter 14, Gerspacher and O'Farrell discuss the dispersion and viscoelastic properties of carbon black filled polymers and correlate these fundamental properties to final-use properties in applications such as in rubber tires. Finally, computer simulations have increasingly been used to understand the synthesis and formation of PNCs as well as understand their properties. Manias and Kупpa (Chapter 15) describe via computer simulations the structural and dynamic properties of polystyrene confined between layered-silicates and Bhardwaj et al. describe results from computer simulations to examine the process of nanocomposites formation.

REFERENCES

1. E.P. Giannelis, *Adv. Mater.* 8, 29 (1996).
2. *Polymer Clay Nanocomposites*, T.J. Pinnavaia, G.W. Beal eds. 2000
3. *Polymer Nanocomposites*, R.A. Vaia, R. Krishnamoorti, eds., American Chemical Society, Vol xxx, Washington, D.C. 2001
4. *Nanocomposites 1999: Polymer Technology for the Next Century*. Principia Partners, Exton, PA 1999
5. M. Alexandre, P. Dubois, *Mater. Sci. Eng.* 28, 2000, 1- 63
6. "Nanocomposites New Low-Cost, High-Strength Materials for Automotive Parts", National Institutes of Technology, ATP Project, 97-02-0047, 1997.
7. Y.S. Lipatov, *Polymer Reinforcement*, ChemTec Publishing, 1995.

Chapter 2

Commercialization of Polymer Nanocomposites

Jon Collister

Edison Polymer Innovation Corporation, 4040 Embassy Parkway, Route
150, Austinburg, OH 44010

The commercial status of polymer nanocomposites is at the very earliest stage of development. Commercial materials are available with both layered clays and carbon nanotubes as the reinforcements for a very limited number of polymers with very specific end-use property requirements. However, current research and development activities and patent positioning that are now underway in both industry and academia seem to indicate that wide-spread use of nanocomposites is imminent.

Introduction

Polymer nanocomposites are a class of materials that have properties that offer significant commercial potential. Any discussion of the commercial status of polymer nanocomposites requires recognition that the term is not a description of a unique material. Polymer nanocomposites are commonly defined as the combination of a polymer matrix resin and inclusions that have at least one dimension (i. e. length, width, or thickness) in the nanometer size range. There are many types of nanocomposite that have received significant research and development including polymer/inorganic particle, polymer/polymer, metal/ceramic, and inorganic based nanocomposites. This review will only consider the polymer/inorganic particle type, since it is the only type of nanocomposite to date that has realized any significant commercial activity.

Several benefits of such a nanocomposite have been identified that allow polymer nanocomposites to compete commercially with traditional materials, including:

- Efficient reinforcement with minimal loss of ductility and impact strength
- Thermal endurance
- Flame resistance
- Improved barrier properties
- Improved abrasion resistance
- Reduced shrinkage and residual stress
- Altered electrical, electronic and optical properties

Enhancements in reinforcement, thermal endurance, electrical conductivity, and improved barrier properties make these materials prime candidates for packaging and automotive applications.

The discussion of commercial products will involve nanocomposites produced using layered clay minerals (montmorillonite, hectorite, etc.) and carbon nanotubes. These are the only examples that have any commercial significance to date. The layered clay materials impart improved mechanical strength and modulus, fire resistance, and barrier properties; while carbon nanotubes (or fibrils) impart electrical conductivity (in addition to the expected increases in strength and modulus). Polyamide (PA) nanocomposites are available both as films for packaging and composites for injection molding and other processes. Carbon nanotubes have been commercially exploited to assist in the electrostatic paintability of automotive components molded from polyphenylene Oxide/Polyamide (PPO/PA) alloys. These two types of nanocomposite comprise almost all of the commercial activity to date and are used as the models that drive the development efforts that are currently underway with other polymers.

Commercial Nanocomposites

Layered Clay Nanocomposites

There are two types of layered clay nanocomposites, intercalates and exfoliates, depending of the organization of the clay layers. Intercalates are obtained when polymer is located between the clay layers and while the layer spacing is increased, there are attractive forces between the clay layers which cause the layers to be in regularly spaced stacks or tactoids. Exfoliates are obtained when the layer spacing increases to the point where there is no longer sufficient attractions between the clay layers to cause a uniform layer spacing. In true exfoliates, the clay layers are randomly dispersed throughout the composite. The amount of separation of the clay layers is determined by the thermodynamic

interactions of the clay layer, the cation residing between the clay layers, and the matrix polymer. Since many properties of the nanocomposite are improved by the degree of dispersion of the nanoparticles; the achievement of exfoliated clay structures is the goal of many of the research activities on-going in nanocomposites.

The most widely utilized nanoparticle reinforcement is montmorillonite. The montmorillonite platelets consist of octahedral alumina sheets sandwiched between two tetrahedral silica sheets. The alumina sheet has some replacement of the aluminum cations (Al^{+3}) by magnesium cations (Mg^{+2}) which provide a net negative charge to the layers. This negative charge is balanced by hydrated inorganic cations positioned in the spacing (galleries) between the aluminosilicate layers. The pristine gallery height is determined by the type of cation residing in the gallery and the degree of hydration.

Organic treatment of the layered clay is required for compatibility with most polymers; although there are some polymers, such as polyethylene oxide (PEO) or polyvinylpyrrolidone (PVP), of sufficient polarity to be able to directly exfoliate non-treated clays.¹ Layered clays are typically rendered organophilic by exchanging the inorganic cation with an organic cation. The ion exchange causes a change in the gallery height that is dependent on the molecular size of the organic cation and the amount of charge residing in the silicate layers.²

Nanocomposites are prepared by mixing the ion exchanged layered clay with monomer (followed by polymerization), melt mixing the layered clay with polymer or by mixing the layered clay with solvated polymer followed by solvent removal. The monomer or polymer can enter the gallery between the clay layers and cause further separation; and if the polymer and the organically treated clay are well matched, exfoliation of the layered clay is achieved.

Commercial sources of some ion exchanged (and otherwise treated) clays are Southern Clay Products and Nanocor. Additional companies who are heavily involved are Rheox, Sud-Chemie, and Kunimine Industries who are involved in the current supply of untreated clay minerals or have capability to produce treated clays, all of these companies are actively involved in marketing and development efforts for nanocomposites.

It is instructive to analyze the claims that are made regarding the properties of these layered clay nanocomposites to help understand the motivation behind the commercial efforts. The first commercial nanocomposite was polyamide 6 that was originally developed by Toyota Central Research and Development. This product is based on in-reactor processing of caprolactam and montmorillonite which has been ion exchanged with the hydrochloride salt of aminolauric acid (12-aminodecanoic acid).³ The properties of this nanocomposite (that contained a just few percent montmorillonite) were found to be substantially improved; especially modulus and thermal endurance. The thermal endurance, as measured by heat distortion temperature, allowed the

material to be used for under-the-hood automotive applications (timing chain cover for Toyota). Due to the low amount of montmorillonite present in the composite, the density was not altered significantly as would have been the case with mineral or glass filled composites, since loading of 30 to 40 percent of mineral or glass fiber would be required to achieve the same heat distortion improvement. Commercial polyamide 6 nanocomposites prepared by the Toyota process are available from Ube, Bayer, and Unitika.

Technology to prepare nanocomposites directly via compounding was investigated by Gianellis⁴ and is used as the process to prepare commercial polyamide 6 compound from RTP.⁵ Comparison of the published properties, review of Xray diffraction studies, and transmission electron microscopy (TEM) images indicates that the degree of exfoliation with the monomer process is slightly greater than with the melt process. This correlates well to the physical properties which are reported to be slightly better for the monomer produced materials. This small improvement in properties must be balanced against the potentially lower cost of the melt process.

The focus of industrial research and development is on both the melt and the monomer exfoliation process. Since there are a number of polymers that do not lend themselves to a monomer process (such as polyolefins), the melt process is the only route available. Nanocomposite materials from polymers such as polyacrylates or methacrylates, polystyrene, SBR, epoxy, polyester, and polyurethane are amenable to the monomer approach.

The property of interest to the food and beverage-packaging producers is the permeability of the materials to ingress of atmospheric contaminants and egress of gaseous or liquid components of the packaged material. In beverage and fatty food containers this relates directly to barrier behavior for CO₂ and O₂. It has been discovered that the platelet nature of exfoliated clays in polymers dramatically reduce the permeability of fluids and gaseous materials through the composite. This is a property well known for clay-like materials since clays are used extensively as barrier materials in pollution containment in environmental applications and is involved in moisture retention of clay containing soils in agriculture.⁶ There have been two mechanisms proposed for the alteration in the permeability behavior; the first involves the "tortuous" path of the diffusing molecule and the second involves the large interfacial volume of the nanocomposite. The "tortuous" path mechanism contends that the clay platelet is non-permeable and that diffusing species has a repeatedly altered vector and therefore a much longer diffusion pathlength.⁷ The large interfacial volume mechanism contends that the large surface area of exfoliated clays (even at low loading) cause the majority of the host polymer to lie close to the clay-polymer interface which in turn restricts the mobility of the polymer molecules and any molecules attempting to diffuse through the polymer. This later concept is supported by research on small molecule interactions with clays which indicates

that organic liquids have a large affinity for the clay surface and have reduced mobility.⁸ It is probable that both mechanisms are involved in reducing permeability. In any event, permeability is reduced for exfoliated nanocomposites and has been commercially exploited. Commercial grades of polyamide 6 for packaging films are available from Ube and Bayer.

Commercial Carbon Nanotube Composites

There has been commercial activity with carbon nanotube reinforced thermoplastics for the automotive market. The property that has been exploited in these applications is the ability of the carbon nanotube to provide conductivity to the composite at very low loading levels. Conductive carbon black fillers have been used to provide conductivity to thermoplastics but the loading requirements are quite high and considerable deterioration in physical properties is realized. The loading requirement with carbon nanotubes for electrostatic painting operations is stated to be as low as 2%.⁹ Although the cost of the carbon nanotubes is quite high, painting cost savings and paint utilization efficiencies are realized that off-set the higher cost of the nanocomposite. Nanotubes are being produced commercially by Hyperion Catalysts International. The diameter of these nanotubes is 10nm and averages eight layers of graphite in the tube wall. It is reported that GE Plastics is commercially using these fibers in a PPO/PA blend¹⁰ for automotive mirror housings for Ford. In addition to the nanotubes, Applied Sciences is producing vapor grown carbon fibers with diameters as low as 100nm which compete with the nanotubes in providing electrical conductivity in thermoplastics.

Rational Behind Commercial Acceptance

This discussion of these three commercial applications demonstrates the decision making that has to be employed when the choice of a material for particular applications must be made. The one advantage that nanoparticles as polymer additives seem to have is that compared to traditional additives, loading requirements are quite low. In the automotive PA nanocomposite the low loading provided reinforcement and thermal endurance at low sacrifice of weight which is important for fuel economy in automobiles. Minor additions of layered clays to packaging materials provide barrier properties that can only be achieved with multi-layer constructions or with chemical treatments and coatings. The carbon nanotubes provide conductivity to the polymer at low enough loading so as to not interfere with the mechanical properties of the composite, allowing the nanocomposite to compete effectively with traditional materials. Typically there are several materials (and associated secondary processes) that can satisfy an individual component's property requirements, therefore the combination of

several characteristics including physical properties, density, appearance, processing, and cost must be carefully considered. Polymer nanocomposites will find application areas justified by unique sets of properties that the inclusion of nanometer scale particles provides.

Anticipated Commercial Activities

Kuraray and Nippon Gohsei are reported to be close to commercialization of ethylene vinyl alcohol (EVOH) for the packaging market. EVOH is currently used in barrier packaging. Unitika is also reported to be close with a polyvinyl alcohol (PVOH) product for the packaging market.¹¹

In the automotive area, both Dow and Montell have conducted significant development of polypropylene (PP) and thermoplastic polyolefin (TPO) based nanocomposites. Dow has been teaming with Magna International and NIST (National Institute of Standards and Technology) in an ATP (Advanced Technology Program) grant to develop novel automotive materials.¹² Dow is reported to have produced experimental materials for processing trials. Montell has been partnering with General Motors (GM) to develop a PP nanocomposite for automotive exterior applications.¹³ They have received considerable press attention and have displayed automotive body panels at trade shows and for trade journals.

Eastman Chemical is reported to be very interested in multi-layer and single layer nanocomposite barrier packages and is pursuing patents.¹⁴ One of the commercial targets appears to be the disposable/recyclable beer bottle market where the current plastic product is a multi-layer construction. There has also been considerable activity in the patent literature concerning nanocomposite blow-molded packages; Tetra Laval has been awarded patents that cite the use of nanocomposites of both single layer and multi-layer construction.¹⁵ These activities indicate that nanocomposites are positioned to become a commercial participant in the near future.

Developing Technology with Commercial Potential

There are a number of developing technologies which are still some time away from commercialization but may have major potential impact. These technologies are:

- **Fire Resistance** – NIST has extensively studied the flammability of layered clay nanocomposites and has found that minor loading results in substantial reduction in flammability. This has been attributed to the build-up of a protective char layer involving the clay.¹⁶ The Air Force has also reported substantial improvement in the ablative properties of materials due to a similar char formation.¹⁷ These results could lead to

new fire resistant composites without the use of halogenated compounds (which are considered to have negative environmental impact) and hydrated inorganic oxides (which require substantial loading).

- Asphalt Modification – Exxon has patented the use of layered clays in elastomer modified asphalt that demonstrate considerable improvement in properties.¹⁸
- Elastomers – Exxon has patented in the area of layered clay containing elastomers citing improvements in air permeability.¹⁹ Additionally, tire companies are reported to have activities underway to assess the performance of layered clays as the reinforcement for tire applications.
- Thermoset Polymers – Considerable technology has been developed for epoxy/layered clay nanocomposites that have application in coatings and composites.²⁰ Technology has also been developed for unsaturated polyesters,²¹ vinyl esters,²² and polyurethanes.²³
- Electrical Applications – There are a variety of applications in development for carbon nanotube or fibrils involving electrostatic dissipation (ESD) and electromagnetic interference (EMI).¹⁰ Automotive fuel systems are a developing area.

Conclusions

The consumption of commercial nanocomposites is very small at the present time, estimated at less than three million pounds in 1999. However, estimates have been made indicating two order of magnitude growth in production by year 2004.¹¹ The pace of commercialization of nanocomposites is uncertain and is in the hands of the resin producers, compounders, converters and end-users, but the property improvements certainly position nanocomposites to be a lively competitor in several market areas. It is anticipated that major growth will be realized when competitive nanocomposites are introduced in automotive and packaging applications with commodity polymers such as polyolefins and polyesters.

References

1. Beall, G. W.; Kamena, K. *Proceedings Antec 1999 Soc. Plast. Eng.*; Brookfield, CT; Vol. III, p. 3973.

2. Grim, R. E.; *Clay Mineralogy*, Second Edition; McGraw-Hill Book Company: New York, NY, 1968; p. 362.
3. US Pat. 4,810,734 M. Kawasumi, et al, (Assigned to Kabushiki Kaisha Toyota Chuo Kenkyusho); March 7, 1989.
4. Vaia, R. A.; Giannelis, E. P. *Macromolecules*; **1997**, 30, 8000-8009.
5. "RTP Claims First Nylon/Organo-clay Compound", *Plastics Additives & Compounding*, 1 (2), June 1999.
6. Velde, B. *Introduction to Clay Minerals*, Chapman & Hall: London, 1992; pp.178-9.
7. Yano, K.; Usuki, A.; Okada, A.; Kurauchi, T.; Kamigaito, O. *J. Polym. Sci., Part A: Polym. Chem.*; **1993**, 31, 2493-2498.
8. Stockmeyer, M. R. *Applied Clay Science*, **1991**, 6, 39-57.
9. Hyperion Catalysts International; Product Literature.
10. Dagani, R.; "Putting the 'Nano' into Composites", *C & EN*, June 7, 1999, p. 32.
11. "Nanocomposites 1999 – Polymer Technology for the Next Century", Multiclient Report, Principia Partners, Exton, PA; 1999.
12. "Nanocomposites: new Low-Cost, High-Strength Materials for Automotive Parts", National Institute of Standards and Technology, ATP Project 97-02-0047, 1997.
13. Pryweller, J. "GM, Montell Pursue Nanocomposite TPO's", *Plast. News (USA)*, 10, (45), 1998.
14. US Pat. 6,034,163 Barbee, R. B., et al, (Assigned to Eastman Chemical Company); March 7, 2000.
15. US Pat. 5,876,812 Frisk P.; Laurent, J., (Assigned to Tetra Laval holdings & Finance, SA); March 2, 1999.
16. Gilman, J. W.; Kashiwagi, T.; "Nanocomposites: A Revolutionary New Flame Retardant Approach", *SAMPE Journal*, Vol. 33, No. 4, July/August 1997.
17. Vaia, R. A.; Price, G.; Ruth, P. N.; Nguyen, H. T.; Lichtenham, J.; *Applied. Clay Science*, **1999**, 15, 67-92.
18. US Pat. 5,652,284 Eidt, Jr., C. M., et al (Assigned to Exxon Research and Engineering); July 29, 1997.
19. US Pat. 5,807,629 Elspass, C. W., et al (Assigned to Exxon Research and Engineering); Sept. 15, 1998.
20. LeBaron, P.C., Wang, Z., Pinnavaia, T. J.; *Applied Clay Science*, **1999**, 15, 11-29.
21. Kornmann, X.; Berglund, L. A.; Sterte, J.; *Polym. Eng. And Sci.*, **1998**, 38; 8; 1351-1358.
22. WIPO Patent Application; WO 99/54393; Polansky, C. A., et al; Oct. 28, 1999.
23. Wang, Z.; Pinnavaia, T. J.; *Chem. Mater.*, **1998**, 10; 3769-3771.

Chapter 3

PMMA Nanocomposites Synthesized by Emulsion Polymerization

Sumanda Bandyopadhyay^{1,3}, Alex J. Hsieh², and
Emmanuel P. Giannelis¹

¹Department of Materials Science and Engineering, Bard Hall, Cornell University, Ithaca, NY 14853

²AMSRL-WM-MA, Army Research Laboratory, Aberdeen Proving Ground, Aberdeen, MD 21005

³Current address: GE India Technology Centre, Expost Prom. Industrial Park, Ph-2, Whitefield Road, Bangalore 560066, India

Well-dispersed (exfoliated) PMMA nanocomposites were synthesized via emulsion polymerization. The nanocomposites retain their transparency in the visible with the montmorillonite nanocomposite showing considerable absorption of UV light. Thermal stability of the nanocomposites is enhanced as evidenced by TGA and a simple burning experiment. The storage modulus and T_g is increased significantly in the nanocomposites. The higher increase of the storage modulus in the rubbery regime of the montmorillonite nanocomposite reflects the higher amount of bound polymer compared to the fluorohectorite nanocomposite.

Nanocomposites based on layered inorganics offer an alternative to conventionally filled polymers and composites. Due to their nanometer phase dimensions the nanocomposites exhibit new and improved properties. These include increased stiffness and strength without sacrificing impact resistance, decreased permeability and swelling in solvents, and increased flame resistance. For example, nylon nanocomposites show a significant increase in modulus and strength as well as heat distortion temperature. (1,2). Tensile strength and modulus have also been reported to increase considerably in epoxy and polyurethane nanocomposites (2-8). Additionally improved barrier properties (9,

10) and swelling in solvents (11) have been reported for several nanocomposite systems. Finally the nanocomposites exhibit increased thermal stability and flame resistance (12-15).

Currently, two synthetic approaches have been adopted. One is based on in-situ polymerization of monomers inside the galleries of the inorganic host. (16-20). The other approach is based on melt intercalation of high molecular weight polymers and it involves annealing a mixture of the polymer and the inorganic host, statically or under shear, above the T_g of the polymer (21-24). The solventless melt intercalation is an environmentally friendly technique and is adoptable to existing processing like roll milling, extrusion and molding.

In the present chapter, we report the synthesis of PMMA nanocomposites by emulsion polymerization. Polymerization of MMA in the presence of smectite silicates has been previously reported (25-28). The focus of all these studies, however, was on how the silicates affect the polymerization reaction rather than the final hybrid product. Additionally, the development of an emulsion route to nanocomposites represents a new avenue.

Experimental

5 ml of MMA (Sigma Chemicals) was added to a round bottom flask containing 95 ml of water (the ratio of monomer to water is approximately 1:19) followed by 0.25 g of silicate (Na^+ montmorillonite, hereafter abbreviated as MMT, or fluorohectorite, FH). The resulting suspension was heated at 80°C with stirring and allowed to equilibrate for 2 hrs. An emulsifier (sodium lauryl sulfate, 0.25 g) is added to allow the reaction to proceed as emulsion polymerization with constant mechanical stirring. 0.0125 g of potassium persulfate is added to initiate the polymerization and the suspension is refluxed at 80°C for 4 hrs.. The emulsion is completely precipitated in excess ethyl alcohol. The precipitate is then filtered and re-precipitated from tetrahydrofuran, washed thoroughly with de-ionized water, filtered and dried under vacuum at 80°C . In one particular case the MMT was modified with 2,2' Azobis(2-methylpropionamide) dihydrochloride and hereafter referred to as AMMT. A schematic (Scheme 1) shows the synthetic route and also the silicate modification.

Table 1: Summary of PMMA and PMMA Nanocomposites Properties

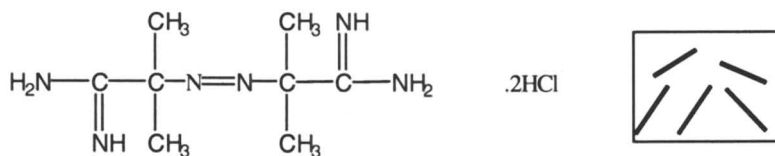
	PMMA	PMMA-MMT	PMMA-FH
Polydispersity index, D	3.49	2.57	2.59
Molecular Weight (g/mol) X 10^3	195.2	221.7	223.0
Glass Transition Temp. T_g , ($^\circ\text{C}$)	115	121	125
Storage Modulus @ RT (GPa)	2.9	9.9	9.3

MMT: montmorillonite

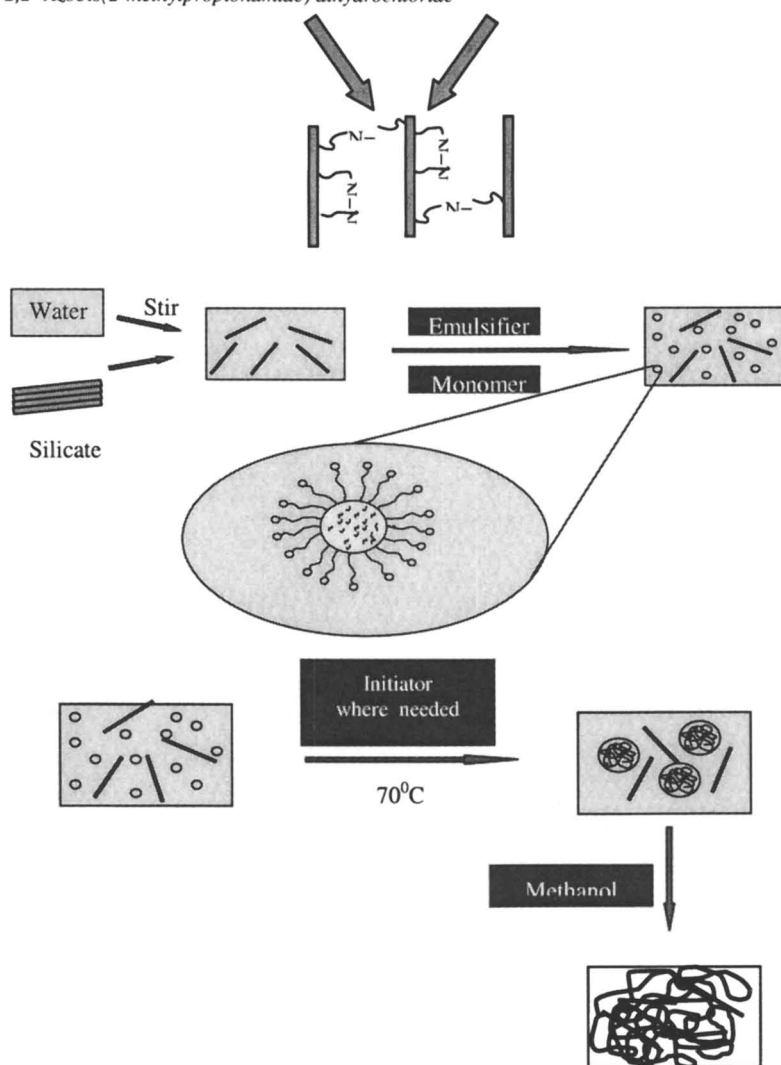
FH: fluorohectorite

The molecular weight of the extracted nanocomposites samples was done on Waters GPC instrument with refractive index attachment using polystyrene standard. X-Ray diffraction was performed using a Scintag PAD X

Schematics for the silicate modification and emulsion polymerization of PMMA nanocomposites



2,2' Azobis(2-methylpropionamide) dihydrochloride



Diffractometer using Cu-K α radiation. The accelerating voltage used was 45kV and the current was 40mA. The TEM samples were examined using JEOL 1200EX transmission electron microscope with an accelerating voltage of 120kV. Samples of 0.2 μm to 0.3 μm thickness were cut using a glass knife Reichert Ultramicrotome and mounted on 400 mesh Gilder gold grid. Thermal degradation was followed by a Perkin Elmer System 7, Thermogravimetric Analyzer. Scans were performed from room temperature to 800 $^{\circ}\text{C}$ at 10 $^{\circ}\text{C}/\text{min}$. For dynamic mechanical analysis a Seiko Instrument, SDM 5200, DMS 200 series was used. The samples were scanned from room temperature to 150 $^{\circ}\text{C}$ at 2 $^{\circ}\text{C}/\text{min}$ at 5Hz and a strain of 0.1%. Absorbance was measured between 200nm and 900nm at a spectral bandwidth of 1 nm and a scan speed of 30nm/sec on a Perkin Elmer spectrophotometer.

Results and Discussion

TEM micrographs of the nanocomposites prepared via emulsion show a well dispersed (exfoliated) sample (Fig. 1). The dispersion is somewhat better in the MMT nanocomposite and is most likely due to the much smaller lateral dimensions of MMT compared to FH. The silicate exfoliation is supported by the featureless XRD patterns (Figures not included) of the nanocomposites.

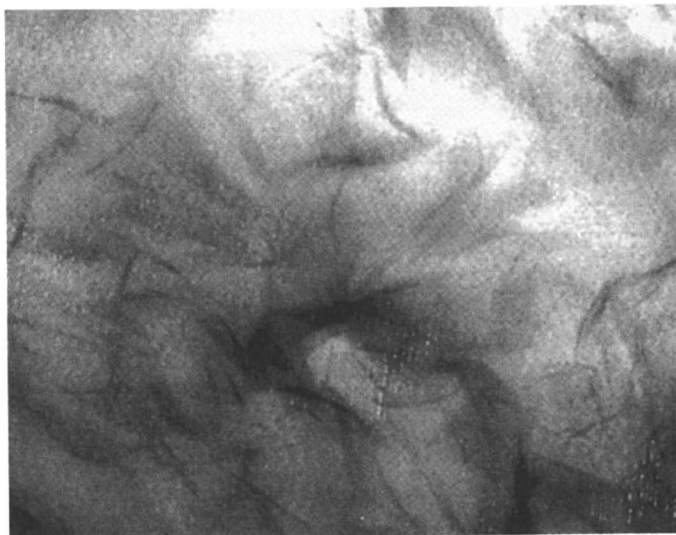


Figure 1: Transmission electron microscope showing the disordered silicate (montmorillonite) in the PMMA matrix.

Table 1 summarizes the molecular weight and the polydispersity of the polymers for all samples prepared by emulsion polymerization. The nanocomposites show

slightly higher molecular weights but much better polydispersity than pure PMMA prepared similarly but in the absence of the silicate. Though the mechanism is still unknown, clearly the presence of silicate effects the polymerization reaction.

Clarity of the samples is very important as PMMA is often used in many applications for its transparency. Films were deposited on clean glass substrates by spin casting a suspension of the nanocomposites in tetrahydrofuran, THF. For comparison a PMMA film was prepared by spin casting a solution of PMMA also in THF. The nanocomposites have somewhat higher absorbance compared to the pure polymer, but the absorbance is well below the limit for transparency. Especially in the case of MMT nanocomposite the sample shows increased absorption in the UV. Thus the nanocomposites combine UV absorption while retaining transparency in the visible.

An important characteristic of polymers is their stability at elevated temperatures. Figure 2 and 3 shows the TGA traces of the pure polymer and the nanocomposites in either nitrogen or oxygen. Thermal degradation of PMMA in nitrogen proceeds in three distinctive steps. The first (low temperature) is due to decomposition of relatively weak head-to-head linkages, the second to chain-end decomposition and the third to random scission within the polymer chain (29). In the present case degradation of PMMA in nitrogen (Fig. 2) follows a two-step process (the first step is absent). The onset of the two steps is at 322 and 380 °C, respectively. The FH nanocomposite appears to decompose also in two steps. The derivative shows that the extent of the two steps is reversed from the corresponding PMMA sample. At the same time, the second peak moves to a slightly higher temperature. In contrast, decomposition of the MMT nanocomposite follows a single step suggesting that only decomposition by random scission takes place.

In contrast to nitrogen, oxygen suppresses the degradation of weak linkages at low temperatures but it enhances the degradation via random scission at higher temperatures for the pure PMMA. Similarly to the pure polymer the nanocomposites show one major decomposition step (Fig. 3). The onset decomposition of FH nanocomposite, however, commences a little earlier but it extends to somewhat higher temperatures than the pure PMMA. In contrast, MMT nanocomposites show a large suppression of decomposition compared to the pure polymer with the decomposition temperature increasing by about 50 °C. Blumstein (25) mentioned that increased thermal stability is not only due to the particular structure of the inserted polymer but steric factors also have an important role to play in the thermal motion of the chain segments in between the clay lamellae. It is also important to point that the extent of polar interaction due to exfoliation of the clay lamellae in the present PMMA nanocomposites could be responsible for a higher thermal stability of the composite system. The

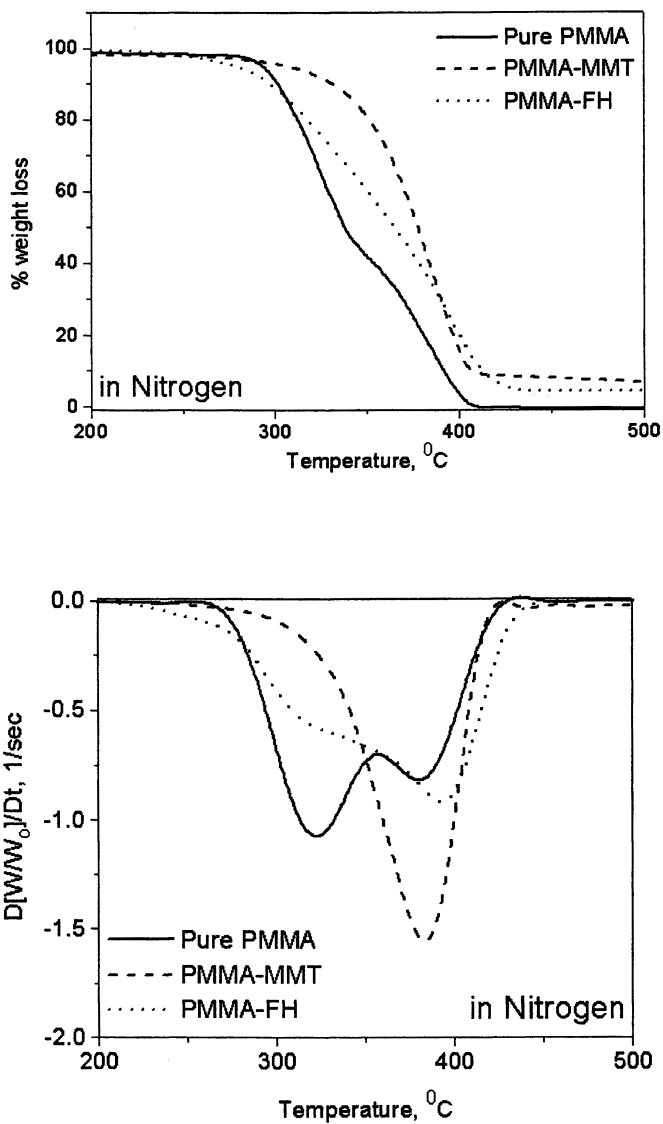


Figure 2: Thermogravimetric traces of the different PMMA nanocomposites in nitrogen.

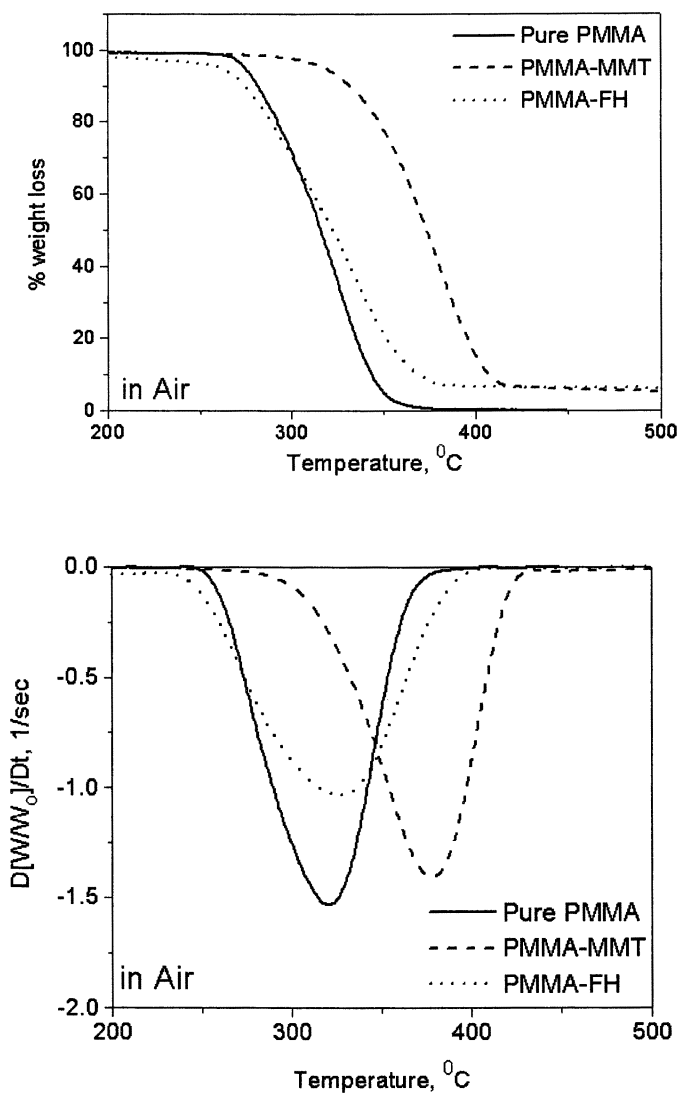


Figure 3: Thermogravimetric traces of the different PMMA nanocomposites in air.

difference of polar interaction existing in MMT and FH could lead to the formation of a different polymer microstructure and hence a difference in the thermal behavior.

There are clearly differences between the two nanocomposites and the pure polymer. In addition, the thermal stability depends if air or nitrogen is used. We are currently attempting to understand and delineate the factors contributing to this behavior. Nevertheless, the thermal stability of the polymer appears to increase in the nanocomposites. The above conclusion is corroborated by a simple burning test using a propane torch. PMMA burns out completely with significant dripping. In contrast, the nanocomposites experience no dripping during burning. Furthermore, the MMT nanocomposite self-extinguishes shortly after the flame is removed. The FH nanocomposite continues to burn but it forms a significant amount of char, which is characteristic of higher thermal stability.

Solomon et al. has observed that clay minerals act as inhibitor for free radical polymerization specifically for PMMA (30). The clay minerals inhibit the free radical reactions by preferential absorption of the propagating or initiating radicals by the Lewis acids and then the reaction either gets terminated by dimerization or disproportionation or by formation of a carbonium ion by electron transfer from the radical to the Lewis acid site. The clay minerals usually made of aluminosilicates and minerals containing higher amount of aluminosilicates are more effective inhibitors. In the present case, MMT is an aluminosilicate while FH contains Mg in the octahedral layer (31). Thus, MMT contains Lewis acid sites but not FH. This might explain the different behavior between the two silicates, MMT and FH, in the nanocomposites. Recently Gilman *et.al.* (32) observed a difference in the flammability behavior of MMT and FH based nanocomposites. They observe a silicate layer reassemble into a multiplayer char after the polymer burns away. The smaller size of MMT lamellae could assist in the reassemble process compared to the large FH lamellae, which disrupts the char formation.

Finally dynamic mechanical analysis was used to measure the viscoelastic properties of the nanocomposites as a function of temperature. In this measurement the in-phase and out-of-phase components of the stress are measured while a sinusoidal strain is applied to the sample. From the in-phase and out-of-phase components the storage (E') and loss modulus (E''), respectively, can be calculated. The ratio $E''/E' = \tan\delta$ is a measure of the energy lost to energy stored per cycle of deformation and has a maximum at thermal transitions. The DMA measurements for storage modulus, E' , with temperature for MMT and FH nanocomposites and pure PMMA are shown in Figure 4. An increase of 6°C in T_g was evident in MMT nanocomposite; the exfoliated silicate-PMMA hybrid resulted from the emulsion polymerization is attributed to this increase in T_g . In addition, the DMA data revealed an-order-of-magnitude increase in the rubbery plateau modulus for the MMT nanocomposite

compared to the pure PMMA. This increase was significant and consistent over the temperature used in this study. Enhancement in the thermo-mechanical properties of PMMA Nanocomposites prepared by emulsion polymerization was also evident in the FH nanocomposite. The latter exhibited an increase of 10°C in T_g and higher E' values above T_g, compared to pure PMMA. However, the increase in the rubbery plateau modulus obtained in DMA was more significant in the MMT than that in FH. This trend might reflect the differences in the amount of strongly interacting polymer (bound polymer) for the two nanocomposites. After extraction in chloroform at room temperature MMT retains 40 % polymer while only 7 % is left in FH. The much higher amount of bound polymer in MMT might act as potential crosslinks increasing the rubbery modulus to a greater extent.

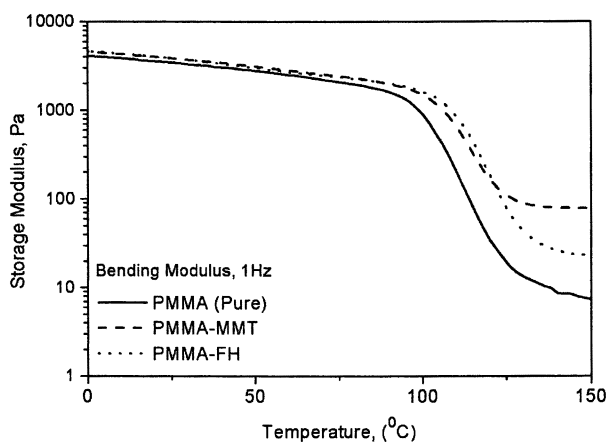


Figure 4: Dynamic mechanical analysis plots for the different PMMA nanocomposites

Table 2 summarizes the results from the characterization of the PMMA end-tethered MMT samples. These samples were prepared by suspension polymerization of MMA in the presence of AMMT. The silent XRD refers to a well dispersed silicate morphology. The T_g from the DMA analysis, however, shows a very slight increase in the temperature and a much higher increase in the rubbery plateau modulus. The increase in the rubbery plateau modulus is evident from the amount of the bound polymer in the AMMT nanocomposite as compared to the MMT (un-tethered) samples.

Table 2: X-ray diffraction and Thermal and Bound Polymer of the nanocomposites

Samples	XRD Initial, nm	XRD Final, nm	DMA, Tg °C	Bound Polymer
Pure	--	-	109.3	--
PMMT	1.106	Silent	121.8	40%
P50	1.209	Silent	126.5	82%

Conclusion

The first synthesis of well-dispersed (exfoliated) PMMA nanocomposites via emulsion polymerization is described. The nanocomposites retain their transparency in the visible with the MMT nanocomposite showing considerable absorption of UV light. Thermal stability of the nanocomposites is enhanced as evidenced by TGA and a simple burning experiment. The storage modulus and Tg is increased significantly in the nanocomposites. The higher increase of the storage modulus in the rubbery regime of the MMT nanocomposite reflects the higher amount of bound polymer compared to the FH nanocomposite. End-tethering of MMT to PMMA increases the amount of bound polymer

Acknowledgement

This work was supported in part by NIST, ARO and Rohm and Haas. We benefited from the use of CCMR central facilities supported by NSF.

References

1. Kojima, Y.; Usuki, A.; Kawasumi, M.; Okada, A.; Fukushima, Y.; Kurauchi, T.; Kamigaito, O., *J. Mater. Sci.*, 1993, 8, 1185.
2. Kojima, Y.; Usuki, A.; Kawasumi, M.; Okada, A.; Fukushima, Y.; Kurauchi, T.; Kamigaito, O., *J. Polym. Sci, Pt. A, Polym. Chem.*, 1993, 31, 983.
3. Lan, T.; Kaviratna, P.D.; and Pinnavaia, T.J., *Chem. Mater.*, 1996, 8, 2628.
4. Lan, T.; and Pinnavaia, T.J., *Chem. Mater.*, 1994, 6, 2216.
5. Wang, J.; Lan, T.; Pinnavaia, T.J., *Chem Mater.*, 1994, 6, 468.
6. Wang Z.; and Pinnavaia, T.J., *Chem. Mater.*, 1998, 10, 3769.
7. Zilg, C.; Thomann, R.; Mulhaupt R.; and Finter, J., *Adv. Mater.*, 1999, 11, 49
8. Newaz, G.M., *Polym. Comp.*, 1986, 7, 176.
9. Messersmith, P.B.; Giannelis, E.P., *J. Polym. Sci, Pt. A, Polym. Chem.*, 1995, 33, 1047.

10. Kojima, Y.; Usuki, A.; Kawasumi, M.; Okada, A.; Fukushima, Y.; Kurauchi, T.; Kamigaito, O., *J. Appl. Polym. Sci.*, 1993, 49, 1259.
11. Burnside, S.D.; Giannelis, E.P., *Chem. Mater.*, 1995, 7, 1597.
12. Lee, J.D.; Takekoshi, T.; Giannelis, E.P., *Mat. Res. Soc. Symp. Proc.*, 1997, 457, 513.
13. Gilman, J.W.; Kashiwagi, T.; Lichtenhan, J.D.; Giannelis, E.P.; Manias, E., 6th European Meeting on Fire Retardancy of Polymeric Materials, Lille, France, September, 24, 1997.
14. Lee, J.D.; Giannelis, E.P., *Polymer Preprints*, 1997, 38, 688.
15. Gilman, J.W.; Kashiwagi, T.; Lichtenhan, J.D., *SAMPE Journal*, 1997, 33, 40.
16. Usuki, A.; Kojima, Y.; Kawasumi, M.; Okada, A.; Fukushima, Y.; Kurauchi, T.; Kamigaito, O., *J. Mater. Sci.*, 1993, 8, 1179.
17. Fukushima, Y.; Okada, A.; Kojima, Y.; Kawasumi, M.; Kurauchi, T.; Kamigaito, O., *Clay Miner.*, 1988, 23, 27.
18. Lan, T.; Kaviratna, P.D.; Wang, M.S.; Pinnavaia, T.J., *Mater. Res. Soc. Symp. Proc.*, 1994, 346, 81.
19. Messersmith, P.B.; Giannelis, E.P., *Chem. Mater.*, 1993, 5, 1064.
20. E.P. Giannelis, *Adv. Mater.*, 1996, 8, 29.
21. Vaia, R.; Ishii, H.; Giannelis, E.P.; *Chem. Mater.*, 1993, 5, 1064.
22. Vaia, R.; Vasudevan, S.; Krawiec, W.; Scanlon, L.G.; Giannelis, E.P., *Adv. Mater.*, 1995, 7, 154.
23. Usuki, A.; Kato, M.; Okada, A.; Kurauchi, T., *J. Appl. Polym. Sci.*, 1997, 63, 137.
24. Usuki, A.; Kato, M.; Okada, A., *J. Appl. Polym. Sci.*, 1997, 66, 1781.
25. Blumstein, A., *J. Polym. Sci., Pt. A*, 1965, 3, 2665.
26. Bhattacharya, J.; Chakraborti, S.K.; Talapatra, S.; *J. Polym. Sci., Pt. A, Polym. Chem.*, 1989, 27, 3977.
27. Biasci, L.; Aglietto, M.; Ruggerio, G.; Ciardelli, F., *Polymer*, 1994, 35, 3296.
28. M.M. Al-esaimi, *J. Appl. Polym. Sci.*, 1997, 64, 367.
29. Hirata, T.; Kashiwagi, T., and Brown, J.E., *Macromolecules*, 1995, 18, 1410.
30. Solomon, D.H.; Swift, J.D., *J. Appl. Polym. Sci.*, 1967, 11, 2567.
31. Newman, A.C.D., *Chemistry of Clays and Clay Minerals*, Mineralogical Society Monograph, Number 6, Wiley-Interscience, New York, 1987.
32. Gimán, J.W.; Jackson, C.L.; Morgan, A.B.; Harris, R.; Manias, E.; Giannelis, E.P.; Wuthenow, M.; Hilton, D.; and Phillips, S.H., *Chem. Mater.*, 2000, 12, 1866.

Chapter 4

Boron Nitride Fillers for Organic Polymer Composites

**R. T. Paine, E. A. Pruss, G. L. Wood, C. Schwierkowski, R. F. Hill,
C. Chapelle, and W. J. Kroenke**

**Center for Micro-engineered Materials and Department of Chemistry,
University of New Mexico, Albuquerque, NM 87131**

Organic polymers commonly used in microelectronic packaging are inherently poor thermal conductors. Hence, functional components encased in these polymers tend to concentrate heat at its source often leading to component failure. In efforts to overcome this problem, materials designers have suggested that improvements might be realized by additions of thermally conductive ceramic fillers to the polymers. Some early successes have been achieved with polymer composites containing silica or alumina powders; however, enhancements have been limited by the modest thermal conductivity of these common materials. In contrast, boron nitride is an excellent thermal conductor and electrical insulator, and BN filled polymers should be especially good materials for dissipating heat. This paper provides a brief overview of the thermal management application field, as well as a summary of recent progress from our group in the development of new BN powders for use in advanced polymer composites.

For some time, the microelectronics industry has used polymers, such as epoxides and polyimides, as component packaging materials in part due to their ease of processing, electrical resistance, moisture resistance and low cost.^(1,2) Unfortunately, organic polymers also have relatively low thermal conductivity (TC) ($\lambda_p = 0.1\text{-}0.4 \text{ Wm}^{-1}\text{K}^{-1}$). This means that heat dissipated by repeated functional operations of a circuit tends to be trapped at the source resulting first in variable component performance and finally in failure. As system miniaturization, power consumption and circuit speeds have rapidly increased, so has the demand for improved thermal management schemes. Device engineers have attempted to address the problem by introducing electrically insulating, thermally conductive fillers into the traditional thermoplastic polymers already in use for packaging.^(1, 3-7) In the first generation of filled composites, silica was selected as the filler of choice primarily due to its low cost.⁽¹⁾ Unfortunately, silica also has a small TC, ($\lambda_F = 1.5 \text{ Wm}^{-1}\text{K}^{-1}$), and the new composites displayed little thermal conductivity enhancement over the pure polymer. This led to a broader evaluation of ceramic powders as potential filler materials for a second generation of composites.⁽⁸⁻⁹⁾

Boron nitride is a well-known ceramic material that is isoelectronic and isostructural with carbon.^(10,11) The more common, stable form, hexagonal boron nitride (h-BN), has a graphite-like solid state structure composed of extended two-dimensional layers of edge-shared six-membered (BN)₃ rings. Pictorially, the structure resembles chicken wire planes stacked on top of each other with the B atoms in one layer above and below the N atoms of upper and lower layers. The intra-planar B-N bonding is strongly covalent while the B-N interactions between planes are relatively weak. This situation gives rise to anisotropic physical properties including an anisotropic TC: $\lambda_F = 2 \text{ Wm}^{-1}\text{K}^{-1}$ out-of-plane and $400 \text{ Wm}^{-1}\text{K}^{-1}$ in-plane.^(12,13) The cubic form of BN is also a good thermal conductor, but like diamond, it is difficult and expensive to prepare. Therefore, it is not currently considered as a polymer filler in large scale microelectronic applications.

Hexagonal BN is obtained from several industrially practiced high-temperature metallurgical or chemical vapor deposition (CVD) reactions.^(10,14) The ceramic is most often produced in powder form although CVD processes can be used to obtain thin films and coatings. On first glance, it would be anticipated that CVD films should be useful for the formation of heat dissipating electrically insulating layers; however, high substrate temperatures are required for the formation of crystalline material. In practice, commercial BN powders that have been used for composites are produced in multi-step processes that employ high reaction temperatures and cheap, readily available starting materials such as boric acid or boron oxides and ammonia, urea and/or melamine. The reactions are driven by the thermodynamic stability of BN, and the reducing reaction atmosphere that removes carbon and oxygen contaminants as stable,

gaseous by-products. Commercial producers adjust several reaction parameters in order to realize a range of powder grades with well defined purity, grain size, particle morphology, sinterability and crystallinity. These properties, in turn, influence powder processability and composite performance. It is important to note that the inherent particle morphology of h-BN is plate-like. This is a macroscopic manifestation of the microscopic chicken wire structure.

Commercial applications for h-BN powders are well-established for the most part in traditional ceramic materials markets.(10,11,14) For example, its high temperature stability in the absence of air and water and its thermal conductivity make h-BN a favorite choice in refractory crucible manufacture. Recently, aggressive R&D and product marketing have produced an expanding applications horizon for BN. This is particularly evident in microelectronics where the high TC, low thermal expansion coefficient and electrical resistivity make BN a potential filler in composite packaging. The primary drawback is the high temperature required to prepare and process BN. The question becomes: Can BN filled polymer composites, with one or more of the favorable target ceramic properties of BN, be achieved without the use of high processing temperatures? In other words, can we obtain "BN ceramic-like materials without firing"? Conceptually, this outcome might be realized by the formation of composites that contain the BN, prepared "off-line" in a traditional manner, homogeneously dispersed in an appropriate polymer matrix. Further, one would anticipate that as the BN filler loading increased, the properties of the composite could become more like the pure BN than the polymer.

In efforts to determine whether BN/organic polymer composites could be made to display useful thermal conductivity pathways, several groups have reported interesting findings.(15-20) For example, Bujard and coworkers,(15-17) in early studies observed modest TC enhancements ($\lambda_c = 1.4\text{-}2.4\text{Wm}^{-1}\text{K}^{-1}$) with 30% loadings. In addition, they noted that the enhancement factors were strongly dependent on particle aspect ratio and volume fraction. Subsequently, studies by Hill(19) at Advanced Ceramics Corporation, using commercial platelet particles indicated that in some cases large TC enhancements were achievable ($\lambda_c > 10\text{Wm}^{-1}\text{K}^{-1}$) with particle loadings above 50 vol%. The composites also showed good flow properties at this loading level. Most recently, Ishida reported dramatically enhanced thermal conductivities ($\lambda_c > 30\text{Wm}^{-1}\text{K}^{-1}$) with highly loaded (78 vol%) composites formed with a benzoxazine polymer.(20) These findings have encouraged several packaging fabricators to use BN powders in proprietary composite formulations. Given the high TC of BN it is reasonable to expect that even higher thermal enhancements might be achieved. Our group has recently been actively exploring this possibility and some recent results involving BN particle modifications are outlined here.

Early experimental and modeling activities(4,5, 21-29) have encouraged the development of particle filled composites. However, despite intense efforts there

remains a great lack of molecular level information on the factors that control phonon transmission and thermal conductivity in biphasic solids. It is clear that thermal conductivity will be maximized in composites having the highest possible filler loadings with maximum particle-particle interactions. In the simple view, this condition provides for the least phonon scattering. Obviously, the optimum packaging material would be one made only of pure thermally conductive ceramic. As suggested above, ceramic thin films would serve this role well, but in all cases so far studied, the processing temperature for the films precludes their use in electronic packaging applications. Particle filled, processible polymers offer the next best alternative, and the key issue—, maximum particle packing—, becomes one in crystal engineering. For example, if the filler is the major thermal conductor, maximum conductivity, in one direction, should be obtained by optimally packing filler particles in the matrix. Of course, the highest filler loading would be generated by fully ordered, parallel packed single crystal fibers (max. packing fraction, $\phi_m = 0.907 - 0.785$),⁽³⁰⁾ BN fiber filled composites should provide excellent thermal management materials. Unfortunately, at this time, BN continuous, crystalline fibers are unavailable in commercially significant amounts for testing of this application. Amorphous and turbostratic BN fibers have been produced⁽³¹⁻³³⁾ but large scale production appears prohibitively expensive for cost conscious electronic use. Reports of BN fiber formation by nitridation of less expensive borate fibers have appeared;⁽³⁴⁾ however, these fibers are also not readily available or fully characterized. Short BN fibers or whiskers are potentially available in large amounts; however, these are likely to produce random packed networks with low packing fractions ($\phi_m < 0.6$).

Another efficient way to pack a filler into a matrix might be accomplished by close packing of mono-sized spheres ($\phi_m = 0.740-0.60$)^(5,30) with polymer occupying the interstitial volume. Of course, a higher packing density might be achieved with bimodal or broad distributions of sphere sizes with small spheres filling some of the voids created by the close packing of the larger spheres. Empirical data confirm that ceramic spheres process and pack more efficiently in a polymer matrix than do platelet particles. For example, SiO₂ microspheres process more easily and to a higher composite density than non-spherical particles.⁽⁵⁾ We would expect the same to occur with BN; however, until recently, only anisotropic platelet particles were known.

Filler packing density is not the only important issue encountered in attempting to optimize composite thermal performance. Since heat flow is supported by phonon transmission, the highest conductivity is obtained when phonon scattering is the lowest. This occurs when there are the fewest defects in the filler, maximum particle-particle contacts and fewest interfaces between the filler and matrix. Of these, particle-matrix interfacial resistance is probably the most important and the most difficult to control. In the case of the common BN

platelet morphology, aligned particles would pack with good density in only one direction (perpendicular to the platelet planes). Unfortunately, this is perpendicular to the *ab* direction that possesses the maximum thermal conductivity. In addition, due to the high aspect ratio, the platelets will likely generate high viscosity in a flowing polymer matrix which does not bode well for achieving high packing fractions.

Are there any alternatives with BN? Can a spherical morphology particle be obtained? In 1989, we reported the first generation of spherical morphology BN by using aerosol pyrolysis of liquid ammonia solutions of poly-(borazinylamine)(35,36). The particles were collected by impact filtration, and the majority were found to be dense, sub-micron sized and unagglomerated. X-ray diffraction analysis indicated that the crystallinity was low. Subsequent annealing of the spheres in N₂ at 1600 °C led to faceting of the spheres and increased crystallinity. In the same time frame, a French group(37) reported the formation of spheres via a gas phase reaction of BCl₃ and NH₃. In both cases the cost of precursors make the spheres too expensive for use in microelectronic packaging. Therefore, we turned our attention to the next questions. Can spherical BN be prepared in large quantities at a low cost? Will these spheres pack efficiently in a polymer matrix? Can the interfacial resistance between BN spheres and matrix polymer be minimized and controlled? Our recent research has been directed toward obtaining answers to these questions.

The immediate goal of our studies became the development of a cost-effective method to prepare spherical morphology BN so that this material might be tested as a new composite filler. Based upon successful applications for production of other ceramic powders, we chose to explore the aerosol assisted vapor phase synthesis method (AAVS). A typical reactor design is shown in Figure 1. With this system we have used chemical precursors that are the same as those used to make commercial BN powders, namely, H₃BO₃, ammonium borates and NH₃.(38) In typical preparations, a saturated aqueous solution of H₃BO₃ or borate salt is placed in the aerosol chamber. Ultrasonic transducers in the chamber generate a mist which is swept with a nitrogen stream from the chamber into a tube furnace heated for example to 1000 °C, and ammonia gas is introduced at the reactor front. The mist droplets flash dry and the boric acid or borate dehydrates while beginning to undergo nitridation by reaction with the ammonia. This mechanistic suggestion is consistent with TGA observation of boric acid samples heated from 25 °C to 1200 °C in an ammonia atmosphere.(39) Here, there is a rapid weight loss of about 15 % from 25 °C to 250 °C and then little (< 5%) weight loss out to 1200 °C. In the AAVS reactor, the total residence time varies with conditions employed, but typical times in a 4 ft. hot zone, (3 inch diameter) are 10-30sec. The resulting white powder is collected on a nylon filter. Typical yields are 0.5-2.0 g/hr. Chemical analyses

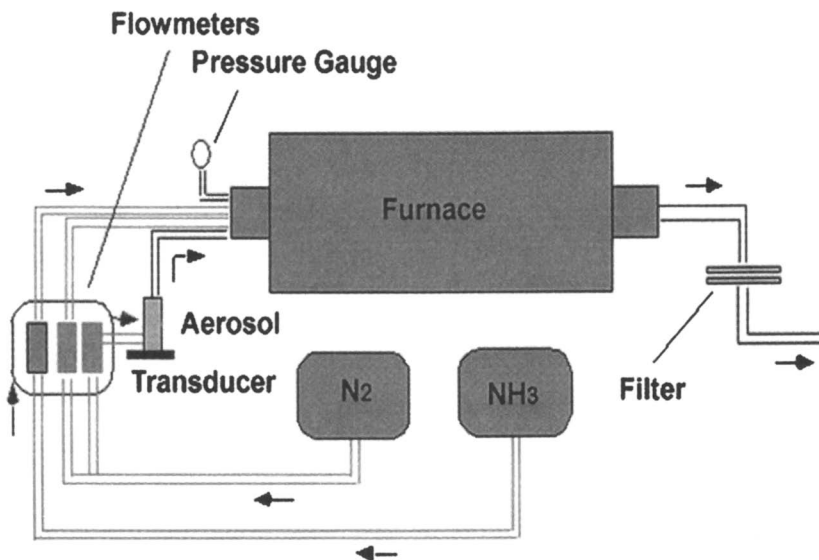


Figure 1. Schematic view of AAVS reactor.

show that the powder is an amorphous oxynitride with a formula BN_xO_y in which the oxygen content may be as high as 50 wt % and as low as 40 wt %. Bulk chemical analysis and X-ray photoelectron spectroscopy (XPS), recorded from powders produced at reactor temperatures of 600 °C, 800 °C, 1000 °C and 1100 °C, show a steady decrease in the amount of bulk oxygen in the collected powders. The XPS data also reveal an increase in the oxygen content progressing from the particle surface to the interior. A scanning electron micrograph (SEM) of a typical powder is shown in Figure 2. Particle sizes range from 0.2-3 microns. Under some reactor conditions some particles are hollow as displayed in Figure 3 and the interior contains unconverted crystalline borate. Under proper conditions, the particles are generally dense and relatively homogeneous in composition. As shown in Figure 4 the powders formed at 600 °C are amorphous to X-rays while the powders formed above a reactor temperature of 800 °C have a turbostratic structure.

The BN_xO_y aerosol powder would be expected to have a low thermal conductivity due to the porous structure and high oxygen composition, and this proves to be correct. Therefore, these powders have been subsequently annealed in an ammonia atmosphere from 1000 °C to 1700 °C. This treatment results in a dramatic decrease in oxygen to as low as 0.5% based upon full chemical analyses of bulk samples. The resulting crystallinity and particle morphology

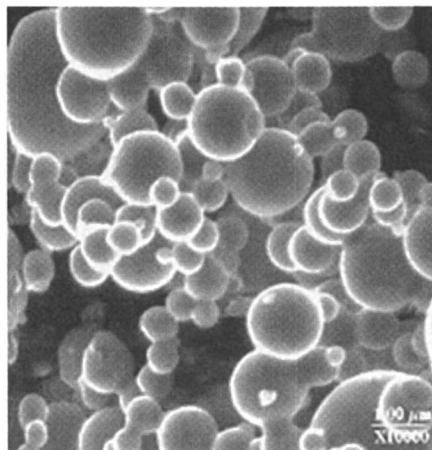


Figure 2. Scanning electron micrograph (SEM) of BN_xO_y powder obtained at 1000 °C reactor temperature.

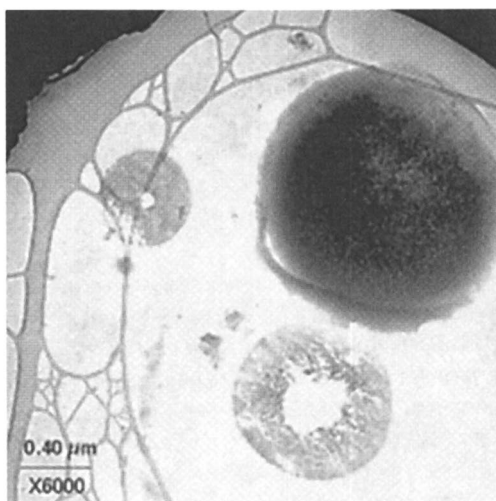


Figure 3. SEM of larger particles.

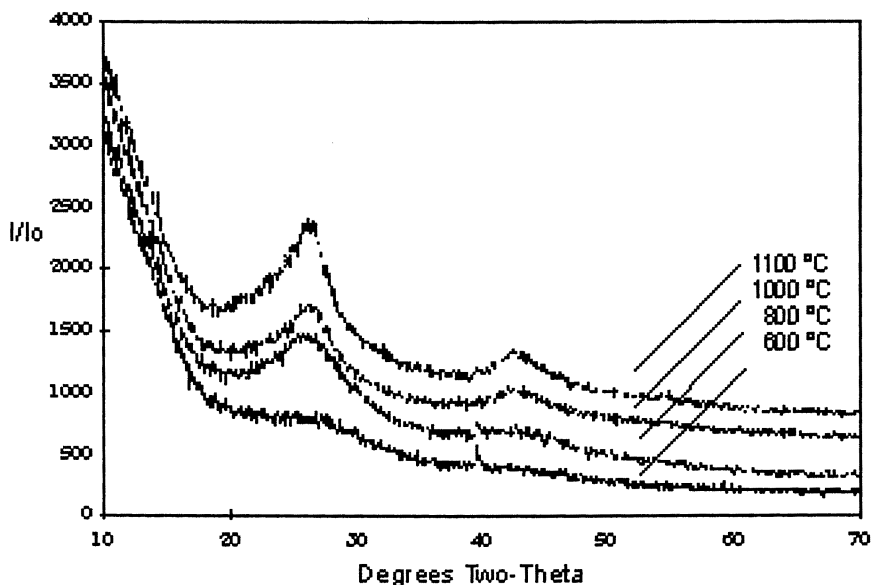


Figure 4. X-ray diffraction scans for BN_xO_y powders formed with reactor temperatures 600 °C to 1100 °C.

depend upon several variables that can be controlled during the annealing process. In particular, the particles can be smooth spheres, bladed spheres or fully bladed as shown in SEMs collected in Figure 5. A transmission electron micrograph (TEM) of the smooth particles is shown in Figure 6. The powder XRD scans for these samples are shown in Figure 7. They show that the crystallinity of these samples is high.

The first efforts to prepare polymer composites using the spherical powders have been made. The smooth powders process well in epoxides and load above 50 vol % producing composites with thermal conductivities approaching $4 \text{ W m}^{-1} \text{ K}^{-1}$. These values are comparable to data obtained with small platelet BN. The bladed spheres are more crystalline and it is expected that they will show further improvements. It is also expected that larger spherical particles could provide even greater enhancements.

The initial results from this study are encouraging and they have stimulated more intense efforts to develop a large scale synthesis for spherical BN particles. This effort has been successful and will be reported separately. In addition, there is much yet to be learned about the processing of these new powders in polymers and that work is on-going in our group at this time.

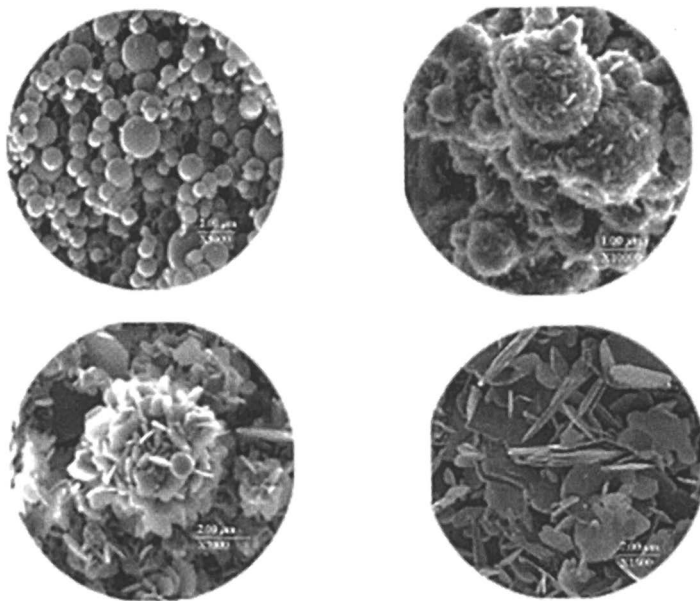


Figure 5. SEM's of annealed particles of BN.

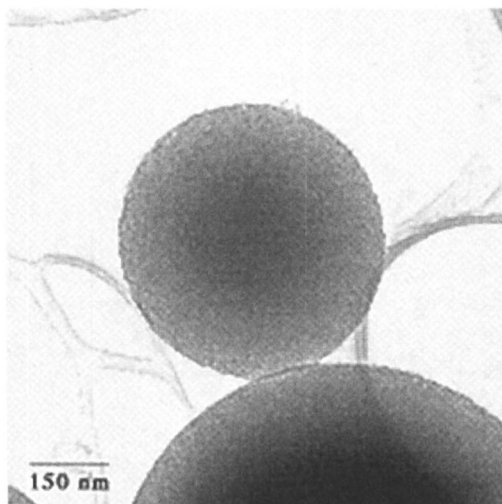


Figure 6. TEM view of smooth BN spheres.

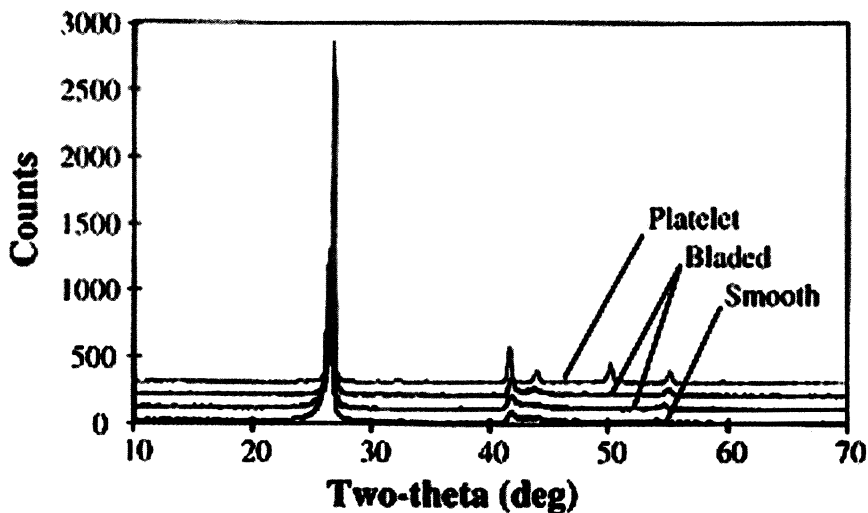


Figure 7. XRD scans for crystalline BN particles having morphologies illustrated in Figure 6.

Acknowledgment is made to the industrial sponsors of the University of New Mexico, Center for Micro-Engineered Materials and the National Science Foundation (Grant EEC-9814446) for financial support of this work. We also thank Advanced Ceramics Corp. for critical materials and discussions relevant to the project.

References

1. Rothon, R. N. in *Adv in Polymer Sci*, **1999**, 139, 67 and references therein.
2. Licari, J. J. *Plastic Coatings for Electronics*. McGraw Hill, N.Y. 1970.
3. Michael, M.; Nguyen, L. *Proc. Inter. Soc. Conf. Thermal Phenomena, IEEE*, **1992**, 246.
4. Bigg, D. M. *Polymer composites*, **1986**, 7, 125.
5. Bigg, D. M. *Adv in Polymer Sci.*, **1995**, 119, 3.
6. Lupinski, J. H.; Moore, R. S. *ACS Symp. Ser.*; **1989**, 407, 1.
7. Hoffman, R. R.; Tye, R. P.; Chervenak, J. G.; *Advances in Thermoplastic Matrix Composite Materials*, ASTM STP 1044, Neway, G. M.; Ed.; Amer. Soc. For Testing and Materials, Philadelphia, 1989, p 146.

8. Bolt, J. D.; French, R. H. *Adv. Mater. Processes, Metal Progress*, **1988**, *7*, 32.
9. Proctor, P.; Solc, J. *IEEE Trans. Comp.; Hybrids and Manuf. Technol.* **1991**, *14*, 708.
10. Paine, R. T.; Narula, C. K. *Chem. Rev.* **1990**, *90*, 73.
11. Narula, C. K. *Ceramic Precursor Technology and Its Applications* Marcel Dekker, N.Y. 1995.
12. Sickel, E. K.; Miller, R. E.; Abrahams, M. S.; Buiocchi, C. J. *Phys. Rev. B* **1976**, *13*, 4607.
13. Simpson, A.; Stuckes, A. D. *J. Phys. C: Solid St. Phys.* **1971**, *4*, 710.
14. *Ullman's Encyclopedia of Industrial Chemistry*, Gerhartz, W. Ed. VCH Publ, Weinheim, 5th Ed., Vol A4, p 300, 1985.
15. Bujard, P.; *Proc. I-THERM-1988*, May, 1988, p 41.
16. Bujard, P.; Kühnlein, G.; *IEEE Trans. Components: Packaging and Manuf. Tech. Part A*, **1994**, *17*, 159.
17. Bujard, P.; Kühnlein, G.; Ino.; Shiobora, T. *IEEE Trans. Components: Packaging and Manuf. Tech. Part A*, **1984**, *17*, 527.
18. Hatta, H.; Taya, M.; Kulacki, F. A.; Harder, J. F. *J. Composite Mater.* **1992**, *26*, 612.
19. Hill, R. F. "Characterization and Performance of Thermally Conductive Epoxy Compounds," *Proc. Tech. Prog. SMTA Nat. Symp.*, Research Triangle Park, N.C.; 1996.
20. Ishida, H.; Rindusit, S. *Thermochemica Acta* **1998**, *320*, 177.
21. Nielsen, L. E.; Landel, R. F. *Mechanical Properties of Polymers and Composites*, Marcel Dekker, New York, 1974 Vol. II, Ch 7.
22. Nielsen, L. E. *J. Appl. Polym. Sci.* **1973**, *17*, 3819.
23. Agari, Y.; Uno, T. *J. Appl. Polym. Sci.* **1985**, *30*, 2225.
24. Agai, Y.; Tanaka, M.; Nagai, S.; Uno, T. *J. Appl. Polym. Sci.* **1986**, *32*, 5705.
25. Wang, C. P.; Bollampolly, R. S. *IEEE Trans. On Adv. Packaging* **1999**, *22*, 54.
26. Cheng, H.; Torquato, S. *proc. Royal Soc. London (A)* **1997**, *453*, 145.
27. Lu, S.;-Y. *J. Appl. Phys.* **1995**, *77*, 5215.
28. Lipton, R. *J. Composite Mater.* **1998**, *32*, 1322.
29. Torquato, S. *Rev. Chem. Eng.* **1987**, *4*, 151.
30. Hoffman, R. R.; Type, R. P.; Chervenak, J. G. *Advances in Thermoplastic Matrix Composite Materials*, ASTM STP 1044, **1989**, 146.
31. Lindquist, D. A.; Janik, J. F.; Datye;, A. K.; Paine, R. T.; Rothman, B. *Chem. Mater.* **1992**, *4*, 17.
32. Weidman, T.; Sneddon, L. G. *Chem. Mater.* **1996**, *8*, 3.
33. Kimura, Y.; Kubo, Y.; Hayashi, N. *Composite Sci. and Tecnol.* **1994**, *51*, 173.

34. Economy, J.; Lin, R. *Boron and Refractory Borides*, Matkovich, V.I.Ed., Springer Verlag: Berlin (1977) p 552.
35. Paine, R. T. "Molecular and Polymeric Precursor to Ceramic Materials," *Abstr. 1st Inter. Ceram. Sci. and Tech. Cong.* Oct. 31, 1989.
36. Lindquist, D. A.; Kudas, T. T.; Smith, D. M.; Xiaomei, Q.; Hietala, S.; Paine, R. T. *J. Am. Ceram. Soc.* **1991**, *74*, 3126.
37. Iltis, A.; Mognier, C. Eur. Patent 0396448, April 20, 1990.
38. Pruss, E. A.; Wood, G. L.; Kroenke, W. J.; Paine, R. T. *Chem. Mater.* **2000**, *12*, 19.
39. Wood, G. L.; Pruss, E. A.; Paine, R. T. unpublished results.

Chapter 5

Surface-Initiated Anionic Polymerization: Tethered Polymer Brushes on Silicate Flat Surfaces

Qingye Zhou¹, Yo Nakamura^{1,2}, Seiji Inaoka¹, Mi-kyoung Park¹,
Yingfan Wang¹, Xiaowu Fan¹, Jimmy Mays¹, and
Rigoberto Advincula^{1,*}

¹Department of Chemistry, University of Alabama at Birmingham,
Birmingham, AL 35294-1240

²Current address: Department of Macromolecular Science, Osaka
University, Toyonaka, Osaka 460-0043, Japan

Recently, there has been much interest in using Surface Initiated Polymerization (SIP) in preparing organic-inorganic *delaminated* nanocomposites. These nanocomposites have generated much interest because of their potential for applications in high barrier coatings, electronic materials, catalysis, and fundamental studies of polymers in confined environments. Polymer clay/silicate composites have been investigated for a number of years. One of the best ways to achieve control of their application properties is by direct covalent attachment of polymer chains to the particle surfaces using appropriate polymerization methods. Here we report the formation of polystyrene films grafted from silicate surfaces by the *living anionic polymerization* of styrene. Activated 1,1-diphenylethylene (DPE)-chlorosilane initiation sites were formed by self-assembled monolayers (SAM) on flat silicate surfaces. We have characterized these films by contact angle measurements, atomic force microscopy, attenuated total

reflection FT-IR, X-ray photoelectron spectroscopy, and ellipsometry. Our results indicate the formation of ultrathin films with unique morphologies and brush densities, as compared to previously polymerized films made by free-radical mechanisms. Thus, they provide insight to differences in anionic versus radical polymerization in surfaces and facilitate new possibilities for block and graft copolymerization from surfaces in the future.

Introduction

Surface Initiated Polymerization (SIP) is a method of preparing an assembly of tethered polymer chains in mutual proximity forming so called "polymer brushes". A huge amount of theoretical work has also been devoted on tethered polymer brushes in comparison to the limited experimental information available on their properties and structure. (1,2,3) This unique geometry at solid interfaces ideally results in end-grafted, strictly linear chains of the same length where the grafting density is sufficiently high with respect to the equilibrium radius of gyration (R_g) of the grafted macromolecules. (4) To avoid steric crowding, the polymer chains are forced to stretch away from the interface, resulting in a brush height (h), which is significantly larger than R_g .

Tethered polymers on flat surfaces have involved polymer physisorption and chemisorption (covalent attachment). For polymer physisorption, diblock copolymers are used where one block strongly adsorbs to the surface. The usually shorter "anchor" block adsorbs strongly onto the surfaces, leaving the remaining "buoy" block, tethered to the interface.(5) For covalent attachment or chemisorption, tethering has been accomplished by grafting preformed polymers to tethering sites, a "grafting to" approach or by polymerizing from surface-immobilized initiators, a "grafting from" approach. These differences are shown schematically in Figure 1. Examples of the latter approach include polymerization using surface-immobilized azo-bis isobutyronitrile (AIBN) analogues,(6) atom-transfer radical polymerization (ATRP),(7) 2,2,6,6-tetramethylpiperidinoxy (TEMPO),(8) cationic (9) and anionic(10) initiators.

The "grafting from" methods have intrinsic advantages in that the grafting density is not self-limiting, i.e. the initiator is bound to the surface and is primarily dependent on monomer diffusion and reactivity. With the "grafting to" approach, as the grafting density increases, the chains have to stretch to allow further grafting, which results in a decrease in the rate of grafting kinetics. (11)

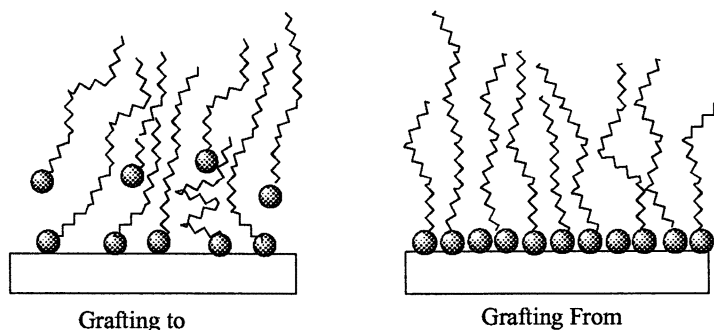


Figure 1. Schematic diagram comparing the grafting to and grafting from approaches with chemisorbed macromolecules. Spheres represent reactive endgroup or initiator.

Organic-inorganic nanocomposites have generated much interest because of their potential for applications in tough and high temperature-compatible, particle-reinforced polymers, coatings, electronics, catalysis, and the study of polymers in confined environments.⁽¹²⁾ One important class of organic/inorganic hybrids that has been developed over the past few years are polymer-layered silicate (PLS) nanocomposites.^(13,14,15) These nanocomposites have generated much interest because of the need for new polymeric materials and composites with suitable barrier properties, e.g. for soldier protection. This includes chemical resistance, selective permeability, resistance to environmental changes, and reduced weight with increased strength. Layered silicates (mica, clay) have been “blended” with polymers to produce two types of structures: 1) *intercalated structures* where a single extended polymer chain is positioned between the silicate layers, resulting in alternating layers of the polymer and the inorganic sheets, with a repeat distance of a few nanometers; 2) *delaminated structures* where the silicate layers are exfoliated and dispersed in a continuous polymer matrix, more like a traditional filled polymer system. A group at the Toyota Research Center in Japan first demonstrated the remarkable properties of PLS nanocomposites using the nylon/montmorillonite system.⁽¹³⁾ They showed that addition of low levels of clay (1-10% by weight) doubled the modulus and tensile strength and increased the heat distortion temperature by 100 °C. These property improvements allow the use of these composites in higher temperature applications (e.g. under the hood in cars). Also, because only a very small amount of the clay is necessary to achieve these property enhancements, the composites are very lightweight. Furthermore, the plate-like nature of the clays give two-dimensional reinforcement compared to the one dimensional reinforcement obtained with

polymer/fiber composites, and, in the case of the intercalated structures, materials with outstanding barrier properties can be generated.

A key factor in all work involving mixtures of polymers with inorganic materials is the nature of the interface. Most of the work on modifying particle surfaces with polymers has focused on physical adsorption of homopolymers or copolymers.¹⁶ However, such adsorbed layers are susceptible to removal, e.g. by exposure to a thermodynamically good solvent. Furthermore, it is often difficult to precisely control the physical structure of such adsorbed layers (thickness, chain orientation, placement of functional groups, etc.). In the case of intercalated nanocomposites incorporating clays, there are difficulties in fabrication due to the close packing of the silicate sheets. This inherent spacing is of the order of 1nm, which is much smaller than the R_g of a typical polymer chain. Thus, there is a large entropic barrier, combined with a strong enthalpic barrier, that inhibits the penetration of the polymer into this region and, consequently the intercalated structure cannot be readily formed by simple adsorption of homopolymers or block copolymers (in melt blending or extrusion processes). The Toyota group overcame this problem and produced composites of clay intercalated with nylon by swelling the clay with caprolactam, which reacts with the charged Montmorillonite surface, followed by addition of more caprolactam or related nylon monomers.⁽¹⁶⁾ While effective with nylon, this is not a method that is widely applicable to various monomers. The polymer is bound to clay by ionic bonds (the common natural type of Montmorillonite is composed of sodium ions and negatively charged Montmorillonite). Vaia and Giannelis have worked extensively with composites of organically-modified layered silicates (OLS).⁽¹⁴⁾ OLS are composed of surfactant modified clays commonly made via a cation exchange reaction. They have emphasized that whether a mixture of polymer and OLS forms an exfoliated, intercalated, or conventional nanocomposite depends critically on the character of the polymer and the OLS. Enthalpic and entropic considerations between polymer, silicate, and surfactant, needs to be defined. Existing guidelines as to the optimum OLS/polymer combinations are unsatisfactory, making hybrid synthesis a laborious trial and error process.

Thus a general method suitable for use with a wide range of monomers/polymers is lacking. Current synthetic methods are incapable of controlling the polymer conformation, graft density, and architecture to produce highly dispersed and processible materials. For delaminated nanocomposites, the best way to achieve property control is by direct covalent attachment of polymer chains to the particles using an appropriate polymerization method. ⁽¹⁷⁾

To address the investigation of polymerizable systems for covalently tethered polymers to clay and silicate surfaces, we have investigated *surface initiated anionic polymerization*. In this article, we report the formation of polystyrene films grafted from a silicate (SiO_x layer) surface by *living anionic*

polymerization of styrene. Activated 1,1-diphenylethylene (DPE)-chlorosilane initiation sites were formed by self-assembled monolayers (SAM) on silicate surfaces (SiO_x layer of a silicon wafer). To our knowledge, the formation of these polymer brushes by the activation of DPE on surfaces has not been previously reported. Previous work on anionic polymerization has focused on other initiators and surfaces.^(10,18) We have characterized these films by contact angle measurements, atomic force microscopy (AFM), Fourier-Transform infrared spectroscopy (FTIR), X-ray photoelectron spectroscopy (XPS), and ellipsometry. As model studies, we need to distinguish the concept of surface initiation from our eventual goal, which is intergallery initiation in silicate (clay) particles. First, it is important to investigate in detail, the anionic polymerization mechanism from ideal (flat silica) surfaces.

Experimental

Synthesis of the Initiator

The initiator was synthesized: 1,1-diphenylethylene (DPE)-chlorosilane as shown in the schematic diagram in Figure 2. The DPE is separated from the silyl group by an alkyl spacer (8 and 11 carbon lengths were synthesized). The intermediate products were analyzed primarily by NMR were found to be consistent with the reported structures and constitution. DPE was specifically chosen to avoid self-polymerization parallel to the plane surface as attached to the surface by SAM.⁽¹⁹⁾ It is then reacted *in-situ* with *sec*-BuLi or *n*-BuLi to activate it for anionic polymerization.

Synthesis of 4-Bromo-DPE (1).

To a 500 mL round-bottomed flask, fitted with a dry nitrogen inlet septum, methyltriphenylphosphonium iodide (31 g, 76 mmol) was suspended in dry THF under nitrogen gas atmosphere. To the suspension was added *n*-BuLi (31 mL of 2.5 M in hexane, 76 mmol) at room temperature with stirring. The mixture immediately became dark red and was stirred continuously for half one hour. 4-bromobenzophenone (20 g, 76 mmol) was then added to the mixture by syringe over a 30 minute period with vigorous stirring at room temperature. After completion of the addition step, the mixture became yellow and was stirred overnight at room temperature under nitrogen atmosphere. It was then diluted with 150 mL of chloroform and 150 mL of diluted hydrochloride acid aqueous solution. The organic phase was collected, washed and dried over MgSO₄. The solvent was removed by rotary evaporation and the resulting residue purified by chromatography on silica gel using *n*-hexane as the eluent. This procedure

resulted in 16.8 g of 4-bromo-DPE as yellow oil (yield). The product can also be purified by distillation. ^1H NMR (CDCl_3) δ 7.44 (2H, d, $J = 8.7$, Ar-H), 7.30 (5H, m, Ar-H), 7.19 (2H, d, $J = 8.7$, Ar-H), 5.44 (2H, d, $J = 3.0$, $\text{C}=\text{CH}_2$). ^{13}C NMR (CDCl_3 , 300MHz): 149.5, 141.4, 140.9, 131.8, 130.4, 128.8, 128.7, 128.4, 122.3, 115.2.

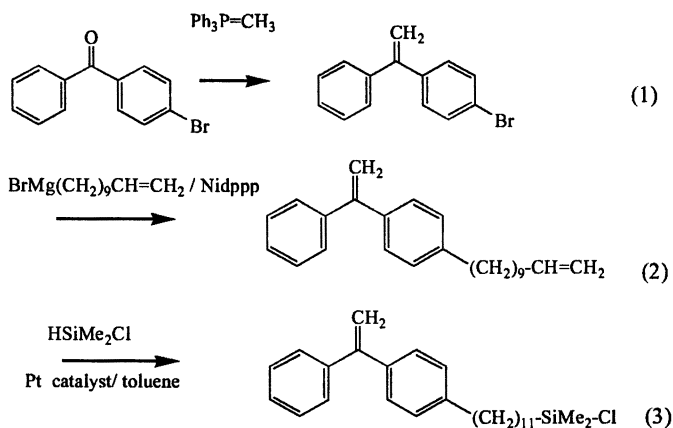


Figure 2. Schematic diagram of initiator synthesis (DPE) functionalized with silane coupling agent and alkyl spacer.

Synthesis of 4-(11'-undecenyl)-DPE (2)

1.5 g (51.8 mmol) of activated magnesium turnings and a small iodine particle were placed in a three-necked flask equipped with a reflux condenser and purged with nitrogen. A portion of a solution of 11-bromo-1-undecene (12 g, 51.8 mmol) in 20 mL of dry diethyl ether was then added to the flask. Following the initiation of the Grignard reaction, the rest of the 11-bromo-1-undecene solution was added over 30 min. After refluxing for 2h, the Grignard reagent was transferred to an addition funnel, and was slowly added to a mixture of 40 mg of 1,3-bisdiphenylphosphinopropane Nickel (II) chloride or $\text{Ni}(\text{dppp})\text{Cl}_2$ and 5 g (19.3 mmol) of 4-bromo-DPE in 20 mL of diethyl ether. After stirring at room temperature for 12 hrs, the mixture was acidified with dilute hydrochloride aqueous solution and extracted with diethyl ether three times. The combined organic extracts were washed with a saturated aqueous Na_2CO_3 solution and dried over anhydrous Na_2SO_4 . Distillation under reduced pressure gave 3.92 g of 4-(undec-9-enyl)-DPE as a colorless oil. ^1H NMR (CDCl_3) δ 7.34-7.32 (5H, m, Ar-H), 7.24 (2H, d, $J = 8.7$, Ar-H), 7.13 (2H, d, $J =$

8.5, Ar-H), 5.44-5.41 (1H, m, -CH=), 5.40 (2H, d, $J = 3.0$, =CH₂), 5.03-5.01 (2H, m, =CH₂). 2.61 (2H, t, $J = 6.6$, -CH₂-), 2.05-1.28 (m, 16H, -(CH₂)₈-). ¹³C NMR (CDCl₃, 300MHz) 150.4, 143.0, 142.2, 139.7, 139.1, 128.8, 128.6, 128.5, 128.0, 114.6, 114.1, 36.1, 34.3, 33.1, 31.9, 29.9, 29.8, 29.7, 29.6, 29.4.

Synthesis of chloride silane-DPE derivative (3).

4-(11'-undecenyl)-DPE (2) (1.73 g, 5.94 mmol) was dissolved in 10 mL of dry toluene followed by addition of (851.5 mg, 9mmol) of chlorodimethylsilane and three drops of the catalyst Platinum(0)-1,3-divinyl-1,1,3,3-tetramethylidisiloxane complex in xylene with N₂ protection. After the mixture was heated overnight under N₂ atmosphere at 50-60 °C, the solvent and unreacted chlorodimethylsilane were removed under vacuum. ¹H NMR analysis indicated that all 4-(11'-undecenyl)-DPE (2) was completely consumed. Yield 1.82g. ¹H NMR (CDCl₃) δ 7.34-7.32 (5H, m, Ar-H), 7.24 (2H, d, $J = 8.7$, Ar-H), 7.13 (2H, d, $J = 8.5$, Ar-H), 5.40 (2H, d, $J = 3.0$, =CH₂), 2.61 (2H, t, $J = 6.6$, -CH₂-), 2.05-0.71 (m, 16H, -(CH₂)₁₀-), 0.29 (s, 6H, -Si(CH₃)₂-).

Self-assembled Monolayers of the Initiator

Self-assembled monolayers of the DPE initiator were prepared as follows: Both glass and silicon wafer substrates were plasma (under Ar, using PLASMOD, March Instruments) and piranha solution (30% H₂O₂ : 70%H₂SO₄, 15 min) cleaned. The substrates were thoroughly rinsed with Milli-Q purified H₂O and dried in an oven (90 °C) overnight before use. Modified gold-coated quartz crystals (QCM substrates) were plasma treated under O₂ conditions. To adsorb the DPE initiators, the cleaned substrates were immersed in 1 mM of the organosilane initiator in toluene solution (under N₂ gas) for more than 12 hours. After reaction, the substrates were sonicated for 15 min. with 1) toluene, 2) toluene: acetone, 1:1 and 3) acetone in sequence. The substrates were then immediately transferred to the vacuum line (under N₂ gas) and sealed. Similar procedures for cleaning and adsorption were adapted for the self-assembly of the initiator on modified gold surfaces. The surfaces were characterized before and after polymerization.

Characterization of the Surface and Polymer Films

One major objective is to compare anionic polymerization on surfaces and their unique properties compared to solution polymerization. The surface properties and chemistry involved in the initiation process may dramatically affect a living polymerization mechanism. Characterization of the surface is

critical in determining the kinetics, mechanism, and stability of surface initiated polymerization. We have used: Atomic force microscopy (AFM)-Molecular Imaging (PicoScan) to investigate surface morphology. This involved the use of Magnetic-AC or MAC modes to minimize tip-surface interaction and sample deformation. The MAC lever consists of a Silicon Nitride based cantilever coated with magnetic films. The force constant is about 0.5 N/m with resonant frequency in air between 90 to 105 kHz. The sample stage has a solenoid mounted underneath the plate. Ellipsometry for thickness measurements was done using a Microphotonics SE 400 Sentech Ellipsometer at an incidence angle of 70° (He-Ne laser, 632.8 nm) using a refractive index value of 1.45 for the SAM and 1.50 for the polymer. Contact angle measurements, both dynamic and static measurements, were done on a MicroCAM contact angle goniometer and gave data for surface energy and wetting characterizations. The measurements were taken at several different spots of the same substrate and the average value reported. Quartz Crystal Microbalance measurements were done on a MAXTEK, QCM system with a PM-740 frequency counter. The Sauerbrey equation was used to relate the mass increase (due to chemisorption) with the frequency change.⁽²⁰⁾ Preliminary cyclic voltammogram measurements were done on the quartz substrate with a Bioanalytical Systems BAS-100B Electrochemical Analyzer. This was done with a Ag /Ag+ working electrode and platinum wire in anhydrous acetonitrile (Aldrich) containing 0.1 M LiClO₄ as supporting electrolyte. Cyclic voltammograms were determined at 100 mVs⁻¹ and were integrated graphically. XPS measurements were made with a Kratos Axis 165 SAM/XPS system (University of Alabama at Tuscaloosa). Size exclusion chromatography (SEC) and matrix-assisted laser desorption/ionization time-of-flight mass spectrometry (MALDI-TOF-MS) were used to analyze the polymers formed in solution. FT-IR ATR measurements were made with the Bomem Prota FT-IR using a variable ATR attachment (Spectratech Model 300) with KRS-5 prism (2.37 R.I.).

Polymerization Procedure for Polystyrene

Styrene was stirred with CaH₂ overnight, degassed 3 times on the vacuum line, and then distilled into the flask containing dibutylmagnesium. After stirring for a few hours, it was distilled into ampoules. Benzene was stirred with CaH₂ overnight, degassed 3 times and then distilled into a flask with BuLi and a small amount of styrene (orange color). The high vacuum apparatus is shown in Figure 3. After placing the SAM-coated glass or silicon wafer (with DPE) in the reactor and sealing, the s-BuLi or n-BuLi (about 1 x 10⁻³ mol in 5 mL hexane) was injected into the purge section through the septum. The solution was left with the substrate overnight. Excess BuLi solution was then removed and the surface was washed several times with degassed benzene to ensure removal of excess BuLi

and impurities. THF or BuOLi was also added into the initiator solution to observe its effect on the initiation of DPE. The styrene monomer was then introduced by breaking the break seal between the reactor and the monomer ampoule. The polymerization was allowed to proceed for periods of a few hours to a few days before it was terminated by MeOH. The samples were taken out of the reactor and immediately washed using Soxhlet extraction procedures for 36 hours. A complete description of the polymerization and characterization results will be reported in a forthcoming publication.(21)

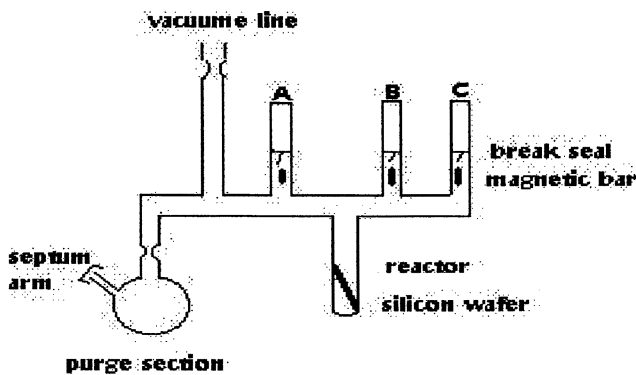


Figure 3. Schematic Diagram of the polymerization set-up under high vacuum and inert conditions. A: ampoule containing THF, B: ampoule containing methanol, C: ampoule containing styrene.

Results and Discussion

Synthesis and Immobilization of the Initiator

The design parameters of the initiator combine: DPE functionality, spacer (alkyl chain), silyl agent (chlorosilane group), and capacity for post-polymerization cleavage. The DPE is separated from the silyl group by an alkyl spacer. DPE was specifically chosen to avoid self-polymerization parallel to the plane surface. The DPE-chlorosilane was then attached to the surface by SAM. The tethered DPE moieties were then reacted with BuLi for activation. The SAM preparation work was done under vacuum or under inert atmosphere (dry box) as appropriate. For controlled dispersion of the grafting sites, variation of initiator density; mixtures and co-adsorption of the DPE derivative with varying amounts of alkyldimethylchlorosilane was used to control the DPE density on the surface

American Chemical Society
Library
1155 16th St, N.W.
Washington, D.C. 20036

while eliminating the Si-OH groups that can interfere with the polymerization.(22)

Ellipsometric measurements on the Si wafer indicated a thickness of about 1.7 nm. The contact angle measurements showed a change from 20° to 82°, reflecting the change in the wetting properties of the surface after chemisorption of the initiator by SAM. AFM measurements did not indicate any clear morphology features compared to that of bare SiO_x surface. We also characterized the adsorption properties of the initiator on modified gold electrode and quartz crystal surfaces.(23) Using QCM, a change of $\Delta F = -144$ (Hz) indicated a thickness of 1.7 nm for the DPE initiator assuming a density of 1 g/cm³. This is consistent with that obtained by ellipsometry.

Using cyclic voltammetry experiments, the DPE pendant groups on the monolayer can be oxidized on a conducting gold electrode surface to quantitatively assess the molecular density of the monolayer. A schematic diagram of the oxidation process is shown in Figure 4. This assumes that 1 electron per molecule is consumed for coupling and 0.5 electron per molecule will participate in the redox reaction (a total of 1.5 electron/molecule will be consumed at the very first cycle. Preliminary cyclic voltammogram measurements indicated that DPE functional groups showed oxidation with the onset of +1000 mV(vs Ag /Ag⁺). The oxidation potential is lower than the background oxidation of the solvent (acetonitrile). Based on the area of the electrode (50 mm²), electron density (16 $\text{\AA}^2/\text{electron}$), and the charge injected (40-80 μC), it was reasonable to conclude that a monolayer of DPE can be formed on the surface.(24) A molecular density value of 24.1 $\text{\AA}^2/\text{molecule}$ was obtained which is typical of a well-packed SAM monolayer bearing electroactive species.

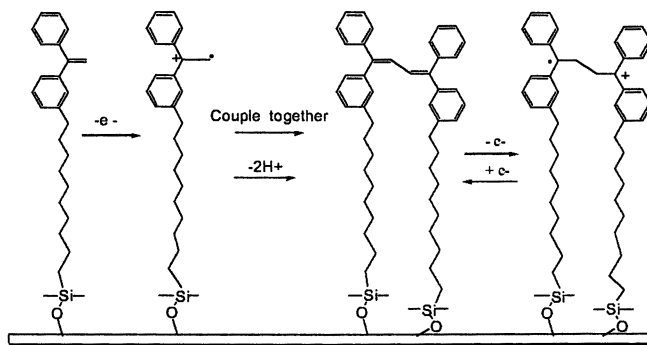


Figure 4. Schematic Diagram of the oxidation onset on the SAM of the DPE-initiator on a QCM crystal (gold electrode) indicating monolayer formation.

Model surfaces of float glass and mica are also currently being investigated. These substrates are idealized surfaces appropriate for several surface sensitive spectroscopic and microscopic techniques. It is important to compare their properties and differences with clay and silica particulate surfaces.(25)

Polymerization and Characterization at the Surface

Using the polymerization procedure, several attempts were made with samples prepared inside the constructed vacuum reaction vessel (SIP B-3, B-4, B-5, S-3 and S-4) and in an inert atmosphere glovebox (SIP-B-9 and SIP-B-6). The polymerization was activated by introducing *n*-Bu-Li or *S*-BuLi, followed by the addition of the monomer. This is shown schematically in Figure 5. After polymerization, all the films were washed for more than 36 hours by Soxhlet extraction in toluene prior to characterization of the surfaces. The following polymerization conditions and results were obtained and summarized in Table 1.

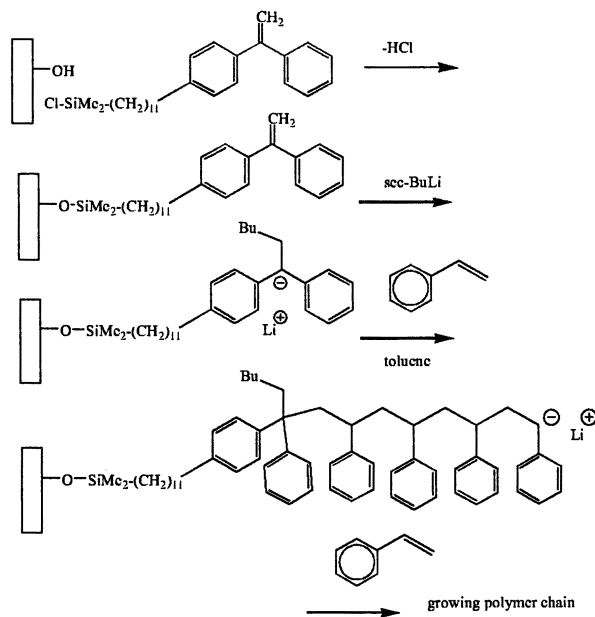


Figure 5. Immobilization of the DPE initiator and activation by the addition of *sec*-BuLi. Monomer is eventually added and results in polymerization.

The data in Table 1 indicates several attempts at polymerization on silicon wafers (attached to glass). The best repeatable attempts obtained films of 16.1 ± 0.2 nm average thickness for dry polystyrene brushes as obtained using ellipsometry. These results are comparable to that obtained by Ulman and co-workers (18 ± 0.2 nm), where they reported homogenous films of uniform coverage.⁽¹⁸⁾ They have estimated a degree of polymerization of $N=382$ and a grafting density of 7-8 chains/ R_g^2 or 3.2-3.6 nm²/chain based on mean-field theory calculations from *in-situ swelling experiments*, monitored by ellipsometry. The use of n-BuLi resulted in better polymerization, as it was easier to remove by washing compared to s-BuLi. This resulted to lower amounts of free initiator species (BuLi) present that may initiate the polymerization of styrene from solution. We have observed this in cases where unremoved BuLi is present in solution. This resulted in polymers with up to $M_n = 100 \times 10^4$, P.D.=1.44, as analyzed by SEC and MALDI. THF was added together with n-BuLi to accelerate the initiation of DPE. We also did not observe any significant improvement with samples prepared (SAM and polymerization) using a glove box procedure with inert atmosphere conditions. Attenuated total reflection (ATR) FT-IR measurements verified the presence of grafted polystyrene based on the functional groups present, 3,100-2,700 cm⁻¹ aliphatic CH and 1506, 733 cm⁻¹ C=C aromatic stretching vibrations (upon comparison with standard polystyrene peaks). Polarized FT-IR measurements will be conducted to determine the preferential orientation of the polystyrene chains.

Table 1. Polymerization Conditions and Results

<i>SAMPLE</i>	<i>Activation</i>	<i>Additive</i>	<i>Thickness in nm *</i>	<i>Contact Angle</i>
SIP-B-3	s-BuLi	none	6.8	95
SIP-B-4	n-BuLi	THF	10.8 (16%)	70
3 days			16.1 (100%)	76
SIP-B-5	n-BuLi	THF	13.4 (16%)	95
5 days			13.7 (100%)	89
SIP-S-3	s-BuLi	BuOli	3.8 (16%)	50
(3 days)			3.9 (100%)	72
SIP-S-4	n-BuLi	THF	6.3 (16%)	61
(5 days)			8.2 (100%)	64
SIP-B-9	n-BuLi	THF	8.9	82
SIP-B-6	n-BuLi	THF	4.7	74

NOTE: * brackets indicate % of DPE initiator with alkydimethylchlorosilane solution (0.0001M) for SAM.

We have investigated the wetting properties of these films. The water contact angle values using the sessile drop is summarized in Table 1. We have found the values to be lower than previously reported values for bulk polystyrene but comparable to previously reported grafted polystyrene brushes of similar thickness. These were verified with hysteresis measurements (advancing and receding). However, no correlation can be made with regards to polymerization time and solvent on the wetting properties and thickness of the films. Likewise the use of 16% vs 100% DPE did not show any clear differences in either contact angle or thickness measurements. This is perhaps due to the poor monolayer mixture properties (further investigations are being made). Thus, contact angle measurements are inconclusive at this point with regards to polymerization trends and conditions and their effect on brush density and polymer conformation.

AFM Investigations

To investigate the surface topography of the grafted films, AFM measurements was made. From the different polymerization conditions we have investigated, we found that the dry films (measured in ambient air) have a consistent morphology made up of holes (surrounded by reliefs) statistically distributed within domains, as shown in Figure 6. The smooth relief regions of the film 0.2-0.4 μm , have an rms of 0.5-0.8 nm. The films prepared with the 16% initiator composition showed regions without polymer films. This general morphology is uncharacteristic of previously reported grafted polystyrene systems using other types of initiators, in particular with the work by Prucker and Ruhe using free radical SIP where they obtained smooth homogeneous films.⁽²⁶⁾

The group of Ulman and co-workers also reported smooth, homogeneous polymer surfaces throughout the entire substrate on the macroscopic as well as microscopic scale with roughness of 0.3-0.5 nm (rms).⁽¹⁸⁾ However, they have reported smaller "dimples" typically 2-3 nm deep, intersected by small areas of defects. These defects consists of dense arrangements of holes (18-20 nm deep, corresponding to the layer thickness measured by ellipsometry) surrounded by rims. These observations are more similar to the morphologies we have found with these films. Thus, compared to their results, we would expect lower degrees of polymerization and grafting density for these films.

However, it is not clear whether the morphology is a result of the polymerization mechanism or is indicative of incomplete initiation or perhaps domain formation after post-polymerization treatment. Since this morphology was consistent for all the samples we investigated, we intend to investigate in detail the properties of the surface initiator and its property before and after

polymerization. One hypothesis is the involvement of "physisorbed initiators" being removed after Soxhlet extraction, thereby producing the holes. Another is the property of the "anionic surface" or nucleophilicity and the surface energy involved, affecting the mechanism of chain growth. Clearly, the use of mixed monolayers for variable initiator density needs further investigation. Efforts are underway to study in detail these hypotheses and parameters using XPS, SEM and QCM and correlate with polymerization results. Thus, we are currently investigating the unusual morphology and correlating it with the characteristics of the surface, density of initiator sites, and surface energy.

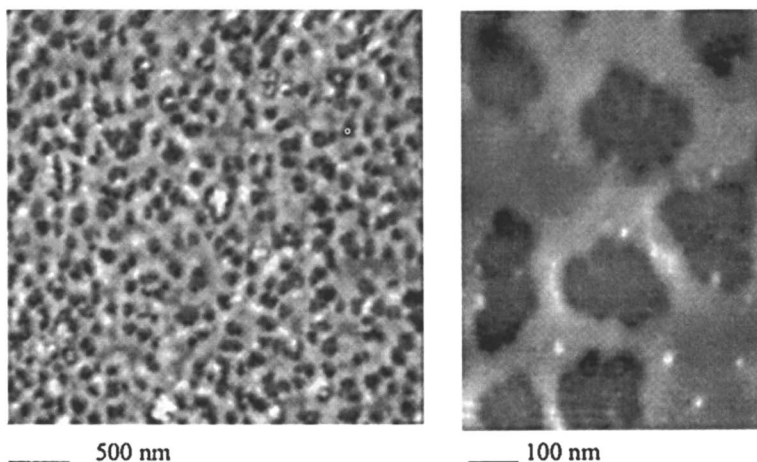


Figure 6. AFM Image of grafted polymer with a relative height up to 27.5 nm (white).

XPS Measurements

XPS of the initiator surface before and after polymerization was made. It is invaluable for determining and monitoring changes on the surface functional groups as a result of decomposition or conversion to reactive species for initiation. The spectra are shown in Figure 7.

Our results showed the presence of the relevant C peak, representing the presence of the polystyrene film on the surface (SIP-B-5 sample). This peak was absent from the XPS spectra of the Si wafer and was small (by integration) on the spectra of the SAM coated substrate (Figure 7a). It is interesting to note that the presence of relevant Si peaks (99.8 for Si and 103.00 for SiO_x) even with the polymerized film indicated the exposure of bare SiO_x surfaces. This is consistent with the morphology observed by AFM where we supposed the depressions (holes) observed to be coincident with the silicate surface. The absence of Li peaks (54.9) is indicative that no active anion is present and all the Li salts have been removed by the Soxhlet extraction and washing process for these sample.

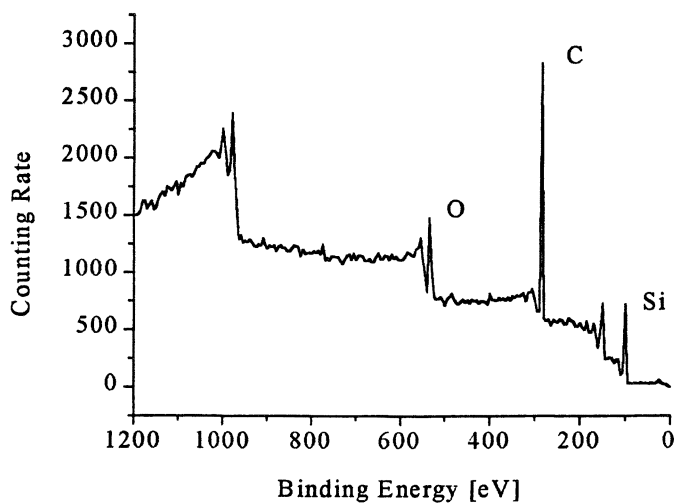
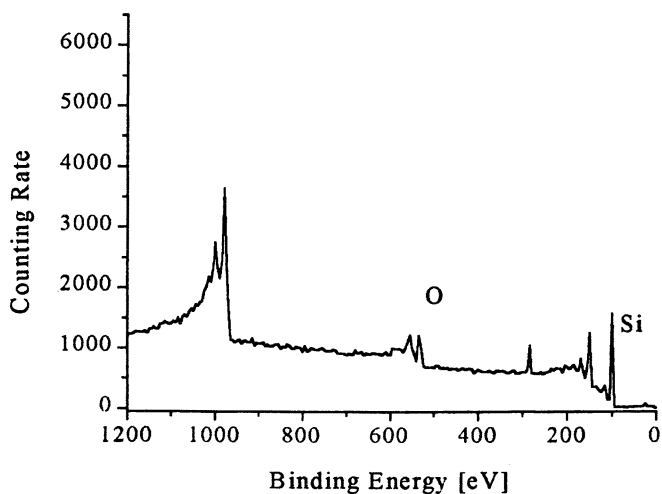


Figure 7. XPS spectra of the Si wafer with (a) SAM of initiator and (b) the polymer film grafted on the Si wafer.

Other parameters of a typical anionic polymerization needs to be investigated: concentration and ratio of monomer, temperature, and solvent. It is important to determine the nucleophilicity of this anionic initiator as compared to other systems. A living polymerization mechanism will allow us to prepare and investigate different block and graft copolymers, end-functionalized polymers, and grafting (branched) architectures. However, is it not possible to obtain more polymer samples using our present methodology. Thus, we are currently conducting polymerization on glass and silica particles (high surface/volume ratio) to obtain high surface areas of grafted polymer. A suitable technique for detachment of the polymer chain from these systems will allow us to characterize the molecular properties, including molecular weight, polydispersity, structure, terminal groups, structure analysis, tacticity, block and graft copolymer architecture. Such analysis can only be completely analyzed when the polymer is detached from the surface. Our fundamental research goal at this point is in understanding of the living surface initiated polymerization; this necessitated the initial use of well-characterized and idealized surfaces. Once we have achieved this objective, we will be applying the methodology to other actual inorganic (clay) surfaces and particulates.

Conclusion

In this article, we have presented our work on the surface initiated anionic polymerization of styrene using a SAM of DPE modified silane initiators on Silicate surfaces. The results indicate the formation of polymer brushes with a unique morphology not typical with analogously observed polymer brush systems. We have used a combined approach of spectroscopic and microscopic surface analysis to probe the system. In the future, we would like to understand the mechanism and efficiency of this initiator system compared to others and to use this initiator on actual silica and clay particles. More importantly, we intend to demonstrate the feasibility of forming block and graft copolymers by surface initiated living anionic polymerization.

Acknowledgment.

Funding for this project from the Army Research Office (ARO) under DAAD19-99-1-0106 is gratefully acknowledged. We acknowledge the XPS measurements by Prof. Greg Szulczewski of the Department of Chemistry, University of Alabama at Tuscaloosa and the use of the electrochemistry set-up with Dr. Juan Pablo Claude (UAB). We also acknowledge Dr. Shuangxi Wang for the re-synthesis of the DPE initiator.

References

1. Wittmer, J. P. ; Cates, M. E. ; Johner, A. and Turner, M. S. *Europhys. Lett.* **1996**, *33*, 397.
2. de Gennes, P.-G. *J. Phys. (Paris)* **1976**, *37*, 1443.
3. de Gennes, P.-G. *Macromolecules* **1980**, *13*, 1069.
4. Sanchez, I. C. *Physics of Polymer Surfaces and Interfaces*; Butterworth: London, 1992.
5. Dan, N.; Tirrell, M. *Macromolecules* **1993**, *26*, 4310.
6. Prucker, O.; Ruhe, J. *Macromolecules* **1998**, *31*, 602-613.
7. Ejaz, M.; Yamamoto, S.; Ohno, K.; Tsujii, Y.; Fukuda, T. *Macromolecules* **1998**, *31*, 5934-5936.
8. Husseman, M.; MalmstroIm, E.; McNamara, M.; Mate, M.; Mecerreyes, D.; Benoit, D.; Hedrick, J.; Mansky, P.; Huang, E.; Russell, T.; Hawker, C., *Macromolecules* **1999**, *32*, 1424-1431.
9. Jordan, R. and Ulman, A. *J. Am. Chem. Soc* **1998**, *120*, 243.
10. Oosterling, M. L. ; Sein, A.; Schouten, A. J. *Polymer* **1992**, *33*, 4394.
11. Dorgan, J. R.; Stamm, M.; Toprakcioglu, C.; Jerome, R.; Fetters, L. J. *Macromolecules* **1993**, *26*, 5321.
12. Giannelis, E. P. *Adv. Mater.* **1996**, *8*, 29.
13. Usuki, A. et al. *J. Mater. Res.*, **1993**, *8*, 1174 ; *ibid*, **1993**, *8*, 1179; *J. Polym. Sci., Polym. Chem.*, **1993**, *31*, 2493; *ibid*, **1993**, *31*, 983; *J. Polym. Sci., Polym. Phys. Ed.*, **1994**, *32*, 625 ; *ibid*, **1995**, *33*, 1039.
14. Vaia, R. A. ; Giannelis, E. P. et al., in *Synthesis and Processing of Ceramics: Scientific Issues*, W. E. Rhine, M. T. Shaw, R. J. Gottshall, and Chen, Y. (Eds.), *MRS Proceedings*, Pittsburgh, PA, 1992; *Chem. Mater.* **1993**, *5*, 1694; *ibid*, **1994**, *6*, 1017; *J. Am. Chem. Soc.* **1995**, *117*, 7568; *Macromolecules*, **1995** *28*, 8080 ; *Chem. Mater.* **1996**, *8*, 1728; *Macromolecules* **1997**, *30*, 7990; *ibid*, **1997**, *30*, 8000.
15. Ginzburg, V. and Balazs, A. *Macromolecules* **1999**, *32*, 5681
16. Fleer, G. J. ; Cohen-Stuart, M. A. ; Scheutjens, J. M. H. M. ; Cosgrove, T. and Vincent, B. *Polymers at Interfaces*, London: Chapman and Hall, 1993.
17. Weimer, M.; Chen, H.; Giannelis, E.; Sogah, D. *J. Am. Chem. Soc.* **1999**, *121*, 1615-1616
18. Jordan, R.; Ulman, A; Kang, J.; Rafailovich, M.; Sokolov, J. *J. Am. Chem. Soc.* **1999**, *121*, 1016-1022
19. Rempar, P. and E. Merrill, *Polymer Synthesis, 2nd Ed.* Uthig and Wepf, Heidelberg, 1991.
20. Sauerbrey, G. *Z. Physik*, **1959**, *155*, 206.
21. Zhou, Q.; Nakamura, Y.; Inaoka, S.; Park, M.; Mays, J.; Advincula, R. in preparation.
22. Wirth, M.; Fairbank, R.; Fatunmbi, H. *Science*, **1997**, *275*, 44.
23. Taylor, D.; Morgan, H.; D'Silva, C. *J. Phys. D: Apply. Phys.* 1991, *24*, 1443.
24. Inaoka, S. and Collard, D. *Langmuir* **1999**, *15*, 3752
25. Van Olphen, H. *An Introduction to Clay Colloid Chemistry*; Wiley Interscience: New York, 1977; 2nd. Ed.
26. Prucker, O.; Ruhe, J. *Langmuir* **1998**, *14*, 6893-6898.

Chapter 6

Predicting the Phase Behavior of Polymer–Clay Nanocomposites: The Role of End-Functionalized Chains

Valeriy V. Ginzburg^{1,2} and Anna C. Balazs¹

¹Department of Chemical and Petroleum Engineering, University of Pittsburg, Pittsburg, PA 15261

²Current address: The Dow Chemical Company, Midland, MI 48674

We develop a multi-scale approach combining density functional theory (DFT) and self-consistent field theory (SCF) to calculate the phase behavior of oblate colloidal particles dispersed in a polymer melt. These particles represent organically modified clay sheets. Into the polymer melt, we introduce a small volume fraction of end-functionalized chains whose end-groups (“stickers”) are attracted to clay surfaces. We show that adding even a small amount of such chains can stabilize exfoliated (isotropic and nematic) morphologies of a composite if the adhesion energy between the sticker and the clay surface is sufficiently large. These results are in qualitative agreement with earlier studies.

Introduction

In recent years, nanocomposites consisting of a polymeric matrix and inorganic clays have become the subject of considerable research efforts due to their remarkable physical and mechanical properties. (1-6) For example, adding

only 2-5 wt % of clay fillers can double the tensile strength and the modulus, (3) or reduce the gas permeability by a factor of 2. (4) Fabricating these materials in an efficient and cost-effective manner, however, poses significant challenges, since clays and polymers are typically immiscible. In particular, the inorganic clay particles consist of stacked silicate sheets, with a typical thickness of 1 nm, and a typical diameter ranging between 20 and 1000 nm. The spacing (“gallery”) between the sheets is on the order of 1 nm, which is smaller than the radius of gyration of typical polymers. Consequently, there is a large entropic barrier that prevents the polymers from penetrating the gallery and intermixing with the clay. Furthermore, even when the sheets are successfully separated and interspersed into the polymer matrix, these high aspect-ratio platelets can form ordered or crystalline structures or can phase separate from the matrix material. Thus, to successfully design new nanocomposites, it is important to describe both the behavior of polymers in the gallery (the intercalation process) and the macroscopic behavior of clay particles in the mixture.

The behavior of polymers in the gallery has been studied extensively in recent years by various experimental and theoretical methods. (2,5-10) Vaia and Giannelis (5,6) proposed a simple lattice mean-field model to calculate free energy profiles as a function of surface separation. Balazs et al. (7-10) used numerical and analytical self-consistent field calculations to analyze the conformational properties of the polymers between the clay sheets and the free energy as a function of separation between the sheets. These calculations indicate whether a given mixture could form an exfoliated or intercalated structure, or result in an immiscible system. In particular, Balazs et al. showed (8,10) that the addition of a small volume fraction of end-functionalized chains could significantly improve the polymer/clay miscibility provided that the end-groups (stickers) have a sufficiently strong attraction to the clay sheets. Calculating the complete phase diagram for the large-scale system, however, requires a detailed balance of all the contributions to the free energy, including the translational and orientational entropy of the clay particles, as well as their excluded volume interactions. Balazs et al. addressed these issues by constructing an approximate free energy expression for a polymer/platelet mixture and taking into account the liquid crystalline ordering of the platelets. (11,12) Ginzburg, Singh, and Balazs (13) then used these results to construct a combined multi-scale model and calculate the phase behavior of mixtures of a polymer melt with organically modified clay sheets. In this paper, we apply the same technique to study how the phase behavior of the mixture is modified by the presence of end-functionalized chains.

The Model

Our multi-scale model combines two approaches, the numerical self-consistent field (SCF) method, and the density functional theory (DFT). We use SCF to calculate effective interaction potentials between the clay sheets. These potentials are due to the enthalpic interactions between the polymer and the surface and the conformational changes in the free energy of polymers confined in the gallery; the potentials are then used as an input to evaluate the effective interaction term in the free energy of the whole system. The relationship between the two components of the theory is sketched in Figure 1.

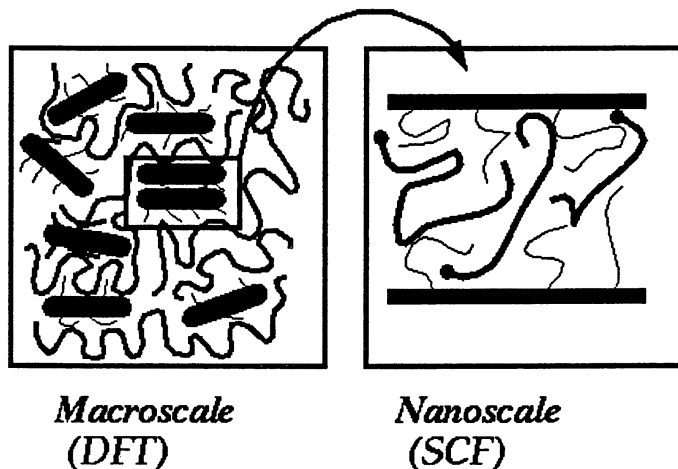


Figure 1. Schematic representation of the combined DFT-SCF approach. The SCF model is used to examine nanoscale interactions between the polymers and two coated surfaces. The SCF-generated potential is used as input for the DFT. Using the DFT, we calculate macroscopic phase diagrams.

Free Energy Density Functional

Our DFT is adapted from the Somoza-Tarazona (14,15) formulation for monodisperse fluids of rigid anisotropic particles. To model colloidal particles dispersed in a polymer melt, we impose the incompressibility condition,

$$\phi + \phi_{\text{gr}} + \phi_{\text{p}} = 1. \quad (1)$$

Here, ϕ is the volume fraction of clay particles, ϕ_{gr} is the volume fraction of the grafted organic modifiers, and ϕ_{p} is the volume fraction of the polymer (which includes both non-functionalized and functionalized chains). For clay sheets that have a diameter D and thickness L , the volume fractions of clay and organic modifiers are related via

$$\phi_{\text{gr}} = \phi(2\rho_{\text{gr}} N_{\text{gr}} v_{\text{m}}/L), \quad (2)$$

where v_{m} is the monomer volume, ρ_{gr} is the surfactant grafting density, and N_{gr} is the length of a surfactant chain. Here, we consider the clay sheets to be thin, oblate ellipsoids of revolution, rather than oblate cylinders or cut spheres. This approximation allows us to use the Somoza-Tarazona free energy density functional without introducing additional adjustable parameters.

The orientational and positional ordering of the clay sheets is described by the single-particle distribution function (SDF) $\gamma(\mathbf{r}, \mathbf{n})$, where \mathbf{r} represents the position of the center of mass of a particle, and \mathbf{n} is the nematic director (which denotes the direction of the short axis of a disk). Following Kventzel et al., (16) we decouple the orientational and positional degrees of freedom,

$$\gamma(\mathbf{r}, \mathbf{n}) = \rho(\mathbf{r}) f(\mathbf{n}), \quad (3)$$

where $\rho(\mathbf{r})$ is the positional SDF (the local density of clay disks), and $f(\mathbf{n})$ is the orientational SDF. The free energy of the system is written as a functional of ρ and f . We write the free energy of the system in the following form,

$$\beta F = \beta F_{\text{id}} + \beta F_{\text{ster}} + \beta F_{\text{int}}, \quad (4)$$

where F_{id} is the free energy of an "ideal gas" of clay sheets and polymers, F_{ster} is the contribution due to the excluded volume effects for the clay sheets, F_{int}

represents the long-range (attractive or repulsive) interactions between clay sheets, and $\beta = 1/kT$.

The first ("ideal") term of the free energy in the rhs of eq 4 can be written as the sum of two parts,

$$\beta F_{id} = \beta F_c + \beta F_p. \quad (5)$$

The "ideal" free energy of clay particles, βF_c , consists of translational and orientational terms,

$$\beta F_c = \int dr \rho(\mathbf{r}) \ln(\rho(\mathbf{r})) + \int dr dn \rho(\mathbf{r}) f(\mathbf{n}) \ln(4\pi f(\mathbf{n})). \quad (6)$$

The "ideal" free energy of the polymer melt, βF_p , includes only the translational (Flory-Huggins) contribution,

$$\beta F_p = (V/Nv_m) \phi_p \ln(\phi_p), \quad (7)$$

where V is the total volume of the system, v_m is the monomer volume and ϕ_p is the volume fraction of the polymer.

For a system of ellipsoidal particles, a semi-empirical steric interaction free energy can be written as, (15,17)

$$\beta F_{ster} = \int dr \rho(\mathbf{r}) \Psi_{hs}(\phi_c^s(\mathbf{r})) [V_{excl}[f]/V_{phe}], \quad (8)$$

where $\Psi_{hs}(x)$ is the semi-empirical Carnahan-Starling (18) function, which describes the excess (non-ideal) free energy density for hard spheres as a function of their packing fraction; $\phi_c^s(\mathbf{r})$ is the "smoothed" local volume fraction of the clay particles (for more details see ref 13). The parameter $V_{excl}[f]$ is the average excluded volume per particle for a given orientational distribution, and V_{phe} is the excluded volume per particle for perfectly aligned ellipsoids.

The sum of the free energy terms in eqs 5 and 8 describes an athermal dispersion of hard oblate ellipsoids in a polymer melt. We suppose that the interaction free energy, βF_{int} , is relatively small compared to the ideal and steric free energy terms, i.e., $|\beta F_{int}| < |\beta F_{id} + \beta F_{ster}|$. In this case, one can assume that the pair correlation function for the particles, $g(1,2)$, is mostly determined by the excluded volume effects (not long-range interactions), and calculate the interaction free energy βF_{int} as,

$$\beta F_{\text{int}} = \int d\mathbf{r}_1 d\mathbf{n}_1 d\mathbf{r}_2 d\mathbf{n}_2 \rho(\mathbf{r}_1) f(\mathbf{n}_1) \rho(\mathbf{r}_2) f(\mathbf{n}_2) \times \\ \delta(1 - \mathbf{n}_1 \bullet \mathbf{n}_2) g(1,2) V(\mathbf{r}_1 - \mathbf{r}_2), \quad (9)$$

where the mean-field pair correlation function $g(1,2) = 0$ if particles overlap, and is equal to 1 if they do not overlap. This form is similar to the traditional way of representing enthalpic interactions between anisotropic particles. The delta-function in the rhs of eq 9 allows only those configurations in which interacting disks are parallel. Such an approximation is reasonable for very anisotropic particles where side-by-side configurations have significantly larger "contact" area than either side-to-edge or edge-to-edge configurations. In addition, since this potential is highly anisotropic, it is likely to promote the formation of smectic and columnar phases. The potential function $V(\mathbf{r})$ is assumed to have the following generic form,

$$V(\mathbf{r}) = (\pi/4) D^2 (1 - [r_{\perp}/D]^2) U(z), \quad (10)$$

where $\mathbf{r} = (x,y,z)$, and $r_{\perp} = (x^2 + y^2)^{1/2}$. The interaction potential per unit area, $U(z)$, is just the potential calculated from the SCF model, as described above.

When evaluating the integral over positions and orientations of particles (the rhs of eq 9), we use the orientational lattice approximation. (19) In this approach, particle orientations are restricted to being along the x, y, or z directions only. Such an approximation is necessary to reduce the number of degrees of freedom and thus, make it possible to analyze the whole phase diagram within a reasonable time frame.

In order to describe the thermodynamic behavior of the system, it is necessary to minimize the free energy for all possible phases (isotropic, nematic, smectic, columnar, and crystal) for each value of ϕ , and find the lowest free-energy state. After that, coexistence regions can be found by means of applying the Maxwell rule, or, equivalently, by equating the chemical potentials of the particles and the polymer for the different phases. The minimization is done using a variational approach in which the SDF is parameterized by specific functions that reflect the symmetry of a given phase.

Self-Consistent Field Calculations

To complete the free energy functional, it is necessary to calculate the interaction potential per unit area, $U(z)$, for the clay sheets. For this, we employ the self-consistent field method of Scheutjens and Fleer. (20) In this method, the phase behavior of polymer systems is modeled by combining Markov chain statistics with a mean-field approximation for the free energy. The equations in

this lattice model are solved numerically and self-consistently. Using this model, we consider two infinite parallel plates at a distance z apart, immersed in a bath of molten polymer. The short surfactant chains of length N_{gr} are grafted uniformly on each of the two plates with a grafting density ρ_{gr} . After solving the equations and finding the equilibrium polymer and surfactant density profiles, we calculate the free energy density F/A for each value of the plate separation z . Repeating this calculation for different separations, one obtains the effective potential per unit area, $U(z)$. The detailed description of the SCF calculation of the interparticle potentials and the qualitative discussion of their influence on the morphology of polymer/clay composites is discussed elsewhere. (13)

Model System

We consider a mixture of organically modified clay sheets (with diameter $D=30$ nm, and thickness $L = 1$ nm) with a polymer melt consisting of non-functionalized Gaussian chains with chain length $P = 300$. (21) To this melt, we add $\Phi = 5\%$ of the end-functionalized chains with length $N = 100$. The first monomer on this chain is considered to be the sticker. (22) The parameter χ_{sc} describes the interaction between the sticker and the clay surface. To relate this Flory parameter to the corresponding experimentally relevant value (adsorption energy ϵ in units of kT), we must divide χ_{sc} by 6, the coordination number in this lattice calculation. The interaction parameter between all the other monomers and the clay surface is set to $\chi = 1.0$, reflecting the incompatibility between typical polymers and hydrophilic clay surfaces. The two clay surfaces are covered with organic modifiers; the length of the modifiers is $N_{\text{gr}} = 5$ and the grafting density of these chains is fixed at $\rho = 0.2$ chains/nm². Again the interaction energy between the modifier monomers and the surface is set to $\chi = 1.0$.

Results and Discussion

SCF Calculations

The SCF-calculated free energy profiles for various values of $\epsilon = \chi_{\text{sc}}/6$ are shown in Figure 2. It can be seen that for $-4.0 \leq \epsilon \leq 0$, the values of the free energies, $U(z)$, are positive, indicating that the penetration of the polymers into the gallery (and thus, the intermixing of polymer and clay) is unfavorable. At some threshold value $\epsilon^* \approx -4.2$, however, the free energies become negative and the intermixing of the polymer and clay becomes favorable. This result is

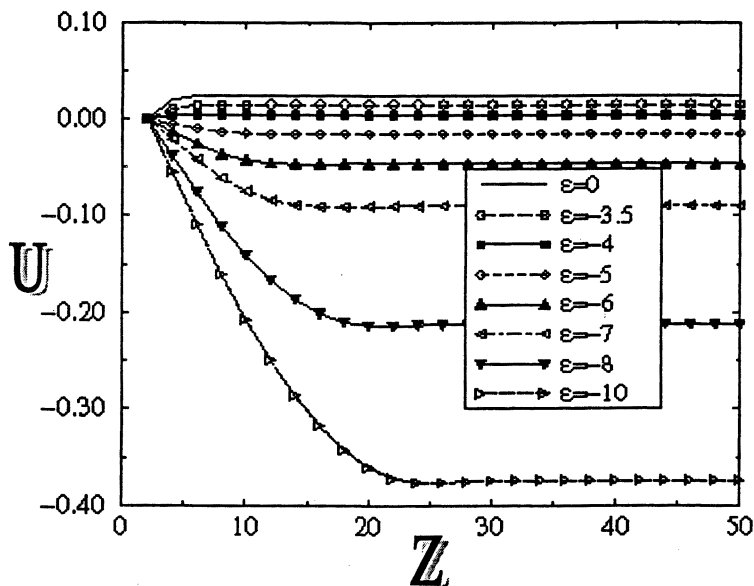


Figure 2. Free energy density, U , vs. separation, Z , for two parallel plates with grafted chains, $\rho_{gr} = 0.2$, $N_{gr} = 5$, in the presence of polymer melt with $\Phi = 0.05$ of end-functionalized chains. Different curves correspond to the different values of the adhesion energy ϵ between the end group and the clay surface. As the adhesion strength, $|\epsilon|$, is increased, the free energy at large separation decreases and becomes negative.

consistent with the earlier numerical and analytical SCF calculations of Balazs et al. (7-9)

Through the SCF model, we can calculate the fraction of surface sites occupied by the stickers for the different values of ϵ . As expected, the number of adsorbed species increases as the sticker-surface interaction becomes more attractive (ϵ becomes more negative). For example, for $\epsilon \approx -5$, roughly 3% of the surface sites are occupied by the stickers, while for $\epsilon \approx -7$, the adsorbed amount saturates at approximately 5%. At this value of ϵ , essentially all the functionalized chains are bound to the surface. This adlayer of long chains gives rise to an effective repulsion between the clay sheets.

The long, anchored chains also promote favorable intermixing between the coated surface and the bulk polymers. To highlight this behavior, we calculate density profiles for the system with separation $H=12$ for two values of ϵ , $\epsilon = -5.0$ (strongly adsorbing end-functionalized chains), and $\epsilon = 0.0$ (non-adsorbing chains). The results are depicted in Figure 3. It can be seen that in the first case ($\epsilon = -5.0$), there is significant overlap between the bulk polymers and the

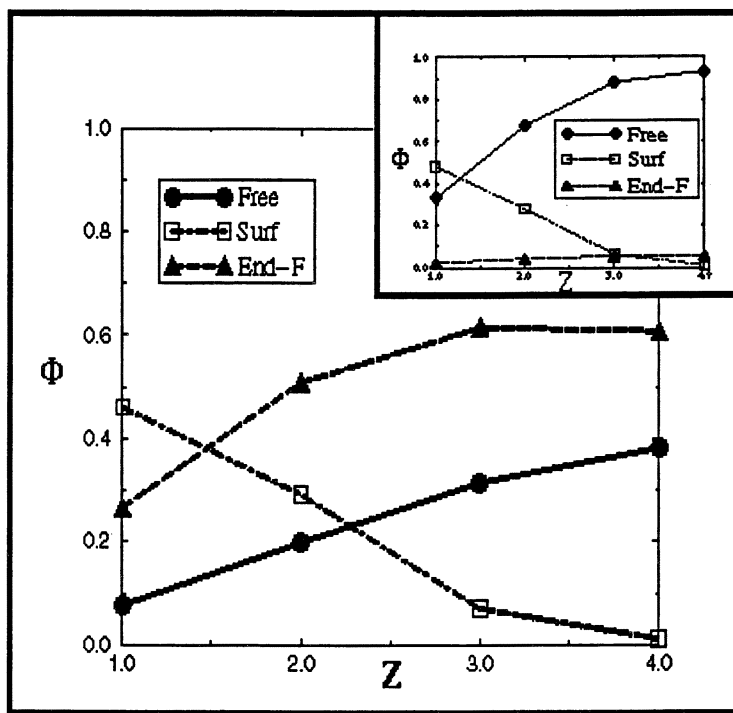


Figure 3. Density profiles for the grafted chains (squares), end-functionalized polymer (triangles), and non-functionalized polymer (circles) between the two parallel surfaces with separation $H = 12$. Here, Z is the distance from the surface (mirror symmetry is assumed). The value of the sticker-clay energy ϵ is -5.0 (main plot) and 0.0 (inset). Note that for $\epsilon = 0$, there is almost no end-functionalized polymer in the gallery, while for $\epsilon = -5$, there is a significant intermixing between the grafted chains, end-functionalized polymer, and non-functionalized polymer.

adsorbed chains. In particular at $Z = 4$, the layer contains roughly 60% functionalized chains and 40% nonfunctionalized chains (with essentially no surfactant). In contrast, when $\epsilon = 0$ and there are no $N = 100$ chains anchored to the surface, there is very little overlap between the interface and the polymers at $Z = 4$.

Phase Diagrams

The above SCF calculations indicate that addition of the functionalized chains can promote the separation of the clay sheets within the polymer matrix. Calculation of the phase diagram, as a function of ϵ and ϕ , will indicate whether or not the sheets ultimately form a thermodynamically stable, dispersed phase. The phase diagram for our model system is shown in Figure 4. Our goal is to isolate the conditions where the mixture forms an isotropic or nematic phase since these morphologies correspond to exfoliated composites (where the sheets are relatively uniformly dispersed through the melt.) As can be seen for small negative ϵ , the system exhibits a broad region of two-phase coexistence between a polymer-rich isotropic phase and the clay-rich crystallites. In terms of the SCF results, this would correspond to an immiscible mixture. As the adhesive energy $|\epsilon|$ is increased, however, the polymer and clay become more miscible, and the two-phase regions shrink ($-3.5 > \epsilon > -5$). For $\epsilon \approx -4$, we estimate that one can obtain exfoliated (isotropic and nematic) morphologies for as high as $\phi = 0.12$ clay volume fractions. In this region, the anchored chains promote the favorable intermixing between the polymers and the clay sheets (as predicted by the SCF free energy calculations) and sterically stabilize the mixture, giving rise to an entropic repulsion between the sheets.

As the clay-clay repulsion becomes stronger, the phase diagram is dominated by the new "plastic solid" (or "house-of-cards") structure. Here, the disks exhibit three-dimensional positional ordering, but no orientational ordering (see ref 13 for more details). This phase should exhibit the dynamical properties of a solid or a gel (unlike the liquid-like isotropic and nematic phases). At larger volume fractions, orientational ordering must take place, and we observe a plastic solid -- columnar (PS -- Col) transition. This transition is similar to the one found by Brown et al. (23,24) in their studies of platelike particles of nickel hydroxide. (In their studies, a repulsive potential was induced by electrostatic interactions; we expect that the polymer-induced entropic repulsion should produce similar effects for the polymer/clay systems.)

In order to study the sensitivity of the phase diagram to variations in the concentration of end-functionalized chains, we repeated both the SCF and DFT calculations for $\Phi = 0.01$ (the volume fraction of end-functionalized chains in the melt was reduced by a factor of 5). The only difference between the two cases was that the threshold value for favorable intermixing between the

polymers and the clay sheets shifted from $\epsilon = -3.5$ (for $\Phi = 0.05$) to approximately -5.0 (for $\Phi = 0.01$). Correspondingly, the phase diagram (shown in Figure 5) shifted downward for the $\Phi = 0.01$ example; the overall features of the diagram remain the same as the $\Phi = 0.05$ case. This result is to be expected since the amount of available end-functionalized chains in the melt is decreased and thus, higher values of $|\epsilon|$ are needed to promote the adsorption of these species.

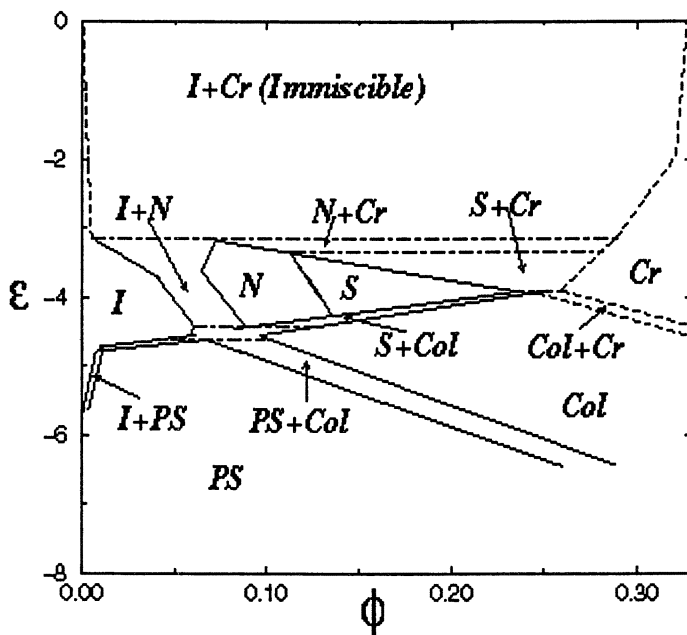


Figure 4. Phase diagram for polymer/clay mixture with $\Phi=0.05$ end-functionalized chains. Here, ϕ is clay volume fraction, and ϵ is the sticker-clay adhesion energy. Phases: *I* -- isotropic, *N* -- nematic, *S* -- smectic (lamellar), *Col* -- columnar, *Cr* -- crystal, and *PS* -- plastic solid (house-of-cards). Dashed lines represent approximate locations of phase transition boundaries where exact calculation is impossible; dot-dashed lines correspond to various triple points.

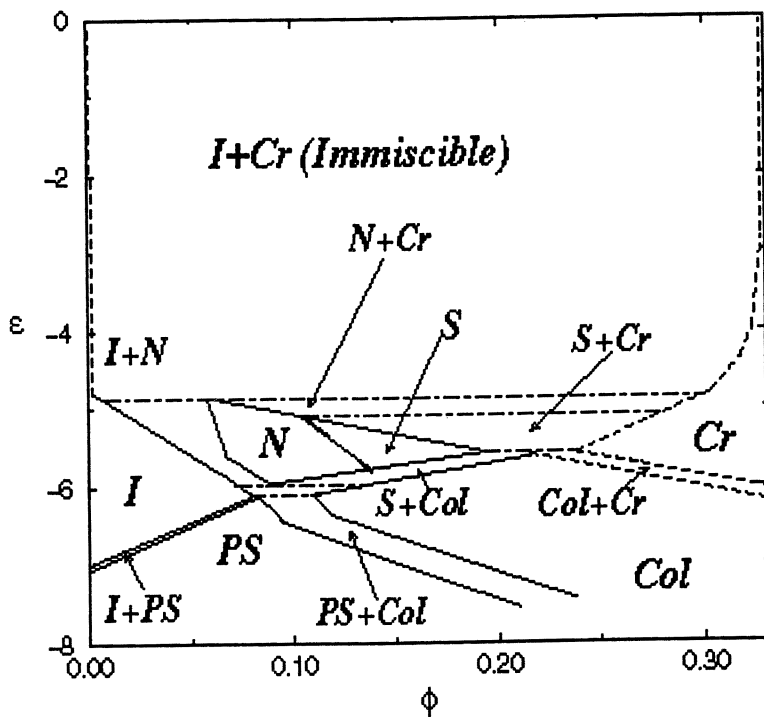


Figure 5. Same as Figure 4, but with $\Phi=0.01$.

Conclusions

We investigated the phase behavior of a mixture containing organically modified clay, non-functionalized polymers and a small volume fraction of end-functionalized chains. The parameter ϵ characterizes the interaction between the terminal functional group and the surface. For small negative ϵ , the system is completely immiscible. As the sticker/surface attraction is increased, the system exhibits isotropic and nematic morphologies at relatively low clay volume fractions ($\phi \leq 0.12$). These structures correspond to thermodynamically stable, exfoliated composites. Finally, when the surface/sticker attraction is increased even further, the system exhibits a plastic solid morphology at low ϕ , and a columnar phase at very high ϕ . The plastic solid phase probably indicates the formation of gel-like network structure where the adjacent plates are oriented at right angles between each other, and the overall orientation is isotropic.

Our results show that the addition of even a small amount of end-functionalized (“one-sticker”) chains can be sufficient to produce stable exfoliated or intercalated morphologies, provided that the adhesion between the stickers and the clay surface is sufficiently high. The value of the threshold adhesion energy ϵ_{tr} depends on the volume fraction Φ of the functionalized chains in the melt; as Φ is increased, ϵ_{tr} decreases. The detailed description of the relationship between ϵ_{tr} , Φ , N , and P will be the subject of future studies.

The proposed technique can be applied to describe the equilibrium phase behavior of other model nanocomposite or polymer/colloid systems. The resulting phase diagrams can be used as guidelines for the development of new thermodynamically stable organic/inorganic hybrid materials.

Acknowledgments

This work was supported by The Dow Chemical Company, the Army Office of Research, the NSF through Grant No. DMR -9709101, and ONR through Grant No. N00014-91-J-1363.

References

1. LeBaron, P. C.; Wang, Z.; Pinnavaia, T. G. *Appl. Clay Sci.* **1999**, *15*, 11–30, and references therein.
2. Giannelis, E. P., Krishamoorti, R., Manias, E., *Advances in Polymer Science* **1999**, *138*, 107 - 147, and references therein.

3. Kojima, Y.; Usuki, A.; Kawasumi, M.; Okada, A.; Kurauchi, T.; Kamigaito, O. *J. Polym. Sci.: Part A: Polym. Chem.* **1993**, *31*, 983-986.
4. Yano, K.; Uzuki, A.; Okada, A.; Kurauchi, T.; Kamigaito, O. *J. Polym. Sci.: Part A: Polym. Chem.* **1993**, *31*, 2493-2498.
5. Vaia, R. A.; Giannelis, E. P. *Macromolecules* **1997**, *30*, 7990-7999.
6. Vaia, R. A.; Giannelis, E. P. *Macromolecules* **1997**, *30*, 8000-8009.
7. Balazs, A. C.; Singh, C.; Zhulina, E. *Macromolecules* **1998**, *31*, 8370-8381.
8. Zhulina, E.; Singh, C.; Balazs, A. C. *Langmuir* **1999**, *15*, 3935-3943.
9. Balazs, A. C.; Singh, C.; Zhulina, E.; Lyatskaya, Y. *Accounts of Chem. Research* **1999**, *32*, 651-657.
10. Kuznetsov, D. V.; Balazs, A. C. *J. Chem. Phys.* **2000**, *112*, 4365-4375.
11. Lyatskaya, Y.; Balazs, A. C. *Macromolecules* **1998**, *31*, 6676-6680.
12. Ginzburg, V. V.; Balazs, A. C. *Macromolecules* **1999**, *32*, 5681-5688.
13. Ginzburg, V. V.; Singh, C.; Balazs, A. C. *Macromolecules* **2000**, *33*, 1089-1099.
14. Tarazona, P. *Phys. Rev. A* **1985**, *31*, 2672-2679.
15. Somoza, A. M.; Tarazona, P. *J. Chem. Phys.* **1989**, *91*, 517-527.
16. Kventsel, G. F.; Luckhurst, G. R.; Zewdie, H. B. *Mol. Phys.* **1985**, *56*, 589-610.
17. Ginzburg, V. V.; Glaser, M. A.; Clark, N. A. *Liq. Cryst.* **1997**, *23*, 227-234.
18. Carnahan, N. F.; Starling, K. E. *J. Chem. Phys.* **1969**, *51*, 635-636.
19. Sokolova, E. P.; Vlasov, A. Yu. *J. Phys. Condens. Matter* **1997**, *9*, 4089-4101, and references therein.
20. Fler, G.; Cohen-Stuart, M. A.; Scheutjens, J. M. H. M.; Cosgrove, T. Vincent, B. *"Polymers at Interfaces"; Chapman and Hall: London 1993.*
21. The effective SCF potential $U(z)$ and thus, the overall phase behavior, is strongly dependent on the chain length P . As P is increased, the polymer and clay become strongly immiscible. For shorter chains (small P), the miscibility increases. For more detailed discussion, see Refs. 7-9, 11-12.
22. The location of the sticker group on the chain could strongly influence the effectiveness of the end-functionalized polymer in exfoliating the clay. By placing the sticker at the end of the chain, one could achieve the best results. Indeed, if the sticker is placed in the middle of the chain, the absorbed layer would be shorter and denser than when it is placed at the end. Thus, the effective repulsion between the brushes would be stronger in the case when the sticker is at the end of the chain (see Refs. 9, 13 regarding the role of the effective brush length).
23. Brown, A. B. D.; Clarke, S. M.; Rennie, A. R. *Langmuir* **1998**, *14*, 3129-3137.
24. Brown, A. B. D.; Ferrero, C.; Narayanan, T.; Rennie, A. R. *European Phys. Journal B* **1999**, *11*, 481-489.

Chapter 7

Carbon Black Structure and Associations in Filled Rubbers

Rex P. Hjelm

Manuel Lujan, Jr., Neutron Scattering Center, Los Alamos National
Laboratory, Los Alamos, NM 87545

Small-angle neutron scattering has provided information on the structure and shape of carbon black and the structure of carbon black networks in rubber composites. Determining the structure of these materials by neutron scattering required distinguishing among sources of scattering, such as from the shape and internal structure of the particles and from voids and other defects in the material. This was done by filling the materials with mixtures of deuterated and non-deuterated fluids—the method of contrast variation. In this work, we considered the morphology and internal structure of carbon black particles and aggregates. All blacks studied here show a core-shell like morphology with an outer graphitic shell and an amorphous, core. The amorphous core is continuous through the aggregate, giving a structure rather like a peanut. The surfaces of the carbon black were smooth out to lengths of 10 Å. Our results demonstrated that there was a common structure in experimental and production carbon blacks. The different carbon blacks studied differed in the aggregate/agglomerate morphology at long length scales. We also looked at the interactions of carbon black aggregates in rubber composites.

Carbon black-elastomer composites are examples of nanocomposites consisting of microphases of a polymer matrix and hard, filler reinforcement. Carbon black structure is hierarchical. Spheroid particles are fused into aggregates, the basic, irreducible unit in the carbon black hierarchy. Aggregates associate reversibly by van der Waal's forces to form agglomerates. There is a substantial body of work on carbon black structures and carbon black-elastomer composites (1). Even so, over 90 years after the discovery of the effect of carbon black on rubber, there is controversy on the reinforcing mechanism. Ideas center on particle size and surface structure relating to associations with the elastomer, aggregate shape and the extent and morphology of agglomerates. The viscoelastic properties of the filler network and the polymer are thought to be highly important, as well as the interactions of carbon black with the elastomer. The hydrodynamic properties of the filler included rubber complex, related to the complex morphology, is also thought to play a large role in the mechanical properties of these materials. An understanding of the mechanical properties of reinforced rubber therefore requires a picture of the structure of the material *in situ*.

Our objective is to provide structural information on carbon black and carbon black-elastomer composites. This includes the morphology and internal structure of carbon black particles and aggregates; the association of aggregates in rubber composites; and the associations of elastomer and carbon blacks. In this paper, we review our results on the structure of aggregates as probed by small-angle neutron scattering. This technique provides a probe of the material on length scales that is relevant to the material properties.

One difficulty in determining structure-property relationship in polymer composites is due to their complexity. In general, there are several possible contributions to the scattering signal arising from fluctuations in scattering length density, $\rho(\mathbf{r})$, which varies with position, \mathbf{r} , with density and chemical composition. These structural features include the structures of the matrix, the filler, and the matrix-filler interface and from defects, such as voids and cracks.

How can we sort out the sources of scattering observed in these materials? Model systems and examination of the isolated components play an important role. However, even simplified systems require a means of manipulation to remove the ambiguity in the scattering. This means is provided by the technique of contrast variation.

Experimental

Small-angle Neutron Scattering

The concept behind small-angle neutron scattering (SANS) is the same as scattering from electrons or x-rays, except that neutron scattering is almost entirely from nuclei. There are two important consequences of this. First, neutron nuclear interactions are relatively weak. The result is that neutrons

penetrate material more than electrons or x-rays. Thus, SANS provides nanoscale and molecular scale structural information in the bulk, and one can study carbon black suspended in fluids or *in situ* with elastomers. The second consequence is that the neutron scattering length, b , the measure of scattering amplitude, is not monotonic with atomic number (Table I). Hence, neutrons are able to see the distribution of light elements. Furthermore, for neutrons there are often significant differences in b from isotopes of the same elements: hydrogen and deuterium (Table I) is particularly important in this regard.

Table I. Scattering Lengths of Some Light Elements and Hydrogen Isotopes

Element	Scattering length (fm)
^1H	-3.7403
^2D	6.675
C	6.6484
N	9.2600
O	5.8050

Elastic scattering results from fluctuations in the scattering length density, $\rho(\mathbf{r})$, with position in the sample, \mathbf{r} , which is sum of the b 's of the atoms (Table I) in a volume at \mathbf{r} divided by that volume. Thus, $\rho(\mathbf{r})$, is the sample structure reported by a neutron scattering measurement and reflects density and chemical composition variation in the sample. The scattered intensity, $I(Q)$ is reported here as the differential cross section per unit mass ($\text{cm}^2 \text{mg}^{-1}$) as a function of the magnitude of the scattering vector, Q . For elastic scattering, $Q = (4\pi/\lambda) \sin\theta$, where λ is the neutron wavelength and 2θ is the scattering angle. The $I(Q)$ is proportional to the Fourier transform of $\rho(\mathbf{r})$, squared:

$$I(Q) = K \left\langle \left| \int \rho(\mathbf{r}) \exp(-i\mathbf{r} \cdot \mathbf{Q}) d\mathbf{r} \right|^2 \right\rangle. \quad (1)$$

For particles not correlated in position and orientation, the expression in the angle brackets is the spherical averaged form factor, $\langle P(Q) \rangle$. The constant, K , in Eq. (1) is proportional to $\Delta\rho^2$, $\Delta\rho = \bar{\rho} - \rho_s$, which is the contrast between the average scattering length density of the particle, $\bar{\rho}$, and the background scattering length density, ρ_s .

Particle Structure Characterization

The size, R , and mass, M , of the particles can be determined by the Guinier approximation,

$$I(Q) = \frac{\phi V^2 \Delta\rho^2}{M} \exp\left(-\frac{Q^2 R_g^2}{3}\right), \quad (2)$$

which applies over the domain $Q < R^{-1}$. In Eq. (2), ϕ is the volume fraction of particles, V is the particle volume, and R_g is the radius of gyration. Once the size of the particle is known, the models can be refined by calculating $\langle P(Q) \rangle$ for different models and fitting them to $I(Q)$.

Particle areas per unit mass, S , are measured over length scales, $QR \gg 1$, where the scattering can be described by a *Porod-law*,

$$I(Q) = 2\pi S \Delta\rho^2 Q^{-4}. \quad (3)$$

When there are particle interactions, so that the positions and or orientations are correlated in some way, it is necessary to reinterpret Eq. (1) as

$$I(Q) = S'(Q) \langle P(Q) \rangle. \quad (4)$$

Here, $S'(Q)$ is the effective structure factor, which arises from particle correlation. Eq. [4] applies rigorously to solutions of monodispersed, spherical particles. $S'(Q)$ has been reformulated to approximate the scattering from suspensions of non-spherical, polydisperse particles (2).

Contrast Variation

Scattering is a quadratic function of contrast, and SANS provides a unique capability to change $\Delta\rho$ by suspending the sample in fluids having different weight fractions of deuterated fluid, $f_{c_6\rho_2}$. Because K in Eq. (1) is proportional to $\Delta\rho^2$, the scattering intensity is quadratic with contrast: (3,4,5)

$$I(Q) = \Delta\rho^2 I_\Omega(Q) + \Delta\rho I_{\Omega\xi}(Q) + I_\xi(Q). \quad (5)$$

The basic scattering functions, $I_\Omega(Q)$ and $I_\xi(Q)$, arise, respectively, from the solvent-excluding parts of the structure, $\Omega(\mathbf{r})$, and from the internal fluctuations, $\zeta(\mathbf{r})$. The function, $I_{\Omega\xi}(Q)$, is the scattering from correlation between $\Omega(\mathbf{r})$ and $\zeta(\mathbf{r})$. In this representation, the structure is defined as the sum of the shape and internal structure terms; thus, $\rho(\mathbf{r}) = \rho_s + \Delta\rho\Omega(\mathbf{r}) + \zeta(\mathbf{r})$. The method of contrast variation allows one to distinguish between scattering from external (accessible to the fluid) and internal (inaccessible to the fluid) interfaces.

The Guinier approximation (Eq. (5)) yields the contrast dependence at $Q = 0$,

$$(I(0))^{1/2} = \sqrt{\frac{\phi}{M}} V \Delta\rho, \quad (6)$$

and the contrast dependence of R_g ,

$$R_g^2 = R_c^2 + \frac{\alpha}{\Delta\rho} - \frac{\beta}{\Delta\rho^2}. \quad (7)$$

In Eq. (7), R_c is the R_g of $\Omega(\mathbf{r})$, α is proportional to the second moment of $\zeta(\mathbf{r})$ and β is proportional to the first moment-squared of $\zeta(\mathbf{r})$.

To compute the different scattering functions in Eqs. (5) and (7) we need an estimate of $\bar{\rho}$. This may be determined from the chemical composition and sample density. If we can use Eq. (6), then we may interpolate a plot of $\sqrt{I(0)}$ versus ρ_s to $\Delta\rho = 0$ to give $\bar{\rho}$. The slope from this plot gives V .

Polydispersity and Chemical Heterogeneity

The method of contrast variation was developed for homogeneous particle populations (3). In general, particle populations can have two distinct types of heterogeneity, polydispersity in size and shape and in composition and or density, ρ . We refer to the later as chemical heterogeneity. We have derived the appropriate statistical forms for Eqs. (5) to (7) to account for heterogeneity (7), assuming that all of the particles are measured at high contrast.

In a chemically heterogeneous population, not all the particles can be contrast matched at $\rho_s = \bar{\rho}$. Thus, the easily distinguishable characteristic of chemical heterogeneity is that $I(Q)$ for $Q = 0$ in Eq. (6) will not go to zero as $\rho_s \rightarrow \bar{\rho}$. The plot of $\sqrt{I(0)}$ versus ρ_s and fitted to Eq. (6) using only the high contrast points will yield average values for $\bar{\rho}$ and V :

$$\bar{\rho} = \left[\frac{\int_x f(x)V^2(x)\rho^2(x)dx}{\int_x f(x)V^2(x)dx} \right]^{\frac{1}{2}} \quad \text{and} \quad V = \left[\int_x f(x)V^2(x)dx \right]^{\frac{1}{2}}, \quad (8)$$

where the integration is over a structural or compositional parameter, x , (*e.g.* particle radius, density, chemical composition, *etc.*) and $f(x)$ is the probability density of x .

The R_c , α , and β calculated using Eq. (7) are the respective z-averages,

$$R_c^2 = \frac{\int_x f(x)V^2(x)R_c^2(x)dx}{\int_x f(x)V^2(x)dx}, \quad \alpha = \frac{\int_x f(x)V^2(x)\alpha(x)dx}{\int_x f(x)V^2(x)dx}. \quad (9)$$

A calculation of β for heterogeneous samples is highly problematic.

The average shape function calculated from Eq. (5) is the number average,

$$I_\Omega(Q) = \int_x f(x)I_\Omega(Q|x)dx, \quad (10)$$

The observed I_ζ is

$$I_\zeta(Q) = \int_x f(x)\rho(x)^2 I_\Omega(Q|x)dx - 2\bar{\rho} \int_x f(x)\rho(x)I_\Omega(Q|x)dx + \bar{\rho}^2 I_\Omega(Q) + \int_x f(x)\rho(x)I_{\Omega\zeta}(Q|x)dx - \bar{\rho} \int_x f(x)I_{\Omega\zeta}(Q|x)dx + \int_x f(x)I_\zeta(Q|x)dx, \quad (11)$$

and the measured $I_{\Omega\zeta}$ is,

$$I_{\Omega\zeta}(Q) = 2 \int_x f(x)\rho(x)I_\Omega(Q|x)dx - 2\bar{\rho}I_\Omega(Q) + \int_x f(x)I_{\Omega\zeta}(Q|x)dx \quad (12)$$

In the absence of chemical heterogeneity ($\rho(x) = \bar{\rho}$), Eqs. (8) to (10) reduce to the respective number averages.

Measurements

Using the method of contrast variation, we studied carbon black suspensions or a carbon black-elastomer composite with polyisoprene (prepared as “bound” rubber (5) remaining after extensive Soxhlet extraction with good solvents. The samples were suspended or swollen in various cyclohexane mixtures, each having different $f_{C_6D_{12}}$ (0, 0.25, 0.5, 0.75, and 1.0), using sonication. For one set of studies an experimental CB, HSA, was used. The samples were actively suspended during the measurements. Measurements were done on the suspended HSA samples and HSA-polyisoprene bound rubber composites using the Low-Q Diffractometer, LQD, at the Manuel Lujan Scattering Center, Los Alamos National Laboratory. For a second set of studies carbon blacks N330, XHL81 and HSA were suspended, as above, the allowed to settle. The SANS instrument, D11, at the Institute Laue-Langevin was used for these measurements.

Results and Discussion

The Structure of an Experimental Carbon Black, HSA

Contrast variation measurements of suspended HSA in cyclohexane having different $f_{C_6D_{12}}$ show significant difference in scattering shape and magnitude (4). The values from the contrast-dependence of the Guinier analysis (Eqs. (2), (6) and (7)) of HSA are summarized in Table II ($\beta \approx 0$). These values are the averages given by Eqs. (8) and (9). The value of $\bar{\rho}$ is consistent with that calculated from the density and chemical composition ($6.1 \cdot 10^{10} \text{ cm}^2$) and V is consistent with TEM observations. The large positive value of α shows that the aggregates have a shell-core structure, with a graphitic outer shell and amorphous carbon core, with voids consistent with TEM (1) and STM (8). The amorphous core is continuous through the aggregate, giving the aggregate a structure rather like a peanut (Fig. 1).

The basic scattering functions, computed from the SANS data using Eq. (5), are shown in Fig. 2. $I_{\Omega}(Q)$, which is the average given in Eq. (10), was fitted to a prolate ellipsoid of revolution 290 Å by 1500 Å (Fig 2a), showing that the aggregates on average are quasi-linear and consist of 5 to 6 particles. This is consistent with stereo-TEM studies (9). $I_{\Omega}(Q)$ obeys Porod's Law (Eq. (3)); thus, the aggregates have smooth surfaces on length scales greater than 10 Å. The aggregate surface area, S , can be measured (Table 2) from the Porod law dependence. The functions, $I_{\zeta}(Q)$ and $I_{\Omega_{\zeta}}(Q)$, are consistent with the core shell model derived from α (Figs 2b and 2c). In particular the negative values of

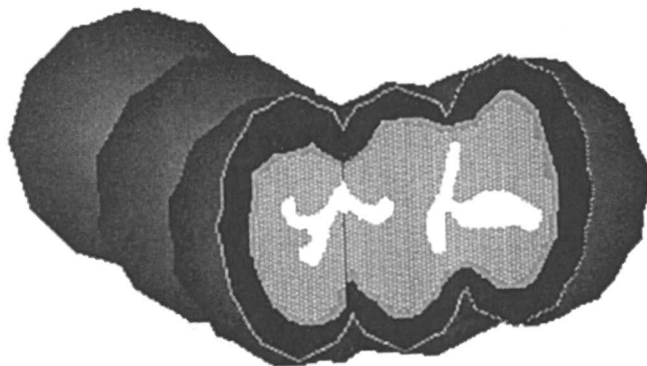


Figure 1. Schematic of the Carbon Black Aggregate Structure. The structure consists of a quasi-linear array of fused, spheroid particles. The outer shell of the structure (black) consists of graphitic carbon crystallites, with a core (gray) of less dense void-filled (white) carbon.

Table II. Structural Parameters for HSA

V (nm ³)	$\bar{\rho}$ (cm ⁻²)	R _c (nm)	α	S (m ² g ⁻¹)
5.4 (3) 10 ⁴	5.7 (0.3) 10 ¹⁰	29.3 (4)	2.0 (3) x 10 ⁻²	170 (4)

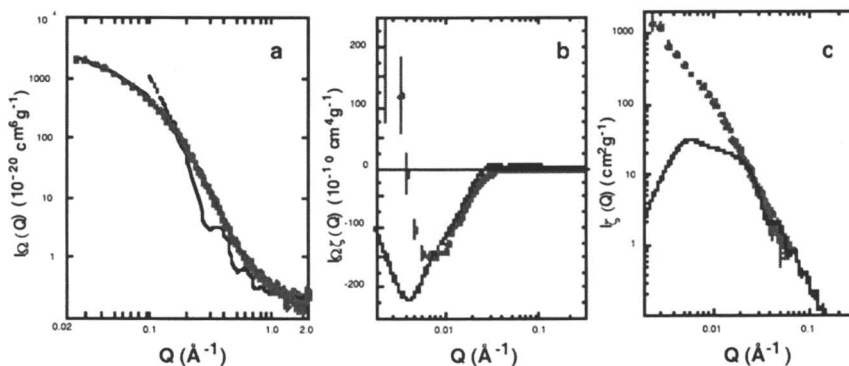


Figure 2. Basic scattering functions of HSA. The basic scattering functions calculated from SANS data using Eq. (5), \circ : a, $I_Q(Q)$; b, $I_{Qc}(Q)$; c, $I_c(Q)$. The lines are the respective expected results for the model in Fig. 1 and described in the text.

$I_{Qc}(Q)$ (Fig. 2b) is a characteristic of the core-shell like structure with the core having a smaller scattering length density than the shell. There are substantial deviations of the experimental values from the model calculations, due to the influence of chemical heterogeneity ($\rho(x) \neq \bar{\rho}$ in Eqs. (11) and (12)).

Other Carbon Blacks

The carbon black used in this study is not one that is used for tire production. The question is to what degree are the structures found here characteristic of production blacks? To answer a question we did SANS measurements on a production, reinforcing carbon black, N330 and an experimental, structured black, XLH81 (10). In these studies the carbon blacks were swelled into the cyclohexane medium by sonication, then allowed to settle. We also measured HSA under similar conditions. The values of $\bar{\rho}$ for these samples are calculated from the contrast dependence of the scatter at very low Q . According to Eq. (5), this dependence will be proportional to $\Delta\rho^2$, assuming

that $I_{\Omega}(Q)$ makes the only important contribution to the scattering in this domain. These values are 5.6 , 5.7 and $5.8 \times 10^{10} \text{ cm}^{-2}$ for HSA, N330 and XLH81, respectively, are consistent with the known chemical composition and with the $\bar{\rho}$ given in Table II.

The shape scattering functions for XLH81, N330 and HSA are identical for Q greater than 0.01 \AA^{-1} (Fig. 3a). These blacks show a Porod law indicating smooth surfaces on length scales greater than 10 , consistent with the results in Fig. 2a. At low- Q the blacks show different power laws. For XLH81 $I_{\Omega}(Q) \propto Q^{-2.3}$. N330 and HSA show power law scattering with an exponent of -2.0 . HSA scattering crosses over to power law scattering at larger Q than N330, indicating the smaller size of the aggregate. If we were to interpret these power law dependencies as the mass (fractal) dimension, these values contrast with the quasi-linear dimension of the HSA aggregate. However, unlike the experiments with HSA, above, in these measurements the carbon blacks were allowed to settle in the solvent, rather than being actively suspended. Thus, in this case the low- Q power law reflects the morphology of the aggregates and agglomerates present in the fluid, not just the aggregates. The differences in the low- Q power law dependence correlates with differences in the appearance of these carbon blacks by TEM (12).

The power law dependence of the scattering observed for N330 is in rough agreement with recent small and ultra small-angle x-ray scattering studies, which gave low- Q power law with an exponent of -1.8 and a Porod region power law with exponent -3.8 (13). The small difference in the Porod region can be attributed to the inability of the x-ray technique to distinguish between inner and outer surfaces.

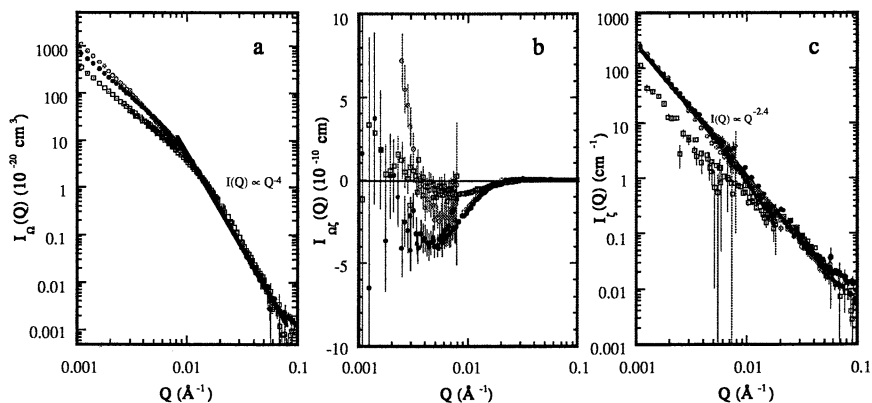


Figure 3. Basic scattering functions of XLH81, N330 and HSA. The basic scattering functions calculated from SANS data using Eq. (5), ●; XLH81, ○; N330, ■; HSA: a, $I_{\Omega}(Q)$; b, $I_{\Omega\xi}(Q)$; c, $I_{\xi}(Q)$. The lines are the power law fits to the data described in the text.

The $I_{\Omega_c}(Q)$ (Fig. 3b) from N330 and XLH81 indicate that they have the same shell-core structure found in HSA (10). This is seen by the negative values of $I_{\Omega_c}(Q)$, which may be larger in XLH81 and N330, than observed in HSA (Fig. 3b). The HSA carbon black in these studies gives the same general form for $I_{\Omega_c}(Q)$ observed in Fig. 2b. Finally, the internal structure function, $I_c(Q)$, for both XLH81 and N399 show a single power law dependence, $I_c(Q) \propto Q^{-2.4}$ down to very low Q (Fig. 3c). Given the complicated form of Eq. (11), it is not possible to interpret this result, except to point out that the same power law dependence is seen in the $I_c(Q)$ for HSA (Fig. 2c) at higher Q .

Carbon blacks are produced by a furnace process in which oil feed stock is introduced as an aerosol into an oxidizing flame. According to the standard model of this process, the aerosol droplets are burnt to produce spheroid particles. The inner parts of the particles are not completely oxidized: graphitic carbon is confined to the particle surface, leading to a core shell structure with hydrogenated, amorphous carbon in the inside of the particle. The particles collide to form aggregates, like beads on a string. The results of experiments using HAS and other carbon blacks (Figs. 2b and 3 b.) suggest, however, that the aggregates do not consist of particles associated like beads on a string. Rather, the particles are fused by the amorphous cores to form a peanut-like structure (Fig. 1) with a graphitic carbon shell surrounding the entire structure. Thus, the particles do not exist as independent entities in the aggregate. Furthermore, our result suggest that the burning and aggregation of the particles into aggregates occurs and similar time scales.

Carbon Black Associations in Elastomer

The SANS of HSA-polyisoprene bound rubber gels is significantly different from that of HSA alone (5). The contrast match point of polyisoprene at $f_{C_6D_{12}} = 0.07$, where only CB scattering should be observed (Fig. 4a) was calculated from the data by interpolation using Eq. (5). For $Q < 0.02 \text{ \AA}^{-1}$ the scattering from HSA is considerably greater than that from the HSA-polyisoprene composite. For Q between 0.02 \AA^{-1} and 0.07 \AA^{-1} the HSA intensity is slightly less than that of the composite (Fig. 4a). The scattering from the two samples becomes indistinguishable for Q greater than 0.07 \AA^{-1} . We have shown (4) that the scattering from suspended HSA (Fig. 4a) is very close to that expected from non-interacting particles. Further, when $f_{C_6D_{12}}$ is between 0 and 0.25, scattering reflects the carbon black aggregate shape with little contribution from the internal structure. Thus, we could use Eq. (4) to calculate $S'(Q)$ (Fig. 4b).

We have not interpreted $S'(Q)$ quantitatively. However, some qualitative features of carbon black associations in bound rubber are apparent. Some features of $S'(Q)$ probably arise from the fact that the carbon black aggregates are elongated. That $S'(Q)$ is significantly smaller than unity at low Q implies that there is strong exclusion of carbon black particle neighbors in the HSA-

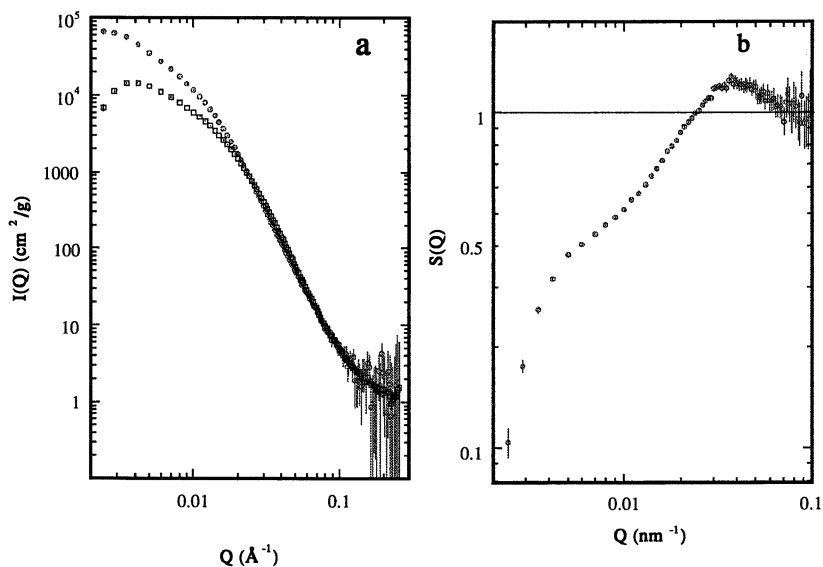


Figure 4. Calculation of the HSA structure factor in an HSA-polyisoprene composite. a: Calculated scattering for HSA and HSA-polyisoprene bound rubber at the polyisoprene contrast match point ($f_{C_6D_{12}} = 0.07$) using Eq. (5),

○; HSA, □; HSA-polyisoprene. b: $S'(Q)$.

polyisoprene, bound rubber composite. It is likely then that on average each carbon black aggregate is separated by a considerable amount of polymer that prevents the aggregate from making lateral associations. On the other hand, the amount of carbon in this sample, 65% by weight in the dried material, is above the percolation limit. Thus, the carbon black aggregates must be touching, or at least have only small amounts of polymer in between, in which case these results must reflect end on association of the rodlike aggregates.

Conclusions

Small-angle neutron scattering provides a probe on length scales that are relevant to nanocomposite polymer systems, such as carbon blacks. The method of contrast variation allows various sources of scattering to be isolated by contrast enhancement and contrast matching. Therefore, a clearer picture of the internal structure and morphology of different carbon blacks has emerged. The studies have shown that the aggregates have a core-shell like structure, rather like a peanut. The existence of a Porod region implies smooth surfaces to length scales down to 10 Å. Different carbon blacks have different long length scale

aggregate/agglomerate morphologies. The morphology of the blacks provides insight on the mechanism of formation. The method also allows the aggregation of the carbon black in the polymer composite to be explored. These results have important implications on the mechanism of reinforcement of rubber by carbon black. Information on the association of the carbon black in HSA-polyisoprene composites when $S'(Q)$ is interpreted should give an understanding of the morphology of the carbon black network in the composite. Information on the carbon black internal and surface structure can lead to a better understanding of carbon black filler rigidity and interactions with polymers.

Acknowledgement

This work was supported by the Office of Basic Energy Sciences of the Department of Energy. This work benefited from the use of the Low-Q Diffractometer at the Manuel Lujan Neutron Scattering Center of the Los Alamos National Laboratory, which is supported by the Office of Basic Energy Sciences of the United States Department of Energy under contract W-7405-ENG-36 to the University of California. This work also benefited from the use of the SANS instrument, D-11, at the Institut Laue-Langevin. The author thanks his collaborators, Michel Gerspacher and Henry Yang of the Sid Richardson Carbon Black Company for helpful discussions and Marilyn Hawley of Los Alamos National Laboratory and Peter Lindner of the Institut Laue-Langevin for help on the experiment on D-11.

References

1. Hess, W.M.; Hurd., C.R. *Carbon Black*, Donnet, J.-B.; Bansal, R.C.; Wang, M.-J. Eds.; Dekker: New York, 1993; pp 91-106.
2. Kotlarchyk, M, and Chen S.-H., *J. Chem. Phys.*, **1983**, *79*, 2461.
3. Ibel, K.; Stuhmann, H.B. *J. Mol. Biol.* **1975**, *93*, 255.
4. Hjelm, R.P.; Wampler, W.; Seeger P.A.; Gerspacher, M. *J. Mat. Res.* **1994**, *9*, 3210.
5. Hjelm, R.P.; Mang, J.T.; Skidmore, C.; Gerspacher, M. *Proceedings of the Workshop on Materials Research Using Cold Neutrons at Pulsed Sources*, World Scientific Publishing, 1999, pp 120-127.
6. Hjelm, R.P.; Wampler, W.; Gerspacher, M. *Mat. Res. Soc. Symp. Proc.* **1996**, *376*, 303.
7. Hjelm, R.P., Mang, J.T., Skidmore, C., and Gerspacher, M., *Proceedings of the Workshop on Materials Research Using Cold Neutrons at Pulsed Sources*, World Scientific Publishing, London, 1999, pp 120-127.
8. Donnet; J.-B.; Custodéro, E. *Carbon* **1992**, *30*, 813.
9. Gruber, T.C.; Zerda, T.W.; Gerspacher, M. *Carbon* **1993**, *31*, 1209.

10. Hjelm, R.P.; Gerspacher, M.; Yang, H.H. *Proceedings of the 153rd Meeting of the American Chemical Society Rubber Division*, Rubber Division, ACS: Akron, OH, 1998, paper 41.
11. Zerda, T.W.; Yang, H.H.; Gerspacher, M. *Rubber Chem. & Tech.* **1992**, *65*, 130.
12. Gerspacher, M. *personal communication*.
13. Rieker, T., Misono, S. and Ehrburger-Dolle, F., *Langmuir* **1999**, *15*, 914.

Chapter 8

An Investigative Study of Polymer Adsorption to Smectite Clay: Polyelectrolytes and Sodium Montmorillonite

Robert Y. Lochhead¹ and Cheri McConnell Boykin^{1,2}

¹Department of Polymer Science, The School of Polymers and High Performance Materials, The University of Southern Mississippi, SS Box 10076, Hattiesburg, MS 39406-0076

²Current address: PPG Industries, 1PPG Place, Pittsburg, PA 15272

This chapter focuses on elucidating the mechanisms of interaction for a series of polymers adsorbed onto montmorillonite clay from aqueous solution. The polymers considered are nonionic, anionic and cationic polyacrylamide copolymers. The amount of polymer adsorbed, its conformation and the exact nature of the anchoring groups on the clay surface are considered. The nonionic polymers act as H-bond acceptors (amide and acid moieties) and donators (acid groups). The cationic copolymers exhibit strong, irreversible interactions with the clay. The anionic copolymers show only weak or no adsorption.

Introduction

Toyota Central Research and Development Laboratories in 1987 (1) reported the initial research on polymer/clay nanocomposites. Researchers there produced a nylon-6 clay nanocomposite that showed dramatically enhanced mechanical properties over the unreinforced nylon-6 (2,3). The special properties that are attained in the clay nanocomposites are dependent upon the dispersion of particles having a high aspect ratio and Toyota's invention spawned intensive worldwide research activity aimed at improving the properties of polymeric materials for use as, for example, external body parts for the automotive industry; heat-resistant polymeric automotive parts in contact with an engine blocks; tire cord for radial tires; food wrap having improved gas impermeability electrical components and food grade drink containers (4).

Smectite clays, such as montmorillonite have been found to be especially advantageous as the discontinuous phase in nanocomposites

Montmorillonite clay is a specific kind of phyllosilicate clay. In its native state, montmorillonite consists of sheets which are of the order of 200 nanometers long and wide, but only 1 nanometer thick. These sheets are stacked like packs of cards and the spacing (or "gallery") between adjacent sheets in the pack is only of the order of 1 nanometer

Clay-based Polymer Nanocomposites

In general, the polymer-clay composites can be divided into three categories: conventional composites, intercalated nanocomposites, and exfoliated nanocomposites. In a conventional composite, the clay tactoids exist unchanged from their original state of stacked sheets in which the matrix polymer is not inserted in the interstices within the stacked layers. The polymer interacts only with external surfaces of the clay particles (tactoids). In an intercalated nanocomposite, the polymer enters the clay layer structure in a crystallographically regular fashion. An intercalated nanocomposite normally is interlayered by only occasional molecular layers of polymer and the properties of the composite typically resemble those of the clay host (5, 6, 7, 8). If the clay is completely exfoliated in a nanocomposite, the individual 1nm-thick clay platelets would be homogeneously dispersed in the polymer matrix (9).

Small molecules can be adsorbed between the sheets of clay. However, the gallery spacing is much smaller than the radius of gyration of typical polymers. Therefore, there is a conformational entropy penalty that inhibits the polymer from entering the gallery (10). The polymer will enter the galleries only if there is sufficient enthalpic interaction between the clay and the penetrating polymer.

In general, the bulk of current knowledge indicates that dispersing clay platelets into a polymer matrix improves the physical properties of that matrix, more so if the platelets are completely exfoliated, improved toughness, increased tensile strength, tensile modulus, flexural strength, and flexural modulus are achieved as compared to the polymer matrix alone.

The patent literature is already rich with inventions that are aimed at enhancing exfoliation of the clay in a polymer matrix. Polystyrene and poly(ethylene oxide) can be directly intercalated into organically-modified layered silicates (11, 12). These intercalates, however, could not be exfoliated. Exfoliation requires pre-treatment of the clay platelets to enhance their interaction with the matrix polymer.

The gallery cations in a natural smectite can be replaced by simple ion exchange process with almost any desired cation, including alkylammonium alkyl phosphonium and other organic cations (13). Treatment of the clay with quaternary alkylammonium salts is the most common method of rendering the clay organophilic and enhancing its miscibility with and dispersion in organic solvents. Thus, in a well-known process, organic ammonium ions can be readily intercalated within the galleries of the phyllosilicate clay structure, and clays so treated can be exfoliated by high shear mixing. This technique was disclosed by Allied Signal for a process in which the clay was treated with a silane or onium coupling agent, in which said agent had reactive groups which could be copolymerized into a polymer matrix (14). The clay was then dispersed in a polymer matrix by screw extrusion, to give the desired nanocomposite (15).

Oligomeric polyetheramines are capable of intercalating into the clay layers to increase the d-spacing from about 1nm to about 4.5 nm. These amines are curing agents that facilitate both exfoliation of the clay and simultaneous curing of the polymer matrix (9).

Carbonyl or carboxylic monomers are also capable of intercalation into the clay galleries and the treated clay can be exfoliated in solvents such as alcohols or glycols (16). Amine or amide monomers have been claimed to induce exfoliation of the clay (17). Hydroxyl or aromatic monomers intercalate into the clay interstices by bonding, via a metal cation of the phyllosilicate sharing electrons with two electronegative atoms of one or two intercalant monomer molecules and this facilitates exfoliation into polar solvents(18). The same mechanism is claimed to be responsible for the pretreatment intercalation of sodium montmorillonite with polyvinylpyrrolidone or poly(vinylalcohol) (19). The treated clays could be exfoliated into ethylene-vinyl alcohol matrix copolymers (20). Oligomers and low molecular weight polymers are more effective in intercalation than high molecular weight polymers (21) and bilayers and trilayers of polyvinylpyrrolidone can be intercalated into the clay in an aqueous pretreatment that can be enhanced by partial pretreatment of the clay with onium or silane compounds (22). Pretreatment of smectite clays with C₁₀

compounds having polar functionality at one end of the molecule results in intercalates or exfoliates that are useful as plasticizers; for providing increased viscosity and elasticity to thermoplastic and thermosetting polymers, e.g., for plasticizing polyvinyl chloride; for food wrap having improved gas impermeability; for electrical components; for food grade drink containers (23). Exfoliated Laponite[®] has been used in polyolefin layers for improvement of strength and antistatic properties in photographic papers and stock for inkjet printing (24). The nanocomposites can be prepared in different forms. For example, thermoset epoxies (25, 26), elastomers that maintain their properties at elevated temperatures (27) and latex nanocomposites have been claimed (28).

The Interaction of Polyacrylamide Copolymers with Sodium Montmorillonite

It is apparent that the details of the molecular interaction of the polymer coupling agents with the clay is important for the intercalation and exfoliation required to achieve the enhanced properties. This has been the focus of recent work conducted in our laboratory (29) in which the interaction of polyelectrolyte chains with montmorillonite clay was studied. Our principal thrust to this point has been directed towards the investigation of the exact interaction of model pretreatment polymers on sodium montmorillonite as a function of pH of aqueous pretreatment, with no electrolyte added to the system. The goal of this research was to determine: (a) exactly which groups of the polymer interact with which chemical groups of the clay surface; (b) the conformation of the polymer; (c) the amount of polymer adsorbed under different physical conditions; (d) the effect on pretreatment slurry rheology, and to establish the important physical variables that had to be controlled. The nature of the interaction of polymers with particles depends upon the concentration regime of both the particles and the polymer in solution. Thus, in the dilute regime, below the critical overlap concentration, adsorbed polymers will tend to cause bridging flocculation until complete surface coverage is achieved at which point steric stabilization and dispersion of the particles will occur. In the semi-dilute regime, associative stabilization, depletion stabilization and depletion flocculation will all be likely to occur (30,31).

The groups available on the montmorillonite surface depend upon the pH of the aqueous environment. At low pH values, both the face and edges of the clay platelets are hydrogen bond donors, but at high pH both surfaces are hydrogen bond acceptors. The face almost always carries a negative ionic charge, but the edge is ionically positive at low pH and ionically negative at high pH values (32). The zeta potential of the montmorillonite used for this study indicated that the clay particles always carried an overall negative charge.

In our studies, the nature of the chemical bonds in montmorillonite was characterized by FTIR spectroscopy. A typical spectrum is shown in figure 1. The Al-OH stretch, the Si-O stretch, the Al-Al-OH bend and the Si-O-Al bend are prominent in this spectrum. Other peaks are assigned appropriately in figure 1.

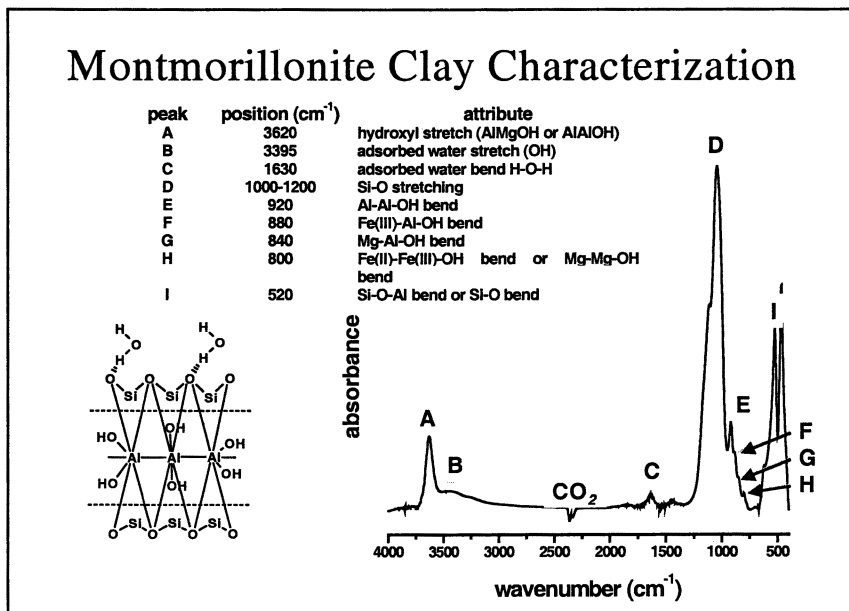


Figure 1. The FTIR spectral characteristics of montmorillonite clay

The Nature of the Chemical Interaction Between Polymer and Montmorillonite

Adsorption isotherms were determined by depletion and measured by UV spectrometry, utilizing the adsorption of the carbonyl group of the polyacrylamide. The plateau adsorption values are shown in Table 1. Adsorption of the polyacrylamide was not favored at alkaline pH values. This is attributed to partial hydrolysis of the polyacrylamide at high pH values.

Table I. The plateau adsorption values for polymers adsorbed to sodium montmorillonite

	Maximum Adsorption (g polymer/g clay)	Maximum Adsorption (g polymer/g clay)	Maximum Adsorption (g polymer/g clay)	Maximum Adsorption (g polymer/g clay)
	<i>Polyacrylamide</i>	<i>PAm-MAAP</i>	<i>Pam-AA</i>	<i>Pam- AMPS</i>
Percent Comonomer	0	14	12	13
pH 3	0.66	2.7	0.92	~0
pH 7	0.59	2.2	~0	~0
pH 10	0.1	4.2	~0	~0

Polyacrylamide homopolymer

The nature of the interaction between chemical groups on the polymer and the clay surface was probed by measuring the extent of the shift in absorbing wavelength of key groups in the polymer and on the clay after intimate mixing of these components. The important groups on the montmorillonite were the Al-OH stretch at 3620cm^{-1} (designated A in figure 1) and the Si-O stretch at $1000\text{-}1200\text{ cm}^{-1}$ (designated D in figure 1).

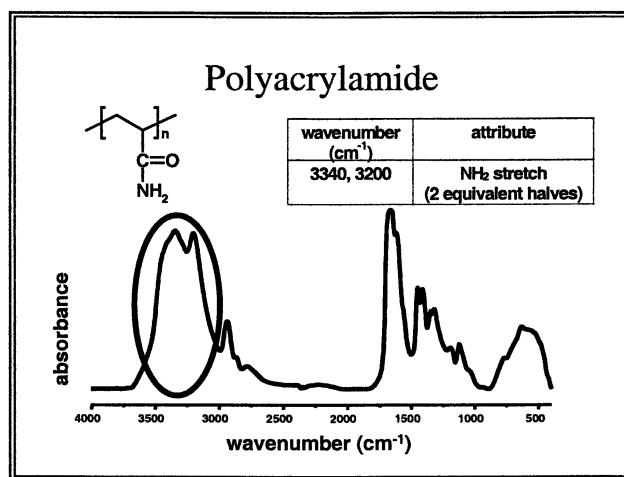


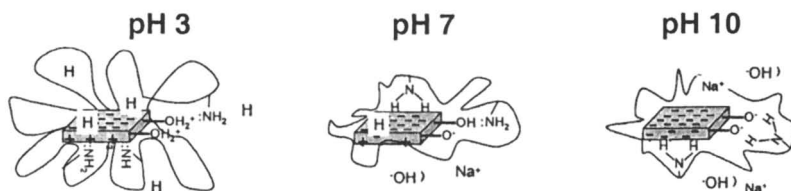
Figure 2: The FTIR spectrum of polyacrylamide

For polyacrylamide, the NH_2 stretches at 3340 and 3200cm^{-1} were useful (figure 2). The limit of the accuracy of measurement was about 2cm^{-1} . This was important to measure, because the clay lattice structure severely constrained the bonds bringing the shifts to within the limit of accuracy. The results are shown in Table II. At all three pH values, the Al-Al-OH stretch of the clay platelet edge shows a shift of -4cm^{-1} and the NH_2 stretch of the acrylamide shows a shift of greater than $+100\text{cm}^{-1}$. Further there is no significant shift in the platelet face Si-O stretch. This is clear evidence for hydrogen bonding of the amide groups of the polymer with the Al-Al-OH f groups of the clay edge at all pH values.

Table II. The FTIR absorption frequency shifts that occur upon interaction of montmorillonite and polyacrylamide.

$$\Delta \text{ abs band } (\text{cm}^{-1}) = \text{peak max}_{\text{after mixing}} - \text{peak max}_{\text{before mixing}}$$

functional group	region (cm^{-1})	$\Delta_{\text{abs band}} (\text{cm}^{-1})$		
		pH 3	pH 7	pH 10
clay edge: Al-Mg-OH or Al-Al-OH hydroxyl stretch	3620	-4	-4	-4
clay face: Si-O stretch	1000-1200	0, 0	0, -6	2, 2
-NH ₂ stretch	3000-3500	115, 189	139, 199	143, 193



The FTIR evidence does not support binding of polyacrylamide to the clay face, except perhaps at pH 10, but it should be noted that the shifts of the Si-O stretch at this pH are of the same magnitude as the experimental error. The nature of the interactions between polyacrylamide and a schematic clay platelet is depicted in the drawings beneath Table II.

Cationic poly(acrylamide-co-methacrylamido-N-n-propyl-3-(trimethyl)ammonium chloride)

For the cationic copolymer of polyacrylamide and methacrylamido-N-n-propyl-3-(trimethyl)ammonium chloride, the NR_3 deformation at 1628cm^{-1} was a useful indicator of the adsorption of this group on the clay surface. The FTIR frequency shifts that occur upon interaction of the polymer with the clay are presented in Table III. In the acid pH range the Al-Al-OH shift of 2cm^{-1} is within the limits of experimental error. Si-O of the clay face shifted 4cm^{-1} and the NR_3 of the polymer shifted by -8cm^{-1} . The NH_2 of the acrylamide group also displayed a shift of similar magnitude to that observed in Table II. At neutral pH and under alkaline conditions, the Al-Al-OH stretch of the clay edge shifted significantly and the other shifts persisted. The interpretation offered to explain these shifts is that the quaternary nitrogen group is binding to the face of the platelet and the amide groups bind to the edge. The NR_3 appears to interact with the plane faces of the clay particles over the entire pH range.

Table III. The FTIR absorption frequency shifts that occur upon interaction of sodium montmorillonite and poly(acrylamide-co-methacrylamido-N-n-propyl(trimethyl)ammonium chloride)

functional group	region (cm^{-1})	Δ abs band (cm^{-1})		
		pH 3	pH 7	pH 10
clay edge: Al-Mg-OH or Al-Al-O hydroxyl stretch	3620	-2	-3	-4
clay face: Si-O stretch	1000-1200	4, -1	3, -1	3, -2
- NH_2 stretch	3000-3500	131, 195	132, 197	125, 196
- NR_3^+ deformation	1536	-8	-10	-7

Anionic poly(acrylamide-co-acrylic acid)

For the anionic copolymer of acrylamide and acrylic acid, the $\text{C}=\text{O}$ absorption band at 1567cm^{-1} and the shoulder at 1569cm^{-1} are suitable to probe the interaction of the polymer with montmorillonite. As shown in Table IV, when poly(acrylamide-co-acrylic acid) is mixed with montmorillonite, the clay edge Al-Al-OH stretch shows significant shifts at pH 3 and pH 7, but not at pH10. The clay face Si-O stretch showed a significant shift only at pH3. The $\text{C}=\text{O}$ stretch showed a shift of 9cm^{-1} at pH 3 and 3cm^{-1} at pH 7 and the amide

shifted at all pH values, but the magnitude of the shift was about one-third of that for polyacrylamide homopolymer. The interpretation offered for these results is that there is binding of the polymer to the clay edge under acid and neutral conditions, and binding of the polymer, presumably hydrogen bonding of the carboxyl groups, to the Si-O of the clay face under acid conditions. The interaction of this polymer with the clay appears to be considerably weaker than that for polyacrylamide homopolymer, and this is attributed to stronger interaction of the acrylic acid copolymer with the solvent (water) and mutual ionic repulsion between the clay and the polymer, especially in the sodium salt form.

Table IV. The shifts in the FTIR absorption frequencies that occur a result of mixing sodium montmorillonite with poly(acrylamide-co-acrylic acid).

<i>functional group</i>	<i>region (cm⁻¹)</i>	<i>Δ abs band (cm⁻¹)</i>		
		<i>pH 3</i>	<i>pH 7</i>	<i>pH 10</i>
clay edge: Al-Mg-OH or Al-Al-OH hydroxyl stretch	3620	-5	-3	-2
clay face: Si-O stretch	1000-1200	5, 0	1, -2	1, 2
-NH ₂ stretch	3000-3500	40, 42	41, 46	18, 3
-C=O stretch	1568	9	-3	1

Poly(acrylamide-co-acrylamidomethylpropanesulfonate)

The C=O stretch at 1565-1545 cm⁻¹ provides a means to measure the interaction of poly(acrylamide-co-acrylamidopropanesulfonate). For this polymer, as shown in Table V, there is a slight shift in the absorption frequency of the Si-O clay face groups and in the NH₂ amide groups, but no shift in the target C=O frequency. It is concluded that this polymer salt of a strong acid interacts only slightly, if at all, with the montmorillonite. Thus, the stronger the acid of the polyelectrolyte, the weaker the interaction with montmorillonite.

The Polymer Conformation at the Clay Interface

The conformation of the adsorbed polymer was probed by measuring the peak broadening of ¹³C NMR of the polymer's C=O groups before and after adsorption to the clay, in accordance with the method developed by Botero *et al* (33). The bound fraction can be calculated from the algorithm¹:

Table V. The FTIR absorbance frequency shifts of upon interaction of sodium montmorillonite with poly(acrylamide-co-acrylamidomethylpropanesulfonate)

functional group	region (cm ⁻¹)	Δ abs band (cm ⁻¹)		
		pH 3	pH 7	pH 10
clay edge: Al-Mg-OH or Al-Al-OH hydroxyl stretch	3620	-2	-2	-2
clay face: Si-O stretch	1000-1200	3, 0	3, 0	3, 0
-NH ₂ stretch	3000-3500	69, 54	84, 47	68, 92
-C=O stretch	1565-1545	0	2	2

$$(\Delta v_{1/2})_{exp} = P \overbrace{(\Delta v_{1/2})_{ref}}^{\text{bound}} + (1-P) \overbrace{(\Delta v_{1/2})_{sol}}^{\text{unbound}}$$

$$P = \frac{(\Delta v_{1/2})_{exp} - (\Delta v_{1/2})_{sol}}{(\Delta v_{1/2})_{ref} - (\Delta v_{1/2})_{sol}}$$

where P is the bound fraction, $(\Delta v_{1/2})_{exp}$ is the experimental line width at half height, $(\Delta v_{1/2})_{ref}$ is the reference for the bound fraction, and $(\Delta v_{1/2})_{sol}$ is the reference for the unbound fraction – (that is for the polymer in solution).

Figure 3 shows the effect of polyacrylamide adsorption on the NMR spectrum. The spectrum for polyacrylamide in solution is labeled 'a'.

The peak width at half height, $(\Delta v_{1/2})$ of the C=O of polyacrylamide in aqueous solution is measured as 23Hz. The adsorption isotherm that corresponds to the NMR spectra is shown on the upper left of the figure. On the rising part of the adsorption isotherm, the $\Delta v_{1/2}$ decreases from infinity at point **e** to 104 Hz at point **c**. This is interpreted as indicating that the polyacrylamide macromolecule adsorbs in a "flat" conformation, mainly as trains, on the surface at low polymer concentrations when the ratio of clay surface to polymer is high. As the polymer concentration increases, the polymer is adsorbed in a more "loopy" conformation until the adsorption plateaus at 0.6 g. polymer per g. clay.

The effect of pH on adsorbed polyacrylamide conformation can be discerned from the NMR spectra shown in figure 4. These spectra were

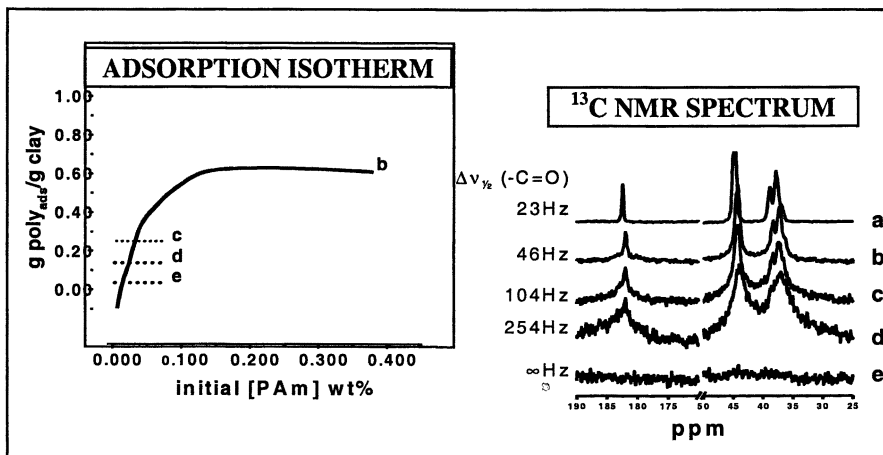


Figure 3. The adsorption isotherm of polyacrylamide on montmorillonite and the corresponding ¹³C NMR spectra.

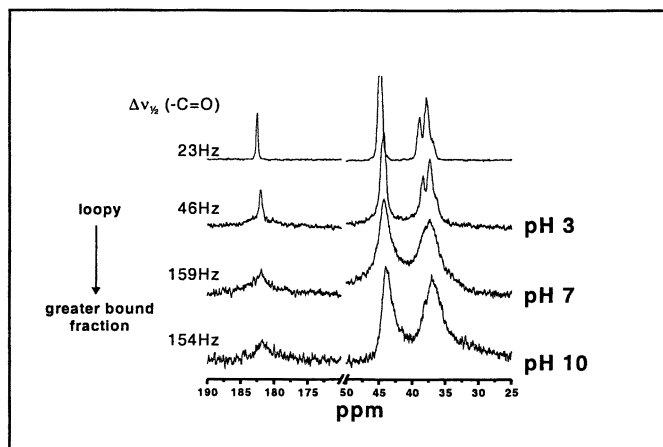
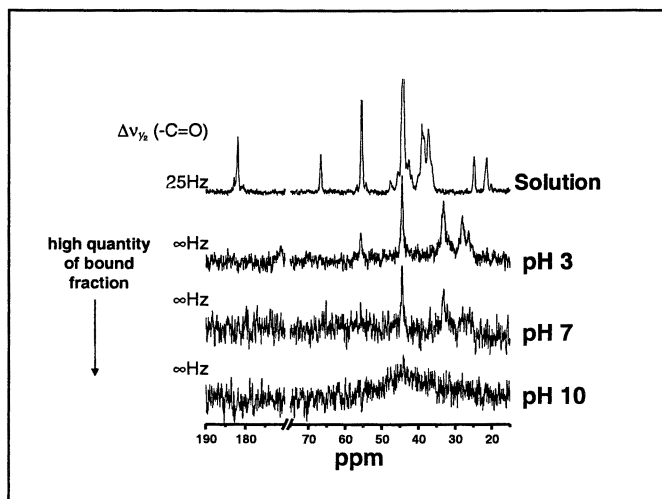


Figure 4. The effect of pH on the adsorbed polyacrylamide ¹³C NMR spectra

measured at the plateau of the adsorption isotherm. Upon increasing the pH from 3 to 10, the $\Delta\nu_{1/2}$ increases from 23Hz to 154Hz, indicating a ‘flatter’ adsorbed conformation with increasing pH.

As shown in figure 5, the NMR spectrum for poly(acrylamide-*co*-methacrylamidopropane(trimethyl)ammonium chloride), containing 14 mole percent of the cationic monomer, merges with the baseline at all pH’s and this is assigned as a $\Delta\nu_{1/2}$ of infinity. A peak width of infinity is interpreted as adsorption of the cationic copolymer in a flat conformation adjacent to the surface.

It is interesting, however, that when this cationic copolymer contained only 3 mole percent of cationic monomer, the $\Delta\nu_{1/2}$ is of the order of 30 to 40 Hz irrespective of pH. This shows that, in the plateau of the adsorption isotherm, the 3 mole percent cationic polymer adsorbed not only in a ‘loopy’ conformation, but the conformation was ‘loopier’ than polyacrylamide homopolymer.



*Figure 5. The effect of pH on the adsorbed poly(acrylamide-*co*-methacrylamido-*N*-*n*-propyl(trimethyl)ammonium chloride) ¹³C NMR spectra. This copolymer contained 14 percent of the cationic comonomer Poly(acrylamide-*co*-acrylic acid)*

Poly(acrylamide-*co*-acrylic acid) adsorbed only at pH 3. The $\Delta\nu_{1/2}$ for the polymer in free solution is 20Hz and the $\Delta\nu_{1/2}$ for the adsorbed polymer at the plateau of the adsorption isotherm is 57 Hz. This is indicative of adsorption in a ‘loopy’ conformation.

Conclusions

This study has shown that polyacrylamide adsorbs to the edge of the platelets of sodium montmorillonite. At low surface coverage, the polyacrylamide is adsorbed in a conformation that is flat and adjacent to the montmorillonite platelet edges. Upon increasing the adsorbed surface coverage, however, the polymer adsorbs in an increasingly 'loopy' conformation.

Incorporation of the cationic comonomer, acrylamido-N-n-propyl(trimethyl)ammonium chloride into polyacrylamide at the level of 14 mole percent, causes the polymer to adsorb to the face of the clay platelet in a conformation that is flat on the adsorbent surface and the equilibrium saturation absorption limit is considerably higher than that for polyacrylamide homopolymer. It is interesting that the copolymer containing only 3 mole percent of the cationic comonomer adsorbed in a more loopy conformation than polyacrylamide homopolymer. This may be caused by repulsion between the edge of the clay and the cationic polyelectrolyte, in a composition that has insufficient cationic character to adsorb on the clay face.

Incorporation of the strongly anionic comonomer acrylamidomethylpropane sulfonate prevents adsorption of the polyacrylamide on montmorillonite clay at all pH values. Similarly, the copolymer of acrylamide and acrylic acid does not adsorb at high pH values, but does adsorb under acid environments in a loopy conformation, apparently to both the face and the edge surfaces of the clay.

If it is hypothesized that intercalation and exfoliation would be favored by 'loopy' adsorption of polymer to the clay platelet surface, then the ideal matrix or coupling polymers, for clay nanocomposites, would be predicted to be those that contain a small proportion of cationic comonomer.

References

1. Usuki, A.; Kojima, Y.; Kawasumi, M.; Okada, A.; Fukushima, Y.; Kurauchi, T.; Kamigaito, O. *J Mater Res.* **1993**, 8, 1179.
2. Gilman, J.W.; Kashiwagi, T. *SAMPE Journal*, July/August **1997**, Vol. 33, No. 4,.
3. Hudson, U. S. Patent 5,910,523, 1999.
4. Frisk, et al. U. S. Patent 5,876,812, 1999.
5. Kato, C. *et al. Clays Clay Miner.* **1979**, 27, 129.
6. Sugahara, Y. *et al. J. Ceram. Soc. Jpn.* **1992**, 100, 413.

7. Vaia, R. A. *et al. Chem. Mater.* **1993**, 5, 1694.
8. Messersmith, P. B. *et al. Chem. Mater.* **1993**, 5, 1064.
9. Pinnavaia *et al.* U. S. Patent 6,017,632, 2000.
10. Balazs, A.C.; Singh, C.; Zhulina, E.; Lyatskaya, Y. *Acc. Chem. Res.*, **1999**, 32, 651.
11. Vaia, R.A. *et al, Chem. Mater.* **1993**, 5, 1694-1696.
12. Vaia, R.A. *et al. Adv. Materials.* **1985**, 7, No. 2, 154-156.
13. Jimenez, G.; Ogata, N.; Kawai, H.; Ogihara, T. *J. App. Polymer Sci.*, **1997**, 64.
14. Christiani *et al.* U. S. Patent 5,385,776. 1998
15. Christiani *et al.* U. S. Patent 5,747,560, 1998.
16. Beall, G. *et al.* U. S. Patent 5,804,613, 1998.
17. Beall, G. *et al.* U. S. Patent 5,880,197, 1999.
18. Beall, G. *et al.*, U. S. Patent 5,830,528, 1998.
19. Ferraro *et al.*, U. S. Patent 5,837,763, 1998.
20. Serrano *et al.* U. S. Patent 5,844,032, 1998.
21. Tsipursky *et al.* U. S. Patent 5,849,830, 1998.
22. Beall, G. *et al.* U. S. Patent 5,877,248, 1999
23. Beall, G. *et al.* U. S. Patent 5,952,095, 1999.
24. Majumdar *et al.*, U. S. Patent 5,891,611, 1999
25. Pinnavaia *et al.* U. S. Patent 5,760,106, 1998.
26. Pinnavaia *et al.* U. S. Patent 5,801,216, 1998.
27. Badesha *et al.*, U.S. Patent 5,840,796, 1998.
28. Elspass *et al.* U. S. Patent 5,883,173, 1999.
29. McConnell-Boykin, C. Ph.D. Dissertation; University of Southern Mississippi, Hattiesburg, MS, **1999**.
30. Sato, T.; Ruch, R. *Stabilization of Colloidal Dispersions by Polymer Adsorption*. Marcel Dekker, New York, NY, 1980, 123.
31. Napper, D.H. *Polymeric Stabilization of Colloidal Dispersions*. Academic Press, London, UK, 1983, 28.
32. van Olphen, H. *An Introduction to Clay Colloid Chemistry*. 2nd ed. John Wiley & Sons, New York, NY, (1977).
33. Bottero, J.Y.; Bruant, M.; Cases, J.M.; Canet, D.; and Fiessinger, F. *J. Colloid Interface Sci.* **1998**, 124, 515

Chapter 9

Mesoscopic Structure of Polymer–Inorganic Nanocomposites

Richard A. Vaia and Derek Lincoln

Materials and Manufacturing Directorate, Air Force Research Laboratory,
2941 P Street, Wright-Patterson Air Force Base, OH 45433

Elucidation of processing / morphology relationships is crucial for optimization of polymer-inorganic nanocomposites. X-ray scattering techniques are discussed and utilized to examine ultra-long range (20-60 nm) mesoscopic order in poly(caprolactam) (Nylon 6)-layered silicate nanocomposites. The high aspect ratio of the layered silicate implies orientational correlation of the layers will occur through excluded volume interactions at ultra-low loadings (0.1-1.0 vol%) as well as facile alignment in shear flows. Furthermore, the presence of the layered silicate alters the crystal form (γ v. α) and lamellae organization of polyamide 6. The layer distribution, size and interactions with the polymer substantially alter the nucleation rate and growth kinetics of the crystal phase. Detailed understanding of this hierarchical polymer–nanoparticle morphology is critical to ascertain the fundamental mechanisms associated with the various physical property enhancements observed for semicrystalline polymer-inorganic nanocomposites.

Introduction

Over the last decade, the utility of inorganic nanoparticles as additives to enhance polymer performance has been established and has motivated increased research and development in filled polymers containing nanoscale (1-100 nm) fillers, i.e. nanocomposites¹⁻⁸. Of particular interest are polymer/layered silicate nanocomposites (PLSN) because of their demonstrated enhancements, relative to an unmodified resin, of a suite of physical properties. These include combinations of increased modulus^{1,2}, strength^{1,2} and heat distortion temperature^{1,2} with decreased thermal expansivity,⁵ permeability^{3,4} and flammability⁶. In contrast to traditional fillers such as talc, carbon black or mica, which normally require loadings of 20wt% or more, these enhancements are achieved with less than 5wt% addition of a dispersion of high aspect ratio aluminosilicate layers (1 nm thick, 20 - 500 nm diameter). The addition of low volume fraction of filler enables utilization of conventional polymer processing technology as well as the potential to maintain a degree of optical clarity. A summary of the structure of the layered silicates, synthesis approaches to fabricate PLSNs, and property enhancements may be found in recent review articles⁷⁻⁹. The most extensively examined and successful resin to date is poly(caprolactam) (nylon 6)^{1,5}.

Understanding processing/morphology relationships is crucial for optimization of PLSNs, but it is only recently receiving increased attention. This understanding is especially critical for semi-crystalline polymers, such as poly(caprolactam), where a synergistic relationship between inorganic and polymer morphology exists^{10,11}. The final properties of semi-crystalline PLSN will depend to a large degree not only on the distribution of layered silicate but also the influence of layer distribution and degree of the polymer-silicate interactions on polymer crystallization and crystallite morphology.

To provide a better understanding of the issues associated with characterizing the development of complex morphologies in PLSNs, this article will discuss morphological features of poly(caprolactam) – layered silicate nanocomposites determined by x-ray scattering. After a brief review of potential PLSN morphologies and experimental issues associated with x-ray scattering from PLSNs, ultralong range (20-60 nm) mesoscopic order in poly(caprolactam) –layered silicate nanocomposites is discussed. Finally, the impact of this layer distribution and constituent interaction on polymer crystal morphology and elevated-temperature phase behavior of poly(caprolactam) is considered¹².

PLSN Morphology

As with other multiphase systems exhibiting nano (1-100 nm) and mesoscale (100-500 nm) order (such as biopolymers, block-copolymers, colloidal suspensions, and liquid crystals), physical properties ranging from toughness to optical clarity are determined by morphology on various length scales. For

PLSNs, this corresponds to the distribution of the layered silicate and its effect on the morphology of the polymer.

Two idealized polymer-layered silicate structures are conventionally discussed: *exfoliated* and *intercalated* (Figure 1). Fully exfoliated PLSNs consist of individual nanometer-thick silicate layers 'randomly' suspended in a polymer matrix. Interfacial area (i.e. the interface between inorganic and polymer) to mass ratios approaching 700 m²/g will result, implying interfacial properties contribute substantially to the physical characteristics of the PLSN. In contrast, intercalated structures result from polymer penetration and expansion of the original silicate crystallites to a thermodynamically defined equilibrium spacing^{13,14}. The primary particles (crystallites or tactoids) consist of well-ordered, alternating polymer/silicate layers with a repeat distance of a few nanometers and have been utilized as a model system to examine dynamics of ultra-confined polymer layers¹⁵.

In practice, many systems fall short of these idealized morphologies because fabrication of PLSNs requires physical mixing of polymer (or monomer) with micron-scale agglomerates comprised of hundreds of crystallites and thus thousands of layers. More commonly, intermediate states or mixed morphologies occur (Figure 1). These arise from inhomogeneities (size and composition) inherent in natural smectites, processing factors, or kinetic aspects associated with translational mobility of large aspect ratio plates in a viscoelastic medium. Although the greatest property enhancements are anticipated to arise from true 'exfoliated' morphologies, these 'intermediate' morphologies also contain nanoscopic, high aspect ratio particles (for example consisting of a mixture of individual layers and aggregates containing 3-5 layers) and have been demonstrated to provide property enhancements⁸. In general, realistic PLSN morphologies, whether thermodynamic or metastable, are comprised of a hierarchical structure with primary features associated with individual layers and secondary features associated with arrangement of individual layers or of stacks of layers.

As a first order demonstration of the complexity of PLSN morphologies, consider the packing of high aspect ratio plates. Due to the large anisotropy of the silicate layer (diameter/thickness ~ 20-500), thermodynamically stable structures with positional (smectic) and orientational (nematic) ordering, paralleling liquid crystalline phases observed for discotic mesogens, are anticipated for PLSNs. Although the silicate layers are not infinitely rigid, their phase behavior and dynamics can be semi-quantitatively understood using classical excluded-volume arguments. The critical concentration, c^* , (or volume fraction ϕ^*) in which excluded volume interactions impose orientational order on the layers, is proportional to the inverse of the aspect ratio of the layer. $c^* \sim 0.1-1$ vol% for commonly used layered silicates and is substantially less than conventional loadings. Additionally, high aspect ratio layers are easily oriented in shear flow. For a collection of oriented plates, the mean spacing between plates, d , will depend on concentration, ϕ , and plate thickness, $2H$ ($d \sim 2H \phi^{-1}$).

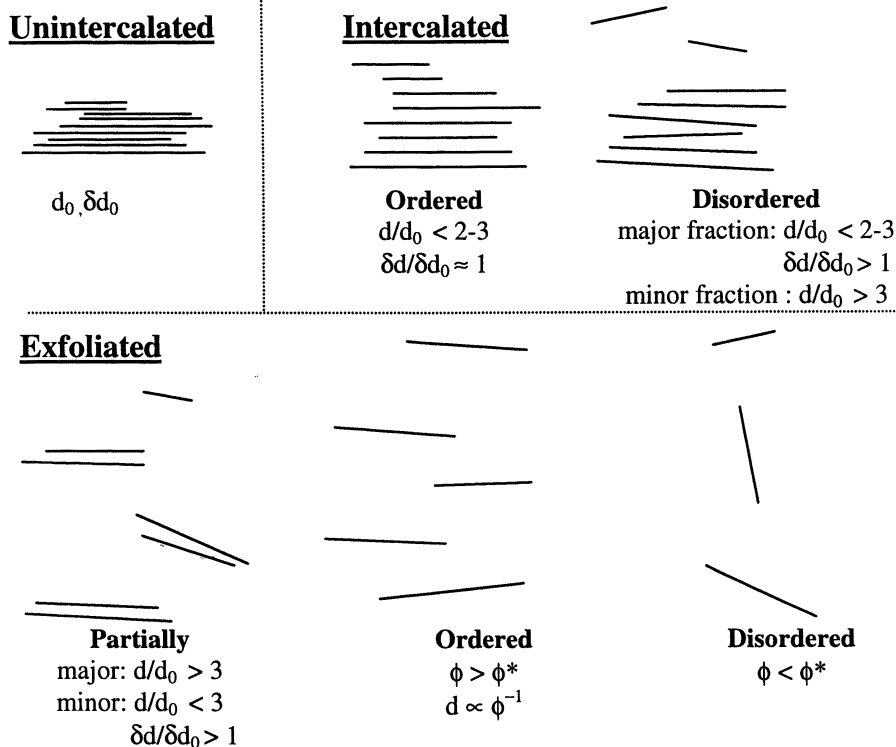


Figure 1. Idealized representations of various nanoscale arrangements of layered silicate in PLSN. Empty space represents polymer and dark lines represent layers oriented perpendicular to the surface of the page. d_0 and δd_0 are the initial spacing and variation in layer spacing of unintercalated crystallites, respectively. The classes can be differentiated based on the relative change and variation of layer spacing upon combination with polymer (d and δd), relative volume fraction of single layers and layer stacks, and the dependence of single layer separation on silicate volume fraction (ϕ). Differentiation ($d/d_0 > 3$) is qualitatively based on experimental observations.

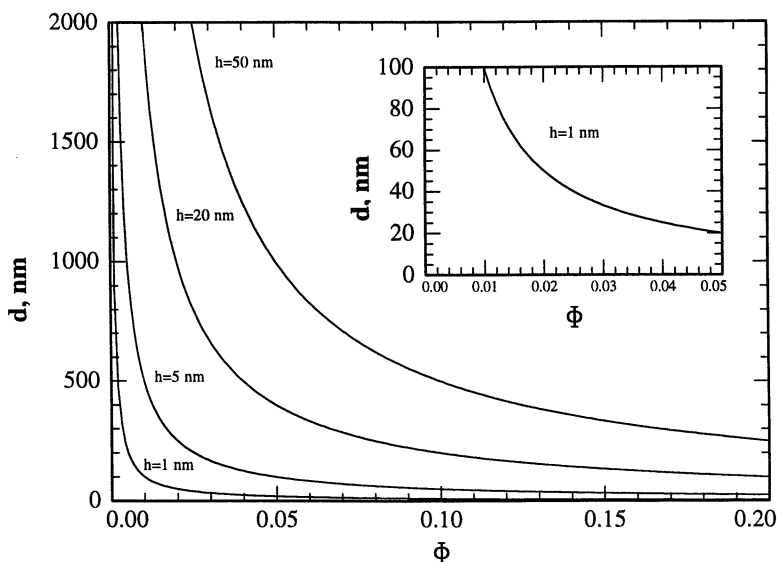


Figure 2. Equilibrium distance between uniformly aligned and dispersed plates at various volume fractions of plates, ϕ . Distance between plates decreases as ϕ^1 . Additionally for a given volume fraction, the distance between plates, d , decreases as the thickness per plate, h , decreases. Increasing the extent of disruption of the crystallite ($h=50$ nm is ~ 50 layers/crystallite; $h=1$ nm is individual layers) greatly decreases the spacing between plates. For a uniformly exfoliated structure ($h=1$ nm), the mean distance between plates is comparable to the radius of gyration of high molecular weight polymers at volume fractions less than 0.05 (inset).

Figure 2 summarizes mean layer spacing for various plate thickness and volume fractions. For example, uniform, parallel arrangement of 1 nm-thick layers at 5 vol% implies that all the matrix material is no more than 10 nm from an interface. This is on the same order as the radius of gyration of high-molecular weight polymers. The influence of preferred layer alignment and nanoscopic separation on the matrix will be especially pronounced for polymers with nanoscopic morphologies, such as block copolymers, liquid crystalline polymers and semi-crystalline polymers, or cross-linked matrices in which the large number of interfaces will alter the topology of the network.

In general, the complex processing-dependent morphologies of PLSNs complicate detailed understanding of the fundamental mechanisms for the property enhancements, especially since different properties are related to morphological features at different length scales (e.g. modulus related to 1-10 nm features (primary PLSN structure) where as toughness is related to 100-1000

nm features (secondary PLSN structure)). Furthermore, the presence of ordered arrangements of layers implies domain boundaries and defect structures exist, paralleling liquid crystal polymers and block copolymers. However, observation, characterization and determination of the importance of these defect-structures to the physical properties of PLSNs are yet to be performed.

X-ray Scattering

Traditionally, observation and detailed characterization of PLSN morphology has predominately relied on wide-angle x-ray diffraction in reflection geometry (WAXD) and transmission electron microscopy^{16,17}. WAXD is useful for rapid characterization, but it is limited in resolution (< 6 nm) and is very sensitive to surface alignment and preparation procedures at the low diffraction angles ($1^\circ < 2\theta < 5^\circ$) necessary for characterization of layered silicates.¹⁸ For example, Figure 3 demonstrates the sensitivity of the diffractogram to sample alignment. In addition, at these low angles, the structure in the near-surface region is preferentially sampled. The penetration depth of x-rays (Cu K_α) at $2\theta=2^\circ$ (4.4 nm) and 5° (1.77 nm) is 4.6 μm and 11.5 μm , respectively, for 100% layered silicate (mass absorption coefficient, $\mu/\rho \sim 50$ cm^2/g , density ~ 2.6 g/cm^3), and 0.46 mm and 11.5 mm, respectively, for 1% layered silicate in polymer (density ~ 1.0 g/cm^3)^{19,20}.

As the dimensions of the morphological features increase, absorption and complete external reflection prohibit the use of reflection geometries, such as Bragg-Brentano, to probe the bulk structure. However, small angle scattering geometries, such as Laue transmission, provide resolution on the order of a few 100 nm with x-ray and neutron radiation. Even larger structures are accessible with Boson-Hardt cameras or 6-circle goniometers. At these length scales, the atomic level details become lost as the dimension of the scattering entity increases. Thus, the scattered intensity can be envisioned as arising from the coherent interaction of incident radiation scattered from a uniform medium with a varying electron (x-ray) or nuclear (neutron) composition. The structure is represented by a continuous function describing the density of scattering entities, $\rho(\mathbf{r})$. Theoretical development and experimental details of scattering, both elastic and inelastic, by x-rays and neutrons are provided by Glater and Kratky²¹. Relative to the extensive use of powder diffraction, relatively few examples of small angle scattering studies of PLSNs are reported. Transmission geometry offers complementary results to these traditional techniques, allowing observation of polymer and inorganic structure as well as real-time observation of morphological change resulting from external stimuli (heat, shear, elongation, etc.). Detailed scattering models, connecting intensity distribution in reciprocal space to real space distribution of two-dimensional layers^{21,22} and core-shell

layered structures²³ are discussed in previous publications as well as their detailed application to PLSN and OLS dispersions²⁴⁻²⁶.

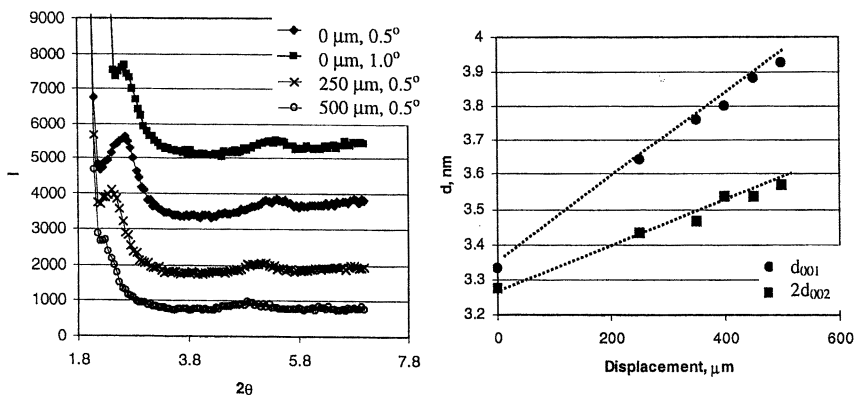


Figure 3. (left) Powder diffractograms from a smooth 1"x2" plaque of Epon 828/Cure W epoxy containing 1wt% Cloisite 30A (Southern Clay Products). The position of the basal reflections and the extent of background scattering depends on the source slits (0.5° and 1.0°) and sample alignment (sample surface 0, 250 and 500 μm removed from focal plane). (right) Summary of the apparent layer repeat distance determined from d_{001} and d_{002} reflections for controlled displacement of the sample surface away from the focal plane.

Results and Discussion

Layered Silicate Morphology

Three nylon 6 – montmorillonite nanocomposites will be discussed. NCH5 (and NCH2, Ube, Inc) are a 5 wt% (and 2wt%) layered silicate/nylon 6 nanocomposite formed through *in-situ* polymerization (detailed elsewhere)²⁷. NLS4 is a 4wt% layered silicate/nylon 6 nanocomposite formed through melt processing (detailed elsewhere)²⁸. Differences in synthesis route result in different polymer-silicate interactions. Ostensibly, approximately 30% and 50% of the poly(caprolactam) chains are end-tethered via an ionic interaction to the silicate surface in NCH2 and NCH5, respectively²⁷. In contrast, polymer-silicate

interactions in NLS4 are expected to be dominated by weak secondary interactions, such as *van der Waals* force²⁸. Note that because of the elevated temperatures ($T > 240^{\circ}\text{C}$) associated with processing of nylon 6 and the relatively low thermal-oxidative stability of nylon 6 and the alkyl ammonium surfactants in the OLSs²⁹, the actual structure of the polymer-layered silicate interface is not known.

Previous bright field electron microscopy^{11,28} indicate that the average diameter of the layers in NCH5 (160 ± 30 nm) are approximately twice as large as those in NLS4 (70 ± 20 nm). In general the mean layer spacing is between 35-45

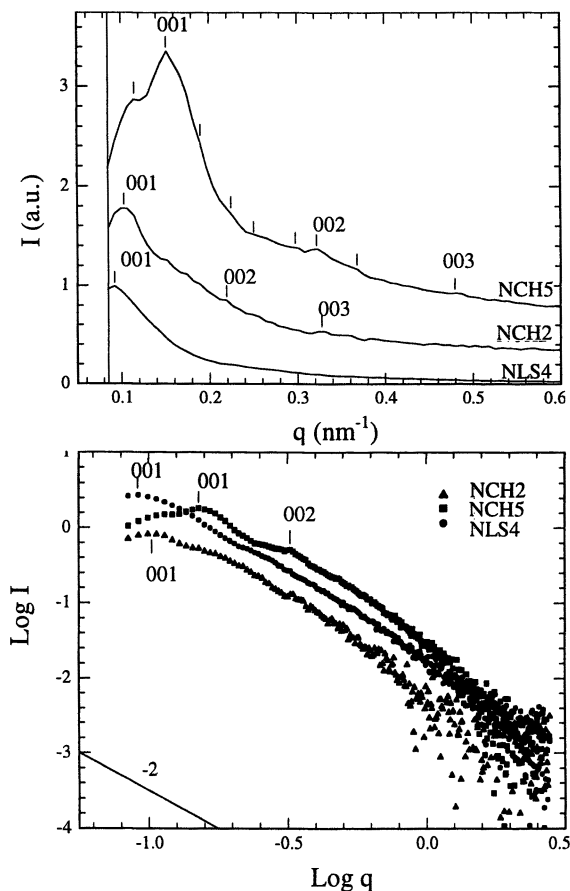


Figure 4. Small angle scattering data at 250°C for NCH5 (5 wt% layered silicate), NCH2 (2 wt% layered silicate) and NLS4 (4 wt% layered silicate). Curves in the I v. q plot (top) are vertically offset and the magnitudes are scaled by 0.54:1.17:1.00 for NLS4:NCH2:NCH5, respectively, for clarity. Data is unmodified in the $\log(I)$ v. $\log(q)$ plot (bottom).

nm in NCH5 and 40-60 nm in NLS4. Quantification of layer distribution from the micrographs is hampered because the image is representative of only an exceedingly small portion of the sample and is the projection of a finite thickness. For example, higher magnification micrographs of NLS4 indicate that layer distribution is not uniform - a small fraction of aggregates containing 2 – 3 layers are observable.

Figure 4 summarizes the background-corrected small angle scattering data at 250°C for the PLSNs³⁰. Small-angle scattering data of neat poly(caprolactam) (Nyl6) at 250°C is commensurate to the background signal. Since 250°C is greater than the melting point of poly(caprolactam) crystallites, the scattering is exclusively associated with the silicate layers dispersed in an isotropic polymer melt. The absence of a strong basal reflection ($q \sim 2 \text{ nm}^{-1}$) indicates a disruption of the original stacking of the silicate layers and is generally indicative of an exfoliated nanocomposite.

Additional details are observable in the scattering pattern beyond the distribution of the original stacking of the silicate layers, however. In this region of reciprocal space, the montmorillonite layers can be adequately approximated as very thin plates (R , radius $\gg 2H$, thickness). The single particle scattering function of an isolated, thin plate is proportional to q^{-2} for $q < H^{-1}$ and exhibits a Guinier region around $qH = 1$ in which the q -dependence increases. Detailed discussion of scattering theory of plates and layered silicates is beyond the scope of this paper, but can be found in references 18, 21, 22 and 25. In the intermediate q -range ($0.4 < q < 2.0 \text{ nm}^{-1}$), removed from the effects of interparticle correlations, the PLSNs exhibit q -dependence around -2.1 , in agreement with plate-like scattering. Additionally, Bragg reflections are observable. For NCH5, a prominent reflection at $q = 0.158 \text{ nm}^{-1}$ and associated order reflections ($q = 0.322 \text{ nm}^{-1}$ ($n=2$); $q = 0.480 \text{ nm}^{-1}$ ($n=3$)) indicate a superstructure with a length of 39.8 nm exists. These results are consistent with previous TEM micrographs (NCH5: 35-45 nm)^{11,28}. Estimation of mean layer-layer spacing, d , (Figure 2) for a uniform nematic-like arrangement of layers at 5 wt% (2.2 vol%) is approximately 45 nm, also in reasonable agreement with the observed reflections. Similarly for NCH2, a prominent reflection at $q = 0.105 \text{ nm}^{-1}$ and associated order reflections ($q = 0.220 \text{ nm}^{-1}$ ($n=2$); $q = 0.320 \text{ nm}^{-1}$ ($n=3$)) indicate a superstructure with a length of 59.8 nm exists.

Reflections very close to the beam stop for both NCH5 and NLS4 ($q = 0.114$ and 0.091 nm^{-1} , respectively) persist after data correction, indicating potential structure at even larger distances (52.5 nm and 69.0 nm respectively). Most surprising of all is the ability to index minor features in NCH5, with signal to noise a few times greater than background, to that anticipated for hexagonal packing of the layers. This higher level spatial correlation between layers was predicted by Balazs et al. at volume fractions between 5 and 40%¹⁴. Additional weak reflections, which are not easily indexed, are also apparent (Figure 4).

The effective aluminosilicate layer thickness can be determined from the high q scattering. For a thin plate, the scattering function at high q asymptotically approaches: $P(q) = 2/(q^2 R^2) \exp(-q^2 H^2 / 3)^{21}$. Hence the effective thickness of the plate (from an x-ray scattering perspective) can be determined from the slope of a plot of $\ln(I(q) q^2)$ versus q^2 . Linear least-square fit to the data in a range larger than the layer thickness yet smaller than layer-layer correlations ($0.1 < q^2 < 1.5 \text{ nm}^{-2}$; $19.8 > d > 5.1 \text{ nm}$) yields an effective layer thickness of 2.7 and 2.3 nm for NCH5 and NLS4 respectively. This is slightly greater than anticipated for an aluminosilicate layer (0.96 nm) and may reflect differences in the interfacial region surrounding the layer. Additional studies are necessary.

Finally, the relative magnitude of the Bragg reflections and total scattered intensity (invariant) varied with sample processing history and even beam location (beam size $\sim 300 \mu\text{m}$) on the sample. For example, the invariant of NLS4 is twice as large as that for NCH5 even though there is less silicate in NLS4. These observations indicate micron or larger domains exist with varying concentration or orientation of the layers parallel to the sample surface (and perpendicular to the incident x-rays). Domains of different orientation may be separated by orientational defects such as observed in liquid crystal polymers and block co polymers. Preferred layer orientation in the extruded pellets has been noted previously.¹⁰ Furthermore, superposition of different layer organization in NCH5 indicates inhomogeneities in the initial concentration have not been equilibrated by processing and may be hindered by defect structures and boundaries. Determination of the translational and rotational diffusion rates of the layers is necessary to understand relaxation and homogenization of these structures in the melt.

Polymer Crystallite Morphology

The 20-60 nm separation of layers results in a bulk material in which crystallization of the poly(caprolactam) is confined to nanoscopic dimensions. This confinement along with polymer-silicate interactions will impact the equilibrium crystal phase and mesoscopic arrangement of crystal lamellae.

Small angle and wide-angle x-ray scattering profiles of quenched PLSNs and pure polymer (liquid- N_2 immersion from $T=250^\circ\text{C}$) are shown in Figure 5. The peaks at $2\theta = 17.4$ and 20.5 in the Nyl6 WAXS profile indicate that the pure nylon 6 crystallized predominantly into the α crystalline phase; whereas, the peaks at $2\theta = 8.6$ and 18.2 for the NCH5 and NLS4 profiles indicate that the nanocomposite samples predominantly contain the γ phase. This is consistent with previous observations^{10,31}. (Note, unequivocal identification of the γ -phase

requires resolution of the 0140 reflection, which is beyond the collected data range³².)

For pure nylon 6, the α crystalline phase is thermodynamically stable and consists of sheets of hydrogen bonded chains formed between anti-parallel chains. The γ crystalline phase is metastable and consists of random hydrogen bonding between parallel chains³². Ito et al. observed that the mechanical properties of the phases, as well as the temperature dependence, was different for the two phases³³. The α -phase exhibits a higher modulus below T_g but a more rapid decrease above T_g than the γ -phase. This implies that the γ -phase has a higher heat distortion temperature. Thus, the relative fraction of these crystalline phases is expected to impact the mechanical properties of the PLSN.

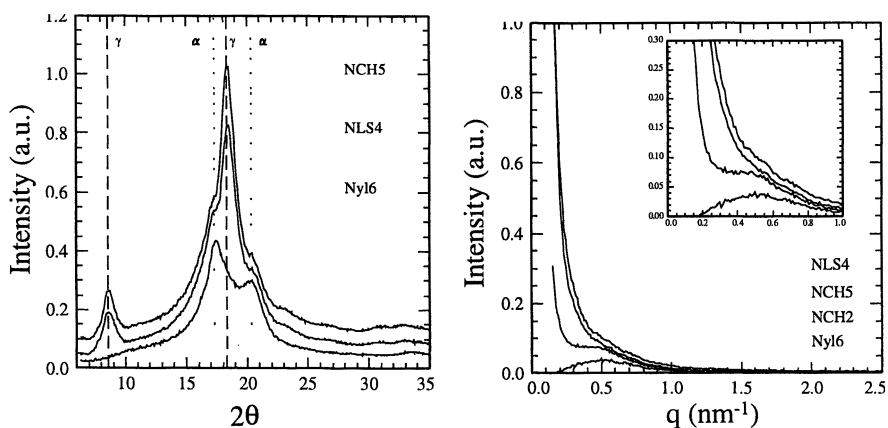
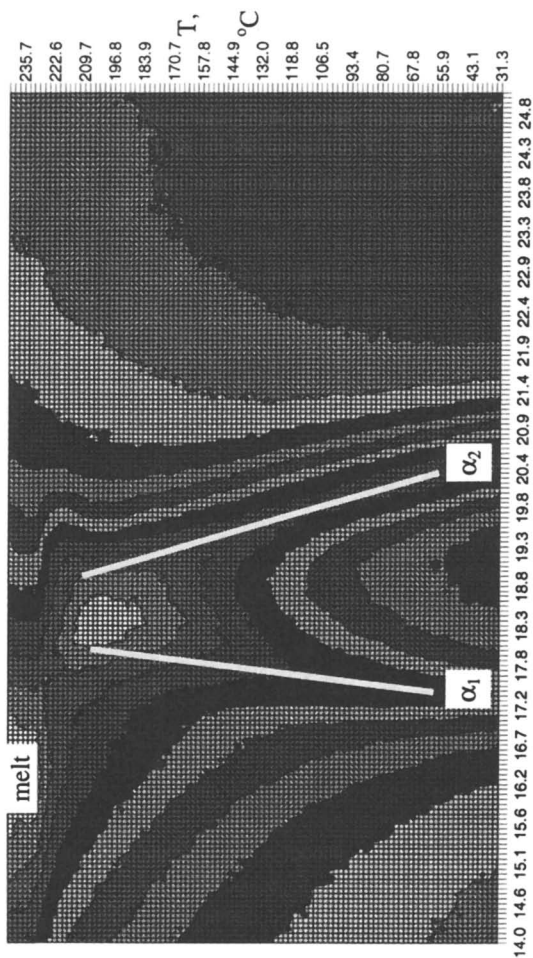


Figure 5. WAXS (left) and SAXS (right) profiles of the quenched pure nylon 6 and nylon 6 nanocomposites. The curves are vertically offset for clarity.

With regard to secondary (mesostructure), the SAXS profile for Nyl6 shows the presence of lamellar crystallites with a periodic spacing of 9.95 nm. In contrast, the profiles for the nanocomposites show a change in the intensity of this reflection with increased concentration of dispersed layers. In the case of tethered polymer chains (NCH2, NCH5), the invariant, lamella spacing and scattering intensity ($q=0.42$ nm⁻¹) decreases with increased addition of layered silicate, indicating that the crystalline material is not arranged in ordered stacks but is disordered. Opposite trends are observed for relatively weak polymer-silicate interactions (NLS4) in which the crystalline regions substantially increase in thickness¹¹. Recent isothermal and nonisothermal crystallization



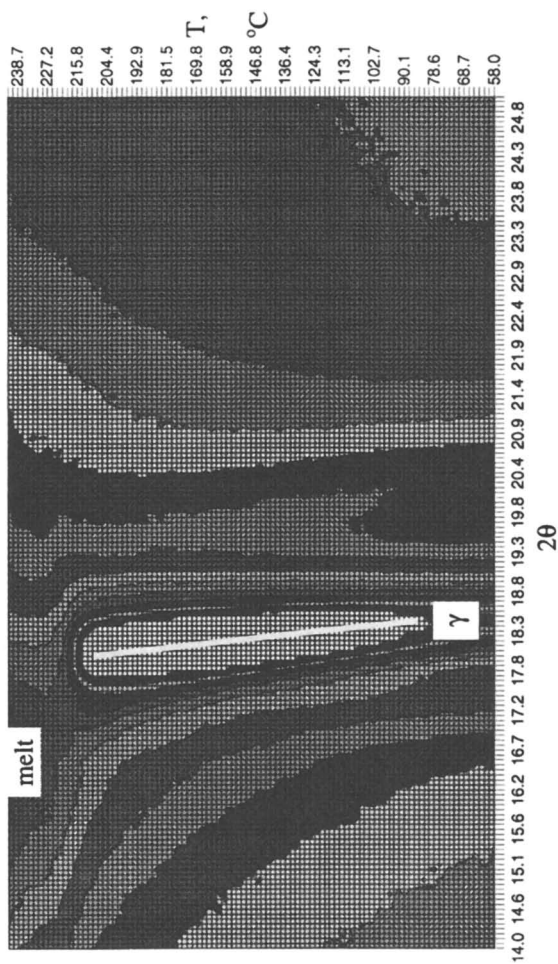


Figure 6. Contour intensity plots of the wide-angle x-ray diffraction patterns ($14 < 2\theta < 24$) collected between 40°C and 240°C (heating at $5^\circ\text{C}/\text{min}$) of pure nylon 6 (top) and NCH5 (bottom).

studies indicate that these mesoscale features are highly process history dependent¹². Optical microscopy indicates that the spherulitic texture of pure nylon 6 is disrupted by the presence of the dispersed silicate layers, producing an axialitic texture. Since the fracture behavior of semi-crystalline polymers is intimately related to the spherulitic texture, the extent to which the lamella organization is altered should impact the mechanism of crack propagation and thus fracture properties of these PLSNs.

Since the phase and arrangement of the polymer crystallites is altered by the presence of the layers, it is important to understand the process by which the morphology develops so as to optimize processing. Figure 6 shows contour intensity plots of the wide-angle diffraction patterns collected between 40°C and 240°C (heating at 5°C/min) of pure nylon 6 and NCH5. For nylon 6 at room temperature, two peaks correspond to the 200 and 002,202 reflections ($2\theta = 17.4$ and 20.5 , respectively) of the α -phase³². As temperature increases, the larger thermal expansion along the 002 direction results in the two peaks merging at the so-called Brill-transition around 150°C. Subsequent melting of the crystallites, occurring around 220°C, results in amorphous polymer scattering ($2\theta = 16.3$). These results are in good agreement with previous studies of phase transition of nylon 6³².

In contrast, one peak corresponding to the 001,200 reflection ($2\theta = 18.2$) of γ -phase nylon 6³² is prominent at room temperature for NCH5. Increasing temperature results in a uniform shift to lower scattering angles (larger lattice spacing) associated with thermal expansion of the lattice. The reflection broadens with increased temperature. Additionally, at temperatures greater than 80°C, new reflections appear corresponding to the development or transformation of a fraction of polymer to the α -phase. These new α -phase-crystallites transform, as observed in the pure nylon 6, at a temperature greater than 150°C to an elevated temperature phase in which crystallographic directions perpendicular to the chain axis are comparable. This phenomenon occurs in all the nylon 6 nanocomposites (NCH5, NCH2 and NLS4) and is more prominent for low volume fraction of silicate layers (NCH2) and weaker polymer-silicate interactions (NLS4). This implies that the thermal process history can produce semi-crystallite PLSNs with the same volume fraction of layered silicate but different crystallite morphologies and thus different mechanical properties. Additionally, evolution of the crystallite structure during elevated temperature use may occur. The detailed process of crystallization and its impact on physical properties is currently being examined. Note that these studies complement recent solid-state NMR studies on the room temperature polymer crystal structure in these nylon 6 nanocomposites²⁹.

Conclusion

The incorporation of layered silicates in the polymer produces complex hierarchical morphologies consisting of a primary structure associated with the individual layers and secondary structures associated with mesoscopic distribution and arrangement of the layers. In general the morphologies are more complex than the traditional intercalated or exfoliated descriptors and more commonly consist of a mixture of layer arrangements. For the nylon 6 nanocomposite system, a secondary structure associated with long-range correlation between the layers occurs, producing an ordered exfoliated morphology. The mesoscopic dimensions of these layer arrangements have substantial impact on the crystalline regions of a semi-crystalline polymer such as nylon 6, which consist of structural features (crystal lamella) of comparable length scales. The crystal phase, lamella structure, and temperature stability depend on layer concentration and polymer-silicate interactions.

Fundamentally, this study implies that not only is the distribution of the inorganic necessary to characterize but also its impact on the structure, dynamics and phase behavior of the matrix polymer is critical to understand. Additionally, the ultralarge internal interfacial area per volume implies detailed understanding of the structure and chemistry of the polymer-inorganic interface is crucial. Thus, understanding the fundamental origin of property enhancements in PLSN requires detailed characterization of silicate distribution as well as its influences on polymer morphology and the subsequent influence of processing (time, temperature and shear) on both.

Acknowledgements

The authors would like to thank Z-G. Wang, B. S. Hsiao, R. Krishnamoorti and F. Yeh for technical contributions and acknowledge partial financial support by the United States Air Force Office of Scientific Research. SAXS and WAXS were performed at the National Synchrotron Light Source, Brookhaven National Laboratory (X27C).

References

1. Kojima, Y.; Usuki, A.; Kawasumi, M.; Okada, O.; Fukushima, Y.; Kurachi, T.; Kamigaito, O. *J. Mater. Res.* **1993**, *8*, 1185.
2. Ke, Y.; Long, C.; Qi, Z. *J. Appl. Polym. Sci.* **1999**, *71*, 1139.
3. Messersmith, P.B.; Giannelis, E.P. *J. Polym. Sci. Part A: Polym. Chem.* **1995**, *33*, 1047.

4. Akelah, A.; Moet, A. *J. Mater. Sci.* **1996**, *31*, 3589.
5. Yano, K.; Usuki, A.; Kurachi, T.; Kamigaito, O. *J. Polym. Sci. Part A: Polym. Chem.* **1993**, *31*, 2493.
6. Gilman, J.W.; Kashiwagi, T.; Lichtenham, J.D. *Int. SAMPE Symp. Proc., Conf. Proc. Of 1997 Meeting*, **1997**, *42*, 1078.
7. Giannelis, E.P. *Adv. Mater.* **1996**, *8*, 29. Giannelis, E.P.; Krishnamoorti, R. Manias, E. *Adv. Poly. Sci.* **1999**, *138*, 108.
8. LeBaron, P.C.; Wang, Z.; Pinnavaia, T.J. *Appl. Clay Sci.* **1999**, *15*, 11.
9. Alexandre, M.; Dubois, P. *Mater. Sci. Eng.* **2000**, *28*, 1.
10. Kojima, Y.; Usuki, A.; Kawasumi, M.; Okada, A. Kurauchi, T.; Kamigaito, O.; Kaji, K. *J. Poly. Sci.: Part B: Polym Phys.* **1995**, *33*, 1039. Kojima, Y.; Usuki, A.; Kawasumi, M.; Okada, A. Kurauchi, T.; Kamigaito, O.; Kaji, K. *J. Poly. Sci.: Part B: Polym Phys.* **1994**, *32*, 625.
11. Vaia, R.A., D. Lincoln, Z-G. Wang, B. S. Hsiao *Polymer*, **2001**, *42*, 1621.
12. Vaia, R.A., D. Lincoln, Z-G. Wang, B. S. Hsiao, R. Krishnamoorti. *Polymer*, **2001**, submitted.
13. Vaia, R.A.; Giannelis, E.P. *Macromol.* **1997**, *30*, 7990.
14. Ginzburg, V.V. Balazs, A.C. *Macromol.*, **1999**, *32*, 5681. Balazs, A.C. et al. *Acc. Chem. Res.* **1999**, *32*, 651.
15. Krishnamoorti, R.; Vaia, R.A.; Giannelis, E.P. *Chem. Mater*, **1996**, *8*, 1728.
16. Vaia, R.A.; Jandt, K.D.; Kramer, E.J.; Giannelis, E.P. *Chem. Mater.* **1996**, *8*, 2628.
17. Morgan, A.B.; Gilman, J.W.; Jackson, C.L. *ACS PMSE Preprints*, **2000**, *82*, 270.
18. Bish D.L.; Post, J.E. eds. *Modern Powder Diffraction, Reviews in Mineralogy, Volume 20*, Mineralogical Society of America, Washinton D.C. 1989.
19. Brindley; G.W.; Brown, G. *Crystal Structure of Clay Minerals and their X-ray Identification*. Mineralogical Society, London, 1980, p. 310.
20. Cullity, B.D. *Elements of X-ray Diffraction*, Addison-Wesley, Reading, MA, 1978. p. 135.
21. Glatter, O.; Kratky, O. *Small Angle X-ray Scattering*, Academic Press, New York, 1982.
22. Drits, V.A.; Tchoubar, C. *X-ray Diffraction by Disordered Lamellar Structures*, Springer-Verlag, New York 1990.
23. Bongiovanni, R.; O'Hewill, R.H.; Rennie, A.R. *Progress in Colloid Polym. Sci.* **1991**, *84*, 299.
24. Ho, D.L; Briber, R.M.; Glinka, C.J. *ACS PMSE Preprint*, **2000**, *82*, 268.
25. Vaia, R.A.; Lui, W *J. Chem. Phys.* submitted **2001**.
26. Medellin-Rodriguez, F.J.; Hsiao, B.S.; Chu, B. Vaia, R.A.; Phillips, S.; Burger, C. submitted *Polymer*, **2001**.

27. Usuki, A. et al. *J. Mater. Res.* **1993**, *8*, 1179. Okada, A.; Usuki, A. *Mater. Sci. Eng: C*, **1995**, *3*, 109.
28. Vaia, R.A.; Price, G.; Ruth, P.N.; Nguyen, H.T.; Lichtenhan, J. *Applied Clay Sci.*, **1999**, *15*, 67.
29. Xie, W.; Goa, Z.; Pan, W-P.; Vaia, R.A.; Hunter, D.; Singh, A. *ACS PMSE Preprint*, **2000**, *82*, 284.
30. Small angle x-ray scattering (SAXS) and wide-angle x-ray scattering (WAXS) were performed at the National Synchrotron Light Source, Brookhaven National Laboratory (X27C, $\lambda = 1.307 \text{ \AA}$, $\Delta E/E = 0.011$) using an EMBL detector [Rapp,G.; Gabriel, A.; Dosiere, M.; Koch, M.H. *J. Nuc. Inst. Meth. Phys. Res.: A*, **1995**, *357*, 178]. Spectra were corrected for sample absorption, background scatter and incident beam fluctuation.
31. Kojima, Y.; Matsuoka, T.; Takahashi, H.; Kurachi, T. *J. Appl. Polym. Sci.* **1994**, *51*, 683.
32. Murthy, N.S. *Polym. Comm.* **1991**, *32*, 301. Murthy, N.S.; Curran, S.A.; Aharoni, S.M.; Minor, H., *Macromolecules*, **1991**, *24*, 3215.
33. Ito, M.; Mizuochi, K.; Kanamoto, T. *Polymer*, **1998**, *39*, 4593.
34. Mathias, L.J.; Davis, R.D.; Jarrett, W.L. *Macromol.* **1999**, *32*, 7958.

Chapter 10

Solution and Solid-State NMR Spectroscopy of Nylon 6–Montmorillonite Clay Nanocomposites

Rick D. Davis¹, William L. Jarrett, and Lon J. Mathias*

School of Polymers and High Performance Materials, University of Southern Mississippi, Hattiesburg, MS 39406–0076

¹Current address: 13420 Daventry Way, Apartment D, Germantown, MD 20874

Nylon 6/montmorillonite clay nanocomposites were characterized by solution and solid state NMR spectroscopy. Solution ¹³C NMR spectroscopy indicates nylon 6 molecular weight is controlled by the concentration of intercalate (ammonium salt of 12-aminolauric acid) and all nylon 6 amine end-groups are protonated and presumably bound to the surface of the clay sheets. It is believed that this interaction between the clay sheets and the polymer chains is what promotes γ crystallite formation over α crystallite. Solid state ¹⁵N CP/MAS NMR spectroscopy indicates that the nanocomposite thermal history dictates the ratio and type of crystallites formed. Solid state ²H NMR spectral and T₁ results are preliminary but indicate the nanocomposite containing component is unlike the amorphous and crystalline domains of nylon 6.

Polymer/clay nanocomposites obtained from surface-treated montmorillonite clay have unexpectedly high property enhancements at low clay content (1-5 wt-%). The improved properties must result from interactions between high surface area clay particles and the polymer. The nature, origin and strength of these interactions are not well understood. In an attempt to better understand the interaction between exfoliated clay and nylon 6, we have applied solution ¹³C NMR spectroscopy, solid state ¹⁵N CP/MAS NMR and solid state ²H NMR spectroscopy to characterization of typical nylon 6/montmorillonite clay

nanocomposites. Preliminary work and experimental details were published previously.^{1,2}

Results and Discussion of NMR Analysis

Solution ¹³C NMR Spectroscopy

Solution ¹³C NMR peak assignments of nylon 6/montmorillonite clay nanocomposites were made based on previous publications.^{3,4,5} A solution ¹³C NMR spectrum of a nylon 6/clay nanocomposite is provided in Figure 1 (aliphatic region) and Figure 2 (carbonyl region) with complete peak assignments listed in Table I and structure illustrations provided in Figure 3. The spectra in Figures 1 and 2 are expanded with the trans-amide conformer peaks off scale to show end-group, ε-caprolactam and cis-amide conformer (denoted with “cis”) peaks. Number average molecular weight (M_n) and amounts of residual ε-caprolactam, acid and amine end-groups, and cis-amide conformers were calculated using relative peak intensities from the solution ¹³C NMR spectra.^{3,4,6} Peaks used for calculations were the CH₂'s in nylon 6 that were α to amine end-groups, α to acid end-groups, α to the nitrogen of cis-amide linkages, and the CH₂ in residual ε-caprolactam that is α to the nitrogen of the amide linkage. Calculated values were ca 5 wt-% residual caprolactam, 1.7 wt-% cis-amide conformers, 1.2 wt-% acid end-groups and 19,100 g/mol molecular weight. These values are similar to those observed for commercial nylon 6.^{3,4} Interestingly, no neutral amine end-groups were observed in the solution ¹³C NMR nanocomposite spectra, apparently because most or all of amine end-groups were protonated (discussed below).

Taking into account the residual ε-caprolactam, a theoretical molecular weight of 20,000 g/mol was calculated based on the assumption that every intercalate (protonated 12-aminolauric acid) bound to the clay surface was available as an initiating species; i.e., one intercalate incorporated per polymer molecule. The theoretical molecular weight was very close to the actual value estimated by NMR spectroscopy (19,100 g/mol), suggesting one intercalate is incorporated into every nylon 6 chain and most or all amine end-groups are protonated. Consistent with this, a peak at 38.6 ppm was observed representing the CH₂ alpha to a protonated amine end-group (ωNH_3^+), based on previous work.³ In fact, when a trace of acid was added to a commercial nylon 6 NMR solution, the amine $\omega\text{-CH}_2$ peak moved upfield from 39.6 ppm to 38.6 ppm, confirming that the 38.6 ppm peak is due to the $\omega\text{-CH}_2$ of protonated amine end-groups. Moreover, the addition of trace acid to the commercial nylon 6 NMR sample did not alter the chemical shift of the $\alpha\text{-CH}_2$ peak of acid end-groups, also consistent with peak position assignments observed in Figure 1.

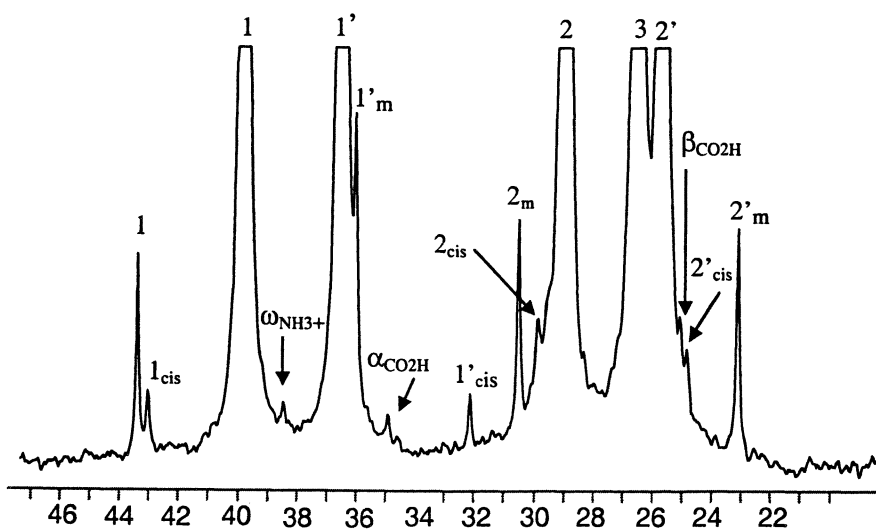


Figure 1. Solution ^{13}C NMR spectra of a nylon 6/clay nanocomposite - expansion of aliphatic region (peak assignments as indicated in Figure 3).

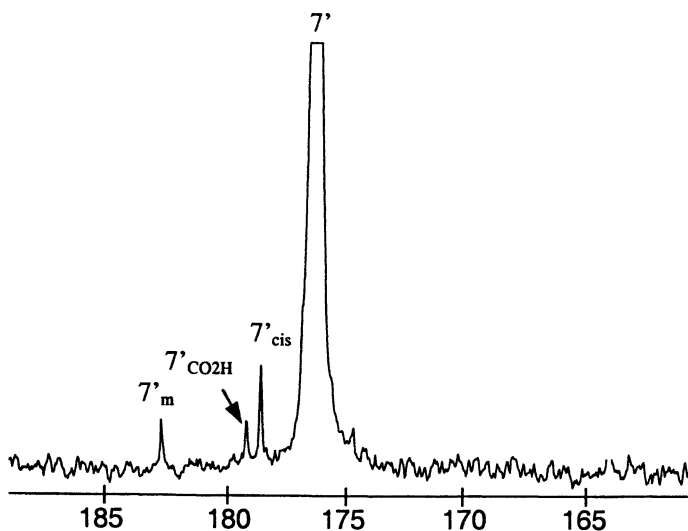


Figure 2. Solution ^{13}C NMR spectra of a nylon 6/clay nanocomposite - expansion of carbonyl region (peak assignments as indicated in Figure 3).

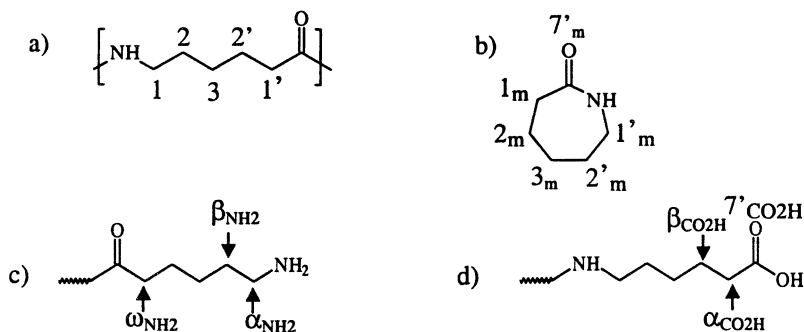


Figure 3. Chemical structure and ^{13}C NMR identifications of a) nylon 6, b) ϵ -caprolactam, c) amine end-group and d) acid end-group.

Table I. Solution ^{13}C NMR chemical shift values of a nylon 6/clay nanocomposite and residual ϵ -caprolactam.

	Nylon 6/Clay Nanocomposite		Residual ϵ -Caprolactam
	<i>trans</i>	<i>cis</i>	
main chain			
1	39.85	43.12	43.40
2	28.81	29.76	30.52
3	26.39	*	*
1'	36.47	32.03	35.70
2'	25.61	24.77	23.12
7'	176.41	178.88	183.44
end groups			
α _{NH2}	not observed		*
β _{NH2}	not observed		*
ω _{NH2}	not observed		*
ω _{NH3+}	38.56		*
α _{CO2H}	35.95		*
β _{CO2H}	24.87		*
7' _{CO2H}	179.11		*
M _n (g/mol)	19,100		*

Solid State ^{15}N NMR Spectroscopy

Solid state ^{15}N CP/MAS NMR spectra of nylon 6 and a nylon 6/montmorillonite clay nanocomposite are provided in Figure 4. Peak

assignments are based on values reported in several papers.^{7,8,9,10,11,12,13} The solid state ^{15}N NMR nylon 6 spectrum, provided in Figure 4a, contains one sharp peak at 84.9 ppm (α crystalline phase) and a significant broad absorption between 77 ppm and 95 ppm (amorphous phase). The nanocomposite spectra, provided in Figures 4b and 4c, each exhibit sharp peaks at 89.3 ppm (γ crystalline phase) and 84.9 ppm (α crystalline phase), and a broad peak spanning this range (amorphous phase). The preferential formation of γ crystallites in nylon 6/clay nanocomposites has been observed by other researchers^{14,15,16,17,18,19,20} and verified in this nanocomposite by x-ray diffraction and thermal analysis. Since α crystallinity is normally thermodynamically favored while γ crystallinity is kinetically favored, nylon 6 crystal structure is dependent on its thermal history and processing; i.e., quenching will result in a small fraction of γ crystallinity. Nylon 6 contained only α crystallites when analyzed as synthesized and after annealing, as shown in Figure 4a and d, respectively. The observation of both α and γ crystallites in the nanocomposite and reprecipitated nanocomposite suggests that the high surface area clay particles facilitates or stabilizes the formation of γ crystallites through a thermodynamic stabilization or enhances kinetic formation through per-ordering of the adjacent chains on the clay surface (see below).

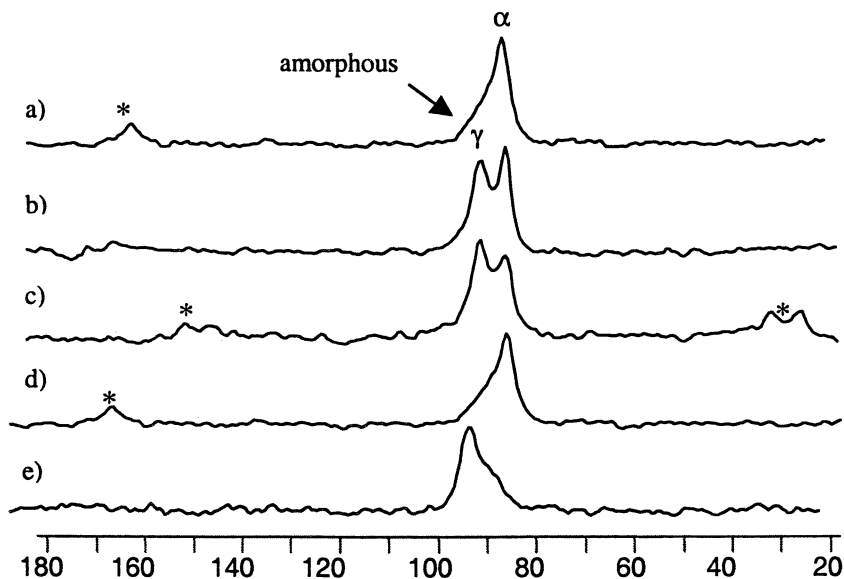


Figure 4. Solid state ^{15}N CP/MAS NMR spectra of a) nylon 6, b) nylon 6/clay nanocomposite, c) reprecipitated nylon 6/clay nanocomposite, d) annealed nylon 6 and e) annealed nylon 6/clay nanocomposite; “*” indicates spinning side-bands.

Annealed solid state ^{15}N CP/MAS NMR spectra of nylon 6 and nanocomposite are provided in Figure 4d and 4e, respectively. Both materials were annealed in the melt under high vacuum then slowly cooled at ca $5\text{ }^\circ\text{C}/\text{min}$, conditions that generate α crystallites in commercial nylon 6 as shown in Figure 4d. These spectra revealed that under these conditions, the nanocomposite contained only γ crystallites, as indicated by a loss of the 84.9 ppm peak, as shown in Figures 4b, 4c and 4d. In other words, annealing of nylon 6 in the presence of clay preferentially leads to the normally kinetic favored γ crystalline phases. Two possibilities exist, either polymer/clay surface interactions induce the γ crystalline phases, or these interactions change the thermodynamics of the system such that the γ crystalline phase is more stable even at nanometer distances from the clay surface. The latter is unlikely. Thus it is believed that kinetics is the controlling factor. That is, because the amine end-groups are tightly bound to the clay surface, but not arrayed on the surface at an interchain distance that allows formation of the layered hydrogen-bonded sheets of the α crystalline phase, the γ crystalline phase is generated by default as the most rapidly formed crystal phase. What we can not explain is why, even on extended annealing, the γ phase is not converted completely to the α phase. This is in sharp contrast to all literature we are aware of related to nylon 6 crystallinity.

Solid State ^2H NMR Spectroscopy

Nylon 6- d_4 , deuterated at the CH_2 's α to the amide linkages, was in-situ polymerized from ϵ -caprolactam- d_4 in the presence of 5 wt-% montmorillonite clay (treated with the ammonium salt of 12-aminolauric acid) producing a nylon 6- d_4 /clay nanocomposite. ϵ -Caprolactam- d_4 was synthesized in the laboratory from cyclohexanone using $^2\text{H}_2\text{O}$ and $^2\text{H}_2\text{SO}_4$.²¹ Solid state ^2H NMR spectral and T_1 studies of a deuterated nanocomposite revealed a three component system, in contrast to the two component system observed in nylon 6- d_4 . Both materials had the same thermal history, polymerized at $260\text{ }^\circ\text{C}$ under nitrogen atmosphere and quenched in water. Thus the differences in T_1 values and number of components are attributed to the presence of clay. Conclusions or interpretation of these results is premature. Nevertheless, a difference in local mobilities due to the presence of clay was clearly observed and is continuing to be probed by solid state ^2H NMR spectroscopy.

Implication of NMR Spectroscopy to Model Possibilities

How γ crystalline phases develop or propagate at large distances away from the surface, and how this overall morphology so drastically effects thermal and physical properties, are questions we are attempting to answer using a variety

of solution and solid state NMR methods. It is clear, however, that basic changes in the molecular organization induced by the clay surface dramatically alters the macroscopic properties. Figure 5 is our perception of a nylon 6/clay nanocomposite based on our NMR results.

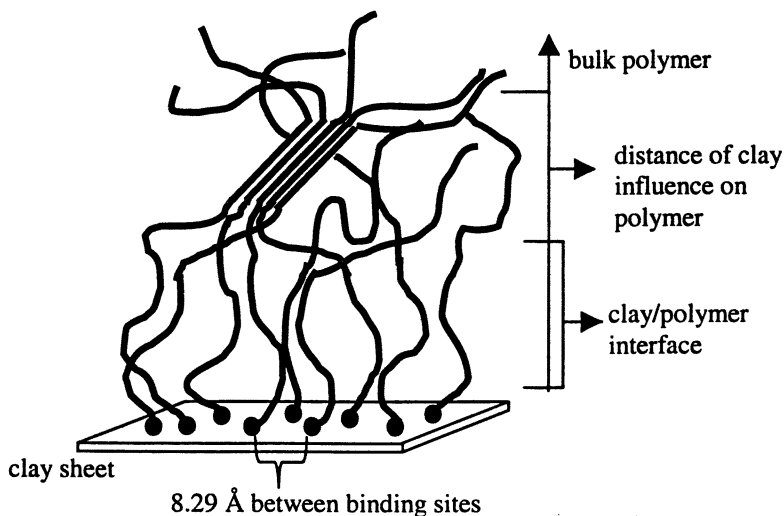


Figure 5. A slice of a nylon 6/clay nanocomposite illustrating polymer end-group binding, the clay/polymer interface and the changeable distance that the clay can influence polymer microstructure.

Based on the theoretical M_n calculated from the known intercalate concentration and the actual M_n calculated from the solution ^{13}C NMR analysis, it is concluded that each intercalate is incorporated into a nylon 6 polymer chain of the nanocomposite, perhaps as the initiating species. In addition, each nylon 6 amine end-group in the nanocomposite is protonated, as indicated by the $\omega_{\text{NH}_3^+}$ peak (38.56 ppm) in the solution ^{13}C NMR spectra, and most likely is bound to the surface of the negatively charged clay platelets. The distance between surface bound polymer chains (d) was calculated as 8.29 Å, using a cation ion exchange capacity (CEC) value of 119 meq/100 g montmorillonite clay, as reported on the MSDS,²² and the following equation.²³

$$[F * a_0 b_0 / 2\pi \text{CEC}]^5 / 2 = d \text{ (Å)}$$

Where $a_0 b_0$ is 46.5 Å and F is the formula weight of a montmorillonite repeat unit adjusted to give a CEC value in units of meq/100 g, 278 mol $(\text{Si,Al})_4\text{O}_{10}/\text{g}$. Both are constant values for montmorillonite clay. The distance of 8.29 Å between bound nylon 6 chains is approximately 2.6 times larger than the distance between

nylon 6 chains in the γ or α crystalline phases (~ 3.1 Å).²⁴ As a result, crystallization should not occur at the clay surface and a new nylon 6 phase is formed, the clay/polymer *interphase*. The clay/polymer *interphase* contains a single clay sheet with polymer chains isotropically oriented away from the clay surface parallel to each other. The orientation of polymer chains is attributed to the protonated nylon 6 amine end-groups being ionically bound to the clay surface.

At some distance from the clay surface, crystallization can occur and with the polymer chains oriented parallel to each other, the γ crystalline structure is formed. Solid state ¹⁵N CP/MAS NMR spectroscopy reveals that the as-synthesized nylon 6 in the nanocomposite forms approximately a 1:1 ratio of α to γ crystalline phases, spectra provided in Figures 4b and 4c. The observation of both crystalline structures indicates that in the nanocomposite, α crystallinity is still thermodynamically preferred, and under normal processing conditions, the influence of clay on polymer microstructure drops off at some distance from the clay surface. Shown by the spectra in Figures 4e and 4a, respectively, the annealed nanocomposite contained only γ crystallites and the annealed nylon 6 consisted of only α crystallites. This indicates the distance from the clay surface that the clay can influence the polymer microstructure can be controlled or enhanced by the samples thermal history. The ability to control the polymer microstructure has significant implications for maximizing the physical property enhancement inherent to nanocomposites. These findings of polymer chain-end fixation as a crucial organizing force has broad impact on understanding nanocomposite behavior. Most important, it points to ways of enhancing the effect of clay reinforcing in other polymer systems.

References

1. Davis, R.D.; Jarrett, W.L.; Mathias, L.J.; Observation of α and γ Crystal Forms and Amorphous Regions of Nylon 6-Clay Nanocomposites Using Solid State ¹⁵N Nuclear Magnetic Resonance *Polymer Preprints* **2000**, *2*, 272.
2. Davis, R.D.; Jarrett, W.L.; Mathias, L.J.; Observation of α and γ Crystal Forms and Amorphous Regions of Nylon 6-Clay Nanocomposites Using Solid State ¹⁵N Nuclear Magnetic Resonance *Macromolecules* **1999**, *32*, 7958.
3. Davis, R.D.; Steadman, S.J.; Jarrett, W.L.; Mathias, L.J.; Solution ¹³C NMR Characterization of Nylon 6,6: Quantitation of Cis-Amide Conformers, Acid and Amine End-Groups and Cyclic Unimers *Macromolecules, in press*
4. Davis, R.D.; Jarrett, W.L.; Mathias, L.J.; Solution ¹³C NMR Spectroscopy of Polyamide Homopolymers (Nylons 6, 11, 12, 66, 69, 610 and 612) and Several Commercial Copolymers *Polymer, in press*.

5. Steadman, S.J.; Mathias, L.J.; High Resolution ^{13}C NMR Spectra of Nylon 66 and Nylon 6 Using 3:1 Trifluoroethanol:Methylene Chloride as Solvent *Polymer Preprints* **1993**, 34, 507.
6. Steadman, S.J.; Mathias, L.J.; A New Non-Acidic Mixed Solvent System for Nylon Nuclear Magnetic Resonance: Cis amide Quantitation in Nylons and Model Amides *Polymer* **1997**, 38, 5297.
7. Powell, D.G.; Mathias, L.J.; Characterization of Nylon 6 by ^{15}N Solid State Nuclear Magnetic Resonance *J. Am. Chem. Soc.* **1990**, 112, 669.
8. Hatfield, G.; Glans, J.; Hammond, W.; Characterization of Structure and Morphology in Nylon 6 by Solid-State ^{13}C and ^{15}N NMR *Macromolecules* **1990**, 23, 1654.
9. Powell, D.G.; Mathias, L.J.; Autran, J.P.; Porter, R.S.; Solid State ^{15}N Nuclear Magnetic Resonance of ^{15}N -labeled Nylon 6 and Nylon 11: Observation of Multiple Crystalline Forms and Amorphous Regions *Mater. Sci. Eng.* **1990**, 126, 253.
10. Johnson, C.G.; Mathias, L.J.; Nylon 13,13 Analysis by X-ray and Solid State NMR Treatment Dependent Crystal Forms *Polymer* **1993**, 34, 4978.
11. Johnson, C.G.; Mathias, L.J.; Solid-State NMR Investigation of Nylon 12 *Macromolecules* **1991**, 24, 6114.
12. Johnson, C.G.; Cypcar, C.C.; Mathias, L.J.; ^{13}C and ^{15}N Solid-State NMR of Copolymers of Nylon 6 and 7: Observation of a Stable Pseudo-hexagonal Phase *Macromolecules* **1995**, 28, 8535.
13. Johnson, C.G.; Mathias, L.J.; Solid-State NMR Characterization of Copolymers of Nylon 11 and Nylon 12 *Solid. St. Nuc. Magn. Res.* **1997**, 8, 161.
14. Kojima, Y.; Usuki, A.; Kawasumi, M.; Okada, A.; Kurauchi, T.; Kamigaito, O.; One-Pot Synthesis of Nylon 6-Clay Hybrid *J. Polym. Sci. Part A: Polym. Chem.* **1993**, 31, 1775.
15. Kojima, Y.; Usuki, A.; Kawasumi, M.; Okada, A.; Kurauchi, T.; Kamigaito, O.; Mechanical Properties of Nylon 6-Clay Hybrid *J. Mater. Res.* **1993**, 8, 1185.
16. Kojima, Y.; Usuki, A.; Kawasumi, M.; Okada, A.; Kurauchi, T.; Kamigaito, O.; Kaji, K.; Fine Structure of Nylon 6-Clay Hybrid *J. Polym. Sci. Part B: Polym. Phys.* **1994**, 32, 625.
17. Kojima, Y.; Usuki, A.; Kawasumi, M.; Okada, A.; Kurauchi, T.; Kamigaito, O.; Kaji, K.; Novel Preferred Orientation in Injection-Molded Nylon 6-Clay Hybrid *J. Polym. Sci. Part B: Polym. Phys.* **1995**, 33, 1039.
18. Kurauchi, T.; Okada, A.; Nomura, T.; Nishio, T.; Saegusa, S.; Deguchi, R.; Nylon 6-Clay Hybrid Synthesis, Properties and Application to Automotive Timing Belt Cover *Japanese Pat. 910584*, **1991**.
19. Usuki, A.; Kojima, Y.; Kawasumi, M.; Okada, A.; Fukushima, Y.; Kurauchi, T.; Kamigaito, O.; Synthesis of Nylon 6-Clay Hybrid *J. Mater. Res.* **1993**, 8, 1179.

20. Liu, L.; Qi, Z.; Zhu, X.; Studies on Nylon 6/Clay Nanocomposites by Melt-Intercalation Process *J. Appl. Polym. Sci.* **1999**, 71, 1133.
21. Work in progress to be reported shortly.
22. Nanacor, Inc., 1500 West Shure Drive, Arlington Heights, IL 60004-7803.
23. Lagaly, G.; Characterization of Clays by Organic Compounds *Clay Minerals* **1981**, 16, 1.
24. Murthy, N.S.; Structure of Iodide Ions in Iodinated Nylon 6 and the Evolution Of Hydrogen Bonds Between Parallel Chains in Nylon 6 *Macromolecules* **1987**, 20, 309.

Chapter 11

Studies of Organically Modified Clays by Scattering Techniques

Derek L. Ho^{1,2}, Robert M. Briber¹, and Charles J. Glinka²

¹Department of Materials and Nuclear Engineering, University
of Maryland, College Park, MD 20742

²Center for Neutron Research, National Institute of Standards and
Technology, Gaithersburg, MD 20899–8562

Organically modified montmorillonites dispersed in a number of organic solvents covering a range of solubility parameters were characterized using small angle neutron scattering and wide angle x-ray scattering techniques. The organic modifier was dimethyl dihydrogenated tallow ammonium. Both unextracted (as-received) and solution extracted organically modified clays were studied. The scattering profiles and dispersion behavior in organic solvents of the dry powder of unextracted and of extracted materials are significantly different in a way that suggests that the organic modifier is present in significant excess in the unextracted material. The wide angle x-ray scattering data indicates that extracted and unextracted clays swell to a similar extent in the organic solvents used, but the extracted material has a stronger tendency to gel. The scattering data indicate that the swollen tactoids of the extracted material are thinner, and therefore more numerous, which may account for the bulk suspension behavior.

Introduction

Sodium montmorillonite (Na^+ -montmorillonite), a natural clay mineral, has been studied extensively by diffraction techniques (1-4). More recently it has been used to form nanocomposites with polymers with significantly enhanced mechanical properties (5-7). Na^+ -montmorillonite, a smectite clay, is a hydrophilic mineral, which possesses a 2-to-1 layered structure with a single octahedral aluminum layer located between two layers of silicon tetrahedra, and has a nominal chemical formula of $[(\text{Al}_{1.67}\text{Mg}_{0.33})\text{Si}_4\text{O}_{10}(\text{OH})_2] \text{Na}_{0.33} \cdot n\text{H}_2\text{O}$ (1-3), which varies depending on the source of the clay. Each layered sheet is about 10 Å thick with literature lateral dimensions of 0.1 μm to more than 1 μm (1-3). This yields a specific surface area of ca. 725 m²/g (1). Through chemical substitution on the surface, Na^+ -montmorillonite can be modified to convert the surface from hydrophilic to organophilic, resulting in clays that are dispersible in common organic solvents. Typically, this is accomplished via a cationic substitution reaction with the surface sodium ion (4). Organic cations may be adsorbed on clay minerals by replacement of the inorganic metal ions saturating the structural negative charge on the silicate layers.

Understanding the structure of organophilic clays and the interaction between clay platelets dispersed in organic solvents is important to characterizing the nanocomposites formed by organophilic clays and polymers. Although small angle neutron scattering (SANS) has been recently used to characterize a variety of unmodified clays dispersed in water (8-10) as well as nanocomposites formed by clays and polymers in water based systems (11, 12), relatively few attempts have been made to investigate organically modified clays dispersed in common organic solvents by scattering techniques. Thus, the motivation of this work is to study the behavior and/or structure of organically modified clays in a variety of organic solvents using SANS and wide angle x-ray scattering (WAXS) techniques.

Experimental

Cloisite Na^+ (CNa), a sodium montmorillonite, and Cloisite 15A (C15A), a dimethyl dihydrogenated tallow montmorillonite, with a cation exchange capacity (CEC) of 0.95 meq/g and 1.25 meq/g, respectively, used in this work are commercial products provided as free-flowing powder by Southern Clay Products, Inc. (13). The tallow consists mainly of C₁₈ carbon chain (14), which has an estimated chain length of ca. 26.7 Å with an all trans structure when fully stretched.

Prior to the SANS and WAXS experiments, the as-received CNa powder was fractionated by sonicating the platelets in deionized water at a mass fraction

of 2% (2 wt%) for 2 min with an ultrasonic probe to narrow the distribution in particle size of CNa clay platelets. The small fraction (fraction 1) was separated as a sediment by centrifuging the dispersion at 5000 rpm for 20 min and discarded. The supernatant was then centrifuged at 7000 rpm for 20 min to obtain a second sediment fraction (fraction 2), which contained most of the remaining clay. Fraction 2 was dried in an oven under vacuum at room temperature for 3 days and used in the experiments. In order to remove excess dimethyl dihydrogenated tallow from the as-received (unextracted) C15A, the unextracted C15A powder was purified by refluxing with hot ethyl alcohol, which was replaced once daily, for 3 days. The purified (extracted) C15A sample was then dried in an oven under vacuum at room temperature for 3 days. The unextracted and extracted C15A clays were then dispersed in benzene, toluene, p-xylene, cyclohexane and octane for the experiments by sonicating the mixtures for 2 min. Table I summarizes the solubility parameter (δ) of the organic solvents (15) used in this work and the appearance of C15A dispersed in the solvents. The literature value of δ for tallow is in the range from 18 (J/m^3)^{1/2} to 28 (J/m^3)^{1/2} (14).

Table I. Solvent Solubility Parameter and C15A Dispersion Appearance

<i>Solvent</i>	δ (J/m^3) ^{1/2}	<i>2 wt% Extracted</i>	<i>2 wt% Unextracted</i>
Benzene	18.8	Transparent Gel	Transparent Dispersion
Toluene	18.2	Transparent Gel	Transparent Dispersion
p-Xylene	18.0	Transparent Gel	Transparent Dispersion
Cyclohexan	16.8	Precipitates	Cloudy Dispersion
Octane	15.6	Precipitates	Cloudy Dispersion

NOTE: δ represents the solubility parameter.

SANS experiments over the q range from 0.004 \AA^{-1} to 0.517 \AA^{-1} were carried out using the 30-m SANS instruments at the National Institute of Standards and Technology (NIST) Center for Neutron Research (NCNR) (16). The incident neutron wavelength (λ) was 6 \AA with a wavelength resolution of $\Delta\lambda/\lambda = 0.11$. The scattered intensity was corrected for background and parasitic scattering (17), placed on an absolute level using a calibrated secondary standard and circularly averaged to yield the scattered intensity as a function of q , where $q = (4\pi/\lambda)\sin(\theta/2)$ (θ is the scattering angle). The incoherent background from the pure solvents was measured, corrected by the volume fraction displaced by the dispersed clay, and subtracted from the reduced SANS data. The data points in the q range from 0.35 \AA^{-1} to 0.45 \AA^{-1} were then averaged to yield the estimated incoherent background from clays, which was subtracted from the data as well. WAXS measurements were performed at room

temperature over the q range from 0.07 \AA^{-1} to 1.06 \AA^{-1} using Ni filtered Cu $K\alpha$ x-rays of wavelength $\lambda = 1.54 \text{ \AA}$. The dry powders of unextracted and of extracted C15A, the dispersions of unextracted C15A in all the deuterated (d-) solvents noted above at 2 wt% concentration as well as the dispersions of extracted C15A in d-benzene, d-toluene and d-p-xylene at 1 wt% concentration were measured by SANS and WAXS. The lateral size of C15A platelets was determined to be in the range of 0.4 \mu m to 1.0 \mu m using atomic force microscopy (AFM) (18).

Theoretical

The CNa platelets can be modeled as individual thin circular discs, i.e. flat cylinders, with a thickness of ca. 10 \AA and a diameter of ca. 0.4 \mu m to 1 \mu m . For monodisperse non-interacting CNa platelets the coherent scattered intensity, averaged over all orientations, is given by (19-21):

$$I_{\text{Single}}^{\text{CNa}}(q) = (\Delta\rho_{\text{CNa}})^2 N_{\text{CNa}} V_{\text{CNa}}^2 \int_0^{\pi/2} \left(\frac{\sin(qh \cos \varphi)}{qh \cos \varphi} \right)^2 \left(\frac{2J_1(qR \sin \varphi)}{qR \sin \varphi} \right)^2 \sin \varphi d\varphi \quad (1)$$

$$\equiv (\Delta\rho_{\text{CNa}})^2 N_{\text{CNa}} V_{\text{CNa}}^2 P_{\text{CNa}}(q)$$

where $2h$ is the axial length (thickness) of the discs, R is the radius, and $P(q)$ is the single platelet form factor. φ is the angle between q and the axis of the disc and $J_1(x)$ is the first order Bessel function. N_{CNa} and V_{CNa} represent the number of CNa clay platelets per unit volume and the volume of a single CNa clay platelet, respectively. $\Delta\rho_{\text{CNa}} = \rho_{\text{CNa}} - \rho_{\text{solvent}}$ is the corresponding scattering contrast with respect to the solvent (21) and ρ_i is the neutron scattering length density (SLD) of species i .

For the C15A clay platelets, assuming that the radius of the platelets does not change on adsorption of a tallow layer (surfactant) and that the only change is in the thickness of the platelet, the simplest model is that of a lamellar clay/tallow (core/layer) structure (22, 23) as illustrated in Figure 1(a). Assuming the neutron SLD of the core and layer are homogeneous in the x-y plane, as shown in Figure 1(b), the coherent scattered intensity from such a core/layer structure is determined by the core and layer neutron SLD profiles, $\rho_{\text{core}}(z) \equiv \rho_c$ and $\rho_{\text{layer}}(z) \equiv \rho_l$. The total coherent scattered intensity from randomly oriented single C15A platelets with a core of volume V_c and a total platelet volume of V_t in the system can be written in the form (22):

$$I_{\text{Single}}^{\text{C15A}}(q) = N_{\text{C15A}} \int_0^{\pi/2} [\Delta\rho_l (V_l f_l(q) - V_c f_c(q)) + \Delta\rho_c V_c f_c(q)]^2 \sin \varphi d\varphi \quad (2)$$

$$P_c(q) = \int_0^{\pi/2} \left[\left(\frac{\sin(qh \cos \varphi)}{qh \cos \varphi} \right) \left(\frac{2J_1(qR \sin \varphi)}{qR \sin \varphi} \right) \right]^2 \sin \varphi d\varphi \quad (3a)$$

$$P_t(q) = \int_0^{\pi/2} \left[\left(\frac{\sin(q(d+h) \cos \varphi)}{q(d+h) \cos \varphi} \right) \left(\frac{2J_1(qR \sin \varphi)}{qR \sin \varphi} \right) \right]^2 \sin \varphi d\varphi \quad (3b)$$

$$P_{t,c}(q) = \int_0^{\pi/2} \left(\frac{\sin(q(d+h) \cos \varphi)}{q(d+h) \cos \varphi} \right) \left(\frac{\sin(qh \cos \varphi)}{qh \cos \varphi} \right) \left(\frac{2J_1(qR \sin \varphi)}{qR \sin \varphi} \right)^2 \sin \varphi d\varphi \quad (3c)$$

where $\langle f_t^2(q) \rangle_\varphi = P_t(q)$ and $\langle f_c^2(q) \rangle_\varphi = P_c(q)$ represent the form factor for the total C15A clay platelet and the core (CNa platelet), respectively, and $\langle f_t(q)f_c(q) \rangle_\varphi = P_{t,c}(q)$ is the cross term. N_{C15A} denotes the number of C15A clay platelets per unit volume and d represents the tallow layer thickness. If an attractive interaction between the platelets is present, the summation of such an attractive interaction over the large platelet surfaces may give rise to a formation of tactoids of parallel platelets as shown in Figure 1(c). The contribution of stacked platelets arising from the inter-platelet interference to the total coherent scattered intensity is considered as a short-range structure factor, $S_s(q)$, which should be multiplied by $f_c^2(q)$, $f_t^2(q)$ and $f_t(q)f_c(q)$ given in equations (3a)-(3c), respectively, to yield the total coherent scattered intensity. Assuming the next neighbor distance in a stack of parallel platelets (tactoid) obeys a Gaussian distribution, the $S_s(q)$ was first calculated by Kratky and Porod (20):

$$S_s(q) = 1 + \frac{2}{N} \sum_{k=1}^N (N-k) \cos(kDq \cos \varphi) \exp[-k(q \cos \varphi)^2 \sigma_D^2 / 2] \quad (4)$$

where φ is the angle between q and the axis of the stacked platelets, N corresponds to the averaged number of platelets per tactoid in the system, and D ($D = 2h + 2d$) and σ_D represent the next neighbor center-to-center distance (the spacing of the lamellar stack) and its Gaussian standard deviation (GSD), respectively. Consequently, the total coherent scattered intensity from randomly oriented non-interacting single tactoids of C15A clay platelets can be written as:

$$I_{\text{Total}}^{C15A}(q) = N_{C15A} \int_0^{\pi/2} [\Delta\rho_l (V_t f_t(q) - V_c f_c(q)) + \Delta\rho_c V_c f_c(q)]^2 S_s(q) \sin \varphi d\varphi \quad (5)$$

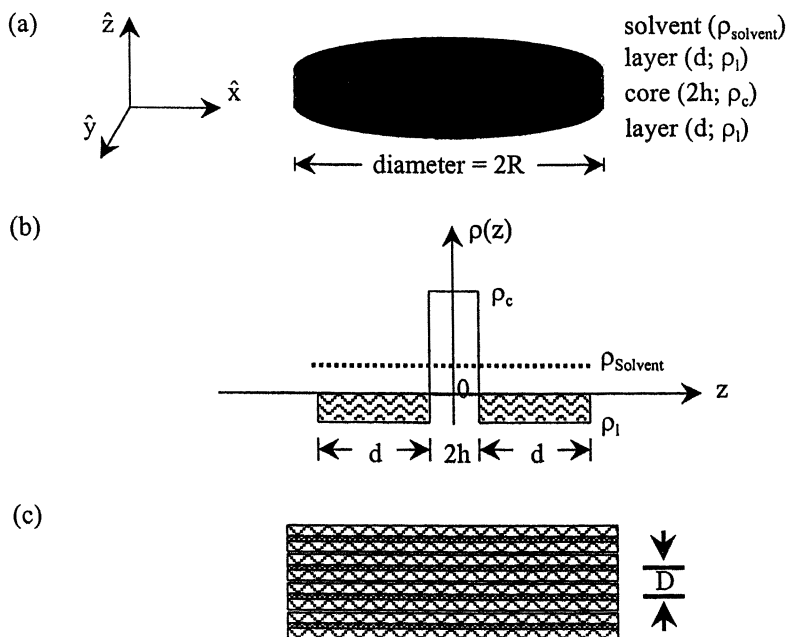


Figure 1(a) Schematic of the structure of a single clay/tallow (surfactant) core/layer C15A clay platelet. (b) Corresponding neutron scattering length density profiles $\rho(z)$ perpendicular to the platelet plane. (c) Schematic of clay platelets present in tactoids.

Results and Discussion

In Figure 2, the spacing of the platelets in dry CNa was found to be $2\pi/q_{\text{peak}} = 9.9 \text{ \AA}$, where $q_{\text{peak}} = 0.63 \text{ \AA}^{-1}$ using WAXS, which is in a good agreement with the literature value (1-3) of ca. 10 \AA . The centrifuged CNa profile shows a better-defined peak than the as-received material indicating that the centrifuged CNa has a better stacking order, probably, due to the relatively slow drying procedure applied compared to commercial processes. The CNa clays gel in deionized water at a concentration of ca. 2 wt%. Nevertheless, no concentration dependence to the SANS was observed in the CNa clay dispersions with increasing concentration from 0.5 to 4 wt% (18). The WAXS profiles obtained from the dry powder of unextracted and of extracted C15A (Figure 3) are significantly different, suggesting that the tallow is present in excess after the modification reaction. Extraction likely removes the excess organic modifier

(tallow) that is not strongly bonded to the clay platelet surface. Precipitated tallow was observed in the room temperature waste solvent after the extraction. The primary peak (001) for the extracted C15A at $q_{\text{peak}} = 0.26 \text{ \AA}^{-1}$ corresponds to a platelet spacing of $2\pi/q_{\text{peak}} = 24.3 \text{ \AA}$. Assuming a model for the platelets as shown in Figure 1(a) and a core (CNA platelet) thickness of 9.9 \AA (Figure 2), a single tallow layer in the dry extracted C15A has a thickness of 7.2 \AA .

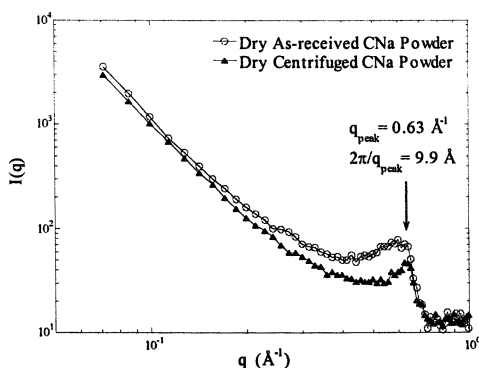


Figure 2. WAXS profiles of as-received and of centrifuged CNA dry powders.

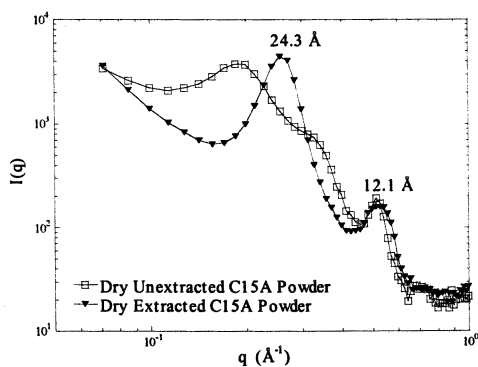


Figure 3. WAXS profiles of unextracted and of extracted C15A dry powders.

Figure 4(a) presents the WAXS profiles of 1 wt% extracted C15A dispersed in benzene, toluene and p-xylene. Three orders of the primary 46.5 \AA spacing are observed for the extracted C15A dispersed in benzene and toluene. Assuming the core of the C15A platelets has a thickness of 9.9 \AA the 46.5 \AA

corresponds to a single tallow layer thickness of ca. 18.3 Å on each side of the clay platelet when dispersed in benzene. These results are consistent with having a swollen tallow layer between the clay platelets. Although the dispersions of extracted C15A in benzene, toluene and p-xylene were optically transparent, the WAXS data indicates that exfoliation of extracted C15A is not complete, e.g., in benzene, but is nearly complete in p-xylene (toluene is intermediate). The WAXS profiles from 2 wt% unextracted C15A dispersed in the solvents shown in Figure 4(b) indicate that the degree of swelling is similar but the peaks are more evident, implying a larger number of platelets per tactoid.

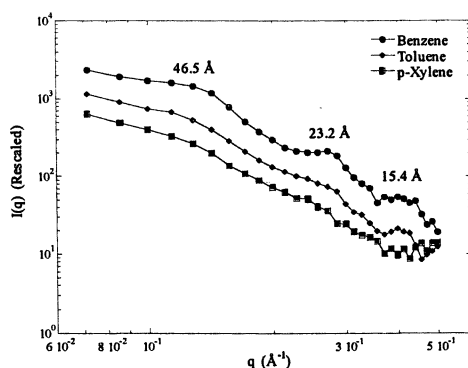


Figure 4(a). WAXS profiles of 1 wt% extracted C15A dispersed in the organic solvents. Profiles are vertically offset for clarity.

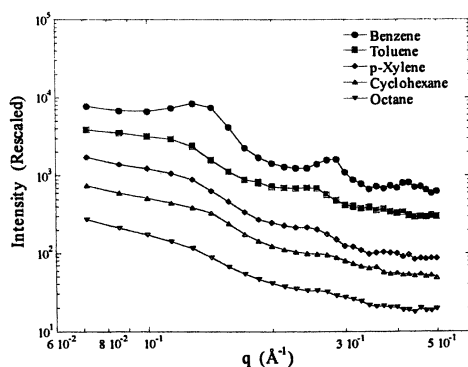


Figure 4(b). WAXS profiles of 2 wt% unextracted C15A dispersed in the organic solvents. Profiles are vertically offset for clarity.

SANS data from 1 wt% extracted C15A dispersed in deuterated solvents and the corresponding fitted profiles (solid curves) are presented in Figure 5(a). Fitting the SANS data shown in Figure 5(a) to equation (5) yields a core (CNa clay) thickness of ca. 9.9 Å and a tallow layer thickness of extracted C15A dispersed in d-benzene of (17.7 ± 0.5) Å, consistent with the value of 18.3 Å obtained from the WAXS measurements discussed in the previous paragraph. The parameters for the volume fraction of the extracted C15A clays, and the SLD of the core (CNa clay) and of the solvent mixture, were known and fixed during the fitting. Since in the q range (0.004 \AA^{-1} to 0.517 \AA^{-1}) used in this work the scattering was not sensitive to the lateral dimension (diameter), larger than ca. 1000 Å, of the clay platelets, the platelet radius of 3000 Å was chosen and fixed for all the calculations presented. Table II gives the fitted parameters of the curves shown in Figure 5(a). The strong neutron scattering contrast between the deuterated solvents and the protonated tallow, which is absent for x-rays, accounts for the differences in the scattering profiles seen in Figures 4 and 5, particularly in the range of $q = 0.1 \text{ \AA}^{-1}$ to 0.3 \AA^{-1} .

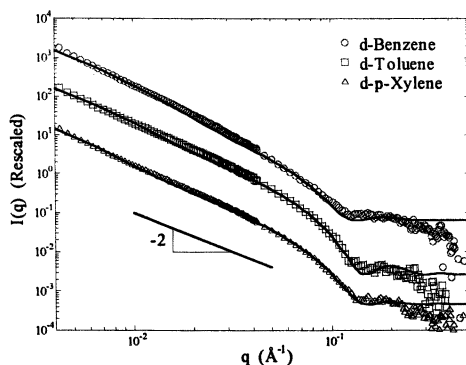


Figure 5(a). SANS data of 1 wt% extracted C15A dispersed in the deuterated organic solvents. Profiles are vertically offset for clarity.

Table II. 1 wt% Extracted C15A Dispersed in Deuterated Solvents

	<i>Benzene</i>	<i>Toluene</i>	<i>p-Xylene</i>
Core Thickness (Å)	9.9 ± 0.3	9.9 ± 0.2	9.9 ± 0.3
Layer Thickness (Å)	17.7 ± 0.5	16.2 ± 0.5	16.1 ± 0.4
GSD of d-Spacing (Å)	1.3 ± 0.1	2.8 ± 0.1	3.7 ± 0.1
No. of Platelets/Tactoid	3.1 ± 0.2	2.1 ± 0.2	2.0 ± 0.3

NOTE: GSD of d-Spacing represents the Gaussian standard deviation of the spacing of the lamellar stack.

From the fits to the SANS data, the tallow layer thickness (d) decreases slightly while the GSD of the spacing (σ_D) of parallel stacked clay platelets defined in equation (4) increases significantly with decreasing solubility parameter (δ) of the solvent, which could explain the diminution of the interplatelet scattering peaks in going from benzene to p-xylene as shown in Figure 4(a). A linear fit to the data in a plot of δ versus d yields $d = (\delta - 10.45)/0.47$ (18). Assuming that the tallow layer is fully stretched (ca. 26.7 Å in length) when the solubility parameter of the solvent equals that of the tallow, i.e., $\delta_{\text{tallow}} = \delta_{\text{solvent}}$, yields an estimated value of $\delta_{\text{tallow}} = 23.0$ (J/m³)^{1/2}, which falls within the literature range of 18 (J/m³)^{1/2} to 28 (J/m³)^{1/2} (14). The increase in d with increasing δ is consistent with the tallow swelling more as the δ of the solvent approaches that of the tallow. It is interesting that the increase in the swelling of the tallow is coupled with a decrease in the GSD of the interplatelet spacing indicating that the tactoid is becoming more ordered. Since the interactions between the alkyl chains, clays and organic solvents are occurring over nanometer length scales, it might be a better method to characterize the interaction strengths by studying atomic polarizabilities, etc. Figure 5(b) shows the SANS data of 2 wt% unextracted C15A dispersed in all the d-solvents given in Table I. Unlike the SANS data given in Figure 5(a), which have a constant slope of ca. -2.36 in the low q regime (0.005 Å⁻¹ to 0.05 Å⁻¹), the slope of the SANS profiles illustrated in Figure 5(b) varies from ca. -3.26 (benzene) to ca. -2.35 (octane).

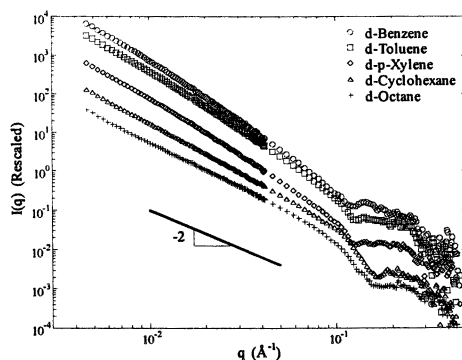


Figure 5(b). SANS data of 2 wt% unextracted C15A dispersed in the deuterated organic solvents. Profiles are vertically offset for clarity.

Suspensions of both unextracted and extracted C15A in d-toluene at a range of concentrations were also explored using SANS. The unextracted C15A with

excess organic modifiers dispersed in d-toluene did not show any significant concentration dependence while the extracted C15A exhibits a concentration dependence. The SANS data and the corresponding fitting profiles (solid curves) of the extracted C15A in d-toluene at different concentrations are given in Figure 6. Fitting the data illustrated in Figure 6 to equation (5) yields the results listed in Table III, which shows that the parameters obtained for the single particle form factor of C15A given by equation (1) are essentially constant as a function of concentration and that the $S_S(q)$ given by equation (4) changes through an increase in the GSD of the spacing of the lamellar stack with decreasing concentration. Even the most dilute concentration sample (0.1 wt%), however, could not be fit by the single particle form factor alone. The stacked platelet model (equation (5)) also fails to fit the 0.1 wt% data in the high q region.

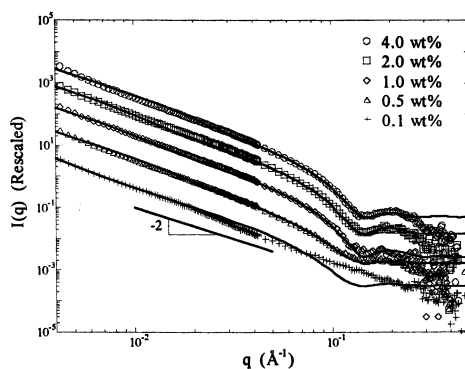


Figure 6. SANS profiles of extracted C15A in deuterated toluene at a range of concentrations. Profiles are vertically offset for clarity.

Table III. Extracted C15A Dispersed in Deuterated Toluene

	0.5 wt%	1.0 wt%	2.0 wt%	4.0 wt%
Core Thickness (Å)	9.9 ± 0.4	9.9 ± 0.2	9.9 ± 0.2	9.9 ± 0.2
Layer Thickness (Å)	16.4 ± 0.6	16.2 ± 0.5	16.8 ± 0.3	16.6 ± 0.3
GSD of d-Spacing (Å)	4.6 ± 0.2	2.8 ± 0.1	2.7 ± 0.1	1.3 ± 0.3
No. of Platelets/Tactoid	2.2 ± 0.3	2.1 ± 0.2	2.0 ± 0.2	2.0 ± 0.2

NOTE: GSD of d-Spacing represents the Gaussian standard deviation of the spacing of the lamellar stack.

Both SANS and WAXS data indicate that as-received and centrifuged CNA clay platelets were fully exfoliated in DI water at a concentration of ca. 0.5 wt% (18). The slope of the 0.5 wt% centrifuged CNA clay platelets dispersed in DI

water was measured to be -2.18 ± 0.02 over the q ranging from 0.01 to 0.1 \AA^{-1} using SANS (18), which is consistent with the reported data (22, 24) of ca. -2.2 for Na^+ -montmorillonite clays dispersed in water. The deviation of the measured slope from the theoretical value of -2.1 in the low q regime for fully exfoliated CNa clay platelets (18, 22) might be due to the CNa clay platelets not being perfectly rigid when dispersed in water (25). The scattering profiles of extracted C15A in *d*-toluene shown in Figure 6 possess a concentration independent slope of -2.36 ± 0.02 , i.e., $I(q) \sim q^{-2.36}$, in the q ranging from 0.004 \AA^{-1} to 0.05 \AA^{-1} . Figure 7 illustrates the calculated scattered intensity with different values of N using equation (5) and the fitted parameters for 1 wt% extracted C15A in *d*-toluene given in Table II. The calculated $P(q)$ ($N = 1$) and the fitted curve in Figure 5(a) ($N = 2$) possess a slope of -2.1 and -2.36 in the low q regime, respectively. The only variable for the calculated $P(q)$ and $I(q)$ given in Figure 7 is the number of platelets per tactoid, N , suggesting that the deviation of slope from -2.1 mainly arises from stacking of clay platelets. The slope increases while the absolute scattered intensity of the peak in the oscillation of the form factor near $q = 0.2 \text{\AA}^{-1}$ decreases with increasing N , which, consequently, might be used to determine the N value. The slope of the calculated $P(q)$ is identical to that of $P(q)$ calculated for CNa platelets (18, 22) indicating that slopes obtained from equations (2) and (1) for ideal thin discs with and without an adsorbed surfactant layer, respectively, would be expected to be the same. Thus, the low- q slope of the scattering from fully exfoliated C15A platelets in organic solvents would be expected to be close to that of fully exfoliated CNa platelets in water.

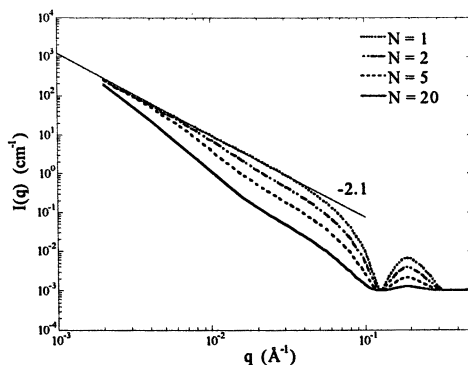


Figure 7. Calculated $I(q)$ with different values of N , the number of clay platelets per tactoid, using equation (5) and the parameters for 1 wt% extracted C15A in *d*-toluene given in Table II.

Conclusions

The structure of unextracted and extracted C15A clays dispersed in a variety of solvents was characterized using SANS and WAXS techniques. It was found that the organic modifier, dimethyl dihydrogenated tallow ammonium, is present in significant excess in the unextracted material. Both unextracted and extracted C15A platelets retain their lamellar structure in benzene, toluene and p-xylene, and swell to a similar degree. A model for the clay/tallow (i.e. core/layer) structure has been established to fit the SANS data presented in this article. The fitted parameters indicate that the thickness of the tallow layer increases while the GSD of the next neighbor center-to-center distance between clay platelets decreases with increasing solvent solubility parameter. The extracted clay dispersion exhibited a concentration dependence to the scattering while the unextracted clay dispersion did not. A concentration independent slope of -2.36 ± 0.02 was observed in the low q region in all the SANS profiles obtained from the dispersions of extracted C15A in the organic solvents used in this work suggesting that the deviation of slope from the theoretical value of -2.1 may arise from stacking of clay platelets. Unextracted C15A is more readily suspended (i.e. shows less tendency to gel or form precipitates) than extracted C15A in the organic solvents studied. The scattering data suggest that the unextracted material disperses as larger tactoids which interact weakly and hence tend to remain suspended.

Acknowledgment

The authors acknowledge the support of the NIST, U.S. Department of Commerce, and the National Science Foundation, through Agreement No. DMR-9423101, in providing the neutron research facilities used in this work. We thank Prof. R. Krishnamoorti at the University of Houston and Dr. B. Hammouda at the NIST for many helpful discussions.

References

1. *Formation and Properties of Clay-Polymer Complexes*; Theng, B. K. G.; Elsevier: New York, **1979**.
2. *Clays*; Worrall, W. E.; Transatlantic Arts: New York, **1968**.
3. *Clay Sedimentology*; Chamley, H.; Springer-Verlag: New York, **1989**.
4. *Chemistry of Clays and Clay Minerals*; Newman, A. C. D.; Wiley: New York, **1987**.

5. Krishnamoorti, R.; Vaia, R. A.; Giannelis, E. P. *Chem. Mater.* **1996**, *8*, 1728.
6. Krishnamoorti, R.; Giannelis, E. P. *Macromolecules* **1997**, *30*, 4097.
7. Mourchid, A.; Lecolier, E.; Van Damme, H.; Levitz, P. *Langmuir* **1998**, *14*, 4718.
8. Ramsay, J. D. F.; Swanton, S. W.; Bunce, J. J. *Chem. Soc. Faraday Trans.* **1990**, *86*, 3919.
9. Ramsay, J. D. F.; Lindner, P. J. *Chem. Soc. Faraday Trans.* **1993**, *89*, 4207.
10. Brown, A. B. D.; Clarke, S. M.; Rennie, A. R. *Progr. Colloid Polym. Sci.* **1998**, *110*, 80.
11. Jinnai, H.; Smalley, M. V.; Hashimoto, T. *Langmuir* **1996**, *12*, 1199.
12. Hatharasinghe, H. L. M.; Smalley, M. V.; Swenson, J.; Williams, G. D.; Heenan, R. K.; King, S. M. *J. Phys. Chem. B* **1998**, *102*, 6804.
13. Certain commercial materials and equipment are identified in this paper in order to specify adequately the experiment procedure. In no case does such identification imply recommendation by the National Institute of Standards and Technology nor does it imply that the material or equipment identified is necessarily the best available for this purpose.
14. *Practical Handbook of Biochemistry and Molecular Biology*; Fasman, G.D.; CRC Press: New York, **1989**.
15. *CRC Handbook of Polymer-Liquid Interaction Parameters and Solubility Parameters*; Barton, A.F.M.; CRC Press: New York, **1990**.
16. Glinka, C.J.; Barker, J.G.; Hammouda, B.; Krueger, S.; Moyer, J.J.; Orts, W.J. *J. Appl. Cryst.* **1998**, *31*, 430.
17. *NG3 and NG7 30-Meter SANS Instruments Data Acquisition Manual*; Cold Neutron Research Facility at the National Institute of Standards and Technology; **1999**.
18. Ho, D.L.; Briber, R.M.; Glinka, C.J. *Chemistry of Materials* **2000**, in press.
19. *Small Angle Scattering of X-Rays*; Guinier, A.; Fournet, G.; Wiley: New York, **1955**.
20. Kratky, O.; Porod, G. *J. Colloid Science* **1949**, *4*, 35.
21. *Polymers and Neutron Scattering*; Higgins, J.S.; Benoit, H.C.; Oxford: New York, **1994**.
22. Bongiovanni, R.; Ottewill, R.H.; Rennie, A.R. *Progr. Colloid Polym. Sci.* **1991**, *84*, 299.
23. Richter, D.; Schneiders, D.; Monkenbusch, M.; Willner, L.; Fetters, L.J.; Huang, J.S.; Lin, M.; Mortensen, K.; Farago, B. *Macromolecules* **1997**, *30*, 1053.
24. Hanley, H.J.M.; Straty, G.C.; Tsvetkov, F. *Langmuir* **1994**, *10*, 3362.
25. Gilman, J.W.; Harris, R.H., Jr.; Jackson, C.L.; Morgan, A.B.; Brassell, L.D.; Hunter, D.L., *ACS PMSE Preprints* **2000**, *82*, 270.

Chapter 12

Thin Film Organically Modified Layered Silicate– Polymer Hybrid Materials

R. Limary and P. F. Green

Department of Chemical Engineering and the Texas Materials Institute,
The University of Texas at Austin, Austin, TX 78712

The structure and morphology of thin film hybrid materials of polymers blended with organically modified layered silicates (OLS) were examined. The polymers were polystyrene (PS), polymethyl methacrylate (PMMA) and PS-*b*-PMMA diblock copolymers. The OLS were montmorillonite modified with an amount of alkyl ammonium surfactant that was equivalent to the charge exchange capacity of the clay, OLS(S), and montmorillonite modified with excess amounts of the organic surfactant, OLS(E). Films ranging in thickness from 30nm to 300nm were cast on SiO_x substrates. X-ray diffraction measurements revealed that the gallery separations of the OLS(S) and OLS(E) clays increased when they were blended with the homopolymers and the copolymer. However, while the final gallery separations in the PS-*b*-PMMA/OLS(S) and PS-*b*-PMMA/OLS(E) hybrid materials were virtually identical, the structure and morphology of the films were vastly different. The gallery separations of the clays in the copolymer hosts were larger than those in the PS and PMMA hosts. Our observations can be rationalized in terms of competing interactions of the polymers and the organic components of the hybrid thin films with the SiO_x substrate and with the “walls” of the layered silicate structures.

Introduction

Hybrid organic-inorganic nanocomposites, produced by dispersing layered silicates, clays, into a polymer host, can exhibit significant improvements in physical properties in relation to the polymer host (1-14). The addition of a few weight percent of layered silicates can increase the modulus and the strength by over 50% in some systems. Significant increases in heat of distortion temperatures and decreases of the thermal expansion coefficients, in comparison to the host material, are well documented. The 2:1 phyllosilicates, or mica-type layer silicates, are commonly used to produce nanocomposites with polymers (6,7,9). Included in this class of materials is the clay mineral montmorillonite, which consists of fused silica tetrahedral sheets sandwiching edge-shared aluminum hydroxide octahedral sheets. Divalent magnesium ions often substitute for the trivalent aluminum ions (8). The negatively charged surfaces of the silicate sheets can be charge balanced by cationic salts. Several layers of these silicate sheets are stacked parallel to each other, held in tandem by dipolar and attractive van der Waals forces, with interlayer spacings, or galleries, on the order of one nanometer apart.

The narrow galleries, combined with the fact that the environment is polar, deter organic polymers from interpenetrating. However, polymers can intercalate the galleries when the silicate surfaces are modified by alkyl ammonium cationic surfactants (9). The surfactant molecules undergo ion exchange with the cationic salts, thereby reducing the polarity of the gallery surfaces and rendering them organophilic. An increase in the gallery heights naturally accompanies this process.

The overall properties of the hybrid material depend on microstructural features. Generally, for the hybrid to exhibit enhanced physical and chemical properties, the layered silicates must interact favorably with the polymer host. Three classes of hybrid polymer/layered silicate (PLS) materials are typically identified: intercalated, exfoliated, and immiscible. Intercalated nanocomposites are formed when the polymer chains become localized between the interlayers of the clay, creating stacked multi-layers of alternating polymer and silicate sheets. Exfoliated nanocomposites are created when extensive interpenetration by the chains delaminate the stacked sheets, resulting in the dispersion of individual sheets throughout the polymer host. On the other hand, unfavorable interactions between the polymer and the clay systems result in the formation of a macroscale composite consisting of agglomerated tactoids of the layered silicate surrounded by polymer chains (an immiscible system).

Thermodynamics play a significant role in determining PLS nanocomposite formation (10-14). The overall chain length and density of surfactants in the galleries, the length of the polymer chains, and enthalpic (polymer/silicate and

the polymer/surfactant) interactions determine the phase behavior of polymer/clay systems. When a polymer chain intercalates a gallery and becomes confined, it experiences a significant loss of conformational entropy while gaining translational entropy. The tethered surfactant chains gain conformational entropy as a result of the finite swelling of the interlayer that accompanies intercalation. From a practical point of view, for the hybrid material to be a viable engineering material, the chains must interpenetrate the galleries of the clay at a rapid rate. This is determined by a combination of favorable gallery clay interactions together with non-equilibrium factors such as processing conditions (14).

Research on hybrid polymer/layered silicate (PLS) nanocomposites has concentrated exclusively on bulk systems and little is understood about thin, sub-micron thick, hybrid films. Films of this dimension offer a range of challenges and opportunities. Properties of sub-micron thick films typically differ appreciably from bulk properties, due largely to a combination of energetic and entropic interactions. For example, sufficiently thin films can be destabilized by long-range intermolecular forces, altering the lateral homogeneity and continuity of the films (15-20). Moreover, changes in properties such as the glass transition temperature, the viscosity, and translational chain diffusion coefficients with decreasing film thicknesses are also well documented in these systems (21). In this chapter, we discuss factors that influence the morphology and stability of PLS materials.

Experimental

Two homopolymers and a copolymer were used in our experiments. The copolymer was a symmetric poly(styrene-*b*-methyl methacrylate) (PS-*b*-PMMA) diblock copolymer with total molecular weight of $M = 65,500$ ($M_{PS} = 33,000$ and $M_{PMMA} = 32,500$) and total degree of polymerization $N = N_{PS} + N_{PMMA} = 642$ ($N_{PS} \approx 317$ and $N_{PMMA} \approx 325$) with polydispersity index $M_w/M_n < 1.06$ from Polysciences, Inc. The homopolymers used were PMMA ($M = 27,000$ with $M_w/M_n < 1.1$) and PS ($M = 30,000$ with $M_w/M_n < 1.06$).

Montmorillonite and three organically modified versions of this clay mineral were used. In the case of one set of the modified clays, identified as OLS(S), the cation exchange capacity (CEC) of the clays was satisfied by using the appropriate amount of cationic surfactant molecules to balance the negative charges on the aluminosilicate surfaces. Therefore the surfactant chains would be tethered to the surfaces. The charge exchange capacities of the other clays, OLS(E) were exceeded. Their galleries contained excess surfactant molecules,

held in place via hydrogen bonding. Table I provides a summary of the clays used in this study. The clays were donated by Southern Clay Products.

Table I. Characteristics of Layered Silicate Materials

<i>Clay</i>	<i>Properties</i>	<i>CEC</i>
Mnt	Unmodified	95 mequiv/100g (pristine)
OLS(S)	Organically modified in stoichiometric portions	95 mequiv/100g (stoichiometric)
OLS(E)	Organically modified in excess portions	125 mequiv/100g (~32% excess) 140 mequiv/100g (~47% excess)

Solutions of clay powders and the polymers were made using toluene. The polymer/layered silicate solutions were spin cast onto SiO_x/Si substrates to create films with thicknesses that ranged from 30nm to 300nm. PLS nanocomposite thin films were annealed at 170°C, above the glass transition temperature of the polymers. We note that this method of preparation produced aggregates of the layered silicates throughout the polymer thin film. In all cases, the films were continuous prior to annealing.

An Autoprobe CP atomic force microscope (AFM) from ThermoMicroscopes was used to probe the topography of the films. Images were obtained in the contact mode. X-ray diffraction (XRD) was used to monitor the angular shift and integrated intensity of the silicate reflections. X-ray powder diffraction spectra were collected on a theta-theta diffractometer (Scintag Inc.) between $2\theta = 1.5$ and 12 deg fitted with a Peltier cooled Si(Li) detector using Cu K α radiation (22).

Results and Discussion

1. X-ray Diffraction

We begin by discussing the X-ray diffraction measurements of the Mnt, OLS(S) and OLS(E) materials. The spacings, d_{001} , of the (001) basal reflections of the clay/polymer systems were measured. The actual gallery spacings can be determined by subtracting 0.95 nm, the thickness of a silicate sheet, from the d_{001} values. The average d_{001} -spacings of the OLS clays are summarized in Table II. The d_{001} value for the OLS(E) clay with 32% excess surfactant is

Table II. XRD d_{001} -spacing Results

<i>System</i>	<i>d_{001}- spacing (nm)</i>
Mnt	1.2
Mnt/PS-b-PMMA	1.2
Mnt/PS	1.1
Mnt/PMMA	1.2
OLS(S)	2.3
OLS(S)/PS-b-PMMA	3.5
OLS(S)/PS	3.0
OLS(S)/PMMA	2.8
OLS(E)	3.1
OLS(E)/PS-b-PMMA	3.6

3.1nm, whereas it is 3.4nm for the 47% excess sample. As expected, the d_{001} value for the OLS(S) clays is smaller, $d_{001} = 2.3\text{nm}$. The excess untethered alkyl ammonium that resides within the galleries accounts for the larger gallery height in the OLS(E) samples.

The d_{001} values of the polymer/Mnt hybrid thin films remained identical to that of Mnt, indicating the absence of intercalation (22). The absence of intercalation in the polymer/Mnt samples is to be expected since intercalation of the pristine Mnt by the polymer chains would cause an increase in the free energy of the system in order to overcome the dipolar forces that attract the layers. Moreover, a decrease of the conformational entropy of the polymer chains would result from confinement. Since there are no other substantial compensating mechanisms, the free energy would increase. Therefore intercalation of the pristine Mnt is not expected and not observed.

There was evidence of intercalation in the copolymer/OLS, PMMA/OLS and PS/OLS hybrid thin films. The d_{001} values were 3.5nm for both the copolymer/OLS(S) and copolymer/OLS(E) films after annealing at 170°C. We note that after the films were solution cast, there was some intercalation of the galleries by the polymer chains and further intercalation occurred upon annealing. The fact that $d_{001} = 3.5\text{nm}$ for the OLS(E) hybrid systems suggests that fewer copolymer chains intercalated the OLS(E) clays than the OLS(S) clays. However, it could also mean that there was an exchange between untethered surfactant chains in the OLS(E) galleries and copolymer chains. This will be addressed in the next section.

Intercalation of the OLS(S) systems is well understood. The barrier associated with separation of the layers is reduced due to the presence of the tethered surfactant chains. When a polymer chain intercalates the galleries, the

polymer gains translational entropy while it loses conformational entropy. The tethered surfactant chains within the galleries gain conformational entropy as a result of the expansion of the gallery from intercalation. As discussed later, PS, PMMA, and the PS-*b*-PMMA diblock copolymer are *incompatible* with the surfactant. Therefore, enthalpic interactions between the polymer chains and the aluminosilicate galleries of the clays, together with the gain in translational entropy of the polymer chains and the gain in conformational entropy of the surfactant chains, appear to be the primary driving force for intercalation.

The data in Table II also indicate that the d_{001} values of the PS/OLS and PMMA/OLS samples are comparable, yet smaller than those of the copolymer/OLS samples. We speculate that it is possible for the copolymer to form an ordered structure within the galleries, which might account for the increased gallery spacing. However, final confirmation of this will have to await further experiments.

Having discussed the intercalation process that can occur in polymer/OLS thin film and bulk hybrid nanocomposites, we now discuss effects that are unique to thin film nanocomposites. We show that while XRD suggested similarities in the behavior of the OLS(S)/copolymer and OLS(E)/copolymer systems, there are significant differences.

2. Microscopy

Images of OLS(E)/copolymer nanocomposite thin films reveal that in the vicinity of the layered silicate aggregates the polymer film is discontinuous, devoid of polymer, while remote regions remain continuous. The discontinuities are more severe in the OLS(E)/copolymer nanocomposite with 47% excess surfactant than in the OLS(E)/copolymer nanocomposite with 32% excess. Figure 1 shows a typical AFM topographical image of the vicinity of an aggregate in a copolymer/OLS(E)-47%. The initial thickness of the film was $h \sim 30\text{nm}$ and it contained 3wt% OLS(E). The accompanying line scan indicates that the local thickness at the edge of the film is $\sim 34\text{nm}$. These discontinuities were present in films of thickness $h < 180\text{nm}$ but were not present in thicker films. It is important to note that examination of films with larger weight fractions of OLS(E) revealed a greater degree of disruption of the film. In this paper, we only concern ourselves with small weight fractions of OLS(E) in order to conveniently examine the effects of the OLS(E) clays on the morphology of the films. The copolymer/Mnt and copolymer/OLS(S) nanocomposite films, in contrast, remained stable, devoid of discontinuities, as shown in the AFM image in Figure 2. The height of the fully developed topographical regions is L .

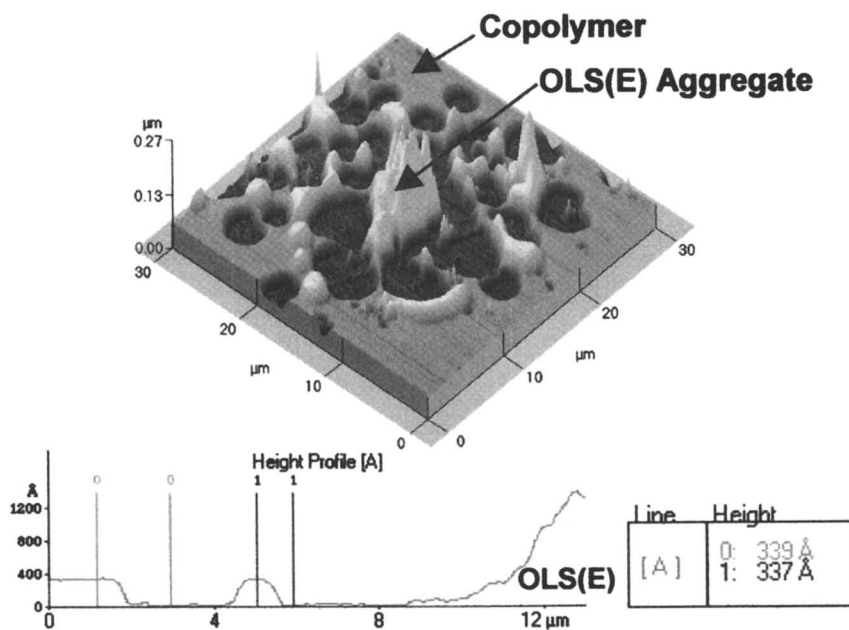


*Figure 1. AFM scan of the destabilized thin film nanocomposite of PS-*b*-PMMA/OLS(E) – 47% excess alkyl ammonium surfactants is shown. A line scan through this image shows the height of the first layer is 34nm. The film contained 3wt% OLS(E), was of initial thickness 35nm and was annealed for 21h at 170°C.*

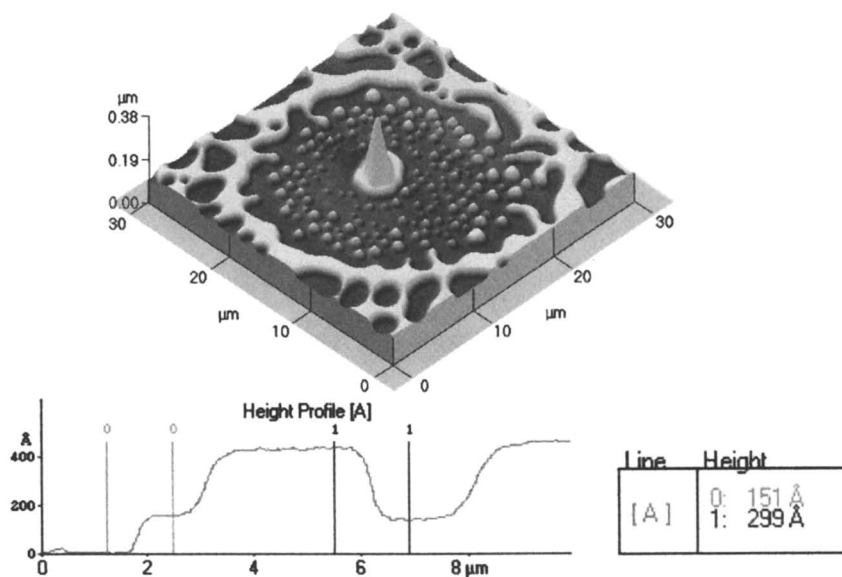


*Figure 2. Shown here is an AFM image of the surface of a PS-*b*-PMMA/OLS(S) film, initially 30nm thick, that was annealed for 138h at 170°C. The film remains stable under these conditions. The line scan is of an edge of the film that was scored to expose the SiO_x prior to annealing. The height of the first layer is 15nm. PS-*b*-PMMA/Mnt films behave in a similar manner.*

Microscopy reveals that the behavior of homopolymer based nanocomposite thin films was different from copolymer based hybrids. All PS based nanocomposite thin films of $h < 150\text{nm}$ were structurally unstable. Figure 3 depicts the morphology of such PS based hybrid films. Under similar conditions, PMMA based nanocomposite thin films were more stable than the PS based films. PMMA/OLS(E) films were unstable, as shown in Figure 4. Below we discuss the origins of structural instabilities in thin films (15-20).

3. Destabilization of Thin Films

The parameter that determines whether a liquid wets a substrate, or instead, forms a droplet with a finite angle of contact is the spreading coefficient S , $S = \gamma_{sv} - \gamma_{ls} - \gamma_{lv}$, where γ_{sv} is the substrate/vapor interfacial tension, γ_{ls} is the liquid/substrate interfacial energy, and γ_{lv} is the liquid/vapor interfacial energy. The condition for wetting is satisfied for $S \geq 0$, whereas for $S < 0$, a droplet of a finite contact angle will form in order to minimize the liquid/substrate interfacial area. The angle of contact a small liquid droplet makes with a substrate is determined by a balance of the interfacial forces at the line of contact. A large droplet, on the other hand, forms a “pancake” shape due to the effects of gravity, and the thickness, h_{eq} , of this layer will be determined by a balance between the gravitational forces and the vertical capillary forces (23).

For films much thinner than h_{eq} , the free energy change per unit area associated with the formation of the film on the substrate is determined by the capillary energies and by the long-range intermolecular van der Waals (VDW), dispersive (apolar), forces: $G(h) = \gamma_{ls} + \gamma_{lv} + P_e(h)$ (15,24). In this equation, P_e is the VDW contribution, which for thin films, $P_e(h) = -A_{132}/(12\pi h^2)$. A_{132} is the effective Hamaker constant and the subscripts 1, 2 and 3 refer to the substrate, surrounding medium and film, respectively. A_{132} is a measure of the strength of interactions between the molecules in the film and those of its surroundings and is determined by the polarizability of the molecules in the medium (24).

Small amplitude thickness modulations at the liquid-air interface exist due to external disturbances, such as thermal fluctuations or mechanical vibrations. For systems in which $A_{132} > 0$, surface perturbations can become amplified by the disjoining pressure, $\Pi = -\partial G(h)/\partial h = -A_{132}/(6\pi h^3)$. The disjoining pressure accounts for the tendency of the film to adjust its thickness in order to minimize the free energy. When $d\Pi/dh > 0$, disturbances are amplified, whereby thicker regions of the film increase in height at the expense of thinner regions of the film. The Laplace pressure, the ratio of the surface tension to the local radius of curvature of the film, tends to oppose the disjoining pressure, thereby stabilizing the film. The disjoining pressure and the Laplace pressure determine a critical wavelength beyond which the instability will grow. If the film is sufficiently

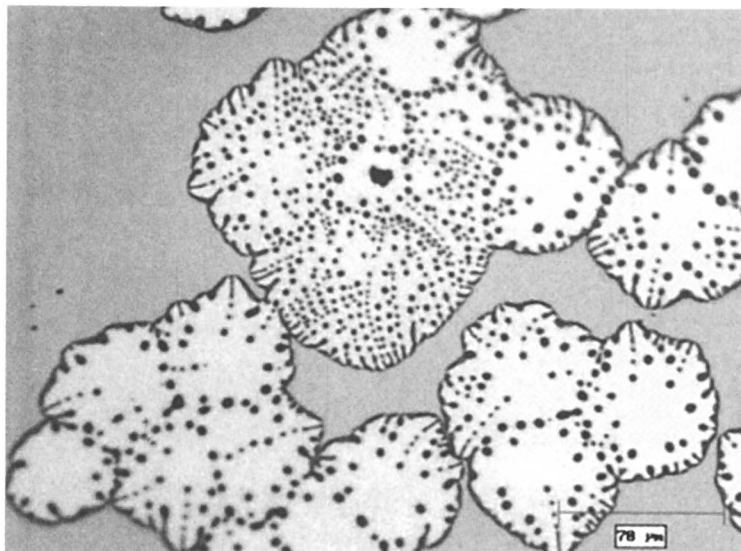


Figure 3. An optical micrograph of the surface of polystyrene/MNt thin film nanocomposite magnified 200x is shown after 30min of annealing at 170°C. Films of $h < 150\text{nm}$ were unstable.

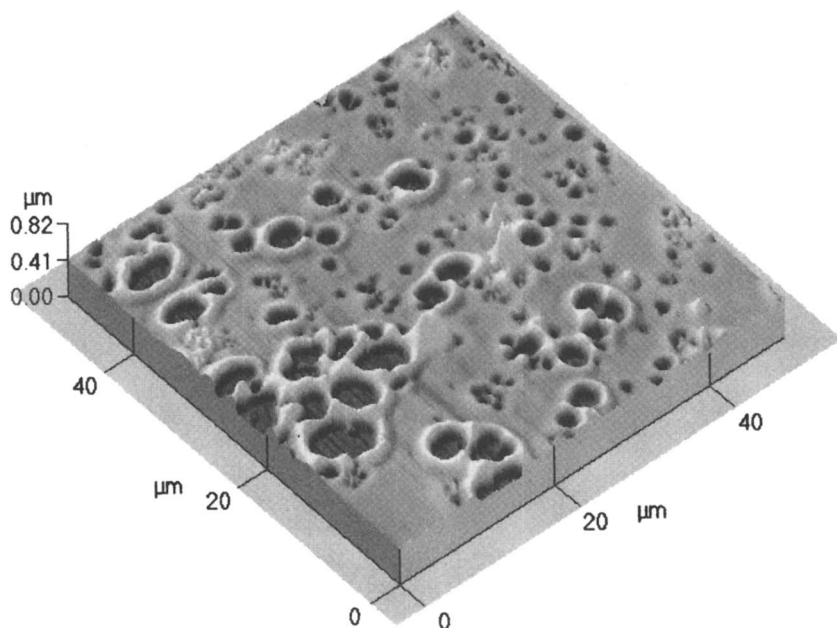


Figure 4. An AFM micrograph of the surface of polymethylmethacrylate/OLS(E)-(47% excess alkyl ammonium ions) film is shown. The nanocomposite contained 7wt% OLS(E), was of initial thickness 90nm, and is shown after 2h of annealing at 170°C.

thin, it will rupture, creating patterns that reflect fluctuations in the local film thickness.

Three classes of patterns have been observed. In one class, cylindrical holes appear at random locations throughout the surface of the film (16,17). The structure evolves via the growth of these holes that subsequently impinge. In the second, asymmetric holes appear randomly throughout the surface of the film (18). The structural evolution is determined by the nucleation rate of the films instead of the growth of holes. In the third, bicontinuous spinodal-like patterns appear spontaneously throughout the surface of the film (19,20).

It is known that the Hamaker constant for polystyrene on SiO_x is less than zero, $A_{132} > 0$ (20), explaining the observation that the PS based hybrid films were completely destabilized (Figure 3). The PS-b-PMMA films, on the other hand, should be stable on SiO_x , where $A_{132} < 0$, yet were destabilized in the vicinity of the OLS(E) aggregates (Figure 1) but not the OLS(S) aggregates (Figure 2). This behavior is discussed below.

4. Ordering and Surface Morphology of Copolymer Thin Films

Symmetric A-b-B diblock copolymers form a lamellar structure of alternating A-rich and B-rich phases below an order-disorder transition temperature ($\chi N > 10.5$). The interlamellar spacing $L \sim N^{2/3} \chi^{1/6}$ if the system is strongly segregated ($\chi N \gg 10.5$). χ is the Flory-Huggins segment-segment interaction parameter (25). In thin films, the lamellae are oriented normal to the substrate if the components have a strong preferential affinity for the substrate and for the free surface (25-28). In the case of PS-b-PMMA, the PMMA component has a strong preferential affinity for the SiO_x substrate, due to polar interactions, and the PS component, with the lower surface energy (at 170°C), preferentially resides at the free surface.

A thin film of this copolymer on SiO_x exhibits characteristic topographical features when its thickness is below a few hundred nanometers (26,27). The surface of a thin uniform film of this copolymer is smooth if its thickness is $h = (n+1/2)L$, where n is an integer. In this film, the first layer of the copolymer in contact with the SiO_x substrate is of thickness $L/2$, whereas subsequent layers are of thickness L . For the PS-b-PMMA diblock copolymer $N = 642$, this thickness $L = 30\text{nm}$ at 170°C (27). The temperature dependence of L is weak since the temperature dependence of χ is weak. If the thickness of the film is $h = (n+1/2)L + \Delta H$, and $\Delta H < L/3$, the surface comprises islands of height L (Figure 5a). When $L/3 < \Delta h < L/2$, a bicontinuous structure of thickness L (Figure 5b) appears at the surface, whereas holes of depth L (Figure 5c) appear at the surface when $L/2 < \Delta H < L$. In essence, the topographical features appear when the condition $h = (n+1/2)L$ is not met. This is favored over the formation

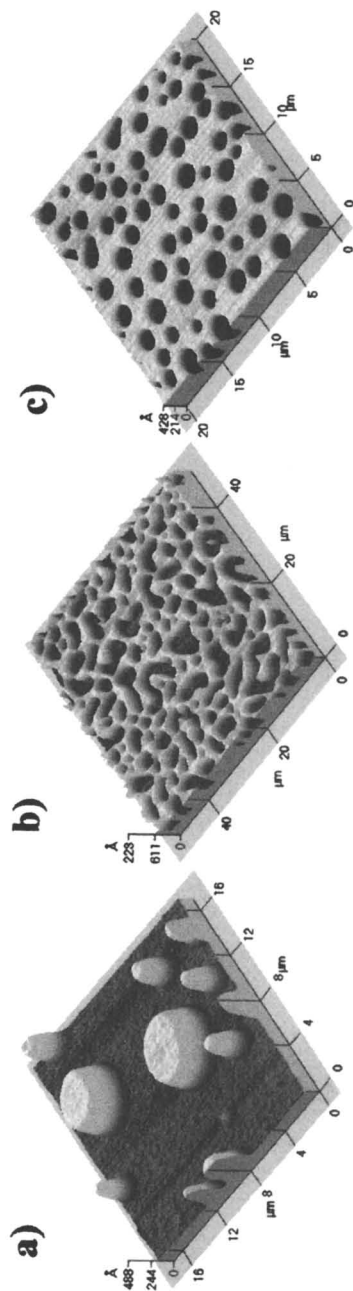


Figure 5. Topographies of a symmetric PS-*b*-PMMA diblock copolymer thin films are shown here: a) islands, b) bicontinuous, and c) holes. The structures are of height L , the dimension of the equilibrium interlamellar spacing.

of a film with an outer layer of sub-optimal thickness less than L . The foregoing argument applies to initially smooth films. However, if the film thickness is non-uniform, then the topography of local regions of the film is determined by the local film thickness, h_{local} .

Another important property of these films on SiO_x is that the edges of these films will restructure upon annealing to form steps (27). The height of the step in contact with the substrate is $L/2$, whereas all other steps are of height L . In short, the topographical features of the film provide an indication of ordering in these materials.

5. Copolymer/OLS Nanocomposites: Morphology

We are now in a position to discuss the differences in the morphologies of the OLS(S)/copolymer, OLS(E)/copolymer and Mnt/copolymer films. Recall that the OLS(S)/copolymer and Mnt/copolymer films were stable, with similar topographies (Figure 2). In the case of the OLS(S)/copolymer and Mnt/copolymer, the copolymer is ordered with the PMMA component of the copolymer in contact with the substrate and the PS component located at the free surface. The height of the first layer of these samples is $H_1 = L/2 = 15\text{nm}$, confirming this. This is typical of the PS-*b*-PMMA copolymer on SiO_x . The topographies of these samples simply reflect the changes in the local film thickness.

The behavior of the OLS(E)/copolymer thin films was different. Dewetting of the copolymer in the vicinity of the OLS(E) aggregates exposed the SiO_x substrate, while remote regions were stable (Figure 1). The topographical features in these films clearly indicate that the copolymer is ordered, even in the vicinity of the OLS aggregates. In these OLS(E)/copolymer samples however, H_1 is slightly larger than L in the vicinity of the OLS(E) aggregates, whereas it is approximately $L/2$ in regions away from the OLS(E) aggregates. A line profile, Figure 6, of the edge of the film in the vicinity of an OLS(E) structure reveals that the height of the first step is $H_1 = 31\text{nm}$, whereas the other is $H_2 = 30\text{nm}$. These dimensions are representative of numerous line scans taken at the edges of the films in the vicinity of the OLS(E) structures. The only conditions under which the first layer would be comparable to L and not to $L/2$ is if the same component of the diblock copolymer resided at the substrate and at the free surface. This component would have to be PS since it has the lower surface energy. This situation is depicted in Figure 7.

The dewetting of the film near the OLS(E) aggregates and the fact that the PS component is now at the free surface and at the substrate suggest two things. First, the copolymer/ SiO_x substrate interactions have been modified such that PS now resides at both interfaces. This would be consistent with the fact that the

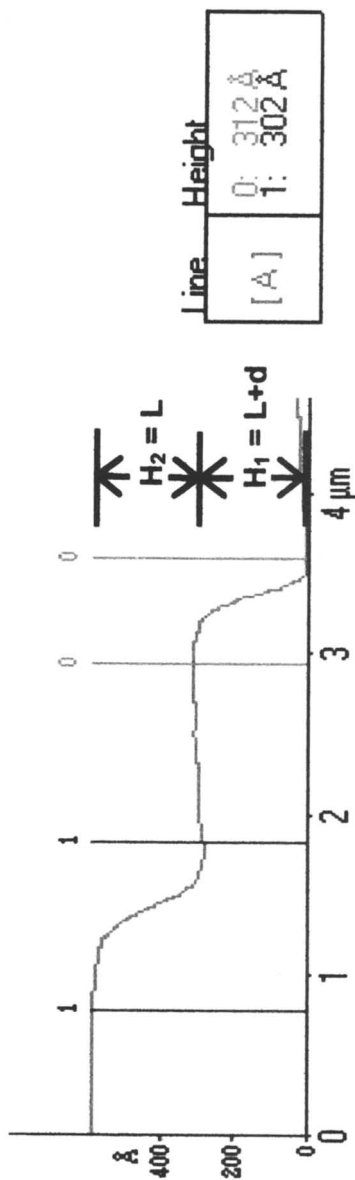


Figure 6. An AFM line scan of the edge of the PS-b-PMMA film in the vicinity of OLS(E) aggregates is shown.

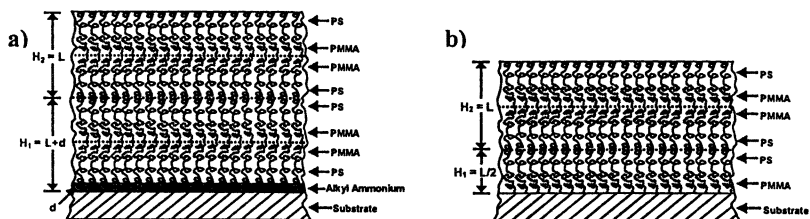


Figure 7. a) An illustration of the arrangement of the ordered symmetric PS-*b*-PMMA on a layer of alkyl ammonium of thickness d . The PS component resides at the free surface and also on this alkyl layer such that $H_1 = L + d$. b) When the PMMA component resides on the substrate, such as SiO_x , PS resides at the free surface and the thickness of the first layer $H_1 = L/2$.

excess organic surfactants have a preferential affinity for the SiO_x substrate over the PS and PMMA components of the diblock. It forms a layer of thickness d , as shown in Figure 7.

Further, we note that the copolymer films only become unstable when they are sufficiently thin. The change in the effective Hamaker constant in the vicinity of the OLS(E) aggregates is consistent with the dewetting in the vicinity of the OLS(E) aggregates. This would be expected if a layer of surfactant formed between the SiO_x substrate and the copolymer.

We might examine the effects of the alkyl ammonium on the copolymer film in more detail by preparing mixtures of alkyl ammonium surfactant with PS-*b*-PMMA diblock copolymer. Normally, the diblock would be stable on the SiO_x substrate, however there were signs of dewetting throughout the film after annealing. When the film thickness is greater than L , the edge of regions that dewet forms steps, indicating an ordered structure. The height of the first step is greater than L , $H_1 = L + d$, where $d \sim 1\text{ nm}$ and $H_2 = L$, indicating that a layer of the surfactants forms on the SiO_x substrate and that PS resides at both interfaces of the film. In regions remote from the dewetted areas, the film is stable and $H_1 = L/2$, characteristic of lamellar orientation on SiO_x where the PMMA-component is located at the substrate and PS at the free surface, as schematically depicted in Figure 7b. Finally we note that if the surfactant was miscible with the copolymer and had a preferential affinity for SiO_x then $H_1 = H_2 = H_3$ and the system would have been stable, at least over a reasonable range of surfactant/copolymer compositions.

Concluding Remarks

We examined the phase behavior and morphology of hybrid PLS thin film nanocomposites on silicon oxide substrates. For the systems examined, polymer chain intercalation does not occur in pristine montmorillonite layered silicate systems but does occur in the OLS thin film systems, as expected. While the effect of the PS, PMMA and PS-*b*-PMMA based thin film materials on the gallery separations are similar to that of bulk systems, the situation regarding the copolymer/OLS(E) nanocomposite thin films is different. An exchange between the copolymer chains with the excess untethered surfactants within the galleries occurs. The surfactant preferentially segregates to the substrate, displacing the copolymer chains. This affects the substrate copolymer interactions, leading to structural changes (dewetting) in the film in the vicinity of the OLS(E) aggregates. These structural changes were not observed in the OLS(S)/copolymer or Mnt/copolymer hybrid thin film materials. It is important to note that for polymer systems that are strongly attracted to SiO_x, such as 5-norbornene-2-methyl-d₃-carboxylate (29), these thin film nanocomposites are stable after annealing. The phase behavior of thin film nanocomposite hybrid materials is dictated largely by the same factors that influence the behavior of bulk materials. However, the relative surfactant/substrate, surfactant/free surface, polymer/free surface and the polymer/gallery wall interactions are additional factors that influence the stability and morphology of the films.

Acknowledgments

R. Limary acknowledges help from S. Swinnea with the X-ray diffraction studies. This work was supported by the National Science Foundation (DMR-0072898), the State of Texas coordinating board advanced technology program (ATP), and the Robert A. Welch Foundation.

References

1. Alexandre, M.; Dubois, P. *Mater. Sci. and Eng.* **2000**, *28*, 1.
2. LeBaron, P. C.; Wang, Z.; Pinnavaia, T. J. *Appl. Clay Sci.* **1999**, *15*, 11.
3. Giannelis, E.P.; Krishnamoorti, R.; Manias, E. *Adv. Poly. Sci.* **1998**, *138*, 108.
4. Dietsche, F.; Thomann, Y.; Thomann, R.; Mulhaupt, R. *J. Appl. Poly. Sci.* **2000**, *75*, 396.

5. Krishnamoorti, R.; Giannelis, E.P. *Macromolecules* **1997**, *30*, 4097.
6. Pinnavaia, T.J. *Science* **1983**, *220*, 365.
7. Theng, B.K.G. *The Chemistry of Clay-Organic Reactions* John Wiley and Sons: New York, 1974.
8. Theng, B.K.G. *Formation and Properties of Clay-Polymer Complexes* Elsevier: New York, 1979.
9. Solomon, D.H. *Chemistry of Pigments and Fillers* Kreiger, Malabar, FL, 1991.
10. Kuznetsov, D. V.; Balazs, A. C. *J. Chem. Phys.* **2000**, *112*, 4365.
11. Ginzburg, V. V.; Balazs A. C. *Macromolecules* **1999**, *32*, 5681.
12. Vaia, R.A.; Giannelis, E.P. *Macromolecules* **1997**, *30*, 8000.
13. Shi, H.; Lan, T.; Pinnavaia, T.J. *Chem. Mater.* **1996**, *8*, 1584.
14. Vaia, R.A.; Jandt, K.D.; Kramer, E.J.; Giannelis, E.P. *Macromolecules* **1995**, *28*, 8080.
15. Brochard-Wyart, F.; Daillant, J. *Can. J. of Physics* **1990**, *68*, 1084.
16. Limary, R.; Green, P. F. *Langmuir* **1999**, *15*, 5617.
17. Segalman, R. A.; Green, P. F. *Macromolecules* **1999**, *32*, 801.
18. Masson J-L.; Green, P. F. *J. Chem. Phys.* **2000**, *112*, 349.
19. Limary, R.; Green, P. F. *Macromolecules* **1999**, *32*, 8167.
20. Xie, R.; Karim, A.; Douglas, J. F.; Han, C. C.; Weiss, R. A. *Phys. Rev. Lett.* **1998**, *81*, 1251.
21. Binder, K. *Adv. Polym. Sci.* **1999**, *138*, 1.
22. Limary, R.; Swinnea, S.; Green, P. F. *Macromolecules* **2000**, *33*, 5227.
23. de Gennes, P. G. *Rev. Mod. Phys.* **1985**, *57*, 827.
24. Israelachvili, J.N. *Intermolecular and Surface Forces* Academic Press: London (1985).
25. See for example: Bates, F.S.; Fredrickson, G.H. *Annual Review of Physical Chemistry* **1990**, *41*, 525.
26. Coulon, G.; Russell, T.P.; Deline, V.R.; Green, P.F. *Macromolecules* **1989**, *22*, 2581.
27. Orso, K.A.; Green, P.F. *Macromolecules* **1999**, *32*, 1087.
28. Coulon, G.; Collin, B.; Ausserre, D.; Chatenay, D.; Russell, T.P. *J. Phy. France* **1990**, *51*, 2801.
29. Smith, M. D.; Saunders, R. A.; Green, P.F. *Macromolecules* **1999**, *32*, 8392.

Chapter 13

Influence of Layered-Silicates on the Rheological Properties of Diblock Copolymer Nanocomposites

Cynthia A. Mitchell and Ramanan Krishnamoorti*

Department of Chemical Engineering, University of Houston,
Houston, TX 77204

The influence of silicate loading and lateral dimensions on the linear viscoelastic properties of a polystyrene-polyisoprene diblock copolymer is studied. Three thermodynamically equivalent organically modified layered silicates differing in lateral dimension are used. The effect of the domain structure of the block copolymer and the level of dispersion of the layered silicate on the rheological properties are examined by comparing data for the nanocomposites in the ordered and disordered state of the block copolymer. Hybrids prepared with 5 wt. % organically modified fluorohectorite (diameter ~ 10 μ) and montmorillonite (dia. ~ 1 μ), demonstrate a notable decrease in frequency dependence at low frequencies in the disordered state, and are understood in terms of a percolated layered silicate network structure. On the other hand, the viscoelastic properties in the disordered state of a hybrid prepared with 5 wt. % organically modified laponite (dia ~ 30 nm) and those in the ordered state for all nanocomposites, demonstrated only minor changes from that observed for the unfilled polymer.

INTRODUCTION

Understanding the rheological properties of polymer layered-silicate nanocomposites is crucial to gain a fundamental understanding of the processability and structure-property relations for these materials. It has been conjectured that, in the case of polymer layered silicate nanocomposites, the melt rheological properties are dictated by a combination of the mesoscopic structure and the strength of the interaction between the polymer and the layered silicate¹. The mesoscopic structure would be crucially dependent not only on the strength of the polymer/layered-silicate interaction, but also on the inherent viscoelastic properties of the matrix in which the layers or collection of silicate layers are dispersed.

Previous studies have addressed the linear and non-linear viscoelastic properties of intercalated and exfoliated layered silicate based nanocomposites with homopolymers and disordered block copolymers¹⁻⁶. Those studies have shown that the dispersion and the ability of the dispersed silicate layers (usually montmorillonite) to form a percolated network structure dominate the linear viscoelastic response. Pseudo-solid like behavior with the presence of a finite yield stress is observed for nanocomposites with silicate loading as low as 3 wt. % for exfoliated montmorillonite and at ~ 5 wt. % for intercalated montmorillonite¹. On the other hand, the non-linear viscoelastic properties of those hybrids, while being altered by the state of dispersion, are dramatically altered by the strength of the polymer layered-silicate interactions^{1,4}.

In this paper we focus on the influence of varying the layered silicate on the linear viscoelastic properties of a block copolymer that undergoes a transition from an ordered lamellar microdomain state to a disordered state with increasing temperature. We study the influence of three organically modified layered silicates with lateral dimensions of the layers being the primary difference: fluorohectorite with an equivalent plate diameter of ~ 10 μ , montmorillonite with a plate diameter of ~ 1 μ and laponite with a diameter of 30 nm. Since the charge exchange capacity (CEC) are different (fluorohectorite - 150 meq / 100 gm, montmorillonite - 90 meq / 100gm and laponite - 75 meq / 100 gm), we have employed organic modifications such that the surface coverage of the layered silicates are roughly equivalent, rendering them thermodynamically equivalent to the intercalation of polymers⁷⁻⁹. By comparing the viscoelastic data in the disordered state (i.e., homopolymer like) to that in the ordered state of the polymer, we examine the influence of the domain structure of the block copolymer and layered-silicate dispersion on the dynamic properties of these hybrids. These studies also form the basis of an investigation to examine the influence of the layered silicates in the ordering kinetics and morphology development of the ordered state in lamellar block copolymers¹⁰.

EXPERIMENTAL

A monodisperse polystyrene - polyisoprene diblock copolymer (PSPI19) prepared by sequential anionic polymerization was used in this study. The molecular weight of PSPI19 is 19,300 and the PS content is ~ 44 wt. % and forms ordered lamellar structures below the order - disorder temperature T_{ODT} of 88.5 ± 0.5 °C. Three organically modified layered silicates were used: an octadecyl trimethyl ammonium modified fluorohectorite (C18F), a dioctadecyl dimethyl ammonium modified montmorillonite (2C18M), and a dioctadecyl dimethyl ammonium modified laponite (2C18L). Layered silicates were cleaned by repeated refluxive distillation using boiling ethanol followed by filtration to remove all excess alkyl ammonium. The absence of any excess alkyl ammonium was ascertained by a silver nitrate test of the supernatant and by thermogravimetric analysis (TGA) of the cleaned and dried layered silicate.

Nanocomposites were prepared by solution mixing appropriate quantities of polymer and the finely ground layered silicates at room temperature in toluene. The mixtures were allowed to dry at room temperature and subsequently annealed at ~ 110 °C in a vacuum oven for ~ 24 hours to ensure removal of any remaining solvent and to facilitate dispersion. Nanocomposites with 1 and 5 wt. % layered silicate were prepared using all three layered silicates.

X-ray diffraction was performed using a Siemens D5000 X-ray diffractometer with Cu- K_{α} radiation ($\lambda = 1.54$ Å) generated at 30 mA and 40 kV. Diffraction measurements were performed over 2θ values from 2 to 10°, in steps of 0.02°, with intensities measured for 1 second at each angle.

Rheological measurements were performed on a Rheometric Scientific ARES rheometer with a torque transducer capable of measurements over the range of 0.2 to 2000 g_f cm. Dynamic oscillatory measurements were performed using a set of 25mm diameter parallel plates with a sample thickness of 1-2 mm and a temperature range of 84 to 94 °C. A time dependent oscillatory strain ($\gamma(t)$) of the form

$$\gamma(t) = \gamma_0 \sin(\omega t) \quad (1)$$

where γ_0 is the strain amplitude and ω is the frequency, is applied and the resulting time dependent linear shear stress ($\sigma(t)$) is interpreted as

$$\sigma(t) = \gamma_0 (G' \sin(\omega t) + G'' \cos(\omega t)) \quad (2)$$

where G' and G'' are the storage and loss modulus respectively. All measurements in this study are linear viscoelastic (i.e., G' and G'' are independent of γ_0) and interpreted using equation 2.

Samples were quenched from the disordered state (94 °C) to a temperature of 85 °C and allowed to equilibrate for ~ 1 hour. The conditions for the growth of the ordered state were chosen so that the system acquired equilibrium rapidly. After ordering, isothermal frequency scans ($0.01 \leq \omega \leq 100$ rad/sec) were conducted at successive temperatures in 0.5 °C increments. Equilibration at the specified temperature was ensured by allowing the samples to equilibrate under quiescent conditions for 15 min after the temperature was reached. Ordered block copolymers are susceptible to shear induced alignment; thus making it necessary to use low strain amplitudes to ensure linearity. In the ordered state strain amplitudes of less than 5% were employed enabling an accurate measurement of the linear viscoelastic moduli over the range of temperatures and frequencies measured.

RESULTS AND DISCUSSION

STRUCTURE

X-ray diffraction spectra for the 5 wt. % nanocomposites using the three different layered silicates are presented in Figure 1. The nanocomposites based on C18F and 2C18M result in intercalated structures, while that prepared with 2C18L exhibits no diffraction peak and is consistent with that of a disordered intercalated or exfoliated structure. Similar results were obtained for the 1-wt. % hybrids and are not shown here. For the intercalated hybrids, the increase in gallery height of ~ 1.3 nm over that of the organically modified layered silicate and ~0.4 nm over PS based nanocomposites is consistent with the findings of Ren et al.¹¹. This increase in gallery height of PSPI intercalated nanocomposites as compared to PS based nanocomposites is notable, and is attributed to inclusion of the thermodynamically unfavorable PI block within the interlayer galleries. Previous studies have demonstrated the thermodynamic incompatibility of homopolymer PI with the layered silicates and have also suggested the development of intercalated hybrids with PS to the presence of favorable interactions between the PS and the silicate surface^{7,8}.

As noted earlier, the three layered silicates are roughly thermodynamically equivalent as a result of the combinations of CEC and organic modification used⁸. Thus, differences in structure of the nanocomposites (intercalated versus disordered), as demonstrated by x-ray diffraction, are primarily attributable to the difference in particle size and the ability of tactoids of smaller layered silicates to disaggregate and exhibit diminished layer-layer registry. If there exist no thermodynamic barriers to the disaggregation of the stacks of layers (tactoids) to single sheets, then the layers can remain uncorrelated with respect to each

other until an overlap concentration of individual layers is achieved. Beyond such an overlap concentration we expect the individual layers to no longer be uncorrelated and in fact form domains with a preferential orientation of the layers. A simple calculation of the overlap concentration of individual layers in a polymer or solvent matrix, suggests that the critical weight fraction for overlap scales as $1/R_h$, where R_h is the radius of an equivalent disc representing a silicate layer. Such a calculation suggests that the overlap concentration for C18F and 2C18L are roughly three orders of magnitude different, with the laponite based hybrids showing considerable overlap only beyond 10 wt. %.

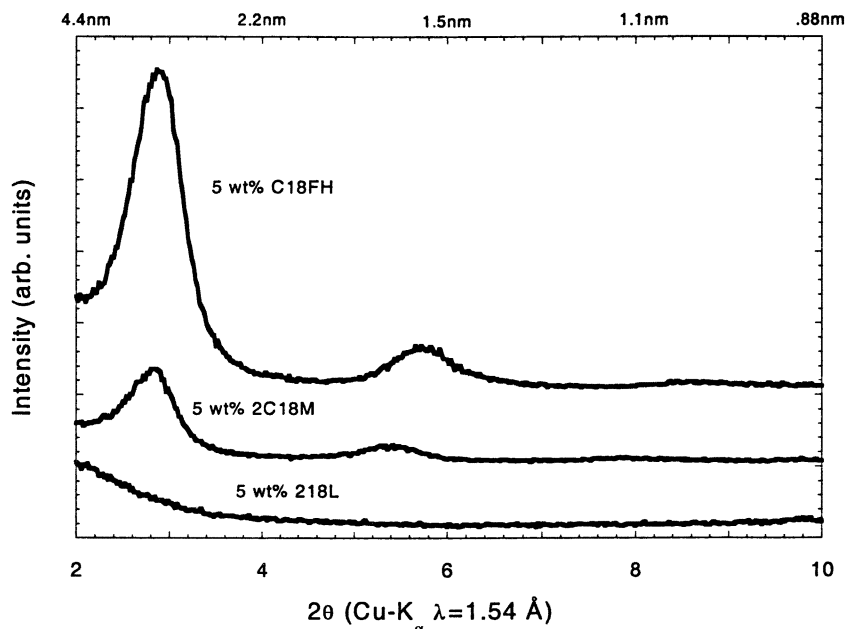


Figure 1 X-ray diffraction spectra for the 5 wt. % nanocomposites using the three different layered silicates. The hybrid prepared with 2C18L exhibits no diffraction peak and is consistent with that of a disordered-intercalated or exfoliated hybrid. The hybrids prepared with C18F and 2C18M exhibit an expansion of gallery height over their respective layered silicates indicating intercalated hybrids.

Based on the diffraction data shown in Figure 1, it is clear that the layer – layer registry improves with increasing particle size. Previously, Gilman and coworkers¹² and Ren et al¹¹ have shown that for hybrids prepared with montmorillonite a wide range of tactoid sizes coexist – ranging from well

intercalated stacks of 30 layers to exfoliated single layers. On the other hand, Vaia et al.¹³ and Manias et al.¹⁴ have shown that for hybrids based on fluorohectorite, the layers are stacked together in well-arranged tactoids even in the presence of strongly interacting polymers. On this basis and the simple geometric arguments presented above, it is not surprising to find that for the PSPI19 based hybrids, those prepared with C18F lead to well-defined intercalated structures, while 2C18L hybrids are disordered intercalated structures (or even delaminated) and the 2C18M hybrids are intermediate with regions which are intercalated and regions where the layers are delaminated.

VISCOELASTICITY

Linear viscoelastic time-temperature superposed mastercurves for PSPI19 obtained by superposing isothermal frequency scans over a temperature range of 84 to 94 °C are shown in Figure 2. For this and all other viscoelastic mastercurves shown in this paper we chose a reference temperature T_0 of 90 °C. The data were shifted using horizontal and vertical shift factors (a_T and b_T respectively, and discussed in detail below) so as to superpose simultaneously all viscoelastic functions at high frequencies, where the relaxation processes are dominated by single-chain processes and changes in mesostructure should have negligible influence. The storage and loss moduli (G' and G'' respectively) at low frequencies fail to superpose below and above the order – disorder transition temperature (T_{ODT}), and we identify the ODT as 88.5 ± 0.5 °C. Above T_{ODT} , (i.e., the disordered state) the viscoelastic functions form mastercurves over the entire frequency regime as evidenced by the data in Figure 2. At temperatures just below T_{ODT} , the viscoelastic functions do not superpose presumably due to the changing microdomain structure in the vicinity of the ODT and also as a result of enhanced composition fluctuations.^{15,16}

PSPI19 is presumed to be lightly entangled based on the known entanglement molecular weights of PS and PI ($M_{e, PS} = 18k$ and $M_{e, PI} = 7k$)¹⁷ and the molecular weight and composition of PSPI19. In the disordered state, below $a_T\omega$ of ~ 7 rad/sec, PSPI19 exhibits pure liquid-like relaxation behavior consistent with that of a disordered polymer.

The longest relaxation time, τ , of a lightly entangled polymer is determined by extrapolating the G' and G'' versus ω lines in the terminal region (disordered state) to the point of intersection, ω_{int} .¹⁸ Depending on the extent of entanglement, the value of τ lies between $2/\omega_{int}$ and $3/\omega_{int}$ (with $\omega_{int} \sim 12.5$ rad/sec) which for PSPI19 is determined to be $\sim 1 - 1.5$ sec at 90 °C.

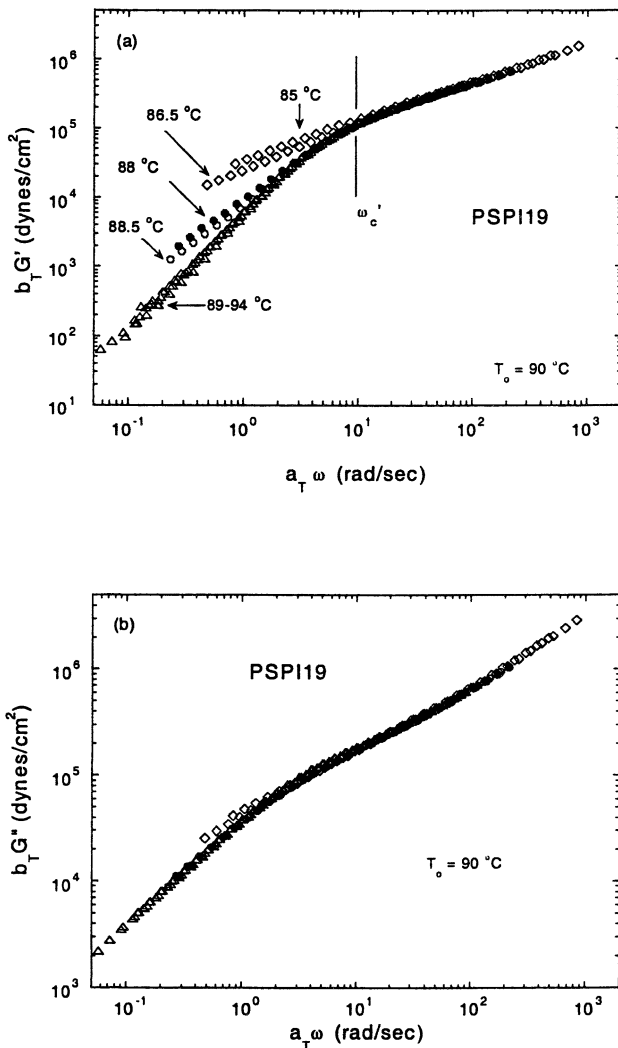


Figure 2. Time-temperature superposed linear viscoelastic moduli: (a) storage modulus, G' and (b) loss modulus, G'' for unfilled PSP119. Data were superposed at high frequencies using both horizontal (a_T) and vertical (b_T) shift factors (Figure 6 and Table 1). We identify a frequency ω_c' in Figure a, the frequency below which G' across the ODT do not superpose.

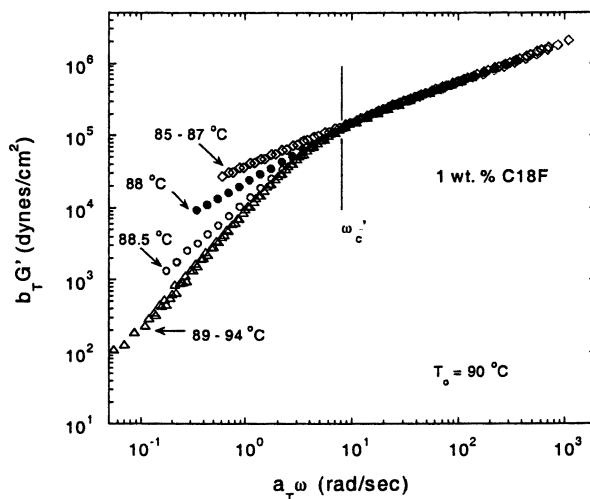


Figure 3. G' mastercurve for the 1 wt. % C18F hybrid. The data for this hybrid are similar to that for the unfilled PSPI19 suggesting that small amounts of layered silicate have negligible effect on the viscoelastic properties of the polymer. Similar data were also obtained for the 1 wt. % 2C18M and 2C18L nanocomposites.

The G' mastercurve for the hybrid prepared with 1 wt. % C18F is presented in Figure 3. Since the storage modulus G' exhibits the most significant changes across the ODT as shown in Figure 2¹⁹, and when layered silicates are added to a disordered block copolymer or homopolymer as shown by Krishnamoorti et al^{2,3} and Ren et al¹¹, we focus only on the changes in the storage modulus G' in the rest of the paper. The data for the 1 wt. % C18F is similar to that for the unfilled PSPI19, aside from a slight enhancement in the value of the modulus at all frequencies. This data is also comparable to that for the 1 wt. % 2C18M and 2C18L nanocomposites (not shown here), and suggests that the addition of small amounts of layered silicate has negligible effect on the viscoelastic properties and the location of the ODT. Increasing the silicate content to 5 wt. % results in further enhancement of G' at all frequencies. Similar to the 1 wt. % hybrids, the high frequency dependence remains essentially unchanged for each of the 5 wt. % layered silicate hybrids (Figures 4 and 5), suggesting that the chain relaxation modes are unaffected by the presence of the layered silicate. However, in the disordered state at low frequencies, i.e., below ~ 7 rad/sec, the 5 wt. % hybrids of 2C18M and C18F (Figure 4) exhibit a notable reduction in frequency dependence which are discussed in detail below. From the viscoelastic mastercurves we conclude that the ODT for the 1 wt. % nanocomposites is unaffected by the addition of the layered silicates, while the ODT for the 5 wt. % nanocomposites, at least from the rheological signatures, appears to be slightly affected by the addition of the layered silicate - decreasing by ~ 1 to 1.5 °C for

the 2C18M and C18F hybrids. For the 5 wt. 2C18L hybrid, on the other hand, the ODT for the block copolymer appears to be unaffected by the addition of the layered silicate.

The temperature dependence of the frequency shift factors (a_T) is shown in Figure 6. The values of a_T are, within the errors of the experiment, independent of the silicate and silicate loading and similar to that of the unfilled polymer. As discussed previously by Ren and coworkers¹¹, this suggests that the temperature dependent relaxation observed is similar to that of the polymer. The data above the ODT are in excellent agreement with that from Ren et al¹¹ on a disordered PSPI block copolymer with roughly the same composition. Also, observed in Figure 6, is a discontinuity in the a_T values at the ODT, with the data above and below the ODT having roughly similar temperature dependence, although the temperature window is too narrow to allow for a critical evaluation of the temperature dependence above and below the ODT. We believe the discontinuity is a result of an abrupt change in the relaxation phenomena, as a result of the thermodynamic and structural changes across the order - disorder transition. The magnitude of the discontinuity is small and comparable for the nanocomposites and the unfilled polymer. A combination of a T_{ODT} in close proximity to the T_g of the PS block and a relatively narrow temperature window of examination allows for a clear exposition of the discontinuity.

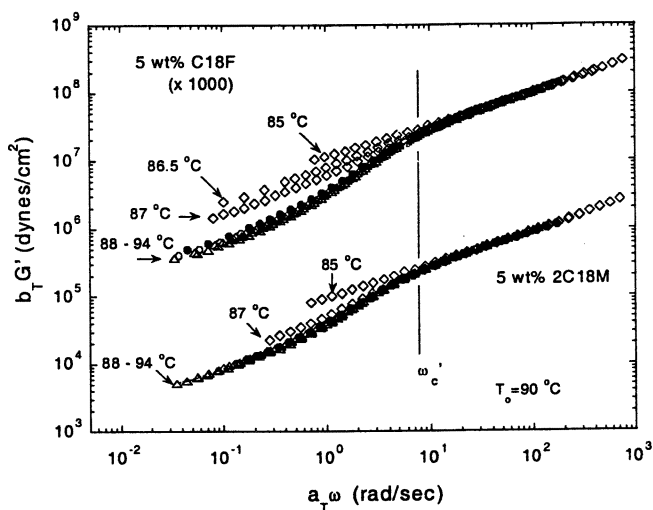


Figure 4. G' mastercurves for the 5 wt. % C18F and 2C18M nanocomposites. The high frequency dependence remains unchanged from that of the unfilled PSPI19 and 1 wt. % hybrids; however, in the disordered state at low frequencies there is a notable reduction in the frequency dependence of G' . In the ordered state on the other hand, the viscoelastic data are qualitatively unaffected by the addition of the layered silicate. A small decrease in T_{ODT} is also observed for both of these hybrids.

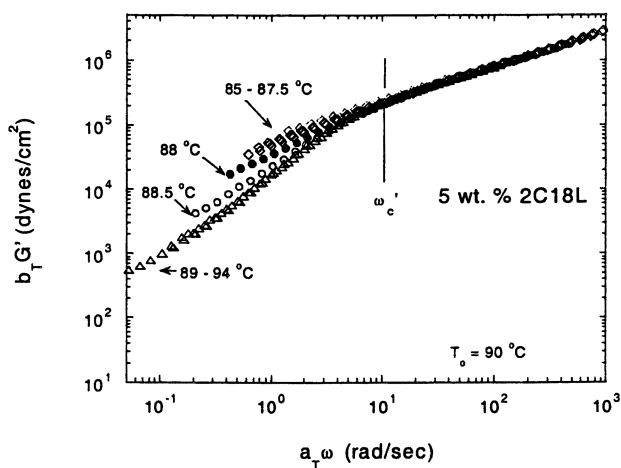


Figure 5. G' mastercurve for the hybrid with 5 wt. % 2C18L. In the disordered state, there is a slight reduction of the frequency dependence at low frequencies. However, in the ordered state, the observed viscoelastic behavior is similar to the unfilled PSP119 and all other nanocomposites.

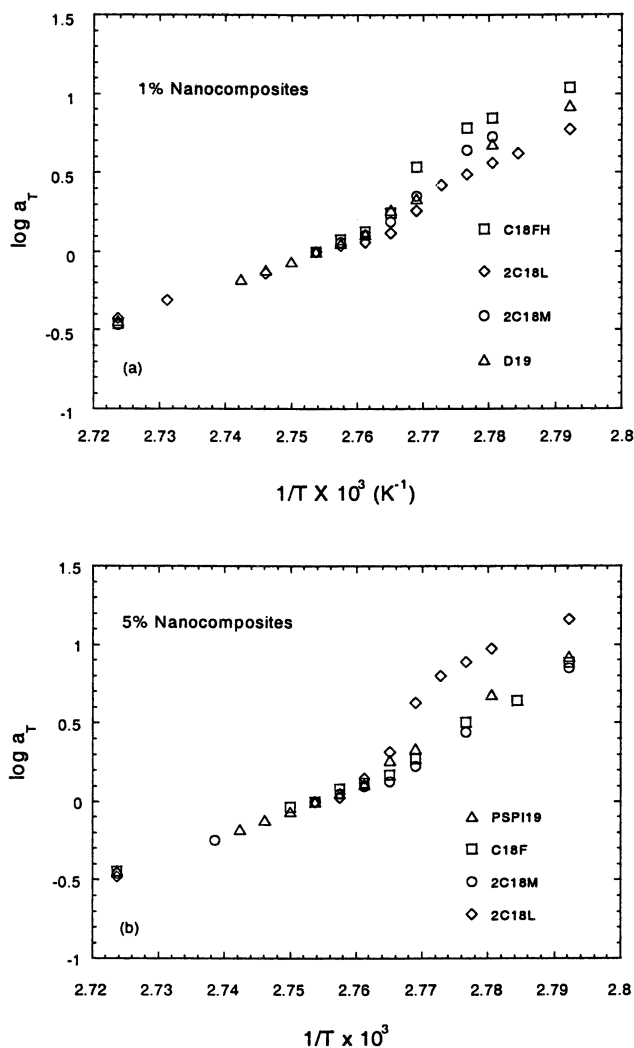


Figure 6. Temperature dependence of the frequency shift factors (a_T) for PSPI19 and the different hybrids examined: (a) PSPI19 + 1 wt. % hybrids (b) PSPI19 + 5 wt. % hybrids.

On the other hand, the modulus shift factors (b_T) shown in Table 1 are large in value below the ODT. However, they do not vary significantly from unity above the ODT. Further, the b_T values do not vary significantly with silicate

loading and, similar to the a_T values, are comparable for the 1 and 5 wt. % silicate loadings within experimental errors. The ordered state temperatures probed are, as mentioned above, in close proximity to the T_g of the PS block and are also just ≤ 4 °C from T_{ODT} . Such proximity to the ODT may suggest considerable changes in the microdomain structure and could lead to additional contributions to the modulus as suggested by Fredrickson and Larson²⁰ leading to b_T values significantly different from unity. Additionally, across the ODT the environment surrounding the high T_g PS changes significantly and results in dramatic changes in the viscoelastic contribution from the PS block and possibly resulting in the large changes in the magnitude of the modulus across the ODT.

Table 1 Modulus Shift Factors (b_T) for PSPI19 and the Different Hybrids

Sample	Temperature °C							
	85.0	86.5	87.0	88.0	88.5	89.0	89.5	94
PSPI19	1.55	1.50		1.10	1.08	0.98	0.97	0.96
1 % 2C18L	1.28	1.28	1.22	1.11	0.92	0.92	0.96	1.03
1 % 2C18M		1.92	1.87	1.40	1.08	1.06	1.03	0.96
1 % C18F	1.77	2.12	2.10	1.77	1.22	1.02	1.04	0.91
5 % 2C18L	2.30	2.17	2.11	1.72	1.24	1.09	1.01	0.96
5 % 2C18M	1.48		1.15	1.00	0.95	1.00	1.00	0.91
5 % C18F	1.95	1.64	1.51	1.13	1.05	1.03	1.02	0.96

The viscoelastic mastercurves presented in Figures 2 - 5 demonstrate the influences of adding layered silicate as well as layered silicate size on the viscoelastic properties in both the ordered and disordered state. As noted previously, the addition of 1 wt. % of the three layered silicates has negligible influence on the viscoelastic properties. In the case of the 2C18M based nanocomposites, the low frequency response of G' in the disordered state suggests a transition from a liquid-like response for the unfilled PSPI19 and the 1 wt. % hybrid to a pseudo-solid like character at 5 wt. % silicate (demonstrated by a near frequency independent G' and G' exceeding G'' at the lowest frequencies). These results are analogous to those of Ren et al.¹¹ where they demonstrated using linear dynamic oscillatory and steady shear measurements that hybrids with ~ 5 wt. % or higher 2C18M (based on PSPI18 and PS30) exhibit pseudo solid like behavior with the presence of a yield stress in steady shear measurements. These results are understood in terms of a quiescent structure of the nanocomposite consisting of tactoids of several tens of layers along with individual layers dispersed that are randomly oriented. Such a structure, beyond extremely low silicate loadings, results in the tactoids and

occasional silicate layers being correlated and hence restricted from free rotation, leading to the presence of a layered-silicate network structure. The average tactoid size (n_{per}) and the critical silicate fraction ($w_{\text{sil,per}}$) for the formation of a silicate network are related by ¹¹:

$$n_{\text{per}} = \frac{4}{3\phi_{\text{per}}} \left[\frac{w_{\text{sil,per}}\rho_{\text{org}}}{w_{\text{sil,per}}\rho_{\text{org}} + (1 - w_{\text{sil,per}})\rho_{\text{sil}}} \right] \frac{R_h}{h_{\text{sil}}} \quad (3)$$

where, R_h is the radius of the hydrodynamic volume and equivalent to the radius of the layered silicate, h_{sil} is the thickness of the silicate layers, and ρ_{org} and ρ_{sil} are the densities of the polymer and layered-silicate respectively. For the case of 2C18M, it turns out that for a $w_{\text{sil,per}}$ of 5 wt.%, the average tactoid size is ~ 30 , and consistent with the stack size based on XRD measurements and direct TEM measurements on analogous systems. Such an average tactoid size suggests an effective anisotropy of the tactoids to be of the order of 5 - 10.

The disordered state data for the C18F based nanocomposites exhibit a similar response to that observed for the 2C18M nanocomposites. The larger layer diameter (roughly ten fold higher than 2C18M) and the higher extent of order (i.e., larger stack size) compensate and result in the data for the C18F to resemble that for the 2C18M based hybrids. On the other hand, the 5 wt. % 2C18L nanocomposite, does not exhibit pseudo solid-like behavior in the disordered state although the frequency dependence of G' is somewhat reduced from that of the unfilled polymer. This contrast between the C18F and 2C18L based nanocomposites is most clearly seen in Figure 7. Based on equation 3 and assuming a tactoid size of 1 (i.e., complete exfoliation), we estimate the $w_{\text{sil,per}}$ as 7 % for the 2C18L silicates. The aggregation of the laponite layers into larger disordered tactoids would lead to an enhancement of this percolation threshold to higher silicate loading. In this light, the differences in the disordered state viscoelasticity for the 2C18L based nanocomposites and that of the 2C18M and C18F based hybrids can be reconciled in terms of dispersion and the resulting differences in effective aspect ratios of the layered silicates.

In contrast, the data for the nanocomposites in the ordered state for all three layered silicates remarkably show little differences to that for the unfilled polymer in the ordered state. Aside from a monotonic increase in the magnitude of the modulus at all frequencies with addition of layered silicate, the frequency dependence of the modulus remains unaffected with increasing amount of the three different layered silicates. For the case of the 5 wt. % 2C18M and C18F, this is a particularly surprising result, as in the disordered state the low frequency data (at comparable reduced frequencies) is dominated by the percolated network structure of the layered silicate. However, the viscoelastic data at low frequencies for ordered block copolymers is dominated by the mesoscopic

granular structure and by the motion of the defects present ²¹. Additionally, the critical frequency ω_c' , designated as the frequency below which the dynamics across the ODT do not superpose, which has often been used to denote the coupling of chain relaxation to microdomain relaxation is unchanged for the nanocomposites in comparison to that of the unfilled polymer. This suggests that the domain structure and the coupling of domain and chain relaxation remain essentially unaffected by the addition of the layered silicate. Thus, the viscoelastic data in the ordered nanocomposites, shown in Figures 3-5 and 7, suggest that the moduli are dominated by the same mechanisms responsible for the increased modulus at low frequencies in the unfilled block copolymers and not by the mesoscopic dispersion and possible percolation of the layered silicates.

CONCLUSIONS

The melt-state linear viscoelastic properties and order-disorder transition temperature (T_{ODT}) of a polystyrene-polyisoprene diblock copolymer were essentially unaltered by the addition of 1 wt. % organically modified layered silicate regardless of lateral dimension of the layered silicate. An increase in the amount of layered silicate to 5 wt. % resulted in a slight lowering in T_{ODT} ($\sim 1 - 1.5$ °C) of the 2C18M and C18F (with layer diameters of ~ 1 and 10 μ respectively) based hybrids as well as a notable reduction of frequency dependence at low frequencies above the ODT. Differences in the linear viscoelastic data upon increasing the layered silicate concentration are attributable to the differences in aspect ratios of the layered silicates, which dictate the level of dispersion and the mesoscopic structure of the hybrids. Consistent with this hypothesis, use of 5 wt. % a much smaller diameter layered silicate (2C18L), which is thermodynamically equivalent to the other two layered silicates, results in only slight alterations to the long time relaxation behavior of the nanocomposites in the disordered state of the polymer. On the other hand, in the ordered state of the block copolymer where the mesoscopic microdomain structure of the ordered copolymer dominates the relaxation behavior, the viscoelastic data for the nanocomposites are qualitatively unaffected by the addition of the layered silicate, and only result in slight increases in the value of the modulus.

ACKNOWLEDGEMENTS

The authors gratefully thank Dr. Adriana S. Silva, Koray Yurekli and Jiaxiang Ren for numerous useful discussions. Funding support from NSF (DMR-9875321), the donors of the Petroleum Research Fund administered by

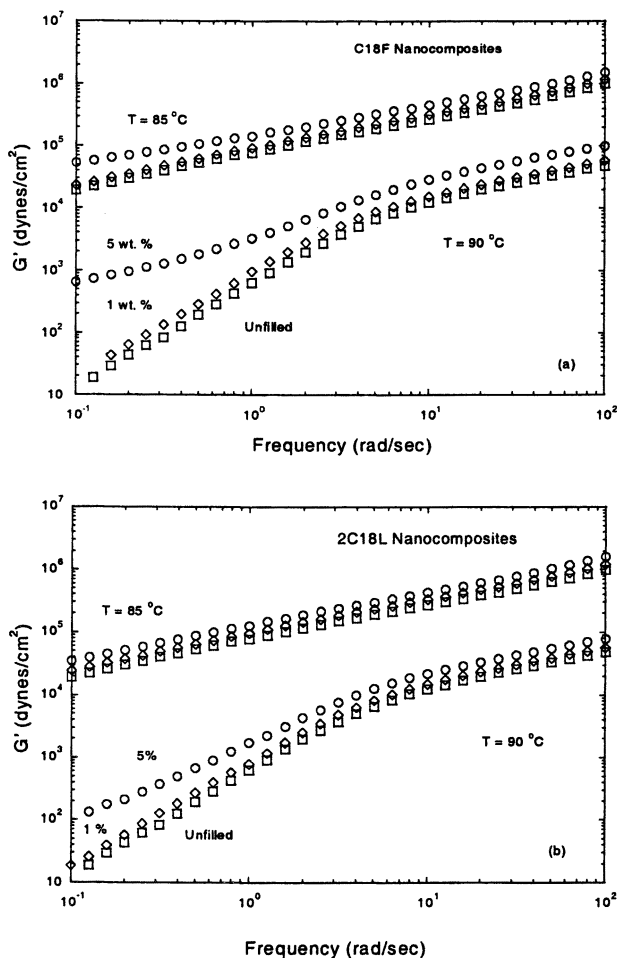


Figure 7. G' of the unfilled PSP119 and (a) the 2C18L hybrids; and (b) the C18F hybrids in the ordered (85 °C) and disordered states (90 °C). While the ordered state data is essentially unaffected by the addition of different layered silicates, the disordered state data (particularly for the 5 wt. % hybrids) demonstrate a significant dependence on the choice of silicate.

the American Chemical Society and from the Texas Coordinating Board (ATP) is gratefully acknowledged. This work made use of TCSUH/MRSEC Shared Facilities supported by the State of Texas through TCSUH and by NSF (DMR-9632667).

REFERENCES

- (1) Krishnamoorti, R.; Silva, A. S. In *Polymer-Clay Nanocomposites*; Pinnavaia, T. J., Beall, G., Eds.; Wiley: New York, 2000; Vol. In Press.
- (2) Krishnamoorti, R.; Giannelis, E. P. *Macromolecules* **1997**, *30*, 4097-4102.
- (3) Krishnamoorti, R.; Vaia, R. A.; Giannelis, E. P. *Chem. Mater.* **1996**, *8*, 1728.
- (4) Krishnamoorti, R.; Giannelis, E. P. *Langmuir* **2000**, Accepted.
- (5) Giannelis, E. P.; Krishnamoorti, R.; Manias, E. *Adv. Polym. Sci.* **1999**, *138*, 107-147.
- (6) Solomon, M. J.; Almusallam, A. S.; Seefeldt, K. F.; Somwangthararoj, A.; Varadan, P. *Macromolecules* **2000**, Submitted.
- (7) Vaia, R. A.; Giannelis, E. P. *Macromolecules* **1997**, *30*, 7990 - 7999.
- (8) Vaia, R. A.; Giannelis, E. P. *Macromolecules* **1997**, *30*, 8000-8008.
- (9) Balazs, A. C.; Singh, C.; Zhulina, E. *Macromolecules* **1998**, *31*, 8370 - 8381.
- (10) Mitchell, C. A.; Yurekli, K.; Krishnamoorti, R. **Manuscript in Preparation**.
- (11) Ren, J.; Silva, A. S.; Krishnamoorti, R. *Macromolecules* **2000**, *33*, 3739-3746.
- (12) Gilman, J. W.; Jackson, C. L.; Morgan, A. B.; Harris, R., Jr.; Manias, E.; Giannelis, E. P.; Wuthenow, M.; Hilton, D.; Phillips, S. H. *Chem. Mater.* **2000**, *12*, 1866 - 1873.
- (13) Vaia, R. A.; Jandt, K. D.; Kramer, E. J.; Giannelis, E. P. *Macromolecules* **1995**, *28*, 8180.
- (14) Manias, E.; Chen, H.; Krishnamoorti, R.; Genzer, J.; Kramer, E. J.; Giannelis, E. P. *Macromolecules* **2000**, Accepted.
- (15) Gehlsen, M. D.; Almdal, K.; Bates, F. S. *Macromolecules* **1992**, *25*, 939 - 943.
- (16) Bates, F. S.; Rosedale, J. H.; Fredrickson, G. H. *Journal of Chemical Physics* **1990**, *92*, 6255.
- (17) Fetters, L. J.; Lohse, D. J.; Milner, S. T.; Graessley, W. W. *Macromolecules* **1999**, *32*, 6847-6851.

- (18) Ferry, J. D. *Viscoelastic Properties of Polymers*; 3 ed.; Wiley: New York, 1980.
- (19) Adams, L. J.; Graessley, W. W.; Register, R. A. *Macromolecules* **1994**, *27*, 6026.
- (20) Fredrickson, G. H.; Larson, R. G. *J. Chem. Phys.* **1987**, *86*, 1553.
- (21) Fredrickson, G. H.; Bates, F. S. *Ann. Rev. Mater. Sci.* **1996**, *26*, 501-550.

Chapter 14

Dispersion and Nucleating Effects of Clay Fillers in Nanocomposite Polymer Films

Vincent Ferreiro, Gudrun Schmidt, Charles Han,
and Alamgir Karim*

Polymers Division, National Institute of Standards and Technology,
Gaithersburg, MD 20899-8542

Nanocomposite polymeric materials offer unique property advantages such as mechanical, electrical, thermal, etc. Such property enhancements are induced not only by the physical presence of the filler but also by the interaction of the polymer with the filler and the dispersion state of the filler. In the first section of the paper, we investigate the case of well dispersed laponite (synthetic clay) filler particles. Thin films cast from solutions of polyethylene-oxide (PEO)-laponite on glass substrates were prepared. Drying of the cast polymer-clay solutions produce transparent nanocomposite films and the laponite dispersion state appears to be trapped in the thin films. An optimal dispersion is obtained for a particular PEO/laponite ratio (r), that we find to be equal to $r \approx 0.66$. In a latter section of the paper, we investigate the case of weakly dispersed clay fillers. We find that weakly dispersed or "stacked" clay fillers can be used as nucleating agents ("seed" crystallization) in the crystallization of a clay-filled polymer blend (PEO / PMMA / Montmorillonite) film. As a function of increasing clay concentration, we make the novel observations that the number of dendritic branches increase substantially and tend to curl.

Introduction

A recent upsurge of interest in polymer-clay nanocomposites due to their potential as low-cost materials with enhanced properties, has resulted in significant research into the synthesis and properties of nanocomposite materials¹⁻⁶. However, much of this effort has been directed into measuring the bulk and solution properties and the chemistry of intercalation and exfoliation of the clay-fillers for forming such materials⁷⁻⁹. In contrast, the material properties of thin films of nanocomposite materials have not been explored to any significant extent. Nanocomposite thin films should pose interesting opportunities for exploiting property enhancements not only due to the available large polymer-clay surface area of contact, but also from geometric confining factors that induce a preferred orientation of the clay platelets relative to the film surface. Such an orientation may generate unique property enhancements like gas and vapor barrier properties in membranes of these materials. However, there have been very few reports on effects of preparation on dispersion and properties of thin nanocomposite films with a film thickness in the micrometer to nanometer scale range. We investigate nanocomposite films in this thickness range with the idea of studying dispersion effects on clay filled polymer film morphology and properties.

We first study the case of well dispersed Laponite (synthetic clay) filler particles. Thin films cast from solutions of polyethylene-oxide (PEO)-Laponite on glass substrates were prepared. Drying of the cast polymer-clay solutions produces transparent nanocomposite films and the Laponite dispersion state appears to be trapped in the thin films. An optimal dispersion is obtained for a particular PEO/Laponite ratio (r), $r \approx 0.66$ for the range of $0.33 < r < 1.66$. We next investigate the crystallization of a clay-filled polymer blend (PEO/PMMA/Montmorillonite) using the nucleating character of weakly dispersed clay fillers. Previous work¹⁰ has shown that the surface enrichment of one blend component about the particles leads to a *counter enrichment* of the other phase about the first layer. This wave-like pattern of composition about the filler particles is probably important for stimulating crystallization about the clay particles. We find interesting dendritic patterns as a function of clay content.

Experimental

PEO/Laponite Films preparation

The synthetic hectorite type clay, Laponite, LRD, was provided by Laporte Industries Ltd¹¹. The clay particles are composed of platelets of high purity and

uniform crystallite size^{12,13}. In an aqueous medium, the clay forms transparent dispersions of disk shaped particles ca. 300 Å in diameter and ca. 10 Å thick^{12,13}. Poly(ethylene-oxide) with a $M_w = 1,000,000$ g/mol was purchased from Polysciences Inc.¹¹. Various concentrations of LRD and PEO were prepared in distilled deionized water and mixed for at least 2 weeks (Table 1). The pH and ionic strength of the solutions were controlled by the addition of NaOH and NaCl, respectively. For all samples in this study a pH value of 10 and a NaCl concentration of 10^{-3} mol/L were used. Under these conditions a flocculation due to the dominance of van der Waals attraction over electrostatic repulsion of the clay particles is avoidable¹⁴. LRD, LRD2, LRD5 solutions were cast on glass slides and dried at 25 °C for 24 h under vacuum. Transparent films with an average thickness of 5 µm were obtained by spreading the filled polymer solution on a glass substrate with a blade. The surface morphology and the roughness of these films have been characterized by AFM.

Table1. PEO/Laponite Film Characteristics

sample	PEO mass fraction, % PEO in solution (D ₂ O)	PEO mass fraction, % PEO in dried films	LRD mass fraction, % LRD in solution (D ₂ O)	LRD mass fraction, % LRD in dried films
LRD	0		3	
LRD2	2	40	3	60
LRD5	5	62.5	3	37.5

PEO/PMMA/Montmorillonite Films Preparation

“Cloisite” (Montmorillonite; MON) clay particles were obtained from Southern Clay Products¹¹. This clay mineral has exchangeable sodium ions, and a cation exchange capacity of ca. 95 meq (milli-equivalent) per 100 g. PEO with average $M_w = 200,000$ g/mol and PMMA of $M_w = 120,000$ g/mol were purchased from Aldrich, USA. MON (1 g) and 50 ml of distilled water at 80°C were placed in 0.1L beaker, and 1 g of distearyldimethyl ammonium chloride was added to the solution. The mixture was stirred vigorously for 1h, then filtered and rinsed three times with 100 ml of hot water to remove NaCl. After being washed with ethanol (50 ml) to remove any excess of ammonium salt, the product was freeze-dried, and kept in a vacuum oven at room temperature for 24 h. The resulting organically modified montmorillonite (OMON) dispersed well in chloroform, although the unmodified montmorillonite (MON) did not disperse. The blend components (PEO/PMMA/OMON) were dissolved in

chloroform at a total mass fraction of 1%, unless otherwise stated. Thin blend films were spin coated onto Si substrates (Semiconductor Processing Co., orientation (100), Type P) at a spin speed of 2000 rounds per minute (rpm). This procedure results in films having a uniform thickness of ≈ 200 nm. Prior to spin coating, the Si wafers were "piranha-etched" to form a native SiO₂ surface layer.

Film Morphology Characterization

Reflective optical images were obtained with an optical microscope (OM) using a Nikon optical microscope with a digital Kodak MegaPlus CCD camera attachment.

All AFM experiments were carried out in air using a Dimension 3100 microscope from Digital Instruments operating in the Tapping modeTM¹¹. In this mode, the cantilever is forced to oscillate at a frequency close to its resonance frequency with an adjustable amplitude. The tip, attached to the cantilever, was a pure silicon single crystal tip (model TSEP) with a radius of curvature of about 10 nm. The tip contacts briefly the film surface at each low position of the cantilever and the amplitude of the oscillation varies. "Height" images are obtained by using the feedback loop that keeps the amplitude at a constant value by translating vertically the sample with the piezoelectric scanner: height measurements are deduced from those displacements. For the engagement we used a ratio $A_{sp}/A_o = 0.9$, where A_o is the free oscillation amplitude and A_{sp} the set-point one^{15,16}. Besides the variation of the amplitude, the dephasing of the cantilever oscillation relative to the signal exciting the piezoelectric driver can be measured: that mode is called "Phase Detection Imaging" (PDI)¹⁷⁻¹⁹ and is usually used to probe local elastic or adhesive properties at the surface. However, in our system, the dynamic force curves show that the phase images do not reveal any difference of mechanical properties between the matrix (PEO) and the fillers. Only, topographic features have been observed, using a ratio $A_{sp}/A_o = 0.8$ which provides a better image contrast. Roughness analyses were also performed on some samples, conducted according to the manufacturer's software program. The root-mean-square (RMS) average of the surface roughness value was calculated as the standard deviation of all the height values within the given area.

Results and Discussion

PEO-Laponite Films

Upon drying, the polymer clay solutions produce transparent nanocomposite films with micro-porous membrane character and elastic properties. These films

(thickness $\approx 5 \mu\text{m}$) were cast from solutions containing 95 % water by mass. We expect that AFM of the dried film may even provide insights into the network character of the polymer in solution. Most reinforcing agents, such as fibers and fillers are large and scatter light, thus reducing light transmittance. Efficient particle dispersion combined with good interfacial adhesion is achieved in the aqueous polymer clay solution and this property is maintained in the film. This is the main reason for transparency. From a practical viewpoint, this allows the exciting possibility of developing strong yet transparent films, coatings and membranes from solution.

AFM images of the pure LRD film (Table 1) are displayed in Figure 1, illustrating the size and orientation of the structured nanoparticles. For comparison the height and phase image of the LRD sample (Figure 1a and 1b) show clay particles which lie flat on the surface. However the RMS roughness of the film is equal to $\approx 12 \text{ nm}$. An arrow in the insert of Figure 1c points to a single platelet. The average diameter of the clay platelets is about 30 nm which is consistent with previous SANS²⁰ experiments and published literature²¹⁻²³. By drying LRD2 we obtain a film with clay particles which are randomly oriented and connected by polymer (Figure 2 a-b). LRD5 dried films exhibit two areas with quite different representative structures (Figure 2 c-d). The first structure is a mesoporous homogeneous film texture with same size particles.

The second structure is a heterogeneous one and contains: 1) domains where only excess PEO is observed (black arrow in Figure 2 c-d) and 2) areas where clay particles are agglomerated (white arrow). In both cases the polymer acts as a connection between particles. LRD2 produces an elastic porous film with clay particles, which are covered and connected by polymer and randomly oriented (Figure 2b). We notice that the RMS roughness of these films decreases with increasing PEO concentration showing that the network produces a smoother surface than the LRD film (RMS roughness (LRD) $\approx 12 \text{ nm}$ and RMS roughness (LRD2 and LRD5) $\approx 5 \text{ nm}$). LRD2 dried films exhibit spherically particles with each particle having the same average diameter compared to one clay platelet (Figure 2b).

In contrast to LRD2, some areas of LRD5 films show domains with excess of PEO. These domains are the white "dots" in Figure 2 c-d. LRD5 solutions studied by SANS and flow birefringence²⁰ show exfoliated clay particles and well dispersed PEO. AFM investigations of LRD5 dried films show that this composition appears to be the critical concentration where a transition from a homogeneous network like structure to a heterogeneous structure occurs. The excess PEO does not contribute to building the network. A more detailed study around this critical concentration will be made in the future. With increasing PEO mass fraction beyond a value of 5 % in a solution, the number and the size of PEO "dots" in a dried film increases, and no isolated clay platelet can be observed since the clay platelets are all polymer covered. In all cases the polymer provides strong connections between clay particles as has been shown by

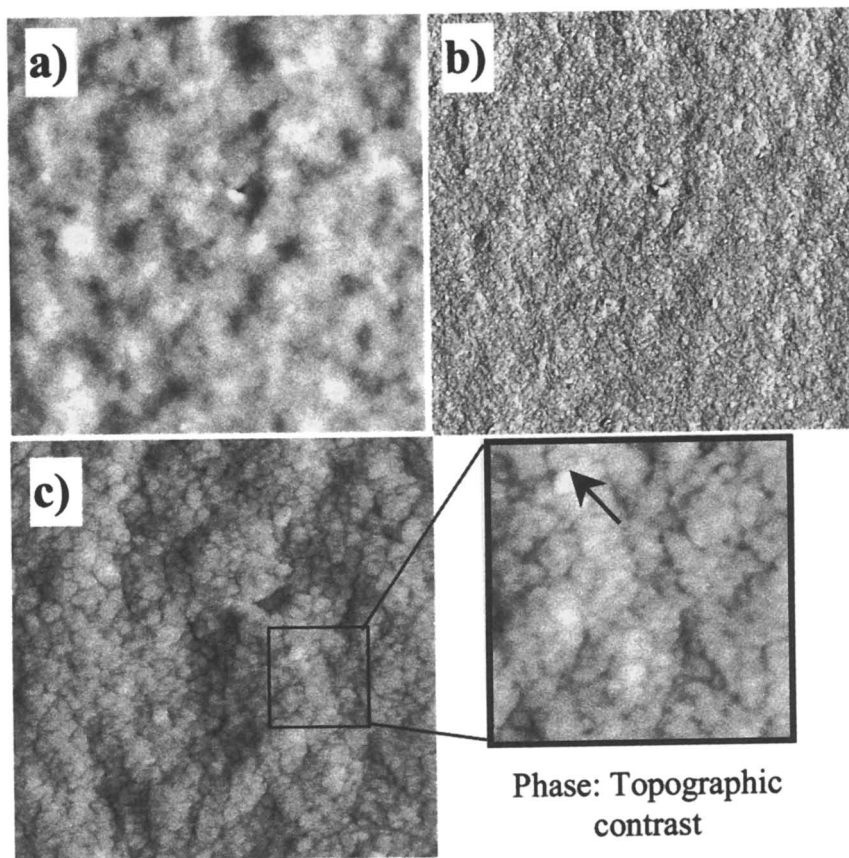


Figure 1. AFM images of LRD film morphology without PEO

a). "Height" AFM image ($3 \mu\text{m} \times 3 \mu\text{m}$) of LRD film , Z range = 48 nm

b). "Phase" AFM image ($3 \mu\text{m} \times 3 \mu\text{m}$) of LRD film, Phase = 34° .

c). On the top right corner a zoom of Fig. 1b show clay flat on with a average diameter of 30 nm ($300 \text{ nm} \times 300 \text{ nm}$), Phase = 55°

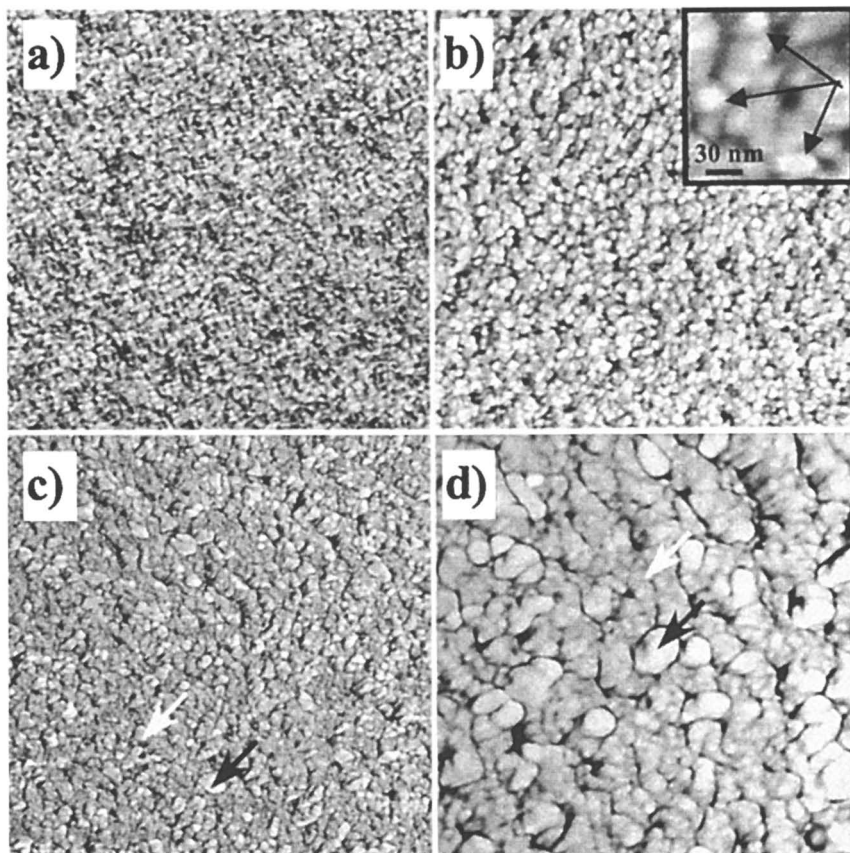


Figure 2. AFM images show the evolution of LRD film morphology as a function of PEO/clay ratio (r)

- a).** "Phase" AFM image ($3 \mu\text{m} \times 3 \mu\text{m}$) of LRD2 film ($r = 0.66$), Phase = 126°
b). "Phase" AFM image ($1 \mu\text{m} \times 1 \mu\text{m}$) of LRD2 film ($r = 0.66$), Phase = 45° (Zoom of Fig. 2a). On the top right corner a zoom of the network is shown ($1 \mu\text{m} \times 1 \mu\text{m}$), phase = 69° . We can see three clay platelet flat on and separated from each other with the same distance. **c).** "Phase" AFM image ($3 \mu\text{m} \times 3 \mu\text{m}$) of LRD5 film ($r = 1.66$), Phase = 111° . **d).** "Phase" AFM image ($1 \mu\text{m} \times 1 \mu\text{m}$) of LRD5 film ($r = 1.66$), Phase = 106° (Zoom of Fig. 2c) showing the PEO in excess and the agglomerated clay particles.

rheology experiments²⁰. Moreover, after annealing the films at 50 °C or after isothermal crystallization in order to crystallize the PEO, no morphological modifications were observed. Additional DSC experiments on LRD2 samples show no crystallization peak in the range of (30 to 200) °C. However LRD5 shows a peak at ≈ 60 °C. While it is possible to form polymer microcrystals inside LRD5, there is not enough PEO chain mobility to crystallize LRD2 because of the strong interactions with the clay fillers within the network. Upon annealing far above the melting temperature of PEO ($T_m = 71$ °C) both films show no dewetting and are stable for hours suggesting there is no degradation of the polymer or film properties.

Preliminary SANS results on both samples show no significant temperature dependence up to 100 °C. However strong concentration dependence was detected ($0.03 \text{ nm}^{-1} > q > 0.3 \text{ nm}^{-1}$), which may be correlated with the morphology as observed in AFM. The clay seems to be completely exfoliated since SANS data show no peaks which would be expected for clay packets.

PEO/PMMA/OMON Films

As a second part of the study, we investigate the case where the clay fillers are weakly dispersed. In this case, we have shown in a previous paper that the clay plays the role of nucleating agents for the crystallization of the PEO. The morphology of polyethylene oxide (PEO) crystallization in a thin film geometry can be "tuned" through spherulitic, seaweed, dendritic and DLA-like crystallization forms through the adjustment of PEO composition and the degree of supercooling. Figure 3 shows the polymer dendrites in a (30/70) mass ratio (PEO/PMMA) blend. The dark features ($\approx 1 \mu\text{m}$ in size) in the optical micrograph correspond to agglomerate clay particle which "seed" the crystallization. The diameter of the clay particle found by TEM on a cast solution OMON/chloroform on copper grid is $\approx 100 \text{ nm}$ as we can see in Fig. 4.

Effect of Temperature and Clay mass concentration on Blend Crystallization Morphology.

After spin-casting, the films were heated to 100 °C for 5 min. in order to melt the PEO. The films are then cooled down to the desired crystallization temperature. PEO/PMMA films were crystallized at different temperatures²⁵. The film thickness was approximately constant ($h = 150 \text{ nm}$) and the clay content was 5 % of the polymer blend mass. A nearly square (equilibrium crystallization) crystal forms for low undercooling (10 °C) and we observe a change to a

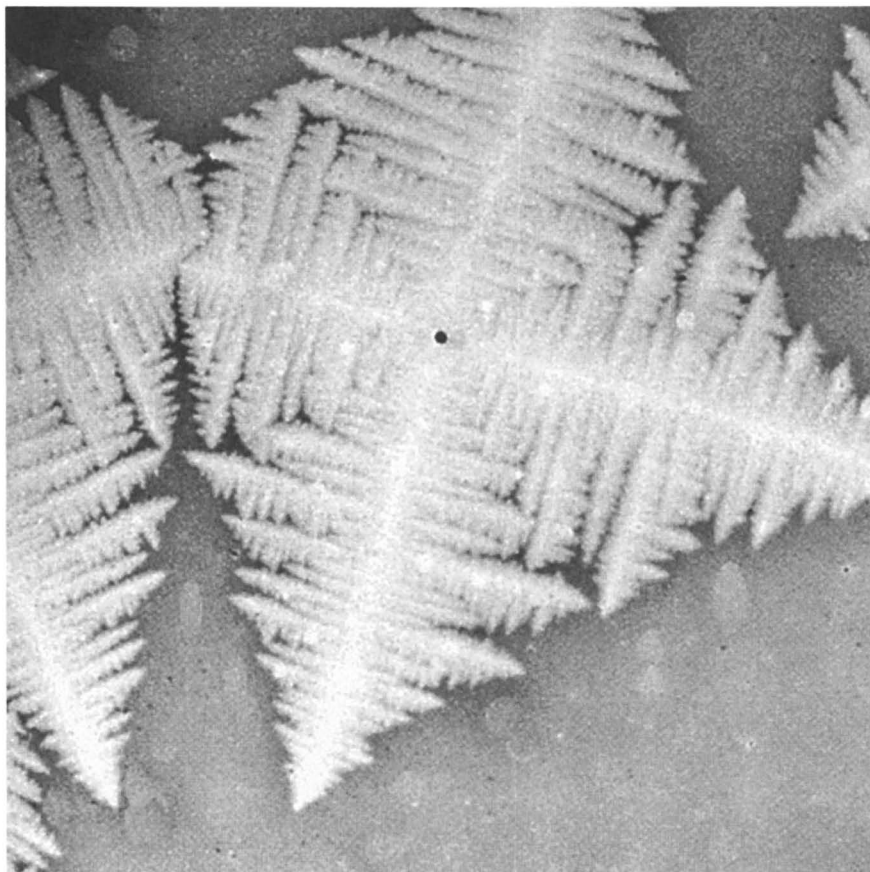


Figure 3. Symmetric dendritic morphology of a (30/70) PEO/PMMA blend film crystallized at 32 °C during 2 h. Optical image shows the regular "star-like" morphology of the dendrites.

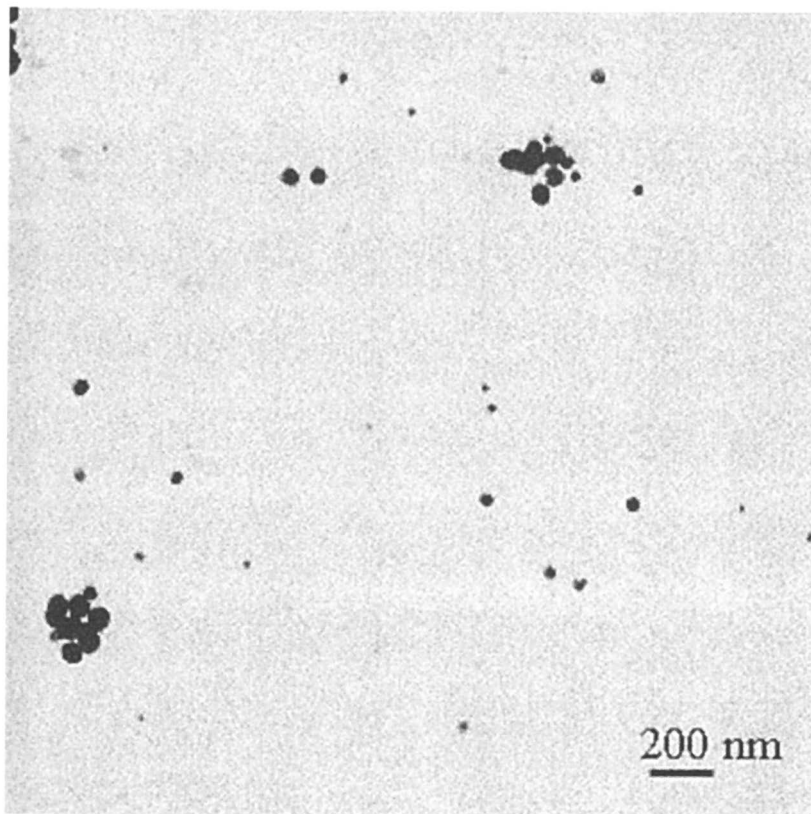


Figure 4. Transmission Electron Microscopy of a dried Clay/Chloroform solution on copper grid. We found a diameter value of the Montmorillonite clay particles between 50 nm and 100 nm.

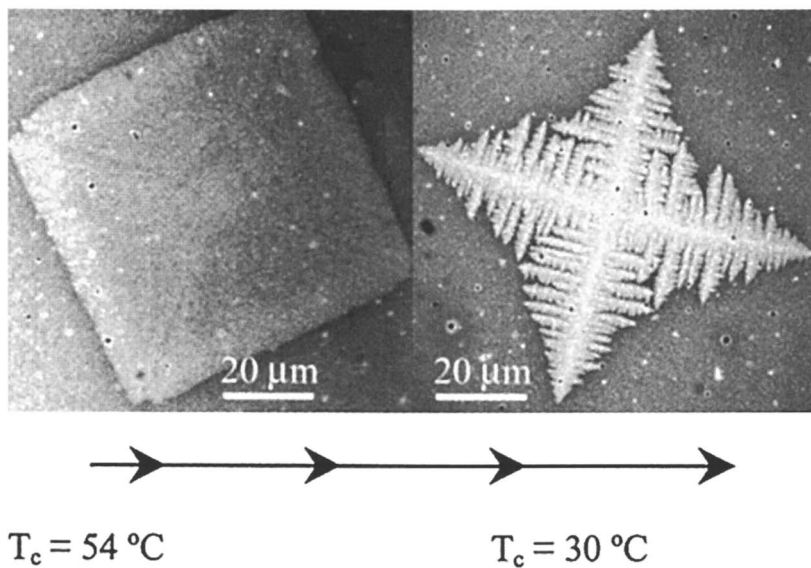


Figure 5. Parameters influencing the morphology of PEO/PMMA blend. Optical images showing the evolution of the dendrite morphology with the degree of undercooling.

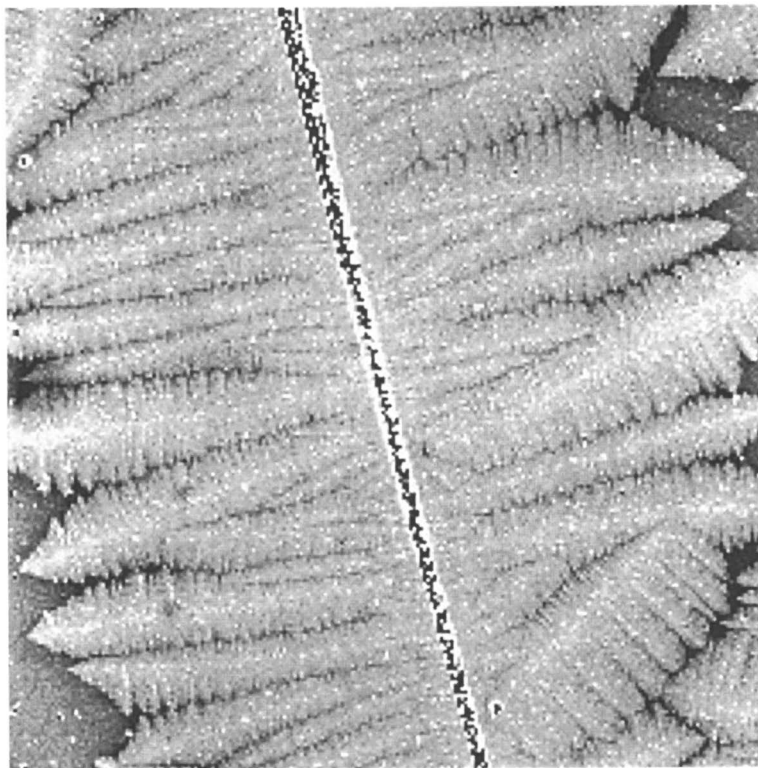


Figure 6. *Optical image showing a dendritic wavefront propagating perpendicularly to a scratch. Crystallization conditions are the same as in Fig. 3, except there is no clay added to the polymer.*

dendritic morphology at high undercooling (35 °C) (Fig. 5) Under identical crystallization conditions (polymer composition, temperature, film thickness) there are no crystallization patterns in the absence of clay particles to nucleate the crystallization. The films are "excitable", however, and scratching a (30/70) PEO/PMMA blend film induces the formation of a dendritic wavefront that propagates to cover the film (Fig. 6). Dust particles were also observed to initiate dendrite growth in PEO/PMMA blend films without the clay filler. We then see that film imperfections can have a large influence on the properties of semi-crystalline blend films.

Adding clay particles can induce other effects than simply nucleate the polymer crystallization. At higher clay content (> 5 %), the interference between competing growth centers (nucleating clay sites) can cause the dendrite arms to further branch, leading to dendrites with an increased numbers of arms. We illustrate this effect in Fig. 7 for a mass fraction of 10 % clay where the relative PEO/PMMA blend composition is again fixed at (30/70). At clay content below 5 %, we only observe dendrites having four arms (See Fig. 3). We also showed in a separate paper that increasing clay particle concentration causes the arm of the dendrite to curl²⁵.

There are no dendrites formed in the blend films without clay or film imperfections (scratches). The local compositional enrichment caused by the clay or defects then appears to be important for nucleating polymer dendrites. There is a subtlety to this heterogeneous nucleation process that was not originally anticipated in the planning of our measurement. The clay particles are nearly spherical in shape [average radius, $R \cong 100$ nm] and have been treated with surfactant to facilitate their dispersal in the polymer blend. We find that the clay particles do not disperse in the pure PEO, but rather segregate to the polymer-air boundary. The PEO films recrystallize into spherulites and appear similar to films without clay. This leads us to the question of how the clay particles could serve to nucleate crystallization in the PEO/PMMA blend. Previous work¹ has shown that the surface enrichment of one blend component about the particles leads to a *counter enrichment* of the other phase about the first layer. This wave-like pattern of composition about the filler particles is probably important for stimulating crystallization about the clay particles. Thus, it is not necessary for an effective nucleating agent to have a favorable interaction with the crystallizing species in a polymer blend.

In summary, we have shown that depending on the preparation of the thin films, whether the clay fillers are well dispersed or weakly dispersed can lead to substantially modifying the morphology and properties of the films. We also found that in the case of mixing clay with a semi-crystalline polymer, the

agglomerated clay fillers can act as nucleating agents for seeding crystalline structure.

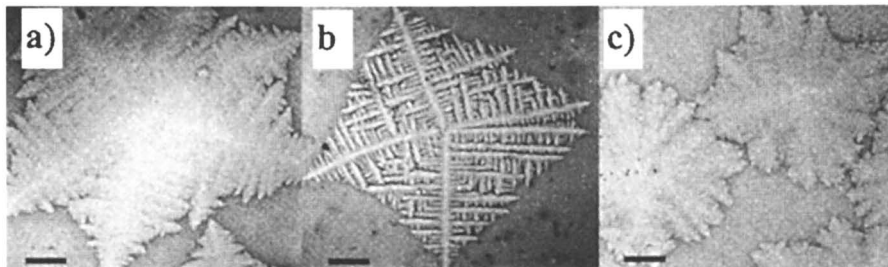


Figure 7. Optical image showing the increase of dendrite branches with the clay mass fraction of polymer. a) 10 %, b) 15 % and c) 20 %.

Acknowledgements

We thank Jack Douglas for useful discussions related to the paper. Gudrun Schmidt acknowledges financial support by the Alexander von Humboldt foundation.

References and Notes:

1. A. Usuki, M. Kawasumi, Y. Kujima, A. Okada, *J. Mater. Res.*, **8**, 1174 (1993);
2. Y. Kojima, M. Kawasumi, A. Okada, Y. Fukushima, T. Kurauchi, O. Kamigaito, *J. Mater. Res.*, **8**, 1179 (1993);
3. A. Okada, A. Usuki, *Mater. Sci. Eng: C*, **3**, 109 (1995);
4. T. Lan, T. Pinnavaia, *J. Chem. Mater.* **6**, 2216 (1994);
5. Z. Wang, T. Pinnavaia, *J. Chem Mater.* **10**, 1820 (1998);
6. K. Yano, A. Usuki, A. Okada, T. Kurauchi, O. Kamigaito, *J. Polym. Sci. A: Polym. Chem.* **31**, 2493 (1993);

7. K. Yano, A. Usuki, A. Okada, *J. Polym. Sci.: Part A: Polym. Chem.* **35**, 2289 (1997);
8. R. Krishnamoorti, E.P. Giannelis, *Macromol.* **30**, 4097 (1997);
9. Intercalation Chemistry, Whittingham M.S., Jacobson A.J. eds., Academic Press, New York, 1992;
10. B.P. Lee, J.F. Douglas, S.C. Glotzer, *Phys. Rev. E* **60**, 5812 (1999);
11. Certain equipment and instruments or materials are identified in this paper in order to adequately specify the experimental details. Such identification does not imply recommendation by the National Institute of Standards and Technology nor does it imply the materials are the best available for the purpose;
12. J.D.F. Ramsay, S.W. Swanton, J. Bunce, *Chem. J. Soc. Faraday Trans.* **86**, 3919 (1990);
13. F. Pignon, A. Magnin, J.M. Piau, B. Cabane, P. Lindner, O. Diat, *Phys. Rev. E.* **3**, 3281 (1997);
14. J.M. Saunders, J.W. Goodwin, R.M. Richardson, B. Vincent, *J. Phys. Chem. B* **103**, 9211 (1999);
15. R. Boisgard, D. Michel, J.P. Aimé, *Surf Sci.* **401**, 199 (1998);
16. J.P. Aimé, D. Michel, R. Boisgard, L. Nony, *Hys Rev B.* **59**, 1829 (1999);
17. S.N. Magonov, V. Elings, M.H. Wangbo, *Surf Sci.* **389**, 201 (1997);
18. S.N. Magonov, J. Cleveland, V. Elings, *Surf Sci.* **375**, 385 (1997);
19. D. Michel, *PhD thesis*, (1997), Université de Bordeaux 1, France;
20. G. Schmidt, A.I. Nakatani, P.D. Butler, A. Karim, C.C. Han, *Macromolecules.* **33**, 7219 (2000);
21. A. Mourchild, A. Delville, J. Lambard, E. Lecolier, P. Levitz, *Langmuir* **11**, 1942 (1995);
22. J.H.M. Hanley, G. Straty, *Langmuir*, **10**, 3362 (1994);
23. F. Pignon, A. Magnin, J.M. Piau, *J. Rheol.* **42**, **6**, 1349 (1998);
24. V. Ferreiro, J. Douglas, E.J. Amis, A. Karim, in press *ACS Proceeding* (2000);
25. V. Ferreiro, J. Douglas, J. Warren, A. Karim, submitted.

Chapter 15

Molecular Simulations of Ultra-Confined Polymers: Polystyrene Intercalated in Layered-Silicates

E. Manias* and V. Kuppa

Materials Science and Engineering Department, The Pennsylvania State
University, University Park, PA 16802

*Corresponding author: manias@psu.edu

Molecular Dynamics simulations are used to explore the structure and dynamics of polystyrene confined in $2nm$ slit pores, between surfactant-bearing mica-type surfaces. The systems simulated resemble experimentally studied intercalated nanocomposites, where polystyrene is inserted between alkyl-ammonium modified fluorohectorite silicate layers. The molecular modeling perspective complements the experimental findings and provides insight into the nature of polymers in nanoscopic confinements, especially into the molecular origins of their macroscopic behavior. Namely, simulations show a distribution of relaxations, ranging from extremely faster and to much slower segmental motions than the ones found in the corresponding bulk polymer at the same temperature. The origins of these dynamical inhomogeneities are traced to the confinement induced density modulations inside the $2nm$ slits. Fast relaxing phenyl and backbone moieties are found in low density regions across the film, and preferentially in the center, whereas slow relaxing moieties are concentrated in the denser regions, especially in the immediate vicinity of the confining surfaces.

Polymers in nanoscopic confinements possess remarkable dynamical heterogeneities which vary on length scales as short as a few Angstroms [1, 2], and manifest themselves macroscopically in a variety of unusual properties. Model systems, that can be interrogated experimentally to study ultra-thin [$\sim 2-5nm$] polymer films confined between solid surfaces, can be created by intercalating high molecular weight polymers in between alluminophyllosilicates [mica-type layered crystals]. Especially where appropriately modified silicates are used to form intercalated nanocomposites, very homogeneous ultra-thin confined polymer structures self-assemble in multilayer

systems, that can be designed to consist exclusively of identical nanoconfined films, and no free –unconfined– polymer [3, 4]. These intercalated materials offer great potential for the study of polymers and liquids in extreme confinements [1–2nm] by employing conventional analytical techniques [3–6].

For this reason, intercalated polymer/silicate nanocomposites have been recently investigated with the emphasis on the fundamentals of nanoscopically confined polymers [5,6]. It has been found that the nanoscopic confinement between solid surfaces affects the polymer behavior in ways that are not intuitively expected. Additionally, in many cases this confinement-modified polymeric structure and dynamics have been shown to dictate the materials response at the macroscopic level [3], causing remarkable enhancements of the materials properties [4].

Here, we report a molecular modeling approach, motivated by the previous experimental studies, aiming in obtaining insight into the confinement induced dynamical processes of ultra-thin polystyrene films in 2nm slit pores. Studying the formation, structure and dynamics of these intercalated structures can lead to a better understanding of polymers in a confined environment or at a solid interface, and at the same time provide the necessary fundamental level knowledge towards the molecular design of polymer/inorganic hybrid materials with desirable properties.

Simulation Model and Details

Inspired by striking new experimental findings of polymer films in 2nm slit pores between alkyl-ammonium modified mica-type surfaces [5,6], we performed extensive Molecular Dynamics (MD) computer simulations of polystyrene (PS) in 2nm slits. Since details about the simulation method and model are given in length elsewhere [7], here we will only mention some of the essential information.

Simulation geometry. The simulation geometry resembles closely the systems studied by NMR [6]. Our simulation box is $2.112 \times 1.828 \times 3.05$ nm in dimensions, with periodic boundary conditions in all three directions [figure 1]. A solid surface with the crystal structure of a synthetic 2:1 mica-type silicate is placed parallel to the xy plane, thus confining the organic molecules in the z direction. The confinement size [3.05nm] was selected to correspond to the experimentally measured X-ray diffraction d -spacing [3] and, after subtracting the wall thickness, it allows for a 2.05nm thin film of organics between the two solid surfaces. The MD runs were carried out in an NVT ensemble, where the number of particles (N) is chosen based on the experimentally measured material amounts. The grafting density of the surfactant chains [which are octadecyl-ammonium molecules] is well-known and characteristic of the silicate surface [8]. Our grafting density [$\sigma_{\text{graft}} = 1/0.97 \text{ nm}^2$ on each wall] corresponds to fluorohec-

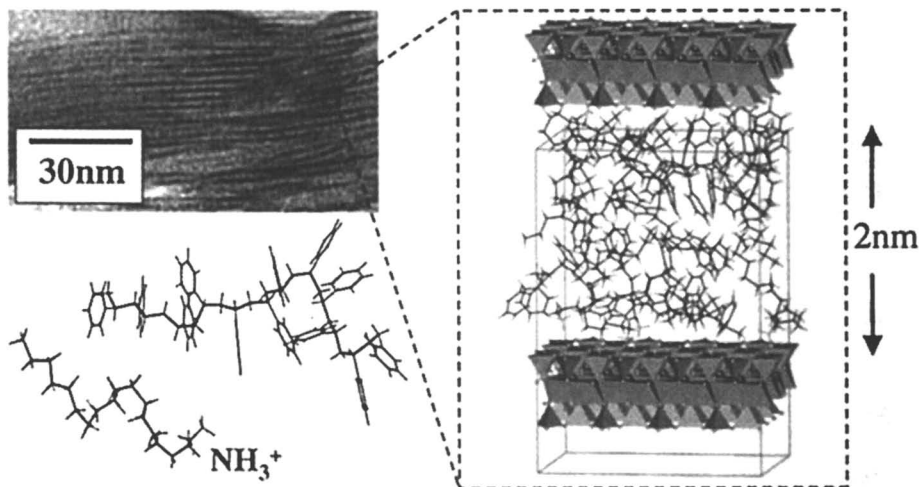


Figure 1 The system under investigation. From top left clockwise: a bright-field TEM detail of the PS/octadecyl-ammonium silicate intercalate [6]; a snapshot of the simulation box; a styrene 12mer (the smaller of the two PS molecules simulated) and the octadecyl-ammonium surfactant molecule.

torite [8], which is the silicate used in the NMR studies, and dictates 8 octadecyl-ammonium cations over the two solid surfaces. Furthermore, from thermogravimetric analysis (TGA) the polymer to surfactant weight ratio can be measured [3], and necessitates for 36 styrene monomers in the slit. Two systems were extensively studied, the first with 3 styrene chains of 12 monomers each, and the second with 3 chains of 24 monomers [in this case the box size is $2.112 \times 3.656 \times 3.05 \text{ nm}$ with 16 surfactant molecules]. Although these chains may be too short to capture the genuine response of long PS macromolecules, they are both longer than the average physisorbed train size of PS in these systems, and also allow for the existence of bridges between the two solid surfaces. Consequently, all the possible segmental dynamics that can develop inside these slit pores can be explored by our MD. Moreover, comparing the two systems with different PS chain lengths does not show any differences in the *segmental dynamics* discussed herein, albeit the substantially longer *chain relaxation times* of the confined 24mer compared to the 12mer.

Force-field. The force-fields for polystyrene, and its interactions with the alkyl-ammoniums [tabulated in table 1], are the same as recent PS simulations by Müller-Plathe [9]. The interactions between the silicate and the organic molecules [styrene and aliphatic chains] is based on our previous simulation work on organic/silicate complexes [8, 10].

Table I. The force-field used in the simulations.*Bonded and non-bonded interactions for the organic species are given [7, 9].*

non-bonded interactions	$V(r_{ij})=4\epsilon [(\sigma/r_{ij})^{12}-(\sigma/r_{ij})^6]+(1/4\pi\epsilon) q_i q_j/r_{ij}$		
	σ [nm]	ϵ [KJ/mol]	q [e]
C	0.3207	0.3519	0.000
C _{ph}	0.3550	0.2940	0.115
C _{ph} ^a	0.3550	0.2940	0.000
H	0.2318	0.3182	0.000
H _{ph}	0.2420	0.1260	-0.115
N	0.2976	0.8767	1.000
bond-stretching potentials	$V(r)=(k_b/2) (r-b_o)^2$		
	b_o [nm]	k_b [KJ/mol]	
C - C	0.153	334720	
C _{ph} - C	0.151	418400	
C _{ph} - C _{ph}	0.139	418400	
C - N	0.133	376560	
C - H	0.109	292880	
C _{ph} - H	0.108	292880	
N - H	0.100	374468	
bond-angle potentials	$V(\theta)=(k_\theta/2) (\theta_{ijk} - \theta_o)^2$		
	θ_o [deg]	k_θ [KJ/(mol rad ²)]	
H - C - H	109.45	306.40	
C - C - H	109.45	366.90	
C _{ph} - C - H	109.45	366.90	
C - C - C	109.45	482.30	
C - C - C _{ph}	109.45	482.30	
C - C _{ph} - C _{ph}	120.00	376.60	
C _{ph} - C _{ph} - C _{ph}	120.00	376.60	
C _{ph} - C _{ph} - H	120.00	418.80	
H - N - H	109.45	306.40	
N - C - H	109.45	366.90	
C - C - N	109.45	482.30	
proper dihedrals	$V_{ijkl}(\phi)=k_\phi [1+\cos(n\phi - \phi_o)] \phi_{cis}=0^\circ \ \& \ \phi \equiv (ijk)\angle(jkl)$		
	ϕ_o [deg]	k_ϕ [KJ/mol]	n
C - C - C - C	0.0	5.88	3
C - C - C - N	0.0	5.88	3
C - C - C - H ^b	0.0	5.88	3
C - C - N - H ^b	0.0	5.88	3
planar (improper) dihedrals	$V_{ijkl}(\xi)=k_\xi (\xi-\xi_o)^2, \ i \text{ central } C_{ph} \text{ and } \xi \equiv (ijk)\angle(jkl)$		
	ξ [deg]	k_ξ [KJ/mol]	
C _{ph} - C _{ph} - C _{ph} - C _{ph}	0.0	167.36	
C _{ph} ⁱ - C _{ph} - C _{ph} - H _{ph} [on <i>i</i>]	0.0	167.36	
C _{ph} ⁱ - C _{ph} - C _{ph} - C [on <i>i</i>]	0.0	167.36	

^a the phenyl carbon connected to the backbone methine.^b the hydrogens of the chain-end methyls and ammoniums.

The solid surface atoms were constrained to their equilibrium positions via harmonic springs, which allowed for thermal vibration; comparative studies with completely immobilized solid atoms did not reveal any differences in the results discussed herein. The temperature was stabilized via a weak coupling to a heat bath by the Berendsen thermostat [11]. Since the silicate surface is negatively charged [for fluorohectorite $-1q_e/0.97\text{nm}^2$] the positive ammoniums have a strong Coulombic attraction to the surfaces, effectively end-tethering the octadecyl-ammoniums on the surfaces.

Initial configurations, and ensemble. Probably the most crucial and important aspect of these simulations is the way we selected to sample the configuration phase-space. A simple Configurational Biased Monte Carlo (CBMC) scheme was developed to produce alkane surfactant configurations [12]. For the polystyrene molecules however –where the phenyl sidechains prohibit the use of a simple CBMC approach– a more elaborate route was necessary: The rotational-isomeric-state (RIS) model was used to create initial polymer conformations of PS. Conformations that fit in the interlayer gallery were chosen, and equilibrated by an off-lattice Monte Carlo scheme that employs small random displacements of the backbone atoms and Orientational Biased Monte Carlo rotations of the phenyl rings; the surfactants were equilibrated by CBMC attempts in coexistence with the polymer chains [12]. It is *critical* to have many independent, well-equilibrated initial configurations of the systems to be simulated: As the polymer is held together by strong covalent bonds, the relaxation of the chains is determined by the *slowest* moving segments along the polymer. Even though mobile segments are expected to exist in large numbers [6] they will be bonded to portions of the polymer that remain “frozen” for timescales vastly longer than what is accessible through MD. Therefore, the only realistic way to explore a large portion of the configurational space is to start with many *independent* initial system conformations and perform productive MD simulations of a few (10-100) nanoseconds. Typically, we used 10 independent initial configurations for each temperature and we followed each system for 100ns at $T=350\text{K}$, 50ns at $T=370$ and 390K , and 10ns at higher temperatures.

Polystyrene in 2nm thin slit pores

Structure of the confined film. In figure 2 the partial density profiles across the slit pore are shown for different components of the confined organic film. These density profiles correspond to the probability of finding the corresponding groups at a certain distance away from the confining solid surfaces, and are calculated through NVT ensemble averages of productive MD runs starting from *distinctly different* initial system configurations. The usage of several –typically ten– different initial configurations for each simulated temperature is essential, because the relaxation times of both

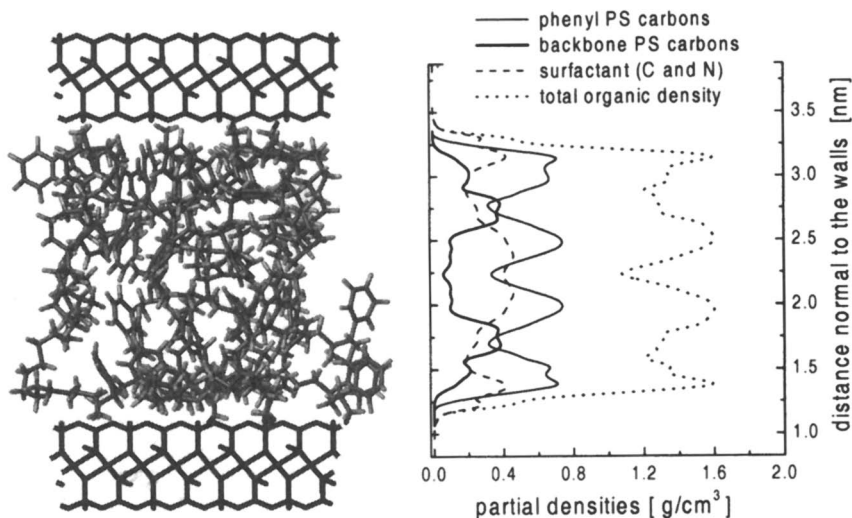


Figure 2 Density profiles across the interlayer gallery. Partial densities of the surfactant carbons and nitrogens (dashed line), the styrene phenyl carbons (light continuous line), styrene methyl, methylene and methine carbons (heavy continuous line), and the total organic density (dotted line) across the slit pore are shown.

the surfactant molecules and styrene chains reach far beyond the 10-100ns time periods simulated in each MD run. The same density profiles can also be calculated based solely on the Monte Carlo scheme used to create the initial systems for the MD, and are the same with the MD profiles within the data accuracy. This agreement between the MC and the MD ensembles is an indication that our MD's actually sample a representative portion of the phase-space.

From figure 2 is obvious that the mass is distributed across the slit pore in a highly inhomogeneous layered fashion. This kind of layering is seen in all simulations of confined systems [ranging from small molecule simple liquids, to alkane oligomers, to grafted alkanes, to generic Lennard Jones chains and realistic polymers]. This layering normal to confining surfaces is attributed to the steric interactions between the walls and the confined fluids, and is macroscopically manifested in SFA experiments by wildly oscillating solvation forces, when confined fluids are squeezed between mica surfaces [13].

In this system, however, there exist several species across the gallery [such as ammonium and aliphatic surfactant groups, as well as aliphatic and aromatic styrene groups] and a preferential layering with respect to the walls is developed. The positively charged ammoniums are found in

direct contact with the silicate walls –even at the highest temperatures studied– whereas most of the aliphatic part of the surfactant is preferentially located at the center of the slit [figure 2]. At the same time, we find that the polymer backbone is predominately located in two well-defined layers, at distances of about 0.3-0.7 nm from each solid surface. Often, a short strand of polymer adopts a bridging configuration perpendicular to, and connecting between, both walls. The phenyl rings, which attach to the backbone at each methine, are similarly found on either side of the backbone, and dominate the organic matter nearest the silicate surface. Finally, while surfactant methylenes are found distributed all across the slit pore, they bunch preferentially in the middle layer. These trends provide some clues as to the origin of the confined film structure: The polar phenyl groups, that interact strongly with the silicate surface, are preferentially located closest to the surface, whereas the aliphatic groups are displaced towards the center of the pore. Obviously, due to the covalent bonds between the styrene phenyls and methines, the backbone cannot be displaced completely in the center of the pore. Similarly, as the head group of the surfactant is tethered via an ionic interaction to the negatively charged silicate, the surfactant cannot be completely displaced from the surface either. As a result, only its aliphatic tails are displaced by the PS in the center of the slit [figure 2].

At first glance, all this detail may seem too theoretical. However, the surface sensitive ^1H - ^{29}Si cross-polarization NMR does provide a direct check of the validity of this layered structure (fig. 4 in [6]). This NMR approach does support the above structural description, and finds the styrene segments –phenyls and backbones– close to the surfaces and the surfactant tails removed towards the center of the slit [6]. Moreover, NMR spectroscopy provides insight on the segmental dynamics of the various moieties in the slit pore, as discussed in the next paragraph.

Segmental dynamics of PS in 2nm slit pores. A combination of surface sensitive ^1H - ^{29}Si cross-polarization NMR and quadrupolar echo ^2H NMR was used to study the segmental dynamics of selectively deuterated PS in 2nm slit pores [6]. From these recent NMR studies a new and quite unexpected picture is emerging for the dynamics of nanoscopically confined polymers, which was further confirmed by dielectric spectroscopy investigations on a polysiloxane system [5]. Namely, a coexistence of fast and slow segmental dynamics is observed over a wide range of temperatures, below and above the bulk T_g . This very wide distribution of segmental dynamics spanned relaxation times that ranged from much faster to much slower than the ones observed in the bulk for all temperatures studied: Very fast motions were observed in the confined polymer for temperatures deep below the bulk T_g , where the corresponding bulk polymer was essentially in a solid-like, immobilized, glassy state [6]; while for temperatures above the bulk T_g , there still exist many segments that remain solid-like and im-

mobilized in the confined systems [6], when at the same temperatures the bulk PS is in a molten, liquid-like state.

Our computer modeling approach aims to unveil the molecular origins of these dynamical inhomogeneities. To this end, we simulated the system depicted in figure 1 for several temperatures in the same T-range of the ^2H NMR experiments. We monitor segmental mobility much like the NMR is doing, by following the relaxation of the C-H bond reorientation. Beyond translation, one can define two types of phenyl reorientations: the “flipping” around the phenyl axis, and the “rocking” of this axis. For the backbone methylenes and methines, C-H reorientation takes place by trans-to-gauche isomerization. For NMR, “mobile” are those C-H bonds that are characterized by relaxation times smaller than the NMR echo spacing [$\tau=20\mu\text{s}$]. In our simulations, and focusing on the phenyl dynamics, we define as mobile those phenyls that are characterized by relaxation times shorter than τ , as measured from the time autocorrelation function of the corresponding C-H bond vectors, or equivalently by the phenyl “flip axis” $\vec{u}(t)$ and/or the normal vector that defines the “rocking axis” [figure 3].

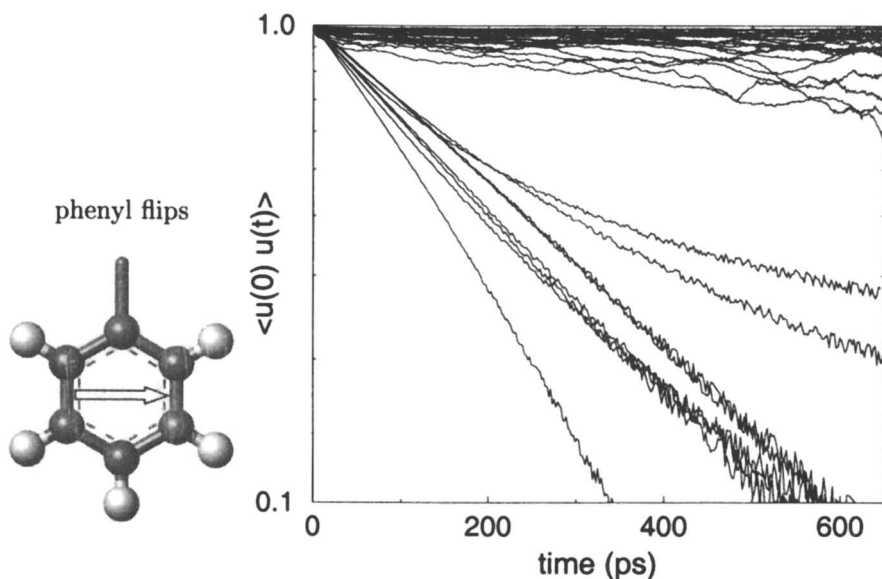


Figure 3 Time autocorrelation function of the phenyl flip vector [$\vec{u}(t)$, shown on the left], for the intercalated PS phenyls at 420K. An ensemble average is calculated over all runs starting from different initial configurations and over multiple time origins in each trajectory of 10ns.

A few of the $\langle \vec{u}(0) \cdot \vec{u}(t) \rangle$ in figure 3 correspond to ultra-fast flipping phenyls, with typical rotational relaxation times (τ_R) of a few tens/hundreds of ps. These are characteristic of PS and are also observed in bulk PS [9], albeit in much smaller populations. The confinement-induced dynamical in-

homogeneities are seen in the family of curves with longer τ_R [smaller slopes correspond to longer relaxation times]. In figure 3 there is a distribution of flip-relaxation times that characterizes the majority of the system's phenyls, and spans the range from 20ns to "infinity" [i.e. lines with slope zero, that correspond to phenyl rings that are immobilized throughout the duration of the MD run]. This distribution of τ_R is typical for all temperatures simulated [350-420K] as far as the relaxation times are concerned, although the number of phenyl rings with faster τ_R is an increasing function of temperature. The other modes studied [7] [phenyl rocking, backbone trans-gauche isomerization] have similar behaviour as the one seen for the phenyl flipping. This distribution of relaxation times is actually confinement-induced, and evidence to this end is provided in the next paragraph.

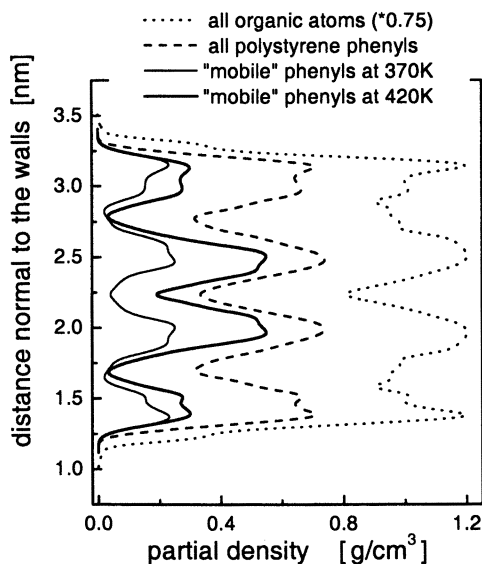


Figure 4 Density profiles normal to the silicates: for all the phenyl carbons (dashed line) and those carbons belonging to mobile phenyls (at 370K light line, and 420K heavy line). With ascending temperature the number of mobile phenyls increases, as can be enumerated by the area under the corresponding profiles, and at the same time, the mobile phenyls are preferentially located in the center of the slit.

Origin of the dynamical heterogeneities. Still focusing on the phenyl ring dynamics, we show in figure 4 the distribution of the carbons belonging to "mobile" phenyl rings, for two temperatures [370K and 420K]. In figure 5a we quantify the percentage of mobile phenyls as a function of temperature. With increasing temperature the number of mobile phenyls increases, and also these mobile rings are located increasingly in the center

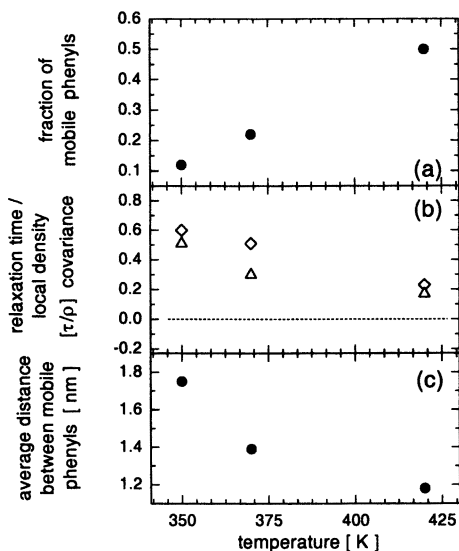


Figure 5 (a) the mobile fraction of phenyls: corresponding to fast orientational relaxations through ring “flips” and/or axis “rocking”. (b) the covariance of the relaxation time and the local density for the mobile phenyls [\diamond flipping, \triangle rocking]. (c) the average distance between mobile phenyls: the decrease with T is due to the increased number of mobile phenyls, and also their tendency to preferential concentrate in the middle of the slit pore bunched in groups.

of the pore; this trend is in agreement with the NMR observations. Since the mobile phenyls are located both in the center of the slit pore, as well as near the surfaces –albeit in smaller numbers– the fast segmental dynamics do not seem to originate from the location of the segments across the pore, as in wider confined alkane films [14]. Motivated from MD simulations in glass forming simple liquids [15], we can check the correlation between the segmental dynamics and the *local* structure inside the confined film. This can be realized through the estimation of the covariance of the segmental relaxation and the local density, defined as:

$$\text{cov}(\tau, \rho) \equiv \frac{\langle (\tau - \langle \tau \rangle) \cdot (\rho - \langle \rho \rangle) \rangle}{\sqrt{\sigma^2(\tau) \sigma^2(\rho)}} \quad (1)$$

where, τ is the segmental relaxation time of a particular phenyl, $\langle \tau \rangle$ is the ensemble average over all phenyls, $\langle \rho \rangle$ is the average density across the slit pore, and ρ is the local density around the phenyl in question. $\sigma^2(\tau)$ and $\sigma^2(\rho)$ are the ensemble variances of the relaxation times and density

respectively. Following this definition, maximum correlation between fast segmental relaxations and low local densities [or equivalently slow segmental relaxations and high local densities] yields a value of $\text{cov}(\tau, \rho) = +1$. Or, for the mobile phenyls of figure 5a:

$$\text{cov} = \begin{cases} +1 & \text{fast segmental dynamics at local density minima} \\ 0 & \text{no correlation between dynamics and density} \\ -1 & \text{fast segmental dynamics at local density maxima} \end{cases}$$

The relaxation time/local structure covariance for the mobile phenyls is shown in figure 5b. For the lower temperatures simulated there exists a strong correlation between the local structure and the segmental relaxation. Namely, the fast relaxing phenyls are located in regions where the local density is low [independent of whether they are close to the walls, or in the center of the slit; and independent of whether the C-H relaxation takes place through “flipping” or “rocking” motions]. As the temperature increases this correlation seems to decay in magnitude, although it still remains positive.

In fact, as the temperature increases, the number of mobile phenyls also increases in such a degree that large volumes in the middle part of the slit consists solely of phenyls with fast segmental dynamics. This reflects in a decreasing average distance between fast relaxing phenyls [as seen in figure 5c]. Furthermore, careful analysis of the MD trajectories reveals that at the lower temperatures there exist a few only segments with fast dynamics, which are isolated from each-other inside the confined film. As the temperature increases, “clusters” of mobile phenyls are formed, especially in the center of the slit pore [figure 6]; however, despite their proximity, the motions of the phenyls within the same “cluster” are not correlated nor cooperative. For all the temperatures simulated [even above 420K] there exists a large number of immobilized phenyl rings in the immediate vicinity of the confining surfaces, where the organic film is locally densified by the silicate surfaces. The relaxation of these slow phenyls is markedly temperature independent, at least for the time scales that our MD simulations probe. This is in general agreement with the cross-polarization NMR studies, which suggest that styrene moieties in the center of the slits are more mobile, while chain elements [phenyls, methylenes, and methines] interacting with the surface are dynamically inhibited.

Similar analysis for the backbone segmental dynamics reveals the same trends as discussed above for the phenyls [7]. That is, fast backbone segmental dynamics are predominately found in regions where the local density is low, and with increasing temperature mostly in the center of the slit pore. Furthermore, an interesting observation is that the fastest relaxing phenyls are covalently bonded to the fastest backbone segments, and the same for the slowest moving backbones and phenyls. This was not obvious, or intuitively expected, as the phenyl segmental relaxation [e.g. through flipping] does not require backbone reorientation. For example, in bulk –unconfined– PS chains phenyl modes are enabled at temperatures below T_g where the

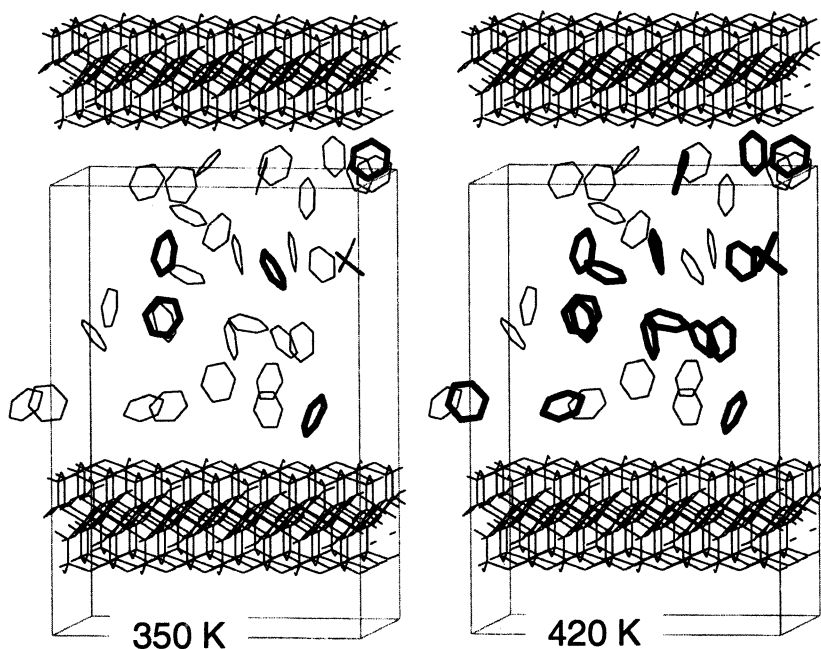


Figure 6 All the PS phenyls are shown and the ones with fast segmental dynamics are highlighted [hydrogen atoms, polymer backbones, and surfactant molecules are omitted for clarity]. To promote comparison, the same system configuration at two different temperatures is shown. At 350K the mobile phenyls are isolated in parts of the system where the local density is low. At 420K regions of closely bunched phenyls with fast segmental dynamics develop, especially in the center of the slit, but there also still exist isolated mobile phenyls in the low local density regions also near the confining walls.

backbone remains rigid; backbone modes start only near T_g . Although a more detailed analysis is necessary, this connectivity between moieties with fast segmental relaxations could be the reason that the phenyl and the backbone dynamics are strongly coupled in the confined films [6].

Effect of the surfactant. Due to the existence of a large number of alkyl-ammonium molecules in our confined systems, that can “plasticize” the polymer, it was not initially clear [6] whether these dynamical inhomogeneities arise from plasticization effects, or whether are confinement induced. On this point, our simulations show that the fast segmental relaxations are not correlated to the surfactant proximity and/or dynamics [figure 7], but originate from the confinement-induced density inhomogeneities [figure 5].

This is further supported by other experimental studies of different sys-

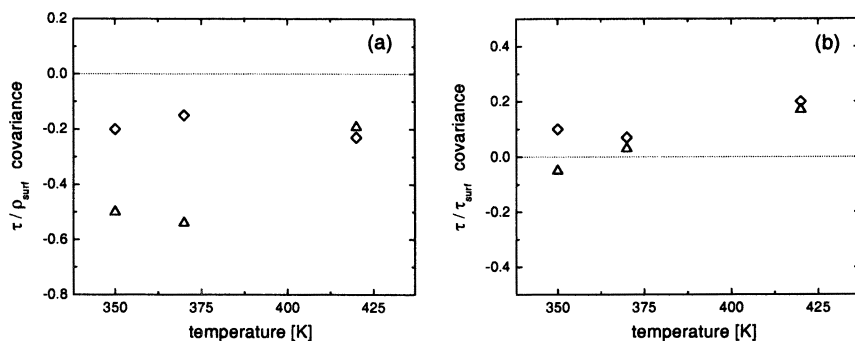


Figure 7 (a) The covariance between the fast phenyl dynamics and the local surfactant density (ρ_{surf}) [\diamond flipping, \triangle rocking]. The existence of surfactant monomers next to the phenyls seems to inhibit fast phenyl dynamics [especially fast “rocking” relaxations]. This is not surprising as the alkyl surfactants can pack much more effectively around the phenyls, than the other styrene monomers, and thus increase the local density promoting slower relaxations in their vicinity. (b) The covariance between the phenyl relaxation and neighboring-surfactant relaxation. Except for the highest temperature there seems to be no correlations between the phenyl and neighboring-surfactant dynamics, i.e. the fast phenyls are not preferentially located next to fast surfactants, and the slow phenyls are not preferentially located next to slow relaxing surfactants. For the highest temperature, there exists a correlation since all moieties [surfactants and phenyls] near the surfaces are slow relaxing [dynamically inhibited], whereas in the center of the gallery all moieties relax faster.

tems, which also provide strong indications that these segmental dynamical are associated with the polymer confinement: (i) ^2H NMR lineshape studies by Zax and coworkers, also observed coexisting fast and slow modes in poly(ethylene oxide) which was intercalated in the same silicate as the PS herein, but in absence of any surfactant whatsoever [16]. In this case, despite the much narrower confinements [0.8nm], the intercalated PEO chains exhibit substantial segmental motion [16]. (ii) dielectric spectroscopy of poly(methyl phenyl siloxanes) [with a T_g more than 150K below the PS T_g] report a similar coexistence of ultra-fast and solid-like (slow) relaxations over a wide range of temperatures [5], and measure an extraordinarily fast relaxation which is completely absent in the bulk -unconfined- polymer.

Comparison to experiments. Finally, we would like to commend on the quantitative comparison between the molecular simulations and the NMR experiments. The simulation enumeration of the mobile fraction underestimates the NMR measured one [6], albeit capturing the correct temperature dependence. This discrepancy can result from several sources,

such as the uncertainties in the relaxation time calculation, and phenomena that become important after the 100ns probed by our MD runs [such as polymer diffusion or desorption]. However, none of these two reasons can adequately account for the deviation between the experimental and simulation values. We believe that the cause of this difference lies in the organic [styrene and alkyl-ammonium] density used in our simulations, which must be higher than the ones in the intercalated experimental systems. Even though we based our densities on the TGA estimated quantities, the gravimetric method may also measure polymers physisorbed on the outside of the silicate stacks, i.e. not in the confined film. Since there exists a very strong dependence between the density and the fast segmental dynamics, minute deviations in density can result in large variations in the system dynamics. Nevertheless, the aim of the simulations is not to quantitatively reproduce the experimental observations, but to reveal the origins of the experimentally observed behavior, and provide insight to the relevant molecular processes. To this end, we feel that the present study was quite successful.

Conclusions

Molecular modeling approaches are employed to explore polystyrene molecules confined in 2nm slit pores, resembling intercalated PS in octadecyl-ammonium modified layered-silicate surfaces. The simulations show that the confined film adopts a layered structure normal to the solid surfaces, with the polar phenyls dominating the organic material adsorbed on the walls, and the aliphatic groups predominately in the center of the pore. This layered structure, with the polar styrene groups preferentially on the surfaces, reflects on previous ^1H - ^{29}Si cross-polarization NMR measurements.

A distribution from ultra-fast to solid-like slow segmental dynamics exists across a wide temperature range, below and above T_g , for both the styrene phenyl and the backbone groups. The mobile moieties concentrate at the center of the slit pore, especially for the higher temperatures. The MD simulations attribute these dynamical inhomogeneities to confinement-induced density inhomogeneities. Namely, the moieties with fast segmental dynamics are located in local density minima. Moreover, MD show that at low temperatures the fast moving species are isolated throughout the confined film, whereas with increasing temperature the mobile moieties increase in number and bunch up in groups, especially in the middle of the pore.

Acknowledgement This work was supported by a Wilson Research Initiation grant from the EMS College at Penn State. We also acknowledge the GroMaCS group of Groningen Univ. (Netherlands) for helpful discussions.

References

- [1] I. Bitsanis and C. Pan. *J. Chem. Phys.*, **1993**, *99*, 5520.
S. Granick, *Science*, **1991**, *253*, 1374.
- [2] E. Manias, G. Hadziioannou, and G. ten Brinke. *Langmuir*, **1996**, *12*, 4587; *Europhys.Lett.*, **1993**, *24*, 99; *Europhys.Lett.*, **1996**, *33*, 371.
- [3] E.P. Giannelis, R.K. Krishnamoorti, and E. Manias. *Advances in Polymer Science*, **1998**, *138*, 107.
- [4] M. Alexandre, P. Dubois. *Mat. Sci. & Eng. R: Reports*, **2000**, *28*, 1.
- [5] S.H. Anastasiadis, K. Karatasos, G. Vlachos, E.P. Giannelis, and E. Manias. *Phys. Rev. Lett.*, **2000**, *84*, 915.
- [6] D.B. Zax, D.-K. Yang, R.A. Santos, H. Hegemann, E.P. Giannelis, and E. Manias. *J. Chem. Phys.*, **2000**, *112*, 2945.
- [7] V. Kuppa and E. Manias. *Colloids & Surfaces A*, *in press.*, **2001**.
- [8] E. Hackett, E. Manias, E.P. Giannelis. *J.Chem.Phys.*, **1998**, *108*, 7410.
- [9] F. Müller-Plathe. *Macromolecules*, **1996**, *29*, 4782.
(updated information on the PS force-field can be found at Müller-Plathe's web site at the Max-Planck Institute, Mainz, Germany).
- [10] E. Hackett, E. Manias, E.P. Giannelis. *Chem. Mat.*, **2000**, *12*, 2161.
- [11] H. J. C. Berendsen, J. P. M. Postma, W. F. van Gunsteren, A. Di Nola, and J. R. Haak. *J. Chem. Phys.*, **1984**, *81*, 3684.
- [12] E. Hackett, E. P. Giannelis, and E. Manias. *J. Chem. Phys.*, *in press*.
- [13] H. K. Christenson. *J. Chem. Phys.*, **1983**, *78*, 6906; D.Y.C. Chan and R.G. Horn, *J. Chem. Phys.* **1985**, *83*, 5311; J.P. Montfort and G. Hadziioannou, *J. Chem. Phys.* **1988**, *88*, 7187; M.L. Gee, P.M. McGuiggan, J.N. Israelachvili, and A.M. Homola, *J. Chem. Phys.* **1990**, *93*, 1895; J. van Alsten and S. Granick, *Macromolecules* **1990**, *23*, 4856; S. Granick, *Science* **1991**, *253*, 1374; H. Hu, G.A. Carson and S. Granick, *Phys. Rev. Lett.* **1991**, *66*, 2758; J. Klein and E. Kumacheva, *Science* **1995**, *269*, 816; J. Israelachvili *Intermolecular and Surface Forces*, Academic Press, **1991**.
- [14] I. Bitsanis and C. Pan. *J. Chem. Phys.*, **1993**, *99*, 5520.
- [15] J. Qian, R. Hentschke, A. Heuer. *J. Chem. Phys.*, **1999**, *111*, 10177.
- [16] S. Wong, S. Vasudevan, R.A. Vaia, E.P. Giannelis, D.B. Zax. *J. Am. Chem. Soc.*, **1995**, *117*, 7568. *ibid Solid State Ionics*, **1996**, *86*, 547.

Chapter 16

A Coarse-Grained Simulation Study of Polymer Melt Intercalation in Layered Nanostructures

R. K. Bharadwaj¹, R. A. Vaia², and B. L. Farmer^{2,*}

¹Systran Federal Corporation, Dayton, OH 45431

²Materials and Manufacturing Directorate, Air Force Research Laboratory, AFRL/MLBP, 2941 P Street, Wright-Patterson Air Force Base, OH 45433

The dynamics of the initial stages of polymer melt intercalation into an initially aligned stack of sheets have been studied using coarse-grained molecular dynamics simulations. The bead-spring model was used to represent both the polymer chains and the sheets comprising the layered nanostructure. The influence of the sheet stiffness and the nature of polymer-sheet and sheet-sheet interactions on intercalation behavior were examined. It is found that sheet stiffness plays a crucial role in determining the ability of a layered nanostructure to intercalate. Nanostructures comprised of very flexible sheets intercalated simultaneously. Sheets possessing intermediate flexibility intercalated sequentially, beginning at the outermost gallery of the layered nanostructure. In contrast, stiff sheets did not intercalate, but sliding behavior occurred when the polymer-sheet interactions were very strong compared to the sheet-sheet interactions. Both intercalation and sheet sliding were found to be highly cooperative processes. These results underscore the importance of explicitly modeling the layered nanostructures if the dynamics and morphology development in these systems are to be understood.

Intercalation of polymers into silicates and aluminosilicates has emerged as a technologically important paradigm for achieving nanoscopic reinforcement of materials (1,2). These polymer layered silicate nanocomposites (PLSN) are synthesized by swelling the interlayer regions of the layered nanostructure by the polymer or a corresponding monomer, ideally creating a uniform distribution of 1 nm - thick layers throughout the polymer matrix. Demonstrated enhancements in the mechanical, barrier, non-flammability and thermal stability properties while retaining ease of processibility of the PLSNs has motivated research into creating nanoscale dispersions of other nanoparticulates, including quantum dots, metal nanoparticles, carbon nanotubes, layered chalcogenides and graphite. Thus, a detailed understanding of the thermodynamic driving forces and kinetics of the intercalation process and subsequent exfoliation in these systems is paramount.

In view of the increased importance of polymer intercalation in organically modified layered silicates (the inorganic cations in the silicate sheets replaced by organic alkylammonium surfactants), the thermodynamic aspects of this process have been recently studied using lattice-based mean field theory (3), as well as self-consistent mean field and density functional theory(4-10) approaches. There it was proposed that the loss of entropy of the polymer chains upon confinement between sheets was compensated by the increased conformational freedom of the tethered surfactant chains as the layers separated, resulting in a stable intercalated structure. For exfoliation (layer delamination and dispersion) to occur, additional enthalpic gains were necessary to drive the system to a stable dispersion of individual silicate layers in the polymer.

Recent computer simulations have provided additional insight into the packing, mobility and relaxation aspects of the intercalated polymer chains and phase relationships in PLSNs. Chain packing and conformational properties of alkylammonium surfactants in silicate layers have been delineated using atomistic molecular dynamics simulations (11) and are consistent with FTIR (12) and NMR studies (13). Coarse-grained molecular dynamics simulations have attempted to address the phenomenon at reasonable spatial and temporal scales (14-17). The flow of a polymer melt, represented by the bead-spring model (18) of Kremer and Grest (KG), into an initially evacuated slit was studied using coarse-grained molecular dynamics simulations. The diffusive characteristics and structure of polymers of two different chain lengths of $N = 12$ and 120 (below and above the entanglement molecular weight of $N \sim 35$ for the KG model) were studied. The results from these simulations were in qualitative agreement with experimental observations (19,20). The kinetics of static (absence of shear mixing) polymer melt intercalation was adequately described by diffusive models yielding an effective diffusion coefficient which decreased with increasing polymer-wall affinity.

Although these previous studies have provided invaluable insight into the molecular scale aspects of intercalation, a realistic representation of the process

requires the incorporation of two additional features. First, layered nanostructures are actually multi-layered and diffusion of the polymer occurs into adjacent galleries simultaneously. Second, in a real system the layered nanostructure is surrounded by a polymer melt in all three dimensions. Swelling of the layered solid by the polymer melt requires the outermost sheets to push into the polymer melt and the associated mass transport of the polymer. Therefore, extra work needs to be performed to create space by pushing against the encircling polymer melt regardless of the propensity for intercalation to occur. Both features are critical for developing an understanding of the initial stages of polymer intercalation, layer exfoliation, and morphology development in these systems. The goal of the present study is to address the encompassing issues concerning the interactions between polymeric melts and layered nanostructures explicitly incorporating the features mentioned above. This generality is extended to consider layered nanostructures of different stiffnesses. We have therefore adopted coarse-grained molecular dynamics simulations to study an ensemble of bead-spring polymer chains surrounding a layered nanostructure. The current discussion will be restricted to the intercalation of polymer melts in the unentangled regime into layered nanostructures of relatively small dimensions.

Simulation Details

The computational model consisted of a stack of sheets immersed in a sea of polymer chains. The bead spring model as described by Kremer and Grest (18) was used to represent both polymer and sheet beads. Nine sheets consisting of 100 beads per sheet (10 beads on edge) with lateral dimensions of $8.1\sigma \times 8.1\sigma$ (where σ is the bead diameter) were placed at the center of the cubic simulation cell. The sheets were oriented so that the planes of the sheets were perpendicular to the laboratory z -axis and with the two edges of the sheets placed parallel to the x and y laboratory axes. The *initial* vertical displacement between the sheets (along z) was set to 1.2σ . A cushion of 2.2σ was added to the left and right, top and bottom, front and back extremes of the sheet assembly. The sheet assembly was surrounded by 1500 polymer chains ($N = 10$) in a volume element determined such that the polymer density was 0.85. This resulted in an overall system density of $\rho^* = 0.8$ (15900 beads) and a dimension of 27.07σ for the cubic simulation cell. The large ensemble of polymer chains was required so that the polymer behaved as an unperturbed melt beyond the immediate vicinity of the sheets. The polymer chains were built as random walks using a bond length of 0.97σ and the criterion $|r_i - r_{i+2}| > 1.02\sigma$, while ensuring that the beads (or their periodic images) did not enter the volume element occupied by the sheets.

The polymer and sheet beads ($\sigma_p = \sigma_s = 1\sigma$) interacted with each other through the 6-12 form of the Lennard-Jones (LJ) potential and the bonded nearest neighbors interacted via the FENE (Finitely Extensible Nonlinear Elastic) potential. The potential parameters given by Kremer and Grest (18) were followed exactly for the polymer. In the case of the sheet, the FENE spring constant was changed to $100 \varepsilon/\sigma^2$ (where ε is the well-depth) to reduce the equilibrium nearest neighbor distance. This prevented the polymer beads from penetrating the sheet. In simulating the sheet, two types of bend interactions were introduced. All three-atom sequences forming a right angle interacted via a bend potential ($U_{\pi/2} = (K_{\pi/2}/2)(\theta - \pi/2)^2$) with $K_{\pi/2}$ set to $100\varepsilon/\text{rad}^2$. Second, all three-atom sequences occurring along the diagonals and the edges of the sheet interacted through a linear bend potential ($U_\pi = K_\pi(1 + \cos\theta)$) (21). By varying K_π it was possible to effect a change in the stiffness of the sheet.

It is useful to summarize the parameter space for the simulations performed in this study. There were three LJ interaction parameters in the system, namely polymer-polymer (ε_{pp}), polymer-sheet (ε_{ps}), and sheet-sheet (ε_{ss}). The polymer-polymer interaction (both intra- and inter-chain) was always repulsive with $\varepsilon_{pp} = 1\varepsilon$ and $r_c = 2^{1/6}\sigma$ in accordance with the KG model. (Note: The commonly used term “always repulsive” might more clearly be thought of as “not attractive”. The interaction is essentially a hard-sphere potential, repulsive when beads are too close, neutral otherwise.) Two values for the polymer-sheet interaction (always attractive) were chosen for study, $\varepsilon_{ps} = 1\varepsilon$ and $\varepsilon_{ps} = 5\varepsilon$ and $r_c = 2.2\sigma$. Intra-sheet interactions were always repulsive with $\varepsilon_{ss} = 1\varepsilon$ and $r_c = 2^{1/6}\sigma$. Both attractive and repulsive potentials were considered for the inter-sheet (beads on different sheets) interactions by changing the cut-off distance to either 1.5σ or $2^{1/6}\sigma$ respectively. Four values of the force constant for the linear bend interactions were chosen, $K_\pi = 1, 10, 100$ and 500ε .

The entire polymer-sheet assembly was subjected to NVT-MD simulations at $\rho^* = 0.8$ and $T^* = 1.0$. The velocity form of the Verlet integrator was used to solve the equations of motion using a time step of 0.004τ (where $\tau = \sigma(m/\varepsilon)^{1/2}$). The velocities were scaled to the desired temperature every 2000 steps and corrected to ensure conservation of momentum. During equilibration, the sheet-sheet interactions were made strongly attractive ($\varepsilon_{ss} = 50\varepsilon$, $r_c = 1.5\sigma$) to prevent intercalation from occurring before the polymer chains equilibrated. The sheets were kept stiff by setting $K_\pi = 100\varepsilon$. The system was subsequently equilibrated for 50,000 MD steps ($200 t/\tau$) using a time step of 0.004τ . The mean squared end-to-end distance ($\langle r^2 \rangle$) and radius of gyration ($\langle r_g^2 \rangle$) of the polymer chains were found to be $13.5\sigma^2$ and $2.3\sigma^2$ respectively. The average system pressure (P^*) was 3.65. Simulations were also performed on the neat polymer (100 chains with $N = 10$) at $T^* = 1.0$ and $\rho^* = 0.85$ giving $\langle r^2 \rangle = 13.0\sigma^2$, $\langle r_g^2 \rangle = 2.18\sigma^2$ and $P^* = 5.1$. These values are in good agreement with $\langle r^2 \rangle = 13.1\sigma^2$, $\langle r_g^2 \rangle = 2.2\sigma^2$, $P^* = 5.2$ reported by Kremer and Grest for the neat polymer system ($N = 10$) at

the same reduced temperature and density. The resulting polymer-sheet structure is shown in Figure 1. A brush-like arrangement of the polymer chains on the sheet plane and edge surfaces is seen. The number fractions of the polymer and sheet beads are plotted as a function of distance in Figure 2. The bead number fraction in the z direction shows nine regularly spaced peaks at intervals of 0.9σ as expected. The number fraction (z) of the polymer beads shows a peak immediately adjacent to the sheet surfaces and thereafter shows a decrease (depletion zone) and fluctuates about a mean value. In contrast, the number fraction profiles in the x (and y , not shown) show no distinct surface polymer layer. This is due to the jagged surfaces formed by the sheet surfaces arising from the close packing arrangement.

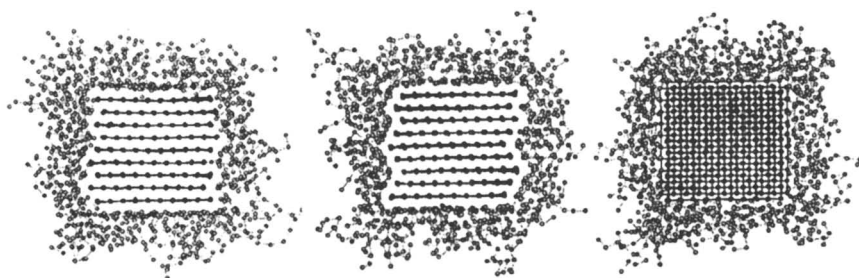


Figure 1. Polymer-sheet configuration after equilibration. Only polymer chains within 2σ of the sheet/edge surfaces are shown in the three views.

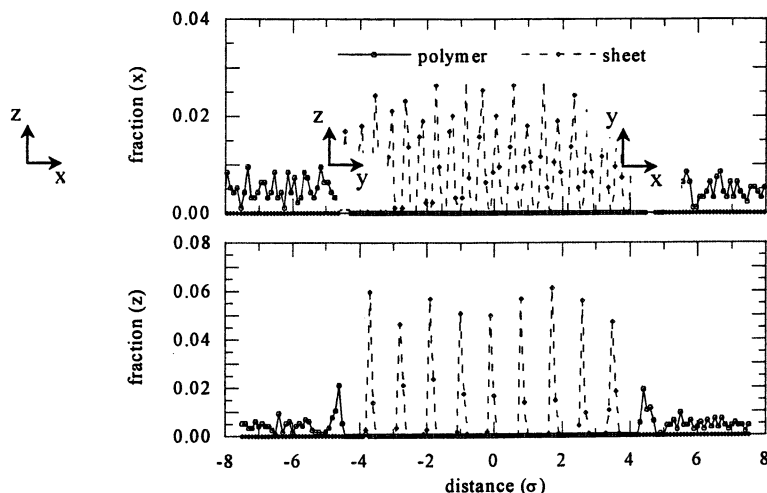


Figure 2. Polymer-sheet number fraction profile in the x and z directions for the initial configuration shown in Figure 1.

Results

In this study, we exclusively address the case where there is no free space available initially between the sheets for the polymer chains to occupy; i.e, the spacing between the sheets is consistent with a closed packed structure, which in the present case is 0.9σ . The real free spacing is arrived at by subtracting one lattice spacing (0.9σ) from this value which leads to an actual spacing of $d = 0.0\sigma$. In order for the polymer chains to occupy space between sheets, the sheets must first be pried apart to allow intercalation. The simulations were performed using different parameters for the sheet stiffness, polymer-sheet and sheet-sheet interactions. The correspondence between the sheet stiffness (K_π) and the stiffness of real layered nanostructures such as graphite or aluminosilicates has not been determined. Mapping the K_π values to reflect the stiffness of the real nanostructures could presumably be done by determining the stiffness of graphite and aluminosilicate sheets from atomistic molecular dynamics simulations or from experiments. The same initial configuration at the end of the equilibration stage (Figure 1) was used for each simulation. The results from these simulations are summarized in Table 1.

Table 1. Simulation results for $d = 0.0\sigma$.

ϵ_{ps}	ϵ_{ss}	$K_\pi = 1\epsilon$	$K_\pi = 10\epsilon$	$K_\pi = 100\epsilon$	$K_\pi = 500\epsilon$
1	1 ^a	No Int.	No Int.	No Int.	No Int.
5	1 ^a	Intercalation	Intercalation	No Int.	No Int.
1	1 ^r	Intercalation	Intercalation	No Int.	No Int.
5	1 ^r	Intercalation	Intercalation	Sliding	Sliding

NOTE: Polymer-sheet interaction ϵ_{ps} was always attractive. The sheet-sheet interaction ϵ_{ss} was set to be both attractive (*a*) and repulsive (*r*) (see text). K_π represents the force constant for linear bend interactions controlling sheet stiffness.

When the polymer-sheet interaction is equal to the sheet-sheet interactions ($\epsilon_{ps} = \epsilon_{ss} = 1\epsilon$) no intercalation was observed irrespective of the sheet stiffness. When $\epsilon_{ps} = 5\epsilon_{ss}$, the sheets with stiffness constants of 1 and 10ϵ underwent intercalation. The stiffer sheets, characterized by the larger stiffness constants of 100 and 500ϵ , did not intercalate. Instead, at large relative strengths of ϵ_{ps} to ϵ_{ss} , stiffer sheets underwent a sliding phenomenon. Sheet sliding emerges as a new mechanism by which layered nanostructures may be dispersed in a polymeric matrix. To examine this sliding process the sheet-sheet interactions were made purely repulsive (LJ potential truncated and shifted at its minimum at $2^{1/6}\sigma$). Under these conditions, the stiffer sheets exhibited a sliding motion where the

sheets were being pushed by the polymer chains. For more flexible sheets ($K_\pi = 1, 10\varepsilon$) intercalation occurred with ease when the sheet-sheet interactions were very weakly attractive or purely repulsive. Sheet stiffness therefore has a profound impact on polymer intercalation. This parallels previous studies by Solin et al. on the role of sheet stiffness in the staging phenomenon of small molecule intercalates in graphite (22). The phenomena of polymer intercalation and sheet sliding are explored in detail in the following sections.

Polymer Intercalation

Polymer intercalation alludes to the swelling of the gallery by polymer chains. The sheets are pried apart by the polymer chains filling the gallery in order to maximize their interaction with the nanostructure. As shown in Table 1, this occurs for the flexible sheets with $K_\pi = 1$ and 10ε with $\varepsilon_{ps} = 5\varepsilon_{ss}$. Since the polymer-sheet interaction is much stronger than the sheet-sheet interaction it is reasonable to expect the polymer to maximize its interaction with the sheets. The structures after 10,000 MD steps ($40 t/\tau$) are shown in Figure 3 for the two values of the sheet stiffness where intercalation was observed. The sheets with $K_\pi = 1\varepsilon$ are essentially fully flexible, but at the same time completely intercalated by polymer chains. It is also seen that the sheets, although intercalated, do not have a regular stacking arrangement. In contrast, a modest increase in the sheet stiffness results in a different intercalation behavior. Increasing K_π to 10ε , the intercalation process proceeds in a step-by-step fashion in which the sheets are intercalated in a sequential manner. It appears that the sheets are being peeled away sequentially, starting with the outermost sheet. In this case ($K_\pi = 10\varepsilon$), the snapshot captures the intercalation process exquisitely showing some sheets that are completely intercalated, some in the process of being intercalated and other sheets that are yet to be intercalated.

To quantify the observed phenomena, two quantities were monitored. These are the distances and the angles between the mean planes of adjacent sheets. Henceforth, the sheets will be represented by the numbers 1 through 9 and the galleries between the sheets denoted by the alphabets *a* through *h*. These are shown in Figure 4 for the two cases. There are nine sheets in the ensemble. Therefore there are eight sheet spacings (galleries) and angles that are labeled in the order of occurrence (in Figure 4, gallery *a* represents the sheet separation between sheets 1 and 2, gallery *b* represents the separation between 2 and 3 and so on). The results presented in Figure 4 corroborate what is visually apparent in Figure 3. For the $K_\pi = 1\varepsilon$ case, intercalation occurs in no specific order with respect to the sheets. Several galleries intercalate in a relatively short time span. This is evidenced by the increase in the sheet separation from the close packed value of 0.9σ to 1.8σ . There appears to be no order with respect to

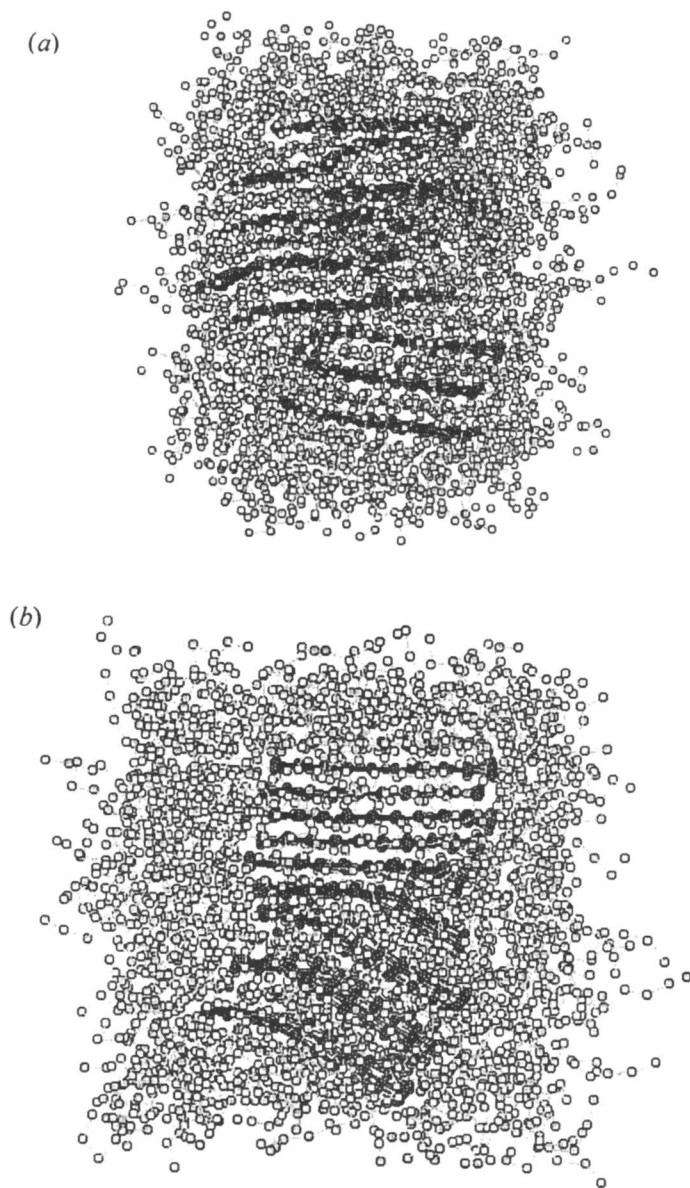


Figure 3. Resulting polymer-sheet configuration after 10,000 MD steps for sheet stiffness constants of (a) $K_\pi = 1\epsilon$, (b) $K_\pi = 10\epsilon$. Polymer chains within 2σ of the sheets are shown.

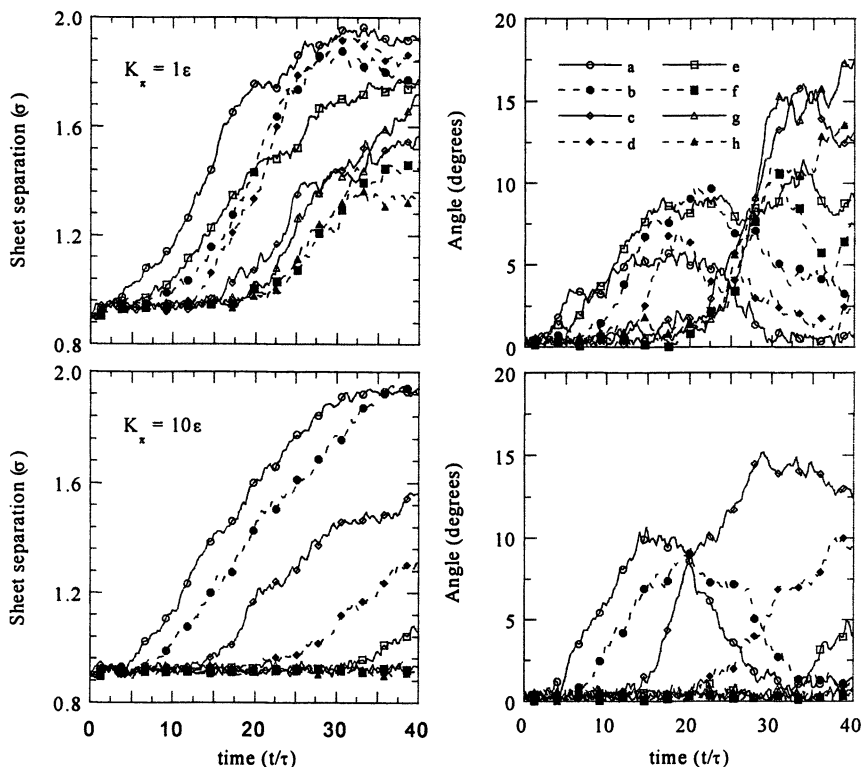


Figure 4. Time evolution of the inter sheet separation (in σ) and angle (in degrees) between the mean plane of the sheets for $K_\pi = 1\epsilon$ (upper panels) and 10ϵ (lower panels).

which gallery intercalates first. Based on the initial increase in the sheet separation, the galleries intercalate in the order *a*, *e*, *b*, *d*, *c*, *g*, *h* and *f*. In addition to the opening of the gallery to accommodate the polymer chains, there is relative translation of the sheets with respect to each other. From Figure 3(a) it may be seen that sheets 1,2 and 3 (numbered from the bottom) intercalate to yield a well aligned stack of alternating polymer chains and sheets layers. Next, sheets 4, 5, and 6 also form a well-aligned stack that is both translated and rotated relative to the stack formed by sheets 1, 2, and 3. Sheets 7, 8 and 9 are incompletely intercalated at this stage.

In the $K_\pi = 10\epsilon$ case, the sheets peel off sequentially as is clearly seen from the sheet separation (lower panel in Figure 4). Intercalation in this case occurs in

a more orderly fashion preserving a well aligned stacking of the sheets. Here, the gallery *a* intercalates first followed by *b*, *c*, *d* and *e* with the other galleries remaining at the equilibrium separation (0.9σ). (The apparent asymmetry between the behavior of the sheets on the top and bottom of the stack arises from the stagger of the sheets after equilibration. The statistical nature of the system causes the sheets to stagger differently and they therefore have different interactions with the surrounding melt at the start of the production phase of the simulation.) The rate of increase in the gallery spacing, if anything, shows a tendency to decrease as the subsequent galleries are intercalated. Galleries *a* and *b* intercalate with identical rates. Gallery *c* in comparison intercalates slower than *b*, gallery *d* is slower than *c* and so on. It is interesting to note that the time interval between the initiation of intercalation in different galleries is smaller than the time it takes for a gallery to be fully intercalated. This means that although there is a delay between the time one layer intercalates and the next one begins, at some point in time it is reasonable to expect several galleries to undergo intercalation simultaneously albeit to various extents.

The change in the inter-sheet angle accompanying the intercalation process also shows a well-defined behavior. During intercalation, the angular change between the layers first shows a maximum and thereafter appears to reduce to 0 degrees, essentially yielding parallel sheets. The importance of using explicit sheets in representing the layered nanostructure in simulations is underscored by this observation. There is considerable cooperativity in the intercalation process involving the local deformation of the individual sheets, as well as opening the sheets in a non-parallel manner. This situation is very different from a simulation of polymer melt flow into a well-defined slit with parallel rigid walls (14-17).

After a layer of polymer chains completely fills the spacing, the sheets are constrained to remain parallel by the polymer layer that associates with both sheets. The polymer beads preferentially locate in the interstitial positions between lattice sites of the sheets. The formation of a single layer of polymer chains in the gallery represents a stable configuration. Running the simulation for a longer duration only resulted in a refinement of the polymer-sheet structure without leading to the formation of multiple layers of polymer chains. This structural refinement is also observed experimentally from X-ray diffraction studies of polymer layered aluminosilicates upon annealing in the melt (23). No dynamic exchange of polymer chains between the melt and the intercalated layer was observed after a single layer of polymer chains was formed between the sheets. Whatever the driving force interactions responsible for intercalation, further influx of polymer is not realized. In these models, as in real systems, intercalation does not lead to exfoliation. This allows us to conclude that the single layer of polymer chains sandwiched between the sheets (after intercalation) behaves as an adhesive leading to an energetically stable structure. Recall that each polymer bead represents several monomer units.

Sheet Sliding

Intercalation was not observed when the sheets were very stiff. This again underscores the importance of local sheet stiffness in determining the ability of a structure to intercalate, irrespective of the polymer-sheet interaction. For the stiff sheets, an entire sheet needs to be moved as a rigid entity in order to create space for the advancing polymer melt, whereas in the flexible sheets, local deformations allow the chains to penetrate the interlayer spacing. Therefore the observed relative sliding of the sheets presents a new mode by which the polymer-sheet interactions may be maximized. The structures obtained after 10,000 steps are shown in Figure 5 for $K_{\pi} = 100$ and 500ε . In this case the simulations were performed with purely repulsive interactions (by truncating and shifting the LJ potential at its minimum at $2^{1/6}\sigma$) between the sheets (the limiting condition for weakly attractive sheets). That is, sheet sliding is observed only when the relative strength of ε_{ps} is far greater than ε_{ss} or equivalently when there is a significant chemical potential gradient. As seen in the structure shown in Figure 5, sheet sliding is more pronounced in the case of the stiffer sheet ($K_{\pi} = 500\varepsilon$). The polymer, with a view to increasing the interaction with the sheet surfaces, exposes the sheets by pushing the sheets along the plane. Note also the push-pull nature of the interactions. Polymer chains on one side push the sheet ahead of them, while polymer chains on the other side tend to pull that same sheet into the melt region. This is a more energetically favorable pathway than prying the very stiff sheets open and subsequently filling the space. The sheets slide past each other whilst retaining the parallel arrangement.

To quantify the sheet sliding phenomenon, the mean squared distances associated with the centers of mass of the sheets was constructed and is shown Figure 6 for $K_{\pi} = 100$ and 500ε . Two features become immediately apparent upon inspection of the displacement characteristics of the sheets. First, the maximum mean squared displacement associated with the $K_{\pi} = 500\varepsilon$ sheets is approximately twice that associated with $K_{\pi} = 100\varepsilon$. Stiffer sheets slide more easily. This is reasonable since the cross section of the sheet is reduced as the stiffness increases by constraining the beads to stay in a well-defined plane. The stiffer the sheet, the easier it is to slice through the polymer melt. Second, sheet sliding appears to be a cooperative phenomenon with pairs of sheets moving at identical rates. This cooperative motion is observed in both cases with some of the sheets remaining stationary. For example, in the $K_{\pi} = 500\varepsilon$ case, pairs of sheets (2, 4), (8, 6) and (7,3) diffuse with identical rates, whereas, sheets 1, 5 and 9 remain essentially stationary. In the $K_{\pi} = 100\varepsilon$ case, there is more scatter with respect to the sheet diffusion. Sheets (3, 4) and (8, 5) slide at the same rates with the rest of the sheets 6, 7, 2, 1 and 9 following in the order of decreasing mean squared displacements. Once all the sheet surfaces have been exposed, the driving force is no longer present since the polymer has already maximized its interaction with the sheets. Thereafter, the sheets remain relatively stationary.

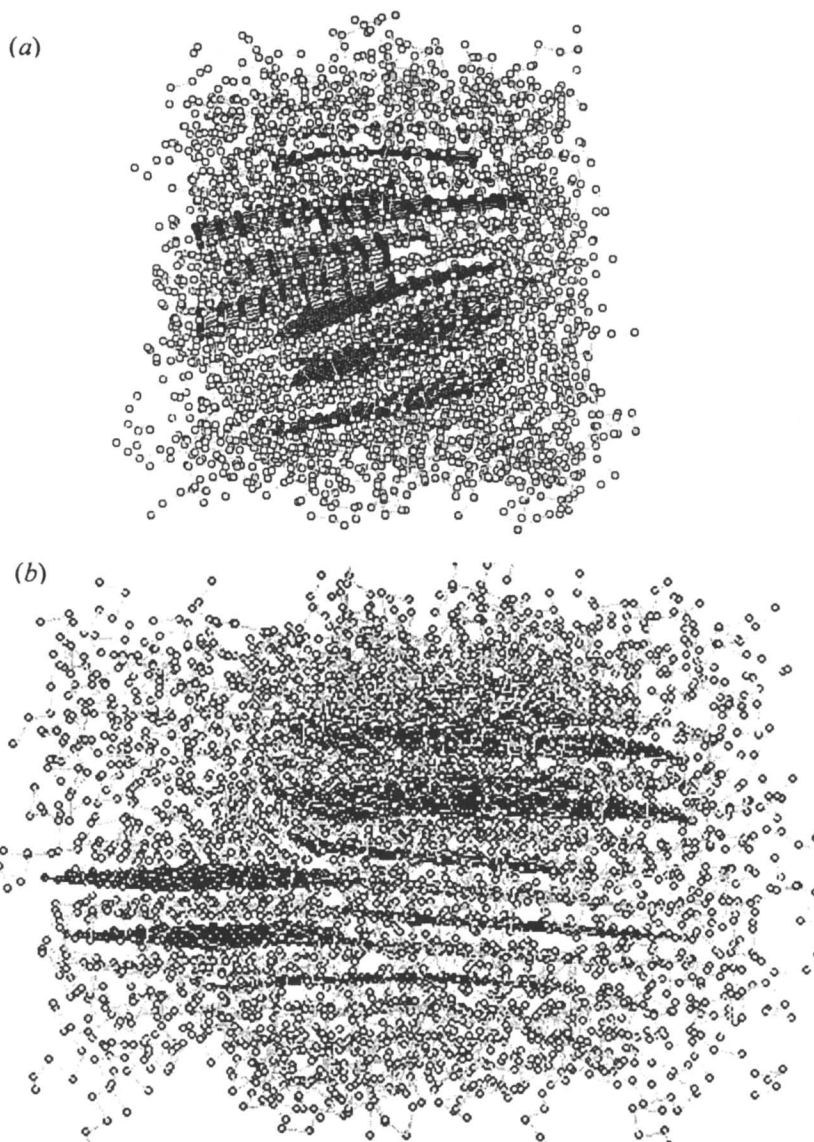


Figure 5. Resulting polymer-sheet configuration after 10,000 MD steps for sheet stiffness constants of (a) $K_{\pi} = 100\epsilon$, (b) $K_{\pi} = 500\epsilon$. Polymer chains within 2σ of the sheets are shown. The lower snapshot has been rotated to provide a better view.

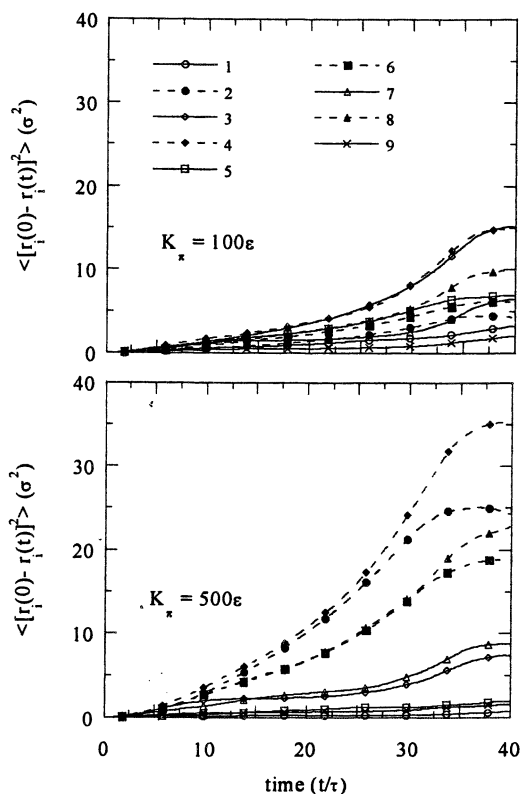


Figure 6. Center of mass mean squared displacements vs. time for the nine sheets for two values of sheet stiffness.

Discussion and Summary

Coarse-grained molecular dynamics simulations were used to study the process of polymer intercalation into a layered nanostructure. The model consists of layered nanostructure immersed in a sea of polymer chains. The layered nanostructure was comprised of sheets that were defined explicitly and completely unrestrained with respect to translational and rotational degrees of freedom. One important conclusion from the study is that sheet stiffness has a profound impact on the ability of a layered nanostructure to be intercalated. Equally important is the observation that intercalation is a highly cooperative phenomenon. Flexible sheets, because of their susceptibility to local deformation intercalate simultaneously. Stiffer sheets, on the other hand, do not

intercalate since this requires large rigid movement of the sheets which is energetically unfavorable. Stiff sheets can instead achieve dispersal in the polymer matrix through a phenomenon of sliding where the sheets are pushed sideways by the polymer melt to maximize the polymer-sheet interactions. In accord with experimental findings, the relative strength of the polymer-sheet to the sheet-sheet interactions ultimately determines the propensity for intercalation to occur.

The above results suggest that stacks of flexible sheets such as graphite should be easier to intercalate than stiff ones such as aluminosilicate sheets. On the other hand, it may not be possible to experimentally observe the sheet sliding phenomenon reported here since it requires a combination of very large polymer-sheet attraction and very weak interactions holding the sheets together. This observation points to the importance of a pre-existing spacing in order for stiffer sheets to be intercalated since wholesale deformations involving opening of the sheet spacings are energetically unfavorable. This observation has an important implication in understanding the intercalation phenomenon occurring in aluminosilicate layers. In this case, the presence of the surfactant chains serves the purpose of increasing the gallery spacing and at the same time providing a cushion of space where local deformations of adjacent sheets may occur. The cooperativity between the polymer diffusion and sheet deformation is crucial to obtaining an intercalated structure. To examine the effect of a pre-existing space between layers, the simulations were extended to consider assisted intercalation where every other sheet in the initial structure was deleted to give $d = 1.8\sigma$. In this case, even the stiffer sheets were intercalated with ease thereby strengthening the above argument.

In general, the simulation points to the necessity of defining the layered nanostructure explicitly if the dynamics and morphology development during intercalation are to be understood. Certainly, the observation of sheet sliding and cooperativity during intercalation would be impossible if not for the explicit representation of the layered nanostructure. The current simulation represents a first step in this direction. Efforts are underway to extend the simulations to studying larger dimensions of the polymer chain (above entanglement molecular weight) and sheet structures. Other extensions involving incorporation of surfactant chains and electrostatic interactions would allow the intercalation phenomenon occurring in layered aluminosilicates to be addressed directly. It is equally important to correlate the stiffness of the nanostructure in the coarse-grained simulation with those for layered nanostructures such as graphite or aluminosilicates. There are several fundamental issues in polymer intercalation that the current simulation methodology is expected to be able to address. For example, the study of kinetic and thermodynamic factors involved in the morphology transition from intercalated to exfoliated structures and resolving the long standing issue of whether capillary forces or specific interactions drive the intercalation process should be amenable to this method.

Acknowledgments

We are indebted to the Materials and Manufacturing Directorate, Air Force Research Laboratory, Wright-Patterson AFB, OH, for support. Dr. X. Duan is thanked for his assistance with the molecular graphics.

References

1. Giannelis, E. P.; Krishnamoorti, R.; Manias, E. *Adv. Polym. Sci.* **1999**, *138*, 107.
2. LeBaron, P. C.; Wang, Z.; Pinnavaia, T. J. *App. Clay Sci.* **1999**, *15*, 11.
3. Vaia, R. A.; Giannelis, E. P. *Macromolecules* **1997**, *30*, 7990.
4. Lyatskaya, Y.; Balazs, A. C. *Macromolecules* **1998**, *31*, 6676.
5. Balazs, A. C.; Singh, C.; Zhulina, E. *Macromolecules* **1998**, *31*, 8370.
6. Balazs, A. C.; Singh, C.; Zhulina, E.; Lyatskaya, Y. *Acc. Chem. Res.* **1999**, *32*, 651.
7. Zhulina, E.; Singh, C.; Balazs, A. C. *Langmuir* **1999**, *15*, 3935.
8. Ginzburg, V. V.; Balazs, A. C. *Macromolecules* **1999**, *32*, 5681.
9. Ginzburg, V. V.; Singh, C.; Balazs, A. C. *Macromolecules* **2000**, *33*, 1089.
10. Kuznetsov, D. V.; Balazs, A. C. *J. Chem. Phys.* **2000**, *112*, 4365.
11. Hackett, E.; Manias, E.; Giannelis, E. P. *J. Chem. Phys.* **1998**, *108*, 7411.
12. Vaia, R. A.; Teukolsky, R. K.; Giannelis, E. P. *Chem. Mater.* **1994**, *6*, 1017.
13. Wang, L. Q.; Liu, J.; Exarhos, G. J.; Flanigan, K. Y.; Bordia, R. *J. Phys. Chem. B* **2000**, *104*, 2810.
14. Lee, Y.; Baljon, A. R. C.; Loring, R. F.; Panagiotopoulos, A. Z. *J. Chem. Phys.* **1998**, *109*, 10321.
15. Baljon, R. C.; Lee, J. Y.; Loring, R. F. *J. Chem. Phys.* **1999**, *111*, 9068.
16. Lee, J. Y.; Baljon, A. R. C.; Loring, R. F. *J. Chem. Phys.* **1999**, *111*, 9754.
17. Lee, J. Y.; Baljon, A. R. C.; Sogah, D. Y.; Loring, R. F. *J. Chem. Phys.* **2000**, *112*, 9112.
18. Kremer, K.; Grest, G. S. *J. Chem. Phys.* **1990**, *97*, 5057.
19. Vaia, R. A.; Jandt, K. D.; Kramer, E. J.; Giannelis, E. P. *Macromolecules* **1995**, *28*, 808.
20. Manias, E.; Chen, H.; Krishnamoorti, R.; Genzer, J.; Kramer, E. J.; Giannelis, E. P. *Macromolecules* **2000**, *33*, 7955.
21. Muller-Plathe, F. *J. Chem. Phys.* **1995**, *103*, 4346.
22. Solin, S. A. In *Chemical Physics of Intercalation*; Bernier, P., et al. Ed.; Plenum Press: New York, NY, 1993, Vol. 2, 161-180.
23. Vaia, R. A.; Vasudevan, S.; Krawiec, W.; Scanlon, L. G.; Giannelis, E. P. *Adv. Mater.* **1995**, *7*, 154.

Author Index

- Advincula, Rigoberto, 39
Balazs, Anna C., 57
Bandyopadhyay, Sumanda, 15
Bharadwaj, R. K., 209
Boykin, Cheri McConnell, 85
Briber, Robert M., 127
Chapelle, C., 27
Collister, Jon, 7
Davis, Rick D., 117
Fan, Xiaowu, 39
Farmer, B. L., 209
Ferreiro, Vincent, 177
Giannelis, Emmanuel P., 15
Ginzburg, Valeriy V., 57
Glinka, Charles J., 127
Green, P. F., 141
Han, Charles, 177
Hill, R. F., 27
Hjelm, Rex P., 71
Ho, Derek L., 127
Hsieh, Alex J., 15
Inaoka, Seiji, 39
Jarrett, William L., 117
Karim, Alamgir, 177
Krishnamoorti, Ramanan, 1, 159
Kroenke, W. J., 27
Kuppa, V., 193
Limary, R., 141
Lincoln, Derek, 99
Lochhead, Robert Y., 85
Manias, E., 193
Mathias, Lon J., 117
Mays, Jimmy, 39
Mitchell, Cynthia A., 159
Nakamura, Yo, 39
Paine, R. T., 27
Park, Mi-kyoung, 39
Pruss, E. A., 27
Schmidt, Gudrun, 177
Schwierkowski, C., 27
Vaia, Richard A., 1, 99, 209
Wang, Yingfan, 39
Wood, G. L., 27
Zhou, Qingye, 39

Subject Index

A

- Adsorption. *See* Polymer adsorption to smectite clay
- Aerosol assisted vapor phase synthesis (AAVS)
 method for spherical morphology boron nitride, 31
 schematic of AAVS reactor, 32*f*
See also Boron nitride (BN)
- Aggregate structure, schematic of carbon black, 77*f*
- Anionic polymerization. *See* Surface initiated anionic polymerization
- Asphalt modification, commercial potential, 13
- Atomic force microscopy (AFM)
 edge of PS-*b*-PMMA film near organically modified layered silicate (excess) OLS(E)
 aggregates, 154, 155*f*
 grafted polystyrene on silicates, 51–52
- Laponite film morphology, 182*f*
- Laponite film morphology as function of PEO/clay ratio, 183*f*
- PMMA/OLS(E) nanocomposite surface, 149, 150*f*, 151*f*
- PS-*b*-PMMA/OLS(E)
 nanocomposites, 146, 147*f*
- PS-*b*-PMMA/OLS(S)
 (stoichiometric) nanocomposites, annealed, 146, 148*f*
See also Hybrid organic-inorganic nanocomposites

B

- Barrier packaging
 commercial activities, 12
 permeability of nanocomposites, 10–11
- Boron nitride (BN)
 aerosol assisted vapor phase synthesis (AAVS), 31
 alternatives, 31
 BN_xO_y aerosol powder, 32, 34
 chemical analyses, 31–32
 commercial applications of h-BN powders, 29
 description, 28
 development of particle filled composites, 29–30
 filler packing density, 30–31
 hexagonal BN preparation, 28–29
 lack of information on phonon transmission and thermal conductivity, 30
 particle-matrix interfacial resistance, 30–31
 preparing polymer composites using spherical powders, 34
 scanning electron micrograph (SEM) of BN_xO_y powder, 33*f*
 schematic of AAVS reactor, 32*f*
 SEM of annealed BN particles, 35*f*
 SEM of larger particles, 33*f*
 thermal conductivity of BN/organic polymer composites, 29
 transmission electron microscopy (TEM) of smooth BN spheres, 35*f*

- X-ray diffraction for BN_xO_y powders, 34*f*
- X-ray diffraction of crystalline BN particles, 36*f*
- Bright field electron microscopy, polymer/layered silicate nanocomposites, 106–107

C

- Carbon black
 - associations in elastomer, 80–81
 - basic scattering functions of sample HSA, 78*f*
 - basic scattering functions of samples XLH81, N330, and HSA, 79*f*
 - contrast variation, 74
 - determining complexity, 72
 - discovery of effect on rubber, 72
 - HSA structure factor in HSA–polyisoprene composite, 81*f*
 - internal structure and morphology, 81–82
 - measurements, 76
 - N330 and XLH81, 78–80
 - particle description, 80
 - particle structure characterization, 73–74
 - polydispersity and chemical heterogeneity, 75
 - Porod–law for particle areas per unit mass, 74
 - power law dependence of scattering for N330, 79
 - production, 80
 - scattering intensity, 73
 - scattering lengths of some light elements and hydrogen isotopes, 73*t*
 - schematic of aggregate structure, 77*f*
 - polypropylene and thermoplastic polyolefin nanocomposites, 12
 - rational behind commercial acceptance, 11–12

- small angle neutron scattering (SANS), 72–73
- structural information, 72
- structural parameters for HSA, 78*t*
- structure of experimental, HSA, 76, 78
- Carbon nanotube, commercial composites, 11
- Clay. *See* Organically modified clays; Polymer adsorption to smectite clay; Polymer/clay nanocomposites
- Clay/polymer nanocomposites. *See* Phase behavior prediction
- Coarse-grained simulations
 - flow of polymer melt, 210
 - See also* Polymer melt intercalation
- Commercialization
 - anticipated activities for nanocomposites, 12
 - asphalt modification, 13
 - benefits of nanocomposites, 8
 - commercial carbon nanotube composites, 11
 - commercial sources of treated clays, 9
 - developing technology with commercial potential, 12–13
 - elastomers, 13
 - electrical applications, 13
 - ethylene vinyl alcohol for packaging, 12
 - exfoliates, 8
 - fire resistance, 12–13
 - first nanocomposite polyamide-6/montmorillonite, 9–10
 - food and beverage packaging, 10
 - hexagonal boron nitride powders, 29
 - intercalates, 8
 - layered clay nanocomposites, 8–11
 - permeability of nanocomposites, 10–11
 - single layer nanocomposite barriers, 12
 - thermoset polymers, 13
- Confined polymers. *See* Molecular

- simulations of ultra-confined polymers
- Contrast variation
 - carbon black suspensions, 76, 78
 - method, 74
 - See also* Carbon black
- Copolymers
 - morphology of copolymer/OLS nanocomposites, 154–156
 - optical micrograph of polystyrene/montmorillonite nanocomposite, 150*f*
 - ordering and surface morphology, 152–154
 - See also* Diblock copolymer nanocomposites; Hybrid organic-inorganic nanocomposites
- Crystallization morphology
 - dendrite branches vs. clay mass fraction of polymer, 190*f*
 - effect of temperature and clay mass concentration, 184, 189
 - parameters influencing PEO/PMMA blend, 187*f*
 - propagating dendritic wavefront, 188*f*
- D**
- Delaminated structures, organic-inorganic nanocomposites, 41
- Density functional theory (DFT)
 - describing thermodynamic behavior of system, 62
 - free energy DFT, 60–62
 - interaction free energy, 61–62
 - multi-scale model, 59–63
 - single-particle distribution function (SDF), 60
 - Somoza–Tarazona formulation, 60
 - See also* Phase behavior prediction
- Diblock copolymer nanocomposites
 - average tactoid size and critical silicate fraction, 171
 - charge exchange capacity (CEC), 160
 - disordered state data for C18F based nanocomposites, 171
 - experimental, 161–162
 - experimental organically modified layered silicates (C18F, 2C18M, 2C18L), 161
 - influence of varying layered silicate on linear viscoelastic properties, 160
 - influences of adding layered silicate and size on viscoelastic properties, 170–171
 - longest relaxation time of lightly entangled polymer, 164
 - modulus shift factors, 169–170
 - monodisperse polystyrene–polyisoprene diblock (PSP119), 161
 - nanocomposites in ordered state, 171–172
 - order-disorder transition temperature, 164
 - preparation, 161
 - rheological measurements, 161–162
 - storage modulus mastercurve for 1 wt% C18F hybrid, 166*f*
 - storage modulus mastercurve for 5 wt% 2C18L hybrid, 168*f*
 - storage modulus mastercurves for 5 wt% C18F and 2C18M nanocomposites, 167*f*
 - structure, 162–164
 - temperature dependence of frequency shift factors, 167, 169*f*
 - understanding rheological properties, 160
 - viscoelastic data in ordered and disordered, 172, 173*f*
 - viscoelastic time-temperature superposed mastercurves for PSP119, 164, 165*f*
 - X-ray diffraction method, 161

XRD spectra, 162, 163*f*
 Diblock copolymers. *See* Hybrid organic-inorganic nanocomposites
 1,1-Diphenylethylene (DPE)
 self-assembled monolayers of
 initiator, 45
 synthesis, 43, 44*f*
 synthesis of 4-bromo-DPE, 43–44
 synthesis of chloride silane-DPE derivative, 45
 synthesis of 4-(11'-undecenyl)-DPE, 44–45
See also Surface initiated anionic polymerization
 Dispersion. *See* Polymer/clay nanocomposites
 Dynamic mechanical analysis, poly(methyl methacrylate) nanocomposites, 22–23

E

Elastomers
 carbon black associations in, 80–81
 commercial potential, 13
 Electrical applications, commercial potential, 13
 Emulsion polymerization
 analytical methods, 16, 18
 clarity for poly(methyl methacrylate) (PMMA), 19
 clay minerals acting as inhibitors for free radical, 22
 experimental, 16, 18
 nanocomposite temperature vs. viscoelastic properties, 22–23
 PMMA decomposition, 19, 22
 PMMA nanocomposites, 17
 schematic of silicate modification, 17
 stability at elevated temperatures, 19
 summary of PMMA and PMMA nanocomposite properties, 16*t*
 synthetic approaches, 16

transmission electron microscopy (TEM) of montmorillonite in PMMA, 18*f*
See also Poly(methyl methacrylate) nanocomposites
 End-functionalized chains. *See* Phase behavior prediction
 Environment, polymer nanocomposites, 1
 Ethylene vinyl alcohol (EVOH), commercial activities, 12
 Exfoliates
 layered clay nanocomposites, 8
 polymer-layered silicate structure, 101, 102*f*

F

Fillers. *See* Boron nitride (BN); Montmorillonite
 Finitely extensible nonlinear elastic (FENE) potential, polymer melt intercalation, 212
 Fire resistance, commercial potential, 12–13
 Food and beverage packaging, permeability, 10–11
 Free radical polymerization, clay minerals as inhibitors, 22
 Frequency shift factors, diblock copolymer nanocomposites, 167, 169*f*

G

Guinier approximation, particle structure characterization, 73–74

H

Hybrid organic-inorganic nanocomposites
 AFM (atomic force microscopy) micrograph of poly(methyl

methacrylate)/organically modified layered silicate (excess) (PMMA/OLS(E)) surface, 151*f*

AFM of edge of polystyrene (PS)-*b*-PMMA film near OLS(E) aggregates, 155*f*

AFM scan of PS-*b*-PMMA/OLS(E), 147*f*

AFM scan of PS-*b*-PMMA/OLS(stoichiometric) (S) annealed, 148*f*

arrangement of ordered symmetric PS-*b*-PMMA, 156*f*

behavior of OLS(E)/copolymer thin films, 154

characteristics of layered silicate materials, 144*t*

destabilization of thin films, 149, 152

dewetting of film near OLS(E) aggregates, 154, 156

effects of alkyl ammonium on copolymer, 156

experimental, 143–144

homopolymers and diblock copolymer, 143

intercalation of OLS(S) systems, 145–146

microscopy, 146–149

montmorillonite samples, Mnt, OLS(S), OLS(E), 143–144

morphology of copolymer/OLS nanocomposites, 154–156

narrow galleries deterring interpenetrating of organic polymers, 142

optical micrograph of surface of PS/Mnt thin film, 150*f*

ordering and surface morphology of (PS-*b*-PMMA) thin films, 152–154

preparation, 144

property dependence on microstructural features, 142

research of films, 143

role of thermodynamics in formation, 142–143

topographies of symmetric PS-*b*-PMMA thin films, 153*f*

X-ray diffraction (XRD), 144–146

XRD d_{001} -spacing results, 145*t*

I

Intercalates

- layered clay nanocomposites, 8
- organic-inorganic nanocomposites, 41
- polymer-layered silicate structure, 101, 102*f*

Intercalation

- behavior of polymers, 58
- monomers into clay galleries, 87–88
- polymer simulation, 215–218
- polymers into silicates and aluminosilicates, 210

See also Molecular simulations of ultra-confined polymers; Polymer melt intercalation

Interface, polymers with inorganic materials, 42

L

Laponite synthetic clay

- atomic force microscopy (AFM), 181, 182*f*
- morphology as function of poly(ethylene oxide) (PEO)/clay ratio, 181, 183*f*

See also Polymer/clay nanocomposites

Layered clay nanocomposites

- commercialization, 8–11
- exfoliates, 8
- first commercial, 9–10
- intercalates, 8
- permeability, 10–11

preparation, 9
 Layered nanostructures. *See* Polymer melt intercalation
 Layered silicates
 grafting polystyrene films, 42–43
 organically modified in nanocomposites, 42
See also Diblock copolymer nanocomposites; Molecular simulations of ultra-confined polymers

M

Melt. *See* Polymer melt intercalation
 Microelectronics industry, organic polymers, 28
 Models. *See* Phase behavior prediction
 Modulus shift factors, diblock copolymer nanocomposites, 169–170
 Molecular dynamics (MD) simulation. *See* Polymer melt intercalation
 Molecular simulations of ultra-confined polymers
 average distance between fast relaxing phenyls, 202*f*, 203
 backbone segmental dynamics, 203–204
 bond-angle potentials, 196*t*
 bond-stretching potentials, 196*t*
 comparison to experiments, 205–206
 covalence between phenyl relaxation and neighboring-surfactant relaxation, 205*f*
 covariance between fast phenyl dynamics and local surfactant density, 205*f*
 covariance of segmental relaxation and local density, 202–203
 density profiles across interlayer gallery, 198*f*
 density profiles normal to silicates, 201*f*
 effect of surfactant, 204–205
 force-fields for polystyrene (PS), 195–197
 formation of clusters of mobile phenyls, 203, 204*f*
 initial configurations and ensemble, 197
 mobile phenyls as function of temperature, 202*f*
 non-bonded interactions, 196*t*
 origin of dynamical heterogeneities, 201–204
 planar (improper) dihedrals, 196*t*
 polymers in nanoscopic confinements, 193–194
 proper dihedrals, 196*t*
 relaxation time/local structure covariance for mobile phenyls, 203
 segmental dynamics of PS in 2nm slit pores, 199–201
 simulation geometry, 194–195
 simulation model and details, 194–197
 structure of confined PS film, 197–199
 system under investigation, 195*f*
 time autocorrelation function of phenyl flip vector for intercalated PS phenyls, 200*f*
 Montmorillonite
 available groups dependence on pH, 88
 chemical interaction with polymer, 89–93
 clay characterization, 89*f*
 description, 86, 128
 nanocomposite with polyamide-6, 9–10
 nanoparticle reinforcement, 9
 organically modified, 128–130
 transmission electron microscopy (TEM) of dried clay/chloroform solution on copper grid, 186*f*

- wide angle X-ray scattering (WAXS)
of dry powders, 133*f*
See also Hybrid organic-inorganic
nanocomposites; Nylon
6/montmorillonite
nanocomposites; Organically
modified clays; Polymer
adsorption to smectite clay;
Polymer/clay nanocomposites
- Morphology
copolymer/organically modified
layered silicate (OLS)
nanocomposites, 154–156
dendritic branches vs. clay mass
fraction of polymer, 190*f*
effect of temperature and clay mass
concentration on blend
crystallization, 184, 189
Laponite (LRD) film morphology as
function of poly(ethylene oxide)
(PEO)/clay ratio, 183*f*
layered silicate, 105–108
LRD film morphology without PEO,
181, 182*f*
parameters influencing
PEO/poly(methyl methacrylate)
(PMMA) blend, 187*f*
polymer crystallite, 108–112
propagating dendritic wavefront
perpendicular to scratch, 188*f*
symmetric dendritic, of 30/70
PEO/PMMA blend, 185*f*
See also Polymer/layered silicate
nanocomposites
- N**
- Nanocomposites
concept, 2–4
properties, 57–58
See also Phase behavior prediction
- Nucleation. *See* Polymer/clay
nanocomposites
- Nylon 6. *See* Polymer/layered silicate
nanocomposites
- Nylon 6/montmorillonite
nanocomposites
annealed solid state ^{15}N NMR
spectra, 122
chemical structure and ^{13}C NMR
identifications, 120*f*
distance between surface bound
polymer chains, 123
first commercial, 9–10
implication of NMR spectroscopy to
modeling, 122–124
nylon 6 and nylon 6/clay composites,
reprecipitated and annealed, 121*f*
slice illustrating polymer end-group
binding and interface, 123*f*
solid state ^2H NMR spectroscopy,
122
solid state ^{15}N CP/MAS NMR
spectra, 120–122
solution ^{13}C NMR chemical shift
values, 120*t*
solution ^{13}C NMR spectroscopy, 118,
119*f*
- O**
- Organically modified clays
calculated scattered intensity with
different number of clay platelets
per tactoid, 138*f*
Cloisite 15A (C15A) sample, 128
Cloisite Na^+ (CNa) montmorillonite
sample, 128
coherent scattered intensity, 130
excess dimethyl dihydrogenated
tallow ammonium in unextracted
material, 139
experimental, 128–130
extracted C15A dispersed in
deuterated solvents, 135*t*
interactions between alkyl chains,

clays, and organic solvents, 136
 neutron scattering length density profiles, 132*f*
 SANS and WAXS (small-angle neutron and wide-angle X-ray scattering) data for CNa, 137–138
 SANS data of C15A dispersed in deuterated organic solvents, 135*f*, 136*f*
 SANS experiments, 129–130
 schematic of clay platelets in tactoids, 132*f*
 schematic of single core/layer C15A clay platelet, 132*f*
 sodium montmorillonite, 128
 solvent solubility parameter and C15A dispersion appearance, 129*t*
 spacing of platelets in dry CNa, 132, 133*f*
 suspensions of unextracted and extracted C15A in d-toluene, 136–137
 theoretical, 130–131
 total coherent scattered intensity, 130–131
 WAXS profiles of C15A dispersed in organic solvents, 134*f*
 WAXS profiles of C15A dry powders, 133*f*
 WAXS profiles of CNa dry powders, 133*f*
See also Hybrid organic-inorganic nanocomposites
 Organic-inorganic nanocomposites
 delaminated structures, 41
 intercalated nanocomposites, 42
 intercalated structures, 41
 interface, 42
 organically modified layered silicates (OLS), 42
 potential, 41–42
 Organic polymer composites. *See* Boron nitride (BN)

P

Permeability
 elastomers, 13
 layered clay nanocomposites, 10–11
 mechanism for altering, 10–11
 pH. *See* Polymer adsorption to smectite clay
 Phase behavior prediction
 density profiles for grafted chains, end-functionalized polymer, and non-functionalized polymer, 65*f*
 describing thermodynamic behavior, 62
 end-functionalized chains stabilizing morphologies, 69
 free energy density functional theory (DFT), 60–62
 free energy density vs. separation, 64*f*
 free energy profiles by self-consistent field (SCF) calculations, 63–66
 ideal free energy of clay particles, 61
 ideal free energy of polymer melt, 61
 interaction free energy, 61–62
 model system, 63
 multi-scale model, 59–63
 phase diagram for polymer/clay mixture, 67*f*, 68*f*
 phase diagrams, 66–67
 potential function, 62
 SCF calculations, 62–63
 schematic of combined DFT–SCF approach, 59*f*
 single-particle distribution function (SDF), 60
 Somoza–Tarazona formulation, 60
 Phase diagrams
 calculating for large-scale system, 58
 model for phase behavior predictions, 66–67
 polymer/clay mixture with end-functionalized chains, 67*f*, 68*f*

See also Phase behavior prediction

Polyacrylamide

adsorption isotherm of, on

montmorillonite, 95*f*

effect of pH on adsorbed ¹³C NMR spectra, 95*f*

Fourier Transform infrared (FTIR)

absorption frequency shifts for, and montmorillonite, 91*t*

FTIR spectrum, 90*f*

interaction with clay, 90–91

See also Polymer adsorption to

smectite clay

Poly(acrylamide-*co*-

acrylamidomethylpropanesulfonate)

FTIR absorbance frequency shifts,

94*t*

interaction with clay, 93

Poly(acrylamide-*co*-acrylic acid)

FTIR absorption frequency shifts for,

and montmorillonite, 93*t*

interaction with clay, 92–93

Poly(acrylamide-*co*-methacrylamido-*N-n*-propyl-3-(trimethyl)ammonium chloride)

effect of pH on adsorbed ¹³C NMR spectra, 96*f*

interaction with clay, 92

Polyamide-6/montmorillonite, first commercial, 9–10

Poly(caprolactam). *See* Nylon

6/montmorillonite nanocomposites;

Polymer/layered silicate

nanocomposites

Polyetheramines, oligomeric,

intercalating into clay, 87

Poly(ethylene oxide) (PEO)

clay in polymer matrix, 87

Laponite film morphology as

function of PEO/clay ratio, 183*f*

parameters influencing morphology

of PEO/PMMA blend, 187*f*

PEO/Laponite films, 180–184

PEO/Laponite films preparation, 178–179

PEO/PMMA/montmorillonite films preparation, 179–180

PEO/PMMA/organically modified montmorillonite films, 184

symmetric dendritic morphology of 30/70 PEO/PMMA film, 185*f*

See also Polymer/clay

nanocomposites

Polyisoprene

carbon black association in, 80–81

structure factor in composite, 81*f*

See also Carbon black

Polymer adsorption to smectite clay

adsorption isotherm of

polyacrylamide on

montmorillonite, 95*f*

algorithm for calculating bound

fraction, 93–94

anionic poly(acrylamide-*co*-acrylic acid), 92–93

cationic poly(acrylamide-*co*-methacrylamido-*N-n*-propyl-3-(trimethyl)ammonium chloride), 92

chemical interaction between

polymer and montmorillonite, 89–93

clay-based polymer nanocomposites, 86–88

effect of pH on adsorbed

polyacrylamide ¹³C NMR spectra, 95*f*

effect of pH on adsorbed

poly(acrylamide-*co*-

methacrylamido-*N-n*-

propyl(trimethyl)ammonium

chloride) ¹³C NMR spectra, 96*f*

FTIR spectrum of polyacrylamide,

90*f*

plateau adsorption values for

adsorbed polymers on sodium

montmorillonite, 90*t*

poly(acrylamide-*co*-

acrylamidomethylpropanesulfonate), 93, 94*t*

- polyacrylamide homopolymer, 90–91
 polymer conformation at clay interface, 93–96
- Polymer brushes, surface initiated
 polymerization (SIP), 40
- Polymer/clay nanocomposites
 AFM (atomic force microscopy) of Laponite (LRD) film morphology as function of poly(ethylene oxide) (PEO)/clay ratio, 181, 183*f*
 AFM of LRD film morphology without PEO, 181, 182*f*
 clay fillers modifying morphology and properties, 189–190
 concentration dependence of small angle neutron scattering (SANS), 184
 dendritic branches vs. clay mass fraction of polymer, 190*f*
 domains with excess PEO, 181, 184
 effect of temperature and clay mass concentration on blend crystallization morphology, 184, 189
 experimental, 178–180
 film morphology characterization methods, 180
 hectorite type clay LRD, 178–179
 heterogeneous nucleation process, 189
 nucleating polymer dendrites, 189
 organically modified
 montmorillonite (OMON) samples, 179–180
 parameters influencing morphology of PEO/poly(methyl methacrylate) (PMMA) blend, 187*f*
 PEO/Laponite film characteristics, 179*t*
 PEO/Laponite film preparation, 178–179
 PEO/Laponite films, 180–184
 PEO/PMMA/montmorillonite films preparation, 179–180
 PEO/PMMA/OMON films, 184
 phase detection imaging (PDI), 180
 propagation of dendritic wavefront, 188*f*
 roughness analyses, 180
 symmetric dendritic morphology of 30/70 PEO/PMMA film, 185*f*
 transmission electron microscopy (TEM) of dried clay/chloroform solution on copper grid, 186*f*
See also Phase behavior prediction
- Polymer/layered silicate nanocomposites (PLSN)
 bright field electron microscopy, 106–107
 contour intensity plots of wide-angle X-ray diffraction patterns, 110*f*, 111*f*
 demonstrating complex morphologies, 101
 effective aluminosilicate layer thickness, 108
 equilibrium distance between uniformly aligned and dispersed plates, 103*f*
 exfoliated structure, 101, 102*f*
 idealized morphologies, 101
 ideal nanoscale arrangements of silicate in PLSN, 102*f*
 intercalated structure, 101, 102*f*
 intermediate or mixed morphologies, 101
 layered silicate morphology, 105–108
 mean layer spacing for various plate thickness and volume fractions, 103
 new α -phase-crystallites transforming at elevated temperature, 112
 nylon 6–montmorillonite nanocomposites (NCH5, NCH2, and NLS4), 105–108
 physical properties, 100
 PLSN morphology, 100–104

- polymer crystallite morphology, 108–112
- processing-dependent morphologies, 103–104
- processing/morphology relationships, 100
- secondary mesostructure, 109, 112
- sensitivity of diffractogram to sample alignment, 104, 105*f*
- small-angle and wide-angle X-ray scattering profiles, 108–109
- small angle scattering data for NCH5, NCH2, and NLS4, 106*f*
- synthesis, 210
- X-ray scattering, 104–105
- See also* Hybrid organic-inorganic nanocomposites
- Polymer melt intercalation
- center of mass mean squared displacements vs. time, 219, 221*f*
 - change in inter-sheet angle with intercalation, 218
 - coarse-grained molecular dynamics (MD) simulations, 221–222
 - distances and angles between mean planes of adjacent sheets, 215, 217
 - extending simulations to larger dimensions, 222
 - finitely extensible nonlinear elastic (FENE) potential, 212
 - flexible vs. stiffer sheets, 221–222
 - intercalation in orderly fashion, 217–218
 - Lennard–Jones potential, 212
 - local sheet stiffness, 219
 - necessity of defining layered nanostructure explicitly, 222
 - polymer intercalation, 215–218
 - polymer-sheet assembly by NVT-MD simulations, 212–213
 - polymer-sheet configuration after 10,000 MD steps, 216*f*, 220*f*
 - polymer-sheet interaction and sheet-sheet interactions, 214–215
 - quantifying sheet sliding phenomenon, 219
 - realistic representation of process, 210–211
 - refinement of polymer-sheet structure with longer simulation times, 218
 - sheet sliding, 219
 - simulation details, 211–213
 - simulation results, 214*t*
 - stacks of flexible sheets, 222
 - swelling of gallery by polymer chains, 215
 - time evolution of inter sheet separation and angle between mean plane of sheets, 217*f*
- Polymer nanocomposites (PNCs)
- advantages, 1
 - arrangement of constituents, 3–4
 - challenge in developing, 2
 - clay-based, 86–88
 - dimensions of added nanoelements, 3
 - internal inorganic-polymer interfaces, 3
 - isotropic and anisotropic nanoscopically-sized particles, 2
 - large internal interfacial area, 2
 - nanocomposite concept, 2–4
 - overview, 4
 - See also* Commercialization
- Polymers, reinforcement alternative, 1
- Poly(methyl methacrylate) (PMMA)
- characterization of PMMA end-tethered montmorillonite (MMT) samples, 23, 24*t*
 - clarity, 19
 - clay minerals as inhibitors in free radical polymerization, 22
 - decomposition, 19, 22
 - dynamic mechanical analysis, 23*f*
 - experimental, 16–18
 - parameters influencing morphology of poly(ethylene oxide) (PEO)/PMMA blend, 187*f*

- PEO/PMMA/montmorillonite films
preparation, 179–180
- PEO/PMMA/OMON (organically modified montmorillonite) films, 184
- properties, 16*t*
- schematic of emulsion polymerization, 17
- stability at elevated temperatures, 19
- symmetric dendritic morphology of 30/70 PEO/PMMA film, 185*f*
- synthetic approaches, 16
- thermal stability, 22
- thermogravimetric traces in air, 21*f*
- thermogravimetric traces in nitrogen, 20*f*
- transmission electron microscopy (TEM), 18–19
- viscoelastic properties as function of temperature, 22–23
- See also* Hybrid organic-inorganic nanocomposites; Polymer/clay nanocomposites
- Polypropylene (PP) nanocomposites, commercial activities, 12
- Polystyrene (PS)
- clay in polymer matrix, 87
- comparing simulation to experiments, 205–206
- effect of surfactant, 204–205
- force fields for simulation, 195–197
- grafting from silicate surface, 42–43
- origin of dynamical heterogeneities, 201–204
- polymerization and characterization at surface, 49–51
- polymerization conditions and results, 50*t*
- polymerization procedure, 46–47
- segmental dynamics in 2nm slit pores, 199–201
- structure in confined film, 197–199
- See also* Hybrid organic-inorganic nanocomposites; Molecular simulations of ultra-confined polymers; Surface initiated anionic polymerization
- R**
- Reinforcement
montmorillonite, 9
polymers, 1
- Rheological properties. *See* Diblock copolymer nanocomposites
- S**
- Scanning electron microscopy (SEM)
annealed particles of boron nitride, 35*f*
BN_xO_y powder, 33*f*
- Self-assembled monolayers, 1,1-diphenylethylene (DPE) initiators, 45
- Self-consistent field (SCF) theory
free energy density vs. separation, 64*f*
free energy profiles, 63–66
multi-scale model, 59–63
SCF calculations, 62–63
See also Phase behavior prediction
- Sheet sliding, simulation, 219
- Silicates. *See* Layered silicates
- Simulations. *See* Molecular simulations of ultra-confined polymers; Polymer melt intercalation
- Single layer nanocomposite barrier, commercial activities, 12
- Small angle neutron scattering (SANS)
basic scattering functions of carbon black HSA, 78*f*
concept, 72–73
organically modified clay C15A in deuterated organic solvents, 135*f*, 136*f*, 137*f*

- scattering intensity, 73
 scattering lengths of light elements
 and hydrogen isotopes, 73*t*
 shape scattering functions for carbon
 black samples, 79
See also Carbon black
- Small-angle X-ray scattering (SAXS)
 nylon 6 and nylon 6 nanocomposites,
 109*f*
 polymer/layered silicate
 nanocomposites, 106*f*, 107
- Smectite clay. *See* Polymer adsorption
 to smectite clay
- Sodium montmorillonite
 description, 128
See also Montmorillonite;
 Organically modified clays
- Solid state ^2H NMR spectroscopy,
 nylon 6/montmorillonite
 nanocomposites, 122
- Solid state ^{15}N NMR spectroscopy,
 nylon 6/montmorillonite
 nanocomposites, 120–122
- Solution ^{13}C NMR spectroscopy,
 nylon 6/montmorillonite
 nanocomposites, 118–120
- Structure. *See* Carbon black;
 Polymer/layered silicate
 nanocomposites
- Surface initiated anionic
 polymerization
 AFM (atomic force microscopy)
 image of grafted polymer, 52*f*
 AFM investigations, 51–52
 characterization methods of surface
 and polymer films, 45–46
 1,1-diphenylethylene (DPE)-
 chlorosilane synthesis, 43, 44*f*
 immobilization and activation of
 DPE initiator, 49*f*
 parameters for future investigation,
 54
 polymerization and characterization
 of surface, 49–51
 polymerization conditions and
 results, 50*t*
 polymerization procedure for
 polystyrene (PS), 46–47
 polymerization set-up under high
 vacuum, 47*f*
 PS on silicate surface, 42–43
 schematic of oxidation process,
 48*f*
 self-assembled monolayers of
 initiator, 45
 synthesis and immobilization of
 initiator, 47–49
 synthesis of 4-(11'-undecenyl)-DPE,
 44–45
 synthesis of 4-bromo-DPE,
 43–44
 synthesis of chloride silane-DPE
 derivative, 45
 synthesis of initiator, 43–45
 XPS measurements, 52, 54
 XPS of initiator surface before and
 after polymerization, 53*f*
- Surface initiated polymerization (SIP),
 preparing tethered polymer chains,
 40
- ## T
- Tethered polymers
 grafting from approach, 40, 41*f*
 grafting to approach, 40, 41*f*
 surface initiated polymerization
 (SIP), 40
See also Surface initiated anionic
 polymerization
- Thermal conductivity, boron
 nitride/organic polymer composites,
 29
- Thermogravimetric analysis,
 poly(methyl methacrylate)
 nanocomposites, 19–22
- Thermoplastic polyolefin (TPO)

- nanocomposites, commercial activities, 12
- Thermoset polymers, commercial potential, 13
- Thin films. *See* Copolymer thin films; Hybrid organic-inorganic nanocomposites
- Transmission electron microscopy (TEM)
 - boron nitride spheres, 35*f*
 - dried clay/chloroform solution on copper grid, 186*f*
 - poly(methyl methacrylate) nanocomposites, 18–19

U

- Ultra-confined polymers. *See* Molecular simulations of ultra-confined polymers

V

- Viscoelastic properties
 - data for ordered and disordered states of diblock copolymer nanocomposites, 171–172, 173*f*
 - frequency shift factors for diblock copolymer nanocomposites, 167, 169*f*
 - modulus shift factors for diblock copolymer nanocomposites, 169–170
 - poly(methyl methacrylate) nanocomposites, 22–23
 - storage moduli for hybrid

- nanocomposites, 166*f*, 167*f*, 168*f*
- time-temperature superposed linear viscoelastic moduli for diblock copolymer nanocomposites, 165*f*
- See also* Diblock copolymer nanocomposites

W

- Wide-angle X-ray diffraction (WAXD), polymer/layered silicate nanocomposites (PLSN), 104–105, 109*f*
- Wide angle X-ray scattering (WAXS) organically modified clay C15A dry powders, 133*f*
- organically modified clay C15A in deuterated organic solvents, 134*f*

X

- X-ray diffraction (XRD)
 - BN_xO_y powders, 34*f*
 - crystalline boron nitride particles, 36*f*
 - organically modified layered silicates, 144–145
 - PMMA end-tethered montmorillonite samples, 23, 24*t*
 - PMMA/OLS, PS/OLS, and copolymer/OLS, 145–146
- X-ray photoelectron spectroscopy (XPS), grafted polystyrene on silicates, 52–54
- X-ray scattering, polymer/layered silicate nanocomposites (PLSN), 104–105, 109*f*